https://ntrs.nasa.gov/search.jsp?R=19880003924 2020-03-20T09:13:18+00:00Z

NASA TM-88227

NASA Technical Memorandum 88227

NASA-TM-88227 19880003924

N88-13306

Interferometric Data for a Shock-Wave/Boundary-Layer Interaction

Stephen E. Dunagan, James L. Brown, and John B. Miles

FOR REFERENCE

NOT TO BE TAKEN FROM THIS ROOM

September 1986

LIBRARY COPY

OCT 20 1986

LANGLEY RESEARCH CENTER
LIBRARY, NASA
HAMPTON, VIRGINIA

NF00941

National Aeronautics and Space Administration

NASA Technical Memorandum 88227

Interferometric Data for a Shock-Wave/Boundary-Layer Interaction

Stephen E. Dunagan,
James L. Brown, Ames Research Center, Moffett Field, California
John B. Miles, University of Missouri, Columbia, Missouri

September 1986

National Aeronautics and
Space Administration

Ames Research Center
Moffett Field, California 94035

N88-13306#

This Page Intentionally Left Blank

ABSTRACT

An experimental study of the axisymmetric shock-wave/ turbulent boundary-layer strong-interaction flow generated in the vicinity of a cylinder-cone intersection has been conducted. The present data are useful in the documentation and understanding of compressible turbulent strong-interaction flows, and are part of a more general effort to improve turbulence modeling for compressible two- and three-dimensional strong viscous/inviscid interactions. The nominal free-stream Mach number was 2.85. Tunnel total pressures of 1.7 and 3.4 atm provided Reynolds number values of $18 \cdot 10^6$ and $36 \cdot 10^6$ based on model length. Three cone angles (12.5°, 20°, and 30°) were studied giving negligible, incipient, and large scale flow separation respectively. The initial cylinder boundary layer upstream of the interaction had a boundary-layer thickness of 1.0 cm. The subsonic layer of the cylinder boundary layer was quite thin, and in all cases, the shock wave penetrated a significant portion of the boundary layer. Owing to the thickness of the cylinder boundary layer, considerable structural detail was resolved for the three shock-wave/boundary-layer interaction cases considered.

The primary emphasis in this study was on the application of the holographic interferometry technique to these flow cases. The density field was deduced from an interferometric analysis based on the Abel transform. Supporting data were obtained using a 2-D laser velocimeter, as well as mean wall pressure and oil flow measurements. The attached flow case was observed to be steady, while the separated cases exhibited shock unsteadiness. Comparisons with Navier-Stokes computations using a two-equation turbulence model are presented. The study illustrates the utility of holographic interferometry for detailed instantaneous flow-field characterization and provides documented data useful in the evaluation of computational schemes.

NOMENCLATURE

a_i	least-squares Abel transform coefficients
a^*	speed of sound at critical conditions
f_i	Abel transform step function
F_i	Abel transform integral function
I	maximum number of annular elements
K	Gladstone-Dale constant
M_∞	free-stream Mach number
n	refractive index
n_0	refractive index value at reference location
N	fringe number function
$\tilde{N}$	approximated fringe number function
P	static pressure
P_t	free-stream total pressure
r	radial coordinate
Re_L	Reynolds number based on length
T	static temperature
T_t	free stream total temperature
u	velocity component in x direction
u_e	u component at edge of boundary layer
x	coordinate along tunnel axis, positive downstream
x_s	location of upstream oil accumulation
x_r	location of downstream oil accumulation
y	vertical coordinate positive upward
y_{shock}	y location of shock
y_1^+	nondimensional boundary layer coordinate at first computational mesh point
z	horizontal component across tunnel
z_1, z_2	z locations of tunnel walls

δ	boundary layer thickness
θ	model cone angle
λ	laser wavelength
ρ	density
ρ_t	free-stream total density
$\Phi(y)$	finite-fringe free-stream fringe number function

Abel transform subscripts

- i subscript for elements of radial phase object field
- j subscript indicating approximated data coordinate
- k subscript indicating raw data coordinate

ACKNOWLEDGEMENTS

The author would like to express appreciation to Dr. John Miles for the expert and friendly instruction provided throughout the duration of this graduate study program. A special thanks is given to Dr. Jim Brown for the encouragement and guidance offered in the experimental phase of this effort. Thanks is given to Dr. C. C. Horstman for his contribution of the Navier-Stokes computations reported herein. Thanks is also given to Mr. Joe Marvin and Mr. Marvin Kussoy for their contributions to the larger experimental program encompassing this specific study. Finally, a word of gratitude is offered to Dr. Bill Warmbrodt for his support in the reporting phase of this work.

Financial support for this effort was provided in part by a NASA Post-Baccalaureate Program grant.

This work is dedicated to my wife Nancy. Her loving support and personal sacrifice have been significant factors contributing to the realization of this objective.

INTRODUCTION

Statement of the Physical Problem

Compressible, turbulent, strong viscous/inviscid interactions often dominate in establishing the flow field over supersonic aerodynamic bodies. One such interaction is the shock-wave/boundary-layer interaction (SW/BLI) which is characterized by significant normal and streamwise pressure gradients, as well as considerable upstream influence effects in the boundary layer. These phenomena frequently precipitate boundary-layer separation.

The accurate simulation of SW/BLI flows is best accomplished with Navier-Stokes computational methods when a suitable turbulence model is employed. However, shock unsteadiness related to the turbulence field occurs when the flow separates, and these computational methods are not able to account for such an effect at this time. Additionally, the boundary-layer turbulence field may include nonequilibrium effects not incorporated in the more widely used turbulence models. A more comprehensive understanding of these interactions is required to enhance accurate turbulence modeling and thereby permit accurate flow prediction to be achieved (Kline, Cantwell, & Lilley, 1982).

Motivation for the Study

With the current emphasis on the development of predictive computational techniques for aerodynamic design and analysis, an essential requirement is the extensive documentation of experimental flows for the verification of computational methods. Documentation of supersonic strong interactions is, however, complicated by the sensitivity of these flows to the intrusive disturbances of pressure or hot-wire probes, as well as undesired end-wall three dimensionality. The accuracy of hot-wire probes in supersonic flows is a matter of continuing question. Certainly, should flow reversal occur, the use of pressure and hot-wire probes is problematic.

Accurate flow-field documentation of compressible strong interactions may be accomplished, however, with nonintrusive methods such as laser velocimetry and holographic interferometry. Within inviscid regions, laser velocimetry and holographic interferometry provide a redundant measurement capability since the velocity and density fields are directly related. Within viscous regions, the two laser, flow-field diagnostic techniques provide a complementary measurement capability useful in understanding these compressible, viscous shear layers.

Acquired data contribute to the documentation of two- and three-dimensional (2-D and 3-D) strong interaction flows of similar geometry. Holographic interferometer instrumentation has been added to the High Reynolds Number Facility at Ames Research Center (along with an evaluation of instrumentation performance in the measurement of supersonic axisymmetric flows). Finally, this study complements contemporary efforts to improve flow and turbulence modeling of compressible, strong interaction flows.

Scope of the Investigation

An experimental study was conducted of the axisymmetric shock-wave/turbulent-boundary-layer, strong-interaction flow generated in the vicinity of a cylinder-cone intersection. An axisymmetric expansion-fan/turbulent-boundary-layer interaction generated at a subsequent (downstream) cone-cylinder intersection has also been included in this study but with secondary emphasis. The mean flow-field characteristics of these strong interactions have been stressed, with a primary reliance on the nonintrusive holographic interferometry measurement technique. Oil-flow, wall-pressure, and laser-velocimeter (LV) measurements have been included to augment interferometric data analysis and to provide experimental redundancy. Three cone angles representing negligible (12.5°), incipient (20°), and large-scale separation (30°) were considered. Two different tunnel total pressures (1.7 and 3.4 atm) provided variation in Reynolds number. This experimental study was conducted as

part of a larger program to improve flow and turbulence modeling of compressible 2- and 3-D strong interactions.

In this study, Navier-Stokes computations were included with only minimal attention to computational details, primarily to illustrate the utility of interferometric data in code performance assessment. Mean flow parameters (shock position, density, and velocity fields) based on the holographic interferometry and laser velocimetry data are compared with Navier-Stokes computations. These comparisons provide not only an evaluation of code performance but also, through the consistent physical models incorporated in the Navier-Stokes solver, a means of verifying agreement of the two primary experimental methods.

REVIEW OF LITERATURE

The concept of the boundary layer wherein the effect of viscosity is limited to regions close to surfaces was explained by Prandtl (1928). Viscous effects in the boundary layer frequently dominate in establishing the global flow field. The viscous-inviscid interaction is an important mechanism by which features of the inviscid field may strongly affect boundary-layer flow and vice versa. One strong viscous-inviscid interaction is the SW/BLI which occurs in supersonic flows at a compression corner or when an externally generated shock impinges on a boundary layer. At transonic speeds, on the upper surface of an airfoil where flow is locally supersonic, a similar interaction may be observed. Though these shock waves may be of lower strength, their effect on the airfoil aft-section boundary layer, which is already encountering an adverse-pressure gradient, are often severe. A graphic representation of each of these interactions is shown in figure 1.

An early experiment in which SW/BLI effects were apparent was reported by Ferri (1940). He observed a repeatable pressure rise (from surface-pressure measurements) and associated boundary-layer separation (from shadowgraph data) near the trailing edge of supersonic airfoils upstream of the trailing-edge shock waves. Following World War II, more detailed investigations for each of the various SW/BLI were conducted (Ackeret, Feldman & Rott, 1947; Fage & Sargent, 1947; Liepmann, 1946). The importance of these flows from practical vehicle design, as well as fundamental fluid dynamics perspectives, was soon widely recognized. In the decades since, many theoretical, analytical, and experimental investigations have been conducted and a great deal of literature on the subject is available. Two extensive reviews (Green, 1970; Adamson & Messiter, 1980) provide a good summary of the literature for 2-D flows. A monograph by Settles (to be published in 1986) represents a current literature review of 3-D interactions with turbulent boundary layers. This literature provides a good basis for my review.

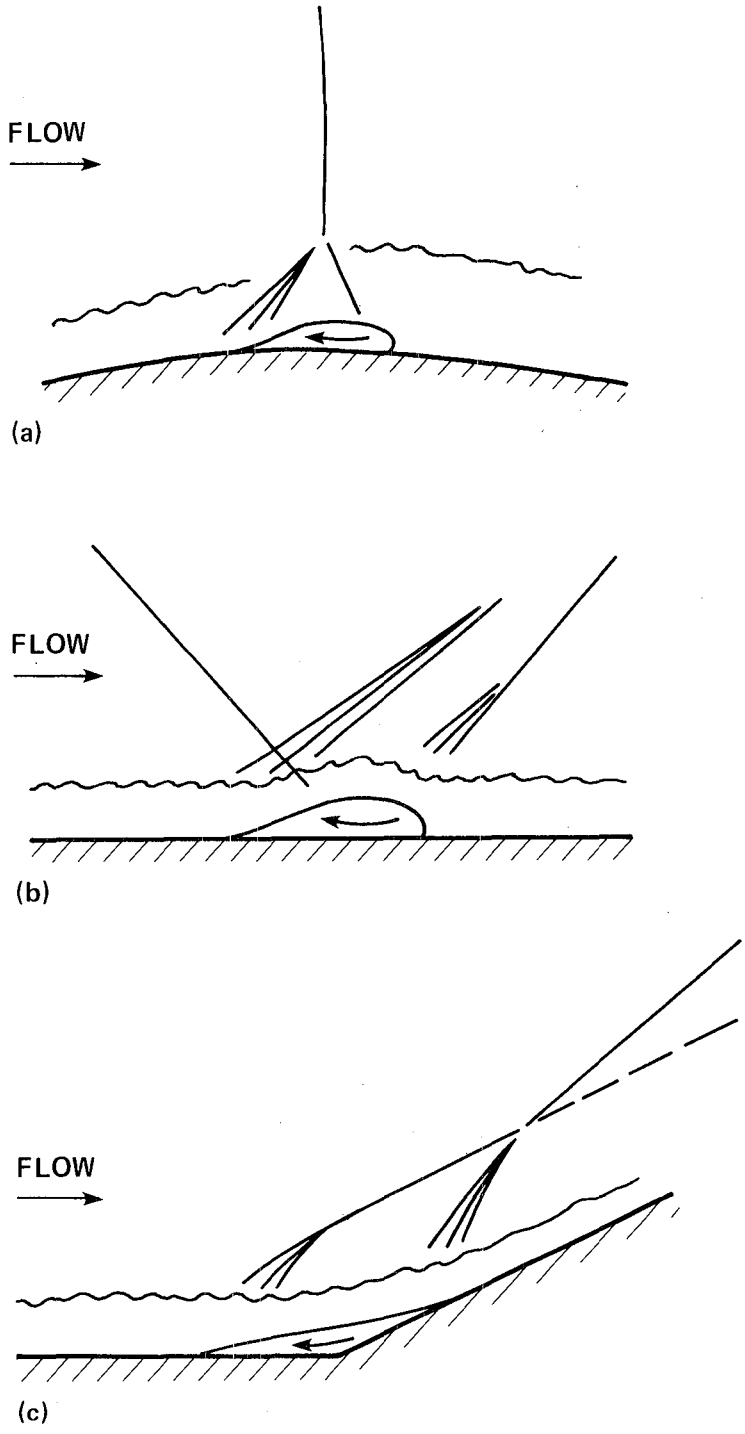

Figure 1. Examples of shock-wave/boundary-layer interactions. (a)Normal shock impinging, (b)oblique shock impinging, and (c)compression corner.

To reasonably limit the topic, I primarily focus on studies with an experimental emphasis. Attention to analytical or computational details is limited to an assessment of their impact on experimental work. Compression-corner or oblique shock impingement in supersonic flows will be emphasized. Transonic SW/BLI work is discussed only when experimental techniques are of particular interest.

Shock-Wave/Boundary-Layer Interactions

Early experimental investigations of the SW/BLI were often included in general studies of separation phenomena such as that of Chapman, Kuehn, & Larson (1957). The interaction was viewed as one means of imposing a strong adverse-pressure gradient on the boundary layer. Much attention was given to the development of analytical and semiempirical formulations (Gadd, 1953; Gadd, Holden, & Regan, 1954; Lighthill, 1953; Gadd, 1957) to predict the onset and extent of shock-induced separation and the accompanying surface-pressure distributions. Experimental results, typically reported in terms of surface-pressure distributions, upstream influence parameters, and occasionally pitot-static pressure (velocity) profiles were often subject to wide disparity and caused controversy as reported by Bogdonoff (1954) and Gadd & Holden (1954). The question of flow two dimensionality was often held responsible for the lack of agreement among researchers.

The principal cause of mean-flow three dimensionality in planar 2-D wind tunnel flows is the interaction of the wall-boundary layers with the shock and model-boundary layer. Such interaction may be avoided if an axisymmetric rather than planar 2-D configuration is employed. Kuehn (1961) investigated the shock-induced separation of a turbulent boundary layer in the compression-corner region of an axisymmetric cone-cylinder configuration and increased the understanding of conditions for which separation can be expected. This work is particularly relevant to this study.

Kuehn (1961, 1959), as well as Chapman et al. (1957), used the 1- by 3-Foot

Supersonic Tunnel at NASA Ames Research Center for their studies. This was a continuous operation tunnel with provision for continuously variable total pressure between the limits of 2 and 59 psia, and continuously variable Mach number (by means of a flexible nozzle) in the range of 1.5 to 6. Sting-mounted models consisted of a basic cylindrical section to which various nose and flare sections were mated. Conic, rounded, and blunt nose sections were used. The cylinder boundary layer was tripped by several different means to ensure a transition to turbulence. Several flares with different cone angles were investigated to determine the effect of different total pressure rises on separation.

Models were instrumented with static pressure ports to obtain surface- pressure distributions. Pitot-pressure surveys of the unperturbed turbulent boundary-layer were made with the flare sections removed to obtain values for the boundary layer thickness, δ, and the velocity-profile shape parameter. Shadowgraph techniques, with either a continuous source for real-time flow visualization or a spark source for photographic recording, were also used.

Kuehn (1961) reported data in the form of surface-pressure distribution curves, each with an accompanying shadowgraph to aid in interpretation of the physical phenomena. The criterion used to experimentally identify the onset of separation is the appearance of a "hump" (i.e., three distinct inflection points) in the surface-pressure distribution curve local to the compression corner. Comparisons were made among various permutations of the model configurations in an attempt to isolate and identify the unique contributions of shock strength (overall pressure rise), Mach number, and Reynolds number to the onset and extent of separation. Secondary effects resulting from model nose configuration, boundary-layer tripping techniques, and cylinder length were also examined. Finally, the effects of heat transfer and compression-corner geometry (sharp versus rounded corner) were briefly considered.

Comparisons with planar 2-D flows (Kuehn, 1959) were made and the trend of an increasing pressure rise to induce separation with decreasing cylinder radius

($r = \infty$ corresponds to planar 2-D) was reported. Kuehn concluded with qualitative descriptions of the effects of the previously mentioned parameters on the onset of separation. Most notably, a decrease in the tendency toward separation with increasing Mach number or with decreasing Reynolds number or pressure rise was reported. This separation tendency correlation with decreasing Reynolds number is in disagreement with other experimental work reported.

Throughout the decade, 1960-1970, several experimental investigations (Lewis, Kubota, & Lees, 1968; Rose, Murphy, & Watson, 1968; Green, 1970) of the 2-D, compression-corner, or externally generated SW/BLI were conducted. The resulting data were in the form of surface-pressure distributions with supporting shadowgraph or schlieren-flow visualization, as well as surface oil-flow patterns, and occasional pitot-pressure boundary-layer surveys. Throughout these studies, the importance of flow two dimensionality was recognized; though indications are that most experimental flows suffered from significant 3-D effects (Reda & Murphy 1972).

Reda & Murphy (1972) investigated the flow associated with the impingement of a nominally 2-D, externally generated shock on a fully developed, turbulent wall-boundary layer. This study addressed several fundamental aspects of the SW/BLI including the documentation of conditions for incipient separation, the processes of flow separation, and the effect of Reynolds number on separation. Experimental techniques were rather typical of then current experimental trends and included surface-pressure and orifice-dam measurements, schlieren and oil-flow surface pattern flow visualization, and pitot-static pressure profiles.

This study was conducted in the NASA Ames 8- by 8-Inch Supersonic Tunnel. Thorough documentation of the empty tunnel flow verified the quality of the experimentally generated flow. Results of this study emphasize the inherent three dimensionality of the shock-induced separation phenomena and associate such three dimensionality with channel side-wall and corner boundary-layer effects. Spanwise surface-pressure uniformity was identified as a necessary but not sufficient condi-

tion for overall flow two dimensionality. The extent of separation was found to be nonlinear with incident shock strength. The observed overall pressure rise required for incipient separation was in agreement with published results (Bogdonoff, 1954; Kuehn, 1959; Bogdonoff, Kepler, & San Lorenzo, 1953; Pickney, 1966; Bogdonoff, 1955; Hammitt & Hight, 1959). However, this agreement is rather unfortunate in the sense that published data were likely subject to a departure from strict two dimensionality as observed in these data.

An investigation by Settles & Bogdonoff (1973) of the axisymmetric compression-corner SW/BLI also addressed the questionable effect of Reynolds number on the onset of shock-induced separation, with a primary emphasis on the acquisition of data in the moderate to high Reynolds number range. This test was performed in the Princeton University 8- by 8-Inch High Reynolds Number Facility at a nominal Mach number of 2.9. The model used was a 2-inch diameter cylinder with an ogive nose having various interchangeable flare attachments. Surface-pressure and pitot-survey data, and schlieren flow visualization photographs were presented. Separation was quantified by the standard upstream influence parameter obtained from surface-pressure distribution curves. The authors reported a flare angle of $16 \pm \frac{1}{2}^{\circ}$ for incipient separation. The effect of Reynolds number on upstream influence was observed to be negligible for attached flows. However, a decrease in upstream influence for increasing Reynolds number in the case of shock-induced separation was reported.

Contemporary investigations by Law (1975) and Roshko & Thomke (1976) emphasize a continuing question of the Reynolds number effect on incipient separation. Law conducted investigations of planar 2-D, compression-corner, and externally generated shock-impingement interactions in the Aerospace Research Laboratories High Reynolds Number 8- by 8-Inch Tunnel at the Wright-Patterson Air Force Base (WPAFB) at a nominal free-stream Mach number of 3. Data were obtained to identify variation of the upstream influence parameter, onset of separation, and

structure of the interaction for several Reynolds number values. Surface-pressure and holographic- interferometry data were taken, along with schlieren and oil-flow photographs for flow visualization.

From the results, Law (1975) concluded that for an increasing Reynolds number, the overall pressure rise required for incipient separation increased. Accordingly, length of separation and upstream influence decreased with increasing Reynolds number for a given shock strength. For a fixed Reynolds number (based on boundary-layer thickness), the overall pressure rise required for separation was reported to be approximately equal for both the compression-corner and externally generated shock/boundary-layer interactions. Three-dimensional effects associated with the side-wall boundary layers were reported to be significant but treatable by reducing the span of the shock generator.

In their investigation, Roshko & Thomke (1976) used the 4- by 4-Foot Trisonic Wind Tunnel at the McDonnell-Douglas Aerophysical Laboratory. An axisymmetric (open center) compression-corner-type model (12-inch cylinder diameter) was used, providing boundary-layer Reynolds numbers of 10^5 to 10^6. Flare angles of 9° to 40° were used to vary the strength of the interaction.

A primary objective of this investigation was to examine the effects of Reynolds number, Mach number, and flare angle over as broad a range as possible in an effort to provide a global picture for comparison with the more limited and Mach number localized data in the literature. Surface-pressure, surface-temperature, and pitot-pressure survey data were analyzed, along with schlieren photographs. The rather extensive results were presented in terms of the upstream influence parameters plotted as a function of Reynolds number for various flare angles at various Mach numbers. Trends are somewhat complex, but in general a decrease in interaction length with increasing Reynolds number was observed for all combinations of Mach number and flare angle.

The mutually contemporary studies of Settles & Bogdonoff (1973), Law (1975),

and Roshko & Thomke (1976) are compatible in many respects. These three investigations provide a basis for making some observations of the height of development in experimental SW/BLI studies circa 1975. Experimental characterization of flows relied heavily on surface-pressure data for the determination of flow separation. Optical flow-visualization techniques were used extensively. Surface oil flow as a technique for identifying separation, as well as flow two dimensionality was popular, though the validity of oil-flow data as a means of quantifying separation was (and still is) being challenged. The ability to directly measure the flow field away from the model surface was rather limited. Pitot surveys were occasionally used, particularly to document the boundary layer in the absence of the shock wave. Typically, intrusive probes have been used to measure the supersonic or reversed flow regions. These probes are ineffective in measuring such flows when upstream influence is an essential mechanism (i.e., SW/BLI). The questions surrounding the use of intrusive probes in these cases highlight the need for nonintrusive measurement techniques.

The interpretation of experimental data was often directed at determining trends in the effect of various flow parameters (i.e., Reynolds number, Mach number, and shock strength) on the degree of separation. While some trends were uniform from experiment to experiment, others (specifically, Reynolds number dependency) were subject to disparity. Furthermore, the fundamental defining mechanisms of separation were (and still are) not universally agreeable. As an additional complexity, the existence and effect of inherent flow three dimensionality in nominally 2-D flows continues to be a problem. I would agree with Roshko (1976) that "the last word on this problem has not yet been written."

Two important developments were beginning to strongly influence the nature of SW/BLI research in the period from 1975 to 1980. Firstly, the advent of laser Doppler velocimetry and holographic interferometry as research tools for the study of aerodynamic flows was making nonintrusive flow-field documentation possible.

Secondly, advances in computer hardware development and computational fluid dynamics (CFD) were making the numerical simulation of complex SW/BLI flows more feasible. As CFD research efforts assumed a role of high priority, experimental studies were formulated to address the needs of researchers for data to guide in the mathematical modeling of flows, particularly in the area of turbulence modeling. Nonintrusive experimental documentation of the global flow field became highly desirable.

An experimental study by Horstman, Kussoy, Coakley, Rubesin, & Marvin (1975) was undertaken to test and guide computational techniques as applied to the solution of a SW/BLI flow. The flow was modeled using the mass-averaged Navier-Stokes equations for compressible flow in cylindrical coordinates with assumed axial symmetry. A predictor-corrector finite-difference scheme of MacCormack (1971) was used solve the differential equations, and the algebraic eddy-viscosity model of Cebeci & Smith (1971) provided turbulence closure. The experimental facility used for this study was the NASA Ames 3.5 Foot Hypersonic Wind Tunnel. Tests were made at a Mach number of 7.2, a total pressure of 34 atm, and a total temperature of 695° K. The model consisted of a cone-ogive cylinder with a concentric, annular, external shock generator and represents one of the few external shock-impingement configurations having axial symmetry. Static-pressure taps, thermocouples, pitot-pressure probes, static-pressure probes, total-temperature probes, and floating element skin-friction gages were used.

Profiles and contours of experimentally measured or deduced mean values for several flow parameters (P, T, ρ, u) were presented and used to evaluate computed parameters. These data were useful in assessing the validity of the numerical simulation and guiding turbulence modeling changes. This study emphasizes the sufficiency of the algebraic model in the calculation of zero-pressure gradient flows and predicting the overall character of the flow field, but shows this zero-equation model to be seriously deficient in predicting the details of the separated region.

Investigations of East (1976), Modarress & Johnson (1979) and Robinson, Seegmiller, & Kussoy (1983) emphasized the need for nonintrusive (optical) instrumentation in the study of SW/BLI flows and particularly focused on the use of LV. The report of Modarress & Johnson (1979) presented laser Doppler velocimeter data for the planar 2-D, externally generated shock-impingement interaction. This investigation was conducted in the Ames 8- by 8-Inch Supersonic Wind Tunnel and used the same model configuration as Reda & Murphy (1973). Special attention was given to the details of LV operation such as particle sizing requirements for accurate flow tracking, velocity biasing, and the use of Bragg-cell frequency shifting. A strong shock wave (pressure ratio of 5) was selected to provide a large region of separated flow.

A two-component LV system was used to measure mean and fluctuating velocities in the nominally 2-D flow. The occurrence of velocity realizations was assumed to be statistically random, permitting the inference of time-based mean and fluctuation data from the ensemble data sets. The LV and pitot-probe mean velocity data were compared in the region of flow separation. The superiority of the LV data for measurements in the interaction and separated flow regions was emphasized. Turbulent velocity data (and derived Reynolds shear stress) were also measured with the LV. This study showed a dramatic increase in turbulence intensity in the vicinity of separation, followed by a diffusion of the turbulence across the boundary layer as the flow moved downstream. An anomaly in the streamwise velocity histogram was observed at the point of separation close to the wall. Although not positively identified as such by the authors, I believe such a bi-modal histogram to be associated with flow unsteadiness as reported by other investigators (Horstman et al., 1975).

Ardonceau (1984) also studied turbulent flow properties in the vicinity of a planar 2-D, compression-corner SW/BLI. Three ramp angles (8°, 13°, and 18°) were selected to provide attached, incipiently separated, and separated flows, re-

spectively. A nonintrusive LV instrument was used in conjunction with a hot-wire anemometer to measure fluctuating velocities. High-speed schlieren photographs were also used to document the time varying nature of the global flow field. The LV data were useful in identifying large-scale structures in the nonequilibrium boundary layer downstream of the interaction which contained large amounts of turbulent energy. Lateral scales on the order of the boundary-layer thickness and a streamwise scale twice as large were measured for these structures. A low-frequency unsteadiness associated with the separation bubble was also identified. Several conclusions were drawn regarding the behavior of the shear and normal stresses (deduced from measured turbulent velocities) in regions of the strong interaction and downstream. This study illustrated the practicality of nonintrusive LV instrumentation in the study of turbulence associated with the SW/BLI and the direct effect of such experiments on turbulence modeling.

In most practical aerodynamic problems, flow geometries are 3D. Having realized a degree of success in the prediction of 2-D flows, researchers are now moving into the realm of more complex (and computationally more expensive), 3-D, SW/BLI configurations. In recent years, there have been several experimental studies (Goldberg, 1975; Settles, Perkins, & Bogdonoff, 1980; Kussoy, Viegas, & Horstman, 1980; Settles, Perkins, & Bogdonoff, 1981; Brosh & Kussoy, 1983; Kussoy & Horstman, 1981; Dolling & Bogdonoff, 1981; Bogdonoff & Settles, 1980; Settles, 1980) of 3-D SW/BLI flows of varying geometry. Researchers conducting these studies have relied heavily on well-established surface and flow-field intrusive measurement techniques and have not developed the more desirable nonintrusive interferometer or LV instruments. This aversion is understandable in view of the much greater complexity encountered in adapting these techniques for 3-D analysis. However, such experimental difficulties must be overcome if high-quality, flow-field data is to become available for use in the evaluation of 3-D predictions.

Several observations arising from this review of literature are helpful in the

formulation of a well-conceived experimental program directed at current needs in the study of the SW/BLI. To maximize the utility of experimental data, a program should provide accurate documentation of the global flow field that is useful in the evaluation of numerical simulations. It is desirable to use an experimental configuration that may be varied from 2D to weakly or strongly 3D. The adverse effects of side-wall boundary layer three dimensionality have been identified, and flow geometries that are highly susceptible to such effects should be avoided. The use of nonintrusive instrumentation is highly desirable to avoid contamination of the flow field by flow effects associated with intrusive probes. Finally, the frequent occurrence of flow unsteadiness in SW/BLI flows precipitates the need for both instantaneous and time-history experimental data.

Currently popular and well-developed nonintrusive experimental techniques are frequently based on optical interference phenomena. Holographic interferometry, laser Doppler velocimetry, and interferometric skin friction are examples of such techniques. Of these methods, holographic interferometry and laser velocimetry are capable of measuring the global flow field. The LV is a highly desirable experimental tool because of its ability to provide turbulent velocity data useful in the assessment of turbulence models. However, the LV has the disadvantage of being a point measurement and, as such, is not ideal for global measurement of temporally unsteady flows. The holographic interferometer is capable of providing an instantaneous, global picture of the density, but is inherently path integrating, making the analysis of 3-D fields complicated. The combined use of the holographic interferometer and the LV has been shown to be an effective approach in studies (Bachalo & Johnson, 1979; Havener & Radley, 1973) of the transonic SW/BLI. Such an approach is appropriate for this study.

The test facility used in this study is instrumented with a two-component LV system providing streamwise and vertical-velocity measurement capability. However, a holographic interferometer capability has not been previously implemented

and must be developed ancillary to this study. It is therefore appropriate to review the literature associated with aerodynamics research and development holographic interferometer systems as a prelude to the development of this new instrument.

Holographic Interferometry

Interferometric techniques were first applied to the study of aerodynamic flows by L. Mach (1892), E. Mach (1878), and L. Zehnder (1891). The basic instrument layout used by these individuals is shown in figure 2. This instrument, referred to as a Mach-Zehnder interferometer, has been used extensively in the study of small-scale aerodynamic flows throughout this century. Although the specifics of holographic interferometry are somewhat more complex, the phenomenological basis for instrument operation is fundamentally the same. Interference of a perturbed object or scene optical wave containing information of interest with an unperturbed reference wave having uniform spatial phase is accomplished in such a way as to yield a fringe pattern describing the spatial distribution of phase in the object wave. It follows that data-reduction techniques developed for Mach-Zehnder interferometer data analysis are generally applicable for holographic interferometer studies as well.

Several studies citing the use of the Mach-Zehnder interferometer in the analysis of aerodynamic flows are of particular interest. Studies by Winckler (1948) and Ladenburg, Winckler, & Van Voorhis (1948) at Princeton University betweeen 1945 and 1950 provide insights into appropriate data-reduction techniques for interferometric analysis of axisymmetric flow fields. The impingement of a supersonic jet on coaxial, conical, and spherical bodies was studied. The path-length integrating nature of a linearly propagating object wave traversing an axially symmetric refractive index field was appropriately modeled using the Abel integral. Details of the fringe analysis procedure describing the inversion of the Abel integral were given. The region just internal to the shock wave was identified as being particularly problematic because of the density discontinuity and corresponding singularity in the fringe

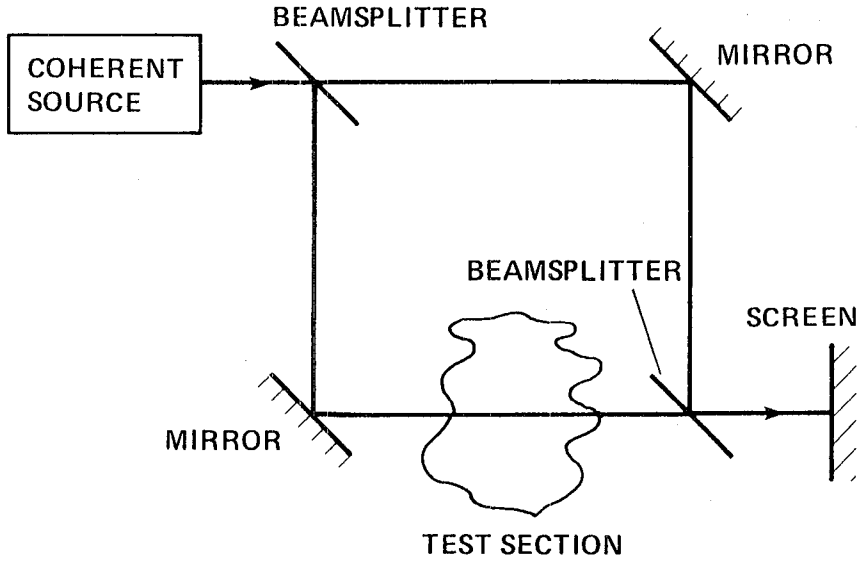

Figure 2. Mach-Zehnder interferometer

field. The density field was documented in terms of constant density (isopycnal) contours. Data were compared with isentropic conic flow solutions and were found to agree reasonably well in the region external to the boundary layer.

Bennet, Carter, & Bergdolt (1952) used the Mach-Zehnder interferometer in the study of projectiles in free flight. Again, the fringe-number singularity at the shock front was a problem. Density contours were presented for flow around cone-afterbody and spherical projectiles.

A technical note by Bradley (1968) is also of interest. He presented a method for inverting the Abel integral which utilized a variable substitution and convolution integral to enhance both the accuracy and tractability of axisymmetric fringe-number data analysis.

With the advent of holography, classical interferometry techniques were enhanced. The principles of holography were first described by Gabor (1948). His targeted application for the technique involved the improvement of magnification capabilities in electron microscopy through holographic construction and reconstruction at different wavelengths. This objective was not realized because of the lack of an appropriate coherent radiation source emitting at X-ray wavelengths. However, Gabor continued to work with holographic applications in the visible wavelength range and was awarded the Nobel prize in physics in 1971 for achievements in this field. The hologram formation and reconstruction methods employed by Gabor are termed "on axis" because of the coaxial orientation of the object and reference waves. Work by Leith & Upatnieks (1962) introduced the "off-axis" holographic technique which is now used in most holography applications.

The use of holographic methods in interferometry was first proposed by Horman (1965). Shortly thereafter, holographic interferometry techniques were used in the analysis of vibrating structures by Powell & Stetson (1965). In this application an interferometric comparison may be made between holographically stored waveforms of diffusely scattered light from the surface of a test object, permitting

evaluation of surface deflections on the order of a fraction of a wavelength. Such an interferometric analysis was not possible prior to the development of holographic methods. Applications involving holographic interferometry for opaque objects (including vibration analysis, strain detection, and nondestructive testing) remain the most popular use for holographic interferometry today. The analysis of transparent or phase objects using holographic interferometry was first done by Heflinger, Wuerker, & Brooks (1965). Since that time, the method has attained some popularity in wind tunnel testing applications.

A review by Trolinger (1974) provides a description of optical and holographic phenomena associated with transparent object holographic interferometry within the broader context of laser instrumentation for flow-field diagnostics. Typical holocamera and reconstruction apparatus layouts are presented. An updated edition of Trolinger's review is expected to be published in 1986 and will provide a more current view of trends and capabilities. A text authored by Vest (1979) is another excellent reference. The physics of hologram formation, reconstruction, and holographic interferometry are presented along with a discussion of various applications related to both opaque and transparent object holographic interferometry.

In the following paragraphs a brief review of several of the more interesting efforts using holographic interferometry in the study of aerodynamic flow fields is presented. Emphasis is placed on instrument design features. Flow-field characteristics are discussed in light of their effect on instrument design rather than their inherent merit from an aerodynamics perspective.

The study by Heflinger et al. (1965) was conducted when lasers were not well-developed research tools but were the subject of research and development. A pulsed ruby laser was used in this study which provided approximately 2 joules per pulse. The Q-switching was performed using a Kerr cell operating in the quarter-wave retardation mode. The poor spatial and temporal coherence of the laser output are apparent from the description of the very strict tolerance limitations on

object-reference beam overlap alignment and path-length matching. High-quality photographic film was the best available holographic recording media. The flow fields surrounding a 0.22-caliber bullet emerging from a gun barrel and in free flight were examined. Such flows were advantageous in that they provided small, portable phase objects which permitted short path lengths that were compatible with the poor coherence properties of the laser output. The normally problematic complication of very high bullet (flow) velocity was easily handled by Q-switched laser operation. This study provided a rather spectacular illustration of the unique capabilities of the holographic interferometer.

Several studies (Matulka & Collins, 1971; Jagota & Collins, 1972; Kosakoski & Collins, 1974) using holographic interferometry techniques were conducted in the early 1970s within the framework of a research program under the direction of D. J. Collins at the Naval Postgraduate School in Monterey, California. At the time, better quality, solid-state lasers were becoming commercially available. The interferometer system employed throughout these studies used a Korad K-1 ruby laser with Pockels cell Q-switching as the primary source of coherent illumination. Holographic recording techniques were further improved by the availability of very high resolution photographic plates.

Each test in this series was directed at the analysis of a particular 3-D flow field. Matulka & Collins (1971) analyzed the flow associated with an axisymmetric air jet discharging into a plenum. It was possible to spoil the axial symmetry of the configuration by tilting the jet discharge at an angle to the optical axis of the interferometer and thus introduce the need for multi-angle viewing and tomographic techniques for data reduction. A rather complex optical layout provided three sets of object and reference beams simultaneously incident on three separate holograms oriented at 0°, 45°, and 90° to the plane of symmetry of the jet. They emphasized the development of a 3-D integral inversion scheme which is suitable for adaptation to the digital computer. Matulka & Collins (1971) concluded that holographic

interferometric techniques have utility in the analysis of flows normally intractable using classical interferometry because of flow three dimensionality or high-speed transients.

These conclusions led to the applications-oriented studies of Jagota & Collins (1972) and Kosakoski & Collins (1974) that followed. However, both of these studies were conducted in wind tunnel facilities which allowed only limited optical access. Accordingly, the complex simultaneous three-view layout was abandoned in favor of an interferometer design that provided a single object beam axis, normal to the wind tunnel windows. Multi-view analysis of these 3-D fields was accomplished by rotating the model within the tunnel, with the assumption that turbulence and wall interference three dimensionality effects as well as flow unsteadiness were negligible. The single-plate, dual-exposure method was used in each of these studies, along with a method in which a diffuser plate is introduced into the object beam ahead of the test section. A small translation of this diffuser plate between the flow-on and flow-off exposures resulted in the formation of finite-fringe interferograms which are more useful than their infinite-fringe counterparts in quantifying the density field in regions of small gradients. Rather large errors were reported for both of the wind tunnel studies. However, such errors are not too discouraging in light of the flow-field complexity coupled with the mathematical complexity of the numerical procedures incumbent to 3-D data reduction.

An experimental program at the WPAFB Aerospace Research Laboratories beginning in the early 1970s has produced several interesting studies (Havener & Radley, 1973; Matulka & Collins, 1971; Havener, 1983; Havener, 1985). The interferometer system described by Radley and Havener (1973) uses an off-axis Toepler schlieren layout. Illumination is provided by a ruby laser with a dye-cell, end-reflector Q-switch. The dual-plate method was used for most of these studies, and a high-precision, dual-plate positioning device with adjustment capability in six degrees of freedom using ultra-precise piezoelectric micrometers is described in their

report. The majority of wind tunnel flow fields studied throughout this program were either planar 2-D (with the object beam propagating in the invariant direction) or axisymmetric.

In a study by Havener and Radley (1973) which is of particular interest to this study, holographic interferometry was used as a stand-alone instrumentation technique in the analysis of a planar 2-D, compression-corner SW/BLI. Two cases corresponding to attached and separated corner flow are reported in their study. To deduce the velocity field from the directly measured density, some assumptions about the variation of total pressure and total temperature in the boundary layer had to be made. The approach adopted here involved an approximation of the static-pressure distribution between the measured wall pressure and the inviscid field-static pressure. The variation of total temperature across the boundary layer and separated region was approximated using a Crocco-type assumption. These assumptions coupled with an equation of state provided the means to compute the velocity field. It is apparent that the analysis of the separated flow field with its attendant, boundary-layer pressure gradients is much more difficult than the analysis of the attached flow. The measured density profiles were reported to be accurate and repeatable. Some 3-D flow unsteadiness was reported in the highly turbulent region downstream of the interaction and was associated with the separation in the compression corner. A reverse flow velocity profile was obtained from interferometric data using the assumptions outlined above. These results were significant in that they provided a nonintrusive measurement in this sensitive flow region.

An impressive aerodynamic holography instrumentation capability was developed throughout the decade of 1970-1980 at Arnold Engineering Development Center. Holography was used in the study of combustion and airborne particle fields by Trolinger, Belz, & O'Hare (1974) as well as in the interferometry application (Sinclair & Whitfield, 1978). O'Hare and Strike (1980) described the most sophisticated of the holographic interferometry systems and presented information on an

accompanying automated, interferogram-processing, data-reduction system.

This interferometer also used a conventional Toepler schlieren layout and had a maximum object-beam diameter of 50.8 cm. For this study, a high-quality pulsed ruby laser was developed. Temperature-tuned, Fabry-Perot etalons were used as both the back and output end reflectors. These provided a highly monochromatic (0.01-angstrom line width) laser output with an accompanying coherence length of several meters. The dual-plate method was used with this system. An alternate layout using a diffusely reflected object beam is also described by O'Hare & Strike (1980).

An automated interferogram analyzing system is also described in this report. The system consisted of a video scanner which permitted TV monitoring of the reconstruction process, a picture digitizer and a display unit providing 640 by 480 pixel resolution. The display unit was interfaced to a minicomputer (for digital image processing), which was in turn interfaced to various hardcopy and data transfer peripherals. This prototype effort addressed the need to process the large amounts of data acquired from this global instrumentation technique; a need that is even more pronounced today (Lee, Trolinger, & Yu, 1985) as holographic interferometry applications become more widespread and the more data intensive analysis of 3-D fields is attempted.

Holographic interferometry work has also been done at NASA Ames Research Center. The first experimental effort is described in a report by Johnson and Bachalo (1978). The optical layout employed for this developmental interferometer system is very similar to that reported by O'Hare and Strike (1980). A Q-switched ruby laser provided illumination and the dual-plate technique was employed. This system was eventually upgraded to provide a more reliable holographic interferometry instrumentation capability in the 2- by 2-Foot Transonic Wind Tunnel. This advanced system is described in detail by Craig (1981). The most notable innovation was the use of a frequency-doubled Neodymium-YAG laser for primary illumination.

This laser is capable of providing a reasonably coherent, high-power, rapidly-pulsed (10-Hz) output. The rapid pulsing capability made the new system much easier to align. Additionally, the frequency-doubled output at a wavelength of 532 nm made it possible to use an argon-ion laser green line (514 nm) in the hologram reconstruction process. This represented a substantial improvement over ruby systems that typically used He-Ne lasers with rather limited power for reconstruction.

Another holographic interferometer system has been developed and implemented in the study of rotorcraft flow fields by personnel in the U.S. Army Aeroflightdynamics Directorate (AVSCOM) at NASA Ames Research Center. This ruby laser based system, described in a report by Kittleson (1983) incorporated several unique features mandated by the complexity of the helicopter rotor flow field. The 3-D nature of the shock system propagating from a rotor spinning at transonic tip velocities coupled with the necessarily large scale of rotor models gave rise to the need for a large field of view for the object beam. A 60.96-cm beam diameter was used. Accessibility limitations for the spinning rotor model, along with the large-diameter, high-f-number optical requirements, resulted in rather long beam path lengths and thus placed greater demands on the coherence quality of the laser as well as path-length matching. The single-plate, dual-exposure technique was employed. Considerable effort was expended in developing automated interferogram digitization and computer-aided tomography data-reduction methods (Becker & Yu, 1985), and a high degree of sophistication has been attained. The results presented in a recent report (Kittleson & Yu, 1985) represent, in my opinion, the current height of development of holographic interferometry capabilities.

The last interferometer system described here was designed and implemented at the Office National d'Etudes et de Recherches Aerospatiales (ONERA) laboratories in France. This system is described in a paper by Surget (1973). In contrast to all previously mentioned systems, this instrument uses a continuous-wave argon-ion laser as the primary illumination source. A mechanical or acousto-optical shutter

was used, which provided a minimum exposure time of a few microseconds. An innovative assembly unique to this system uses a pair of half-wave plates on either side of a simple glass plate for the object-reference beam splitter. This arrangement permitted nearly continuous adjustment of beam ratio without loss of illumination. Such economy was not required for other systems that benefited from the tremendous power levels obtained by Q-switching. This system provided a 14-cm object-beam diameter and used lenses rather than the usual schlieren-grade spherical or parabolic mirrors, and thus eliminated much astigmatism from the system. System packaging was compact, modular, and suitable for versatile implementation in smaller wind tunnels. Data- reduction techniques are outlined in a paper by Delerey, Surget, & Lacharme (1977). Interferometric SW/BLI data reported in another paper by Delerey (1983) appear to be reliable.

The above paragraphs describe a significant sample of the established holographic interferometry research efforts. The work reviewed was done predominantly in this country and in France. Such techniques have also been used by researchers in the Union of Soviet Socialist Republics (Belozerov, Bereskin, Razumosakaya, & Spornik, 1973; Ivanov, Mustafin, Shatilov, & Yushkov, 1975) and the United Kingdom (Tanner, 1966; Bryanston-Cross & Denton, 1984). While there continue to be innovations in system design and capability (Bachalo & Houser, 1984), the above review provides an extensive base from which a well-conceived interferometry system may be developed to match the unique needs of this study.

EXPERIMENTAL DESCRIPTION

An experiment that explored current turbulence modeling needs for SW/BLI flows was designed based on the preceding review of literature. Several important experimental design features are summarized in this section. Experimental data will be most useful if it provides accurate documentation of the global flow field that is helpful in the evaluation of numerical simulations. The adverse effects of side-wall, boundary-layer three dimensionality have been identified, and flow geometries that are highly susceptible to such effects should be avoided. It is desirable to use an experimental configuration that may be varied from 2D to weakly or strongly 3D. The use of nonintrusive instrumentation is highly desirable to avoid contamination of the flow field by flow effects associated with intrusive probes. Finally, the frequent occurrence of flow unsteadiness in SW/BLI flows precipitates the need for both instantaneous and time-history experimental data. These considerations, as well as current turbulence modeling needs are the factors which shaped this study.

Flow Facility

The characteristics and capabilities of available experimental facilities were also considered in the design of this experiment. The principle wind tunnel facility used by researchers in the Experimental Fluid Dynamics Branch at NASA Ames is the High Reynolds Number Channel I. This is an air-operated blow-down facility consisting of a high-pressure (3000 psi) storage reservoir, settling chamber, interchangeable nozzle and test section units, variable geometry diffuser, and optional vacuum sphere or atmospheric discharge. A sketch of the wind tunnel geometry is presented in figure 3. Vacuum sphere capacities provide several minutes of supersonic flow at moderate pressure levels. The tunnel may be operated for much longer periods at transonic conditions.

Supersonic operation of the tunnel may be accomplished by placing a super-

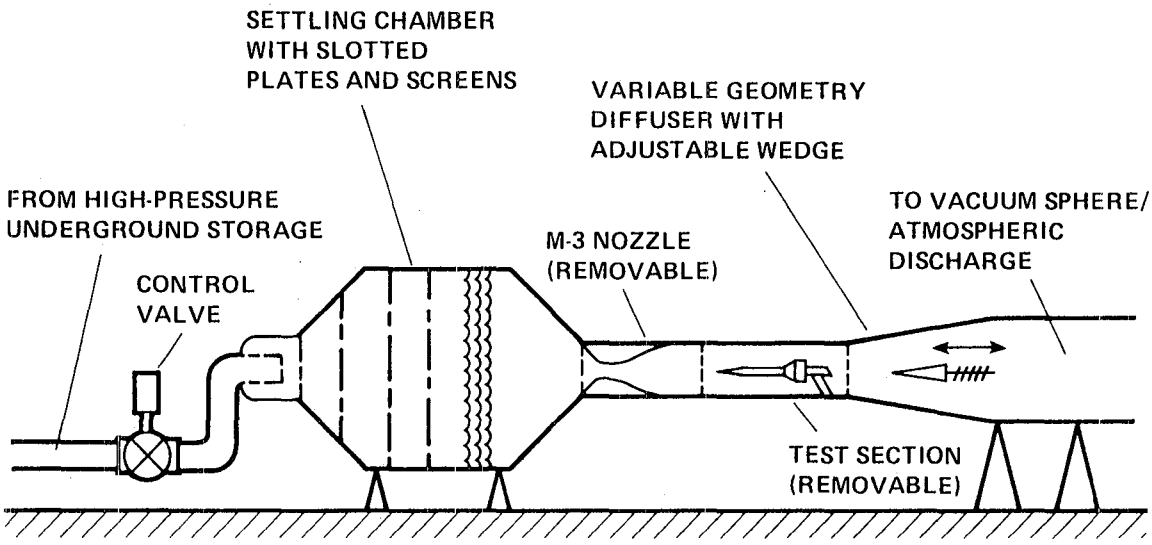

Figure 3. Cutaway view of High Reynolds Number Channel I test facility

sonic nozzle upstream of the test section and opening the variable geometry diffuser to its full extent. The supersonic test section Mach number is determined by the area ratio of the nozzle and is therefore fixed. This facility currently has two interchangeable supersonic nozzles providing nominal free-stream Mach numbers of two or three. Transonic operation may be achieved by locating the test section immediately downstream of the settling chamber contraction. The transonic test section Mach number may be determined from the position of the variable geometry diffuser.

Flow and Model Geometry

A selection of the particular type of SW/BLI flow to be considered (transonic airfoil, supersonic compression corner, or supersonic externally impinging shock) was made before the specifications of experimental design were determined. The transonic flow case was rejected for two reasons. Firstly, the weaker density gradients associated with the weak transonic shocks are not compatible with the application of interferometry instrumentation for the somewhat limited path lengths available in this facility (particularly for an axisymmetric configuration). Furthermore, previous investigators (Bachalo & Johnson, 1979; Delerey, Surget, & Lacharme, 1977; Brown & Viswanath, 1984) had thoroughly studied this problem for larger-scale (longer path length) flows using LV or holographic interferometry techniques.

Of the supersonic interactions, the compression-corner flow was most appropriate for this study. An axisymmetric, compression-corner geometry complemented an established experimental program exploring missile-guidance and control-surface configurations and was, therefore, compatible with existing experimental efforts and apparatus. Experimental documentation of the axisymmetric compression corner would provide a baseline for a systematic investigation of the more complex, computationally challenging, 3-D skewed- or partial-cone geometries. Finally, the axisymmetric, compression-corner configuration would not be subject to the detrimental

3-D, side-wall, boundary-layer interaction effects which frequently complicated the interpretation of planar 2-D flow data.

Having selected a suitable type of interaction, the specifics of the model geometry could then be determined. Details of the model are shown in figure 4. The presence of a thick boundary layer in the interaction zone was sought to enhance resolution. This was accomplished with a long cylindrical section placed upstream of the conic ramp which provided the development of a thick, equilibrium-turbulent boundary layer. The shape of the cylinder tip can critically affect the quality of the cylinder boundary layer. For this reason, a cusp nose was designed to minimize shock-wave development at the model tip and thereby enhance flow uniformity in the interaction zone. The nose and instrumented cylinder sections used in this study were available from previous tests (Brosh & Kussoy, 1983).

The strength of the interaction was varied by changing the compression-corner angles of the slip-on models. A continuous variation of corner angle is not possible for axisymmetric configurations. Therefore, a series of slip-on conic models spanning the range from 12.5° to 30° cone angle in 2.5° increments were machined from aluminum. A preliminary oil-flow study was done to determine cone angles corresponding to negligible, incipient, and large-scale separation. Based on the results of this study, values of 12.5°, 20°, and 30°, respectively, were chosen and pressure instrumented models were made from stainless steel.

Of course, it was necessary to terminate the cone at a finite radius to avoid tunnel blockage problems. Such termination could have easily been accomplished with either an abrupt reduction to the original cylinder radius, or by attaching an afterbody having the maximum cone radius. It was judged that the addition of an afterbody would simplify the mechanics of model instrumentation and additionally provide experimental data for an axisymmetric nonequilibrium turbulent boundary-layer/expansion-corner interaction flow (Dussauge & Gaviglio, 1981) of some interest. Models were designed to locate the expansion corner 6 cm along the

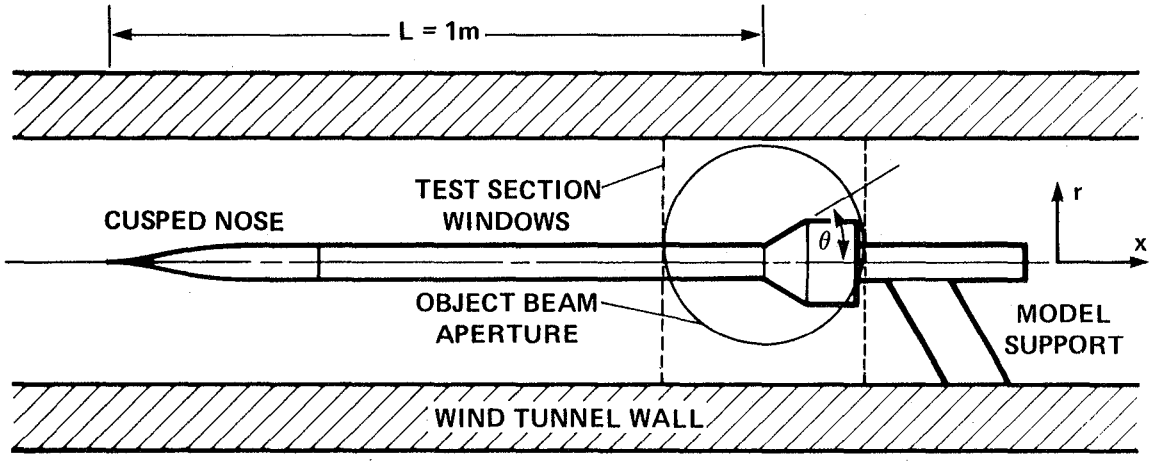

Figure 4. Model configuration in wind tunnel

surface (approximately six times the cylinder boundary-layer thickness) from the compression corner to locate the expansion uniformly downstream of the SW/BLI region of high turbulence production. The model support was located downstream of the test region where its disruptive effects were unimportant. The test section used in this study is 25.4-cm wide and 38.1-cm high. Optical access was provided through a 29.4-cm by 38.1-cm windows of optical crown glass.

The coordinate system for this study is as follows: The x coordinate is aligned with the tunnel axis (see figure 4), and is positive downstream with an origin at the cylinder-cone intersection. The y coordinate is aligned vertically, and is positive upward with an origin at the model surface. The z coordinate is aligned horizontally and is positive in the direction of object beam propagation with an origin on the tunnel centerline. Because of radial symmetry, it is helpful to define a radial coordinate, $r^2 = (y + r_0)^2 + z^2$, where r_0 is the local model radius. The model and surrounding flow field may be completely described in x and r coordinates and are, in this sense, 2D.

The existing Mach 3 nozzle proved to be an appropriate design as several compression-corner SW/BLI studies reported in the literature were done at Mach numbers near 3. Although the nozzle wall contours provide an area ratio corresponding to Mach 3 flow, the presence of side-wall boundary layers resulted in an actual value that was somewhat lower. Measured wall pressures indicated an average Mach number of 2.85. A thermocouple in the settling chamber measured a total temperature between 265 K to 280 K, depending on the ambient temperature. For the flow calculations, an average value of 270 K was used.

The literature (Settles & Bogdonoff, 1973; Law, 1975; Roshko & Thomke, 1976) indicates that the effect of Reynolds number on the onset and extent of separation in SW/BLI flows has not been established to the satisfaction of all investigators. A means of varying the Reynolds number seemed a necessary addition to the experiment. This was accomplished by altering the tunnel total pressure. While tunnel

velocities were affected by this pressure change, the only effect on the nozzle area ratio was a slight change in side-wall boundary-layer thickness. This resulted in a nearly constant Mach number throughout the range of total pressures. Values of 1.7 and 3.4 atm were selected to be compatible with concurrent studies, as well as with the refractive index requirements of the interferometer. The corresponding unit Reynolds numbers were 18×10^6/ m and 36×10^6/ m. The initial cylinder boundary-layer thickness just upstream of the compression corner was measured (from LV profiles) at 1.0 cm.

Measurement Techniques

A summary of the data obtained in this study is presented in table 1. Oil-flow measurements were made to confirm flow symmetry and to determine the extent of the separated region. A sample oil flow is shown in figure 5. The line of oil accumulation is uniform around the model indicating good alignment of the model with the tunnel axis and correspondingly good flow symmetry. Wall-pressure data were obtained along the length of the model and are useful in verifying shock location and strength. Oil-flow and wall-pressure data provide complementary methods of identifying separation. Data at both 1.7- and 3.4-atm total pressure were compared to evaluate Reynolds number effects. Interferometry data providing complete documentation of the density field at both total pressure values for all three models are reported. Mean LV data are reported for the 12.5° model at the lower total pressure to support interferometric technique validation arguments, and for the 30° model to additionally clarify code performance evaluation.

Shock-wave unsteadiness was observed in the interferometer data, particularly for the separated flows. A more quantitative evaluation of this unsteadiness was obtained from high-speed shadowgraph data obtained in a complementary investigation (Brown & Kussoy, work in progress). Such unsteadiness complicated the comparison of interferometric data, which are essentially instantaneous, with LV

TABLE 1. Test Data Obtained for Various Cone Angles.

Total Pressure	Model Cone Angle	O F	S P	H I	L V
1.7 atm	12.5°	yes	yes	yes	yes
	15°	yes	no	no	no
	17.5°	yes	no	no	no
	20°	yes	yes	yes	no
	22.5°	yes	no	no	no
	25°	yes	no	no	no
	30°	yes	yes	yes	yes
3.4 atm	12.5°	no	yes	yes	no
	15°	yes	no	no	no
	17.5°	yes	no	no	no
	20°	yes	yes	yes	no
	22.5°	yes	no	no	no
	25°	yes	no	no	no
	30°	no	yes	partial	no

O F Oil Flow point of Accumulation

S P Model Surface Pressure

H I Holographic Interferometer Profiles (density)

L V Laser Velocimeter Profiles (velocity)

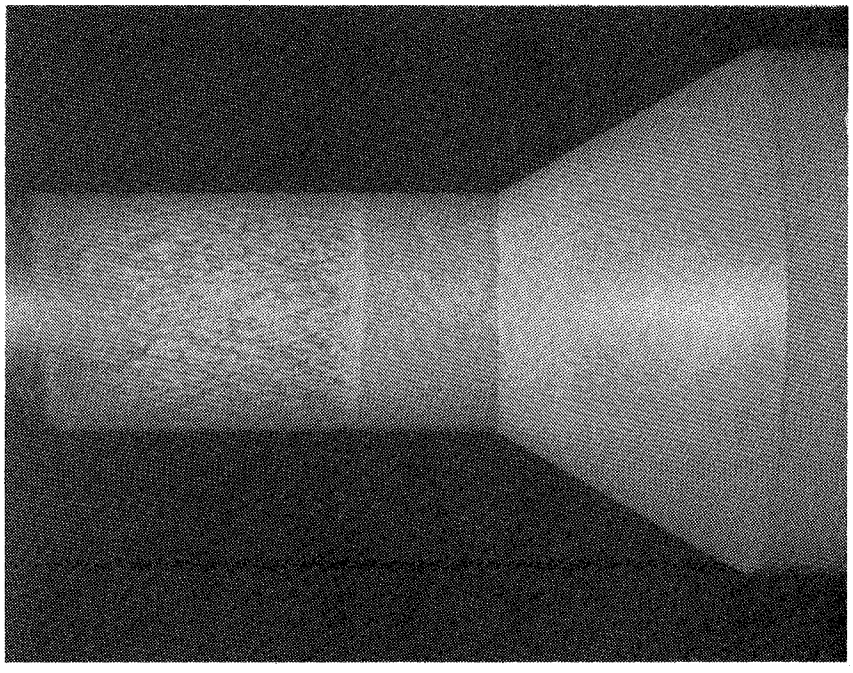

Figure 5. Surface oil-flow pattern for the 30° model; $M_\infty = 2.85$,$P_t = 1.7$ atm, $Re_L = 18 \times 10^6$.

and wall-pressure data, which are time averaged. However, for the three cone angle models reported here, shock unsteadiness was significant for only the 30° model flow. Several instantaneous interferometric data sets were averaged to obtain mean flow data for this unsteady case.

Holographic Interferometer

Classical techniques of Mach-Zehnder interferometry are straightforward and well understood (Shapiro, 1953). However, this experimental technique is not commonly used because of its inherently rigorous demands for high optical element quality and apparatus rigidity. These difficulties may be alleviated using holographic techniques.

While Mach-Zehnder interferometry makes use of the interference of light waves traveling separate paths but united in time, holographic interferometry uses waves traveling nearly the same path but separated in time. These information-carrying waves each encounter the same lenses, mirrors, and tunnel windows so that effective path-length variations are restricted to the refractive index field within the test section. To effect the temporal separation, it is necessary to store one or both of the interfering waves; hence, the hologram.

Hologram construction occurs when an object wave containing information of interest and a mutually coherent, reproducible reference wave are combined so as to interfere in the vicinity of a photoreactive media. Time integration of this superposition yields an intensity field which is recorded. Hologram reconstruction occurs when this record is illuminated by a reconstructing wave duplicating the original reference wave. As this wave interacts with the record media, phase modulation occurs and the wave is diffracted. Phenomenological similarities between the processes of interference and diffraction precipitate a condition in which the diffracted wave duplicates the original object wave. Thus, it is possible to store an object wave containing phase information that describes its traversal of a refractive index field.

A more detailed discussion of holographic phenomena is presented in Appendix A, as well as in books by Vest (1979) and by Collier, Burckhardt, & Lin (1971).

Superposition of two holographically reconstructed waves that have traveled nearly the same path results in a second interference condition wherein the time-integrated, spatial-phase difference of the two beams is manifest as a spatial intensity field. This intensity pattern (or interferogram) may be analyzed to provide information describing any differences that may have existed between the effective optical paths traveled by the two original object waves. The fact that these two waves have encountered the same optical elements greatly relaxes requirements for optical element quality and constitutes the primary advantage of holographic interferometry over classical techniques.

Vibration is a problem associated with classical interferometry. Any vibration of optical elements, even on the order of a fraction of a wavelength, will cause a destabilization of the time-integrated intensity exposure at the interferogram and, thus, degrade data quality. The use of Q-switched, doped-insulator lasers as the coherent source for holographic interferometers is advantageous because these lasers provide very short (10^{-8} sec) exposure times with sufficient energy to activate the photoreactive media. Vibrational amplitudes at these frequencies are infinitesimal, so that washout of hologram fringes is effectively eliminated. Reconstruction may be performed in a vibration-free environment where a high degree of temporal stability of interferogram fringes may be realized. With this approach, vibrational effects are restricted to small changes in path length or beam direction which are uniform over the entire beam aperture and may be compensated for in the reconstruction process.

Although Q-switched exposure times are certainly short enough to freeze any turbulent effects present in a flow field, it must be remembered that refractive index is integrated along the beam path. Since turbulence is inherently 3D, an attempt to utilize interferometry for quantitative turbulence measurement would require sophisticated, 3-D, integral inversion schemes which significantly complicate

experimental methods. The analysis of 2-D planar or axisymmetric fields for mean flow quantities may be accomplished if the turbulence field has spanwise length scales that are small compared to the integration path length.

Holographic interferometry may be performed by interfering one reconstructed wave with a real-time phase-modulated wave (termed real time), by interfering two reconstructed waves recorded in the same media (termed dual exposure), or by interfering two reconstructed waves recorded in separate media (termed dual plate) as discussed by Vest (1979). The dual-plate method was selected for this study because of its versatility. Holograms may be reconstructed to yield shadowgraph and schlieren data, as well as interferograms. Additionally, it is possible to adjust the hologram plates with respect to each other and thereby compensate for the optical misalignment effects of wave shear, lag, and angular deviation introduced by vibration. Furthermore, fringes of known character may be introduced to interferograms to enhance their utility for flow visualization or quantitative data analysis.

The holographic interferometer construction and reconstruction systems that were designed and built for this study are shown in figures 6 and 7. A detailed description of each system with component listings and operation instructions is found in Appendix B. A modular design was used for the construction system. Optical elements were rigidly mounted to three aluminum base-plate modules with heavy aluminum rods. These modules were in turn rigidly attached to the tunnel infrastructure to provide an economical, reasonably vibration-resistant instrument.

An Apollo Laser, Model 22 Q-switched ruby laser, provided illumination. A 5-mw He-Ne laser mounted to the ruby laser rail provided a reference beam for alignment of both the ruby cavity and the down-beam optics. The ruby laser generated pulses of 20-ns duration with 50 mj of energy at 694.3-nm wavelength. The output was split using a high-energy dielectric beamsplitter with 30% reflectance into the object beam. This beam was transmitted under the wind tunnel and onto the object beam expansion module. An inversion lens, L_1, was used to provide

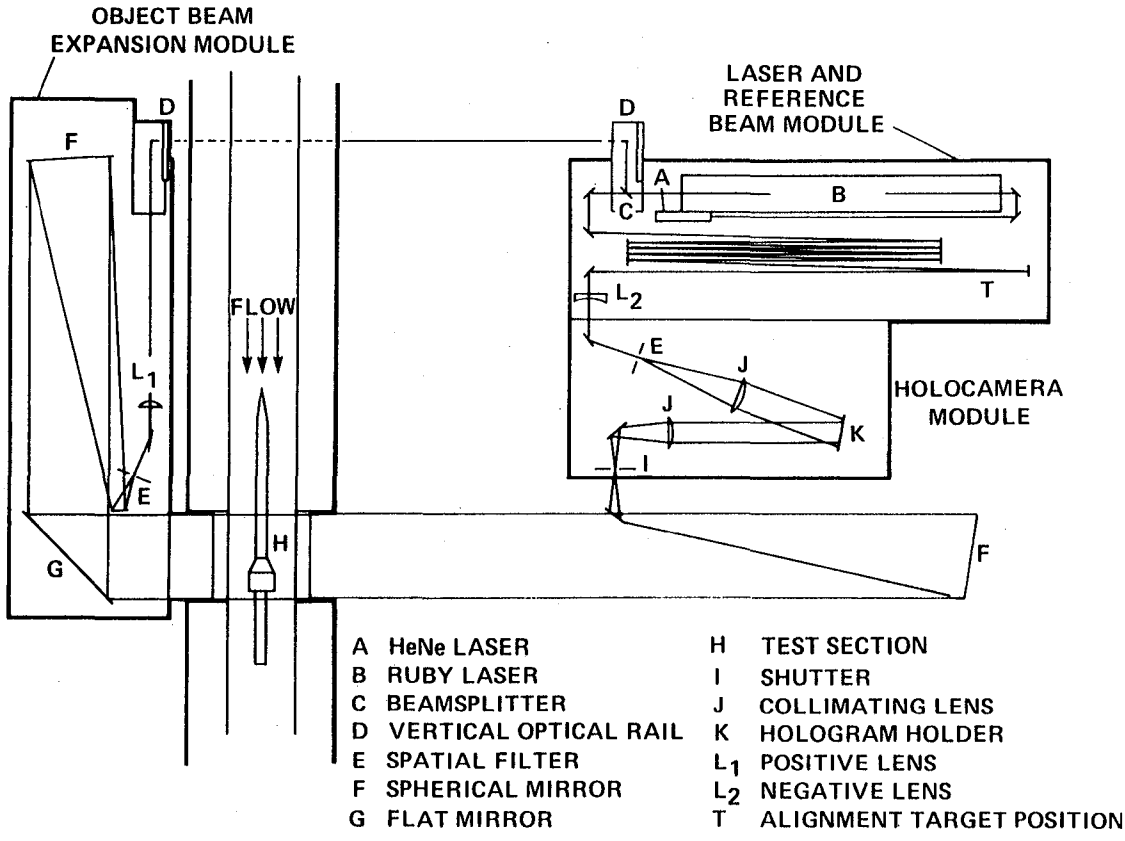

Figure 6. Interferometer layout for hologram construction.

beam ratio adjustment and to maintain proper beam orientation at the hologram. The object beam was then spatially filtered and collimated at a 30.48-cm working diameter.

Following passage through the test section, the object beam was focused through an electronic shutter and recollimated onto the hologram. The reference beam was multiply reflected on the laser module to match the object-beam path length within the coherence length of the laser. Another beam intensity adjustment lens, L_2, was used prior to spatial filtering, beam expansion, and collimation at the hologram. Agfa-Gevaert 10E75 glass plates were used to record simple absorption holograms. The object and reference beams intersected at an angle of 20°, with the hologram inclined equally to each beam. The laser and holocamera modules were bolted together and shared a common support platform. This configuration minimized beam wander and permitted spatial filtering of the reference beam 15.24 m down beam from the laser. The spatial filtering of both beams as far down beam as possible minimized extraneous diffraction patterns. Each module was shielded to contain the hazardous class IV radiation and to permit operation of the holocamera under normal room lighting conditions.

The hologram reconstruction system is shown in figure 7. A Spectra-Physics model 125A He-Ne laser provided 50 mw of continuous wave illumination at 632.8-nm wavelength. The output was spatially filtered and recollimated to duplicate the reference beam used in hologram construction. The dual-plate holder shown in figure 8 provided positive control of relative plate orientation in six degrees of freedom. The original gimbal design decoupled each degree of freedom to simplify reconstruction.

It is necessary to image the centerline plane of the test section on the film plane of the reconstructed interferogram if a clearly focused model is to be obtained. The object beam layout shown in figure 6 provided an image plane approximately 30 cm in front of the hologram. It was, therefore, necessary to employ another lens in the

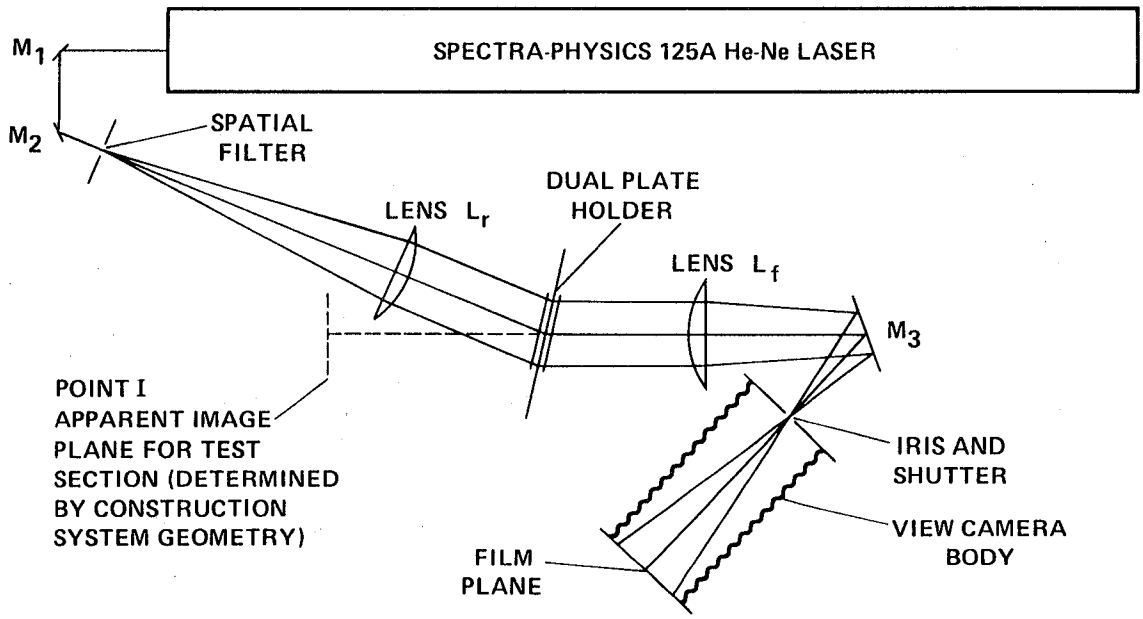

Figure 7. Interferometer layout for hologram reconstruction

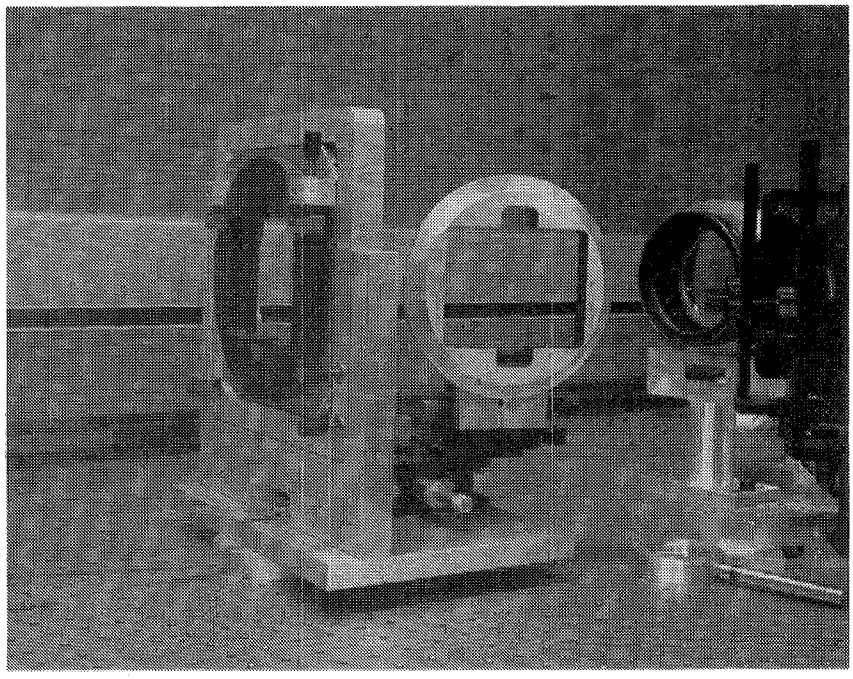

Figure 8. Dual-plate holder

reconstruction setup. This lens additionally permitted the choice of an appropriate magnification ratio for easier visual monitoring during reconstruction.

In this study, interferograms were formed from the reconstruction of an undisturbed (flow-off) object wave that had traversed a test section of uniform refractive index with a perturbed (flow-on) wave that traversed the refractive index field of the flow. The flow-on wave contained information on the refractive index integrated along its path. If no path-length variations had been introduced by vibration or deliberate plate misalignment, the interferogram resulting from the reconstruction process would exhibit infinite-fringe spacing in regions of constant refractive index and would be referred to as an infinite-fringe interferogram. If such variations are not introduced, the interferogram is labeled finite-fringe. For infinite-fringe interferograms, the spatial distribution of fringe number $N(x,y)$, referenced to a zero value at a point in the field, where the refractive index, n_0, is known is given by the expression

$$N(x,y) = \frac{1}{\lambda}\int_{z_1}^{z_2} [n(x,y,z) - n_0]dz \qquad (1)$$

If this refractive index difference, $n(x,y,z) - n_0$, is planar 2-D with object wave propagation in the invariant direction, analysis is straightforward. If the refractive index field is a function of radius, integral inversion is slightly more complex but may be accomplished with Abel transform methods. Both planar 2-D and axisymmetric flow fields have been analyzed using holographic interferometry techniques with a high degree of success (Bachalo & Johnson, 1979; Havener & Radley, 1973; Sinclair & Whitfield, 1978; Surget,1973). If the refractive index field is 3D, analysis is considerably more complicated. Tomography techniques are required to process projected, 2-D fringe-number fields at many angular orientations. Nevertheless, recent work has yielded highly reliable holographic interferometry data for some complex 3-D fields (Kittleson & Yu, 1985).

A discussion of numerical Abel transform methods and their application to the analysis of axisymmetric field interferometric data is found in an article by

Ladenburg, Winckler, & Van Voorhis (1948) and in Vest's book (1961). A method presented by Vest (1979) was initially selected for this study and is outlined in Equations (2)-(5).

For radial symmetry the function, $n(x,y,z) - n_0$, may be replaced by the function, $f(r) = n(r) - n_0$, for a profile at some specified x location. With this change of variable, Equation (1) becomes

$$N(x,y) = \frac{2}{\lambda} \int_{y+r_0}^{R} \frac{f(r) r dr}{\sqrt{r^2 - (y+r_0)^2}} \tag{2}$$

If the refractive index field is approximated to consist of annular regions having constant refractive index, the integral may be replaced by a summation over these many elements

$$N_i = \frac{2}{\lambda} \sum_{k=i}^{I-1} f_k \int_{r_k}^{r_{k+1}} \frac{r dr}{\sqrt{r^2 - {r_i}^2}} \tag{3}$$

For constant radial element spacing, the integral may be replaced by the coefficient

$$A_{ki} = [\sqrt{(k+1)^2 - i^2} - \sqrt{k^2 - i^2}]$$

and Equation (3) becomes

$$N_i = \frac{2\Delta r}{\lambda} \sum_{k=i}^{I-1} A_{ki} f_k \tag{4}$$

This equation yields a set of simultaneous equations which may be solved quite easily, since the coefficient matrix, A_{ki}, is triangular. It is necessary to begin at the outer edge of the phase object with a known value of f_{edge} (usually 0) and work to the center in a manner analogous to peeling an onion.

This approach required values for fringe number, N_i, at equally spaced radial locations, preferably with close radial spacing to reduce numerical errors associated with the constant refractive index element assumption. In light of these requirements, it was necessary to take a critical look at the methods available for translating fringe-number data from the reconstruction process to the data-reduction algorithm.

A method used by Havener (1983, 1985) places fringes at specific locations during the dual-plate reconstruction process for the determination of fringe number for that particular fringe in its unique reconstruction. This method had the advantage of providing fringe-number data at specific locations and permitted close data spacing but it is extremely tedious. Therefore, it is a suitable method only when a few profiles are to be analyzed.

Other techniques involve the recording of an optimum reconstruction on film and subsequent analysis of this single interferogram. Delerey et al. (1983) used a precision microdensitometer interfaced to a microcomputer to obtain fringe-number data along specified profiles. Such a system is capable of providing fringe-number data not only at fringe centers but also at arbitrary profile locations, provided film nonlinearities could be properly modeled. This system provided high- quality data for the planar 2-D, SW/BLI flows reported. But in spite of its automation, a long period of time was required to analyze each interferogram. Automated computer interfaced image analysis systems have been used by O'Hare & Strike (1980) and Becker & Yu (1985) which utilized image digitization cameras and high-resolution display hardware. These systems greatly enhance interferogram analysis capability and speed but have drawbacks associated with initial software development requirements and pixel-limited spatial resolution.

In this study, the need for accurate fringe-field data was pronounced. However, that need had to be balanced against the need to analyze large quantities of data. The experimental objectives called for the analysis of several profiles (15 per interferogram) on each of several interferograms (four or eight, averaged to obtain mean values) for three different models at two different total pressures, a total of 420 profiles. While these requirements suggested that an automated system was needed, equipment cost and setup time were prohibitive. The most sophisticated interferogram digitization hardware available for use in this test was a large, high-resolution graphics tablet.

Based on these considerations, the following approach was adopted to transfer fringe-number data from the reconstruction phase to the computer where it could be transformed. First, a single, finite-fringe reconstruction having optimum fringe orientation was selected and recorded photographically. An enlarged print of this interferogram was then mounted on the graphics tablet and profiles were laid out at 1-cm intervals. Fringe-profile intersections were digitized (two or three iterations per profile to minimize digitization error) and written to a data file which listed fringe number as a function of radius with data present only at radial locations corresponding to fringe-profile intersections. Optimum fringe orientation is discussed in the Results and Discussion section.

This approach did not meet the requirement for closely and uniformly spaced data. It was therefore necessary to employ an intermediate process of data approximation. A smooth approximation method, free of slope discontinuities and matching the raw data as nearly as possible, was required. Cubic-spline techniques appeared to fit these requirements. Therefore, a data-reduction program utilizing a rational (tension) spline was written and applied. It soon became evident that such an approximation technique was not compatible with the Abel transform. Transformed profiles exhibited nonphysical behavior at spline section interfaces, as well as unreasonable oscillations (apparently the result of an amplification by the transformation of the rather minimal oscillations of a spline in high tension).

Evidently, a smoother, more uniform approximation method free of curvature discontinuities was required. One option was to employ least-squares fitting to higher-order polynomials. This method less accurately followed the raw data, but provided much smoother transformed profiles. Ill-condition matrices limited the use of simple geometric series polynomials to low orders. Therefore, a method using orthogonal (Legendre) polynomial sets was employed, permitting higher curve orders limited only by the number of data points available. This least-squares approximation technique did not closely track certain profile shapes and tended to

wander in profile regions of data dropout (as did the spline technique). However, it was deemed the most practical approximation technique available.

Reducing interferometric data became a problem for data in regions just internal to the shock wave. The least-squares data approximation technique often provided fringe-number values for shock-adjacent annular element interfaces that resulted in unrealistically high refractive index values. The physical reasons for this problem are the strong refraction effects at the shock, the presence of some fringe-number offset caused by optical aberration and digitization errors, and possibly the presence of radial nonuniformity associated with "ripple" in the shock surface. These problems are compounded because the polynomial curvefits cannot properly describe the fringe-number variation in the vicinity of the shock wave where $\partial N/\partial y$ becomes infinite. The numerical error accompanying the finite element treatment of this singularity also compounds the problem.

A solution to these problems was achieved through three means. Firstly, weighted "pseudodata" at the shock radius were fed into the least-squares curvefit to tailor the approximated data behavior in the problem region. The pseudodata could be set to zero, a linearly extrapolated value based on adjacent internal data, or a value calculated from the Prandtl-Meyer relations and the known free- stream density (refractive index) value. A similar weighted pseudodata technique was also helpful in eliminating oscillations in the higher-order polynomial curvefit in regions close to the wall where fringe-profile intersections were usually sparse. Secondly, to make approximated data more accurately represent the physical situation, a parabolic fit, $N^2 \propto (y - y_{shock})$, was employed between the outermost valid digitized data point and the shock. To reduce numerical error over the critical elements adjacent to the shock, fringe-number values were approximated with even spacing in fringe number and uneven spacing in y. Thirdly, shock position was relaxed outward. This was the least desirable treatment but was sometimes a necessity. However, only in a few extreme cases (e.g., 3.4-atm total pressure, 20° and 30°

models) did the outward relaxation dimension exceed the 1-mm spatial-resolution limit of the optical system.

The presence of uneven radial spacing for the second treatment described above was incompatible with the Abel transform algorithm of Equation (4). It was therefore necessary to either modify the Abel transform or develop another means of inverting the Abel integral. In anticipation of future applications involving more complex (3-D) fields, the second option was chosen. To meet these needs, a least-squares method of Abel integral inversion was developed for this study. This procedure is described very briefly in the following paragraph. A more in-depth description will be presented in a report by Brown and Dunagan (work in progress).

For this least-squares procedure, the index of refraction is assumed to be composed of the sum of a finite series

$$n(r) = \sum_i a_i f_i(r)$$

where

$$f_i = \begin{cases} 1, & \text{if } r \in [r_i, r_{i+1}]; \\ 0, & \text{otherwise} \end{cases}$$

then, for an axisymmetric phase object, the fringe number is

$$\tilde{N}(y_j) = \sum_i a_i F_i(y_j) \tag{5}$$

where

$$F_i(y_j) = \begin{cases} \int_{y_j}^{r_{i+1}} f_i(r) \cdot (r^2 - y_j^2)^{-\frac{1}{2}} r dr, & \text{if } y_j < r_{i+1}; \\ 0, & \text{if } y_j \geq r_{i+1}. \end{cases}$$

A least-squares analysis is then applied to Equation (5), resulting in a system of equations to be solved for the a_i coefficients. A symmetric matrix results which is easily inverted by Gaussian elimination.

Having approximated the radial fringe-number variation, and then transformed the profiles using the least-squares Abel method, density was deduced by means of the simple relation

$$n = 1 + K\rho \tag{6}$$

where K, the Gladstone-Dale constant, is a property of the gas. This constant is a weak function of wavelength and nearly independent of pressure and temperature over moderate ranges (Merzkirch, 1974). This relation permitted the calculation of density profiles at any desired location. Much of the software developed for the analysis of these interferometric data is presented in flowchart form in Appendix C. These flow charts provide a more specific picture of the various treatments applied.

Interferometer sensitivity (i.e., $\partial N/\partial \rho$) is dependent on path length, laser wavelength, and the Gladstone-Dale constant. This combination is not particularly advantageous for the adjustment of sensitivity to match experimental requirements. For axisymmetric flow fields, the effective path length varies directly with the distance from the model centerline. The flow field considered contained strong density gradients in the region of the shock and weaker density gradients of interest in the boundary layer and separation regions close to the model surface where reduced path length detracts from sensitivity. These conditions made it difficult to select free-stream density values that permit the optimum resolution of data in both the shock and boundary-layer regions. The lower total pressure of 1.7 atm provided only marginal resolution in the boundary layer, but still permitted a continuous determination of fringe number across the strong shock discontinuity. The higher total pressure of 3.4 atm provided finer boundary-layer resolution but fringe tracking in the region of the shock, particularly for the strong shock associated with the 30° ramp angle, became impossible.

Laser Velocimeter

Because this investigation represents the first application of the particular holographic interferometer instrument as described in the preceding section, it is desirable to provide complementary experimental data to permit an evaluation of interferometry system performance. Furthermore, thorough flow-field documentation called for the reporting of pressure, temperature, and velocity data in addition to

the directly measured density. The deduction of these flow parameters from measured density values required several assumptions regarding the physics of the flow. These assumptions are particularly questionable in regions of viscous flow. For these reasons it was appropriate to make a direct measurement of the velocity field with an LV instrument. The laser velocimeter system employed in the present study has been previously used (Robinson et al., 1983; Brown & Viswanath, 1984). This LV system is a 2-D, two-color, forward-scatter system. The fringe patterns of the two channels were oriented at $\pm$ 45° to the tunnel axis with the 40-MHz Bragg-shifted fringes moving downstream. The LV signals were processed by commercially available counters interfaced to a 16-bit minicomputer. Typically, 35,328 individual realizations were acquired at each location.

Artificial seed was injected into the flow to enhance data rates and permit the resolution of rapid turbulent fluctuations. A monodispersed seed mixture consisting of 0.5-μm polystyrene particles suspended in denatured alcohol was used. A new seed injection nozzle was implemented in this test which injected seed mixture into the inlet duct, upstream of the settling chamber. This nozzle system was intended to atomize the seed mixture in such a way that each droplet would contain nominally one sphere. The alcohol vehicle would then evaporate as the droplet progressed downstream, leaving single seed spheres suspended in the test section flow.

As LV data were acquired and compared with interferometric data and the computation, it became apparent that a particle lag problem was degrading the quality of the LV data in the region of the shock. This problem had particularly unpleasant ramifications with respect to future evaluation of turbulent quantities in this SW/BLI study. A simple Stokes flow calculation indicated that the single spheres could be expected to track the flow rather well. After considerable effort and experimentation it was determined that the problem was caused by poor atomization. Apparently, several spheres were present in any given droplet and were coalescing into a larger conglomerate as the alcohol evaporated. This problem was

corrected by modification of the injection system. New sets of LV data were then obtained. Figure 9 shows a comparison of the first and second sets of data. The sharper drop in velocity just internal to the shock indicates better tracking of the flow for the second data set. The first set of LV data has been discarded and appears in the literature only in a paper by Dunagan, Brown, & Miles (1985).

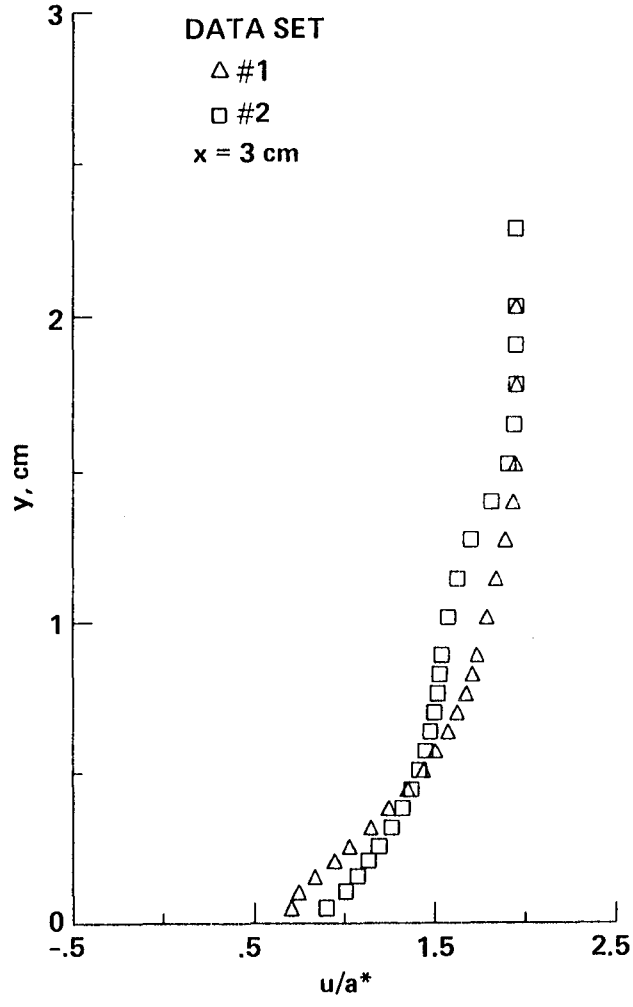

Figure 9. Comparison of LV data sets 1 and 2 for the profile at $x = 3$ cm for the 30° model with $P_t = 1.7$ atm and $Re_L = 18 \times 10^6$.

COMPUTATIONS

Computations were performed by C. C. Horstman using methods outlined in a paper by Horstman & Johnson (1984). The partial-differential equations used to describe the mean flow field are the time-dependent, Reynolds-averaged, Navier-Stokes equations for axisymmetric flow of a compressible fluid. For the turbulence closure, the two equation $k - \epsilon$ turbulence model (Jones & Launder, 1972) was used. The numerical procedure used is the explicit second-order, predictor-corrector, finite-difference method of MacCormack (1982) modified by an efficient implicit algorithm.

The computational domain extended in the flow direction from $x = -5$ to $x = 8$ cm (referenced to an origin at the cone-cylinder intersection) and in the vertical direction from the model surface to $r = 9$ cm. A 65 x 45 mesh was employed with constant mesh spacing in the streamwise direction. Radial mesh point spacing was small ($y_1^+ \simeq 1$) in the boundary layer, increasing with distance from the model surface. A graphic representation of the grid (plotted half density) is shown in figure 10.

The upstream boundary conditions were obtained from a boundary-layer solution that matched the experimentally determined velocity profile, free-stream Mach number, and total pressure. At the downstream boundary, all streamwise gradients in the flow were set to zero. No-slip boundary conditions were applied at the model surface, along with a prescribed constant wall temperature. At the outer boundary, uniform free-stream conditions were used, therefore a comparison of these computations with wind tunnel data must be tempered with a realization of the limit to which the wind tunnel flow simulates a free air environment.

A refined Navier-Stokes prediction method must employ turbulence models to treat the problem of turbulence closure. The development of these models is an area of concentrated theoretical work and provides the main impetus for this study.

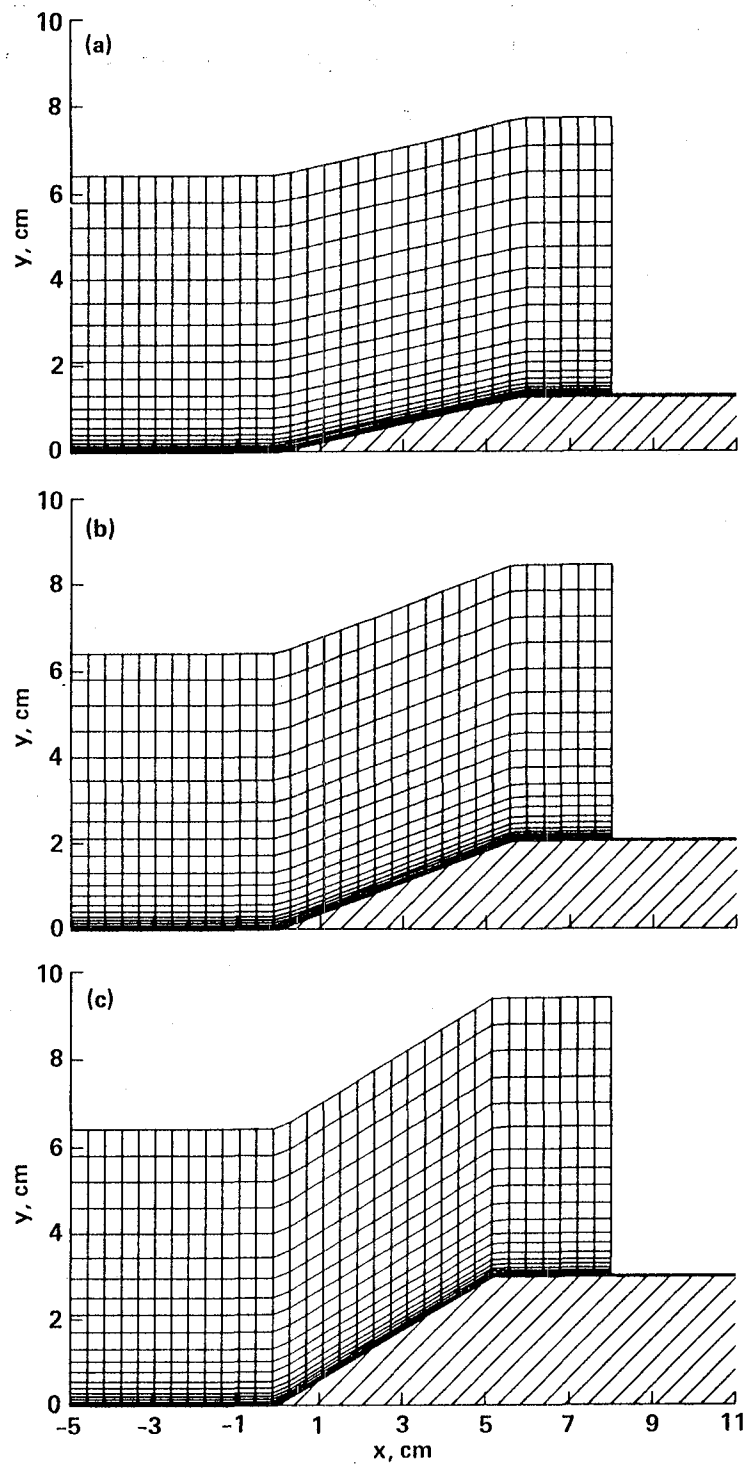

Figure 10. Computational grid (plotted half density). (a) 12.5° model, (b) 20.5° model, (c) 30.5° model.

While the details of the computational method are undoubtedly of interest to many, a discussion of these details is beyond the scope of this investigation. Interested readers are directed to the references if more information is desired.

RESULTS AND DISCUSSION

Interferometric Data Reduction and Error

Sample interferograms for the 30° model at 1.7-atm total pressure are shown in figure 11. The field of view corresponds to the full 30.48-cm object-beam aperture. Figure 11(a) presents an infinite-fringe interferogram reconstructed using the dual-plate method. Some features of the flow may be noted here. On the cylinder upstream of the interaction, the boundary layer is indicated by the single horizontal fringe. As the flow encounters the cone surface, it must be turned through an angle, thus precipitating the formation of a conic-oblique shock. This shock penetrates the subsonic portion of the boundary layer and imposes a strong, adverse-pressure gradient on the flow, resulting in a large, separated flow region in the corner for this 30° model. A weaker separation shock may be observed emanating from the front of the separated region. Flow coming over the separated region again encounters the cone surface at the reattachment point and again must be turned by a compression shock system, which may be observed as a decrease in fringe spacing just downstream of reattachment. These separation and reattachment shock systems coalesce into a strong oblique shock at an x location of approximately 3 cm.

At the cone-afterbody corner, the flow must again be turned through a sharp angle. This precipitates the formation of an expansion fan originating at the corner. This expansion fan propagates out into the flow until it encounters the oblique shock, where one may observe a weakening and downstream bending of the shock. Thus, it may be seen that this interferogram gives a clear view of the shock-wave and separation-zone geometries, as well as the relative strengths of density gradients in the flow. Axial symmetry prohibits a direct inference of density from this interferogram, but a great deal of information may be obtained from a simple visual inspection of this raw data.

Figure 11(b) presents a finite-fringe interferogram with fringes oriented to en-

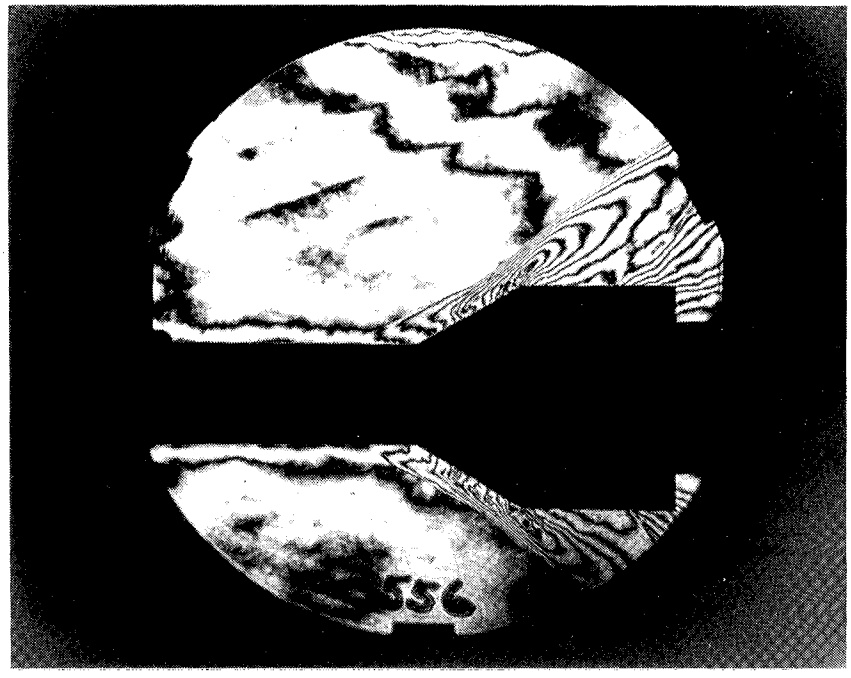

Figure 11(a). Infinite-fringe reconstruction for the 30° model at $M_\infty = 2.85$, $P_t = 1.7$ atm, and $Re_L = 18 \times 10^6$.

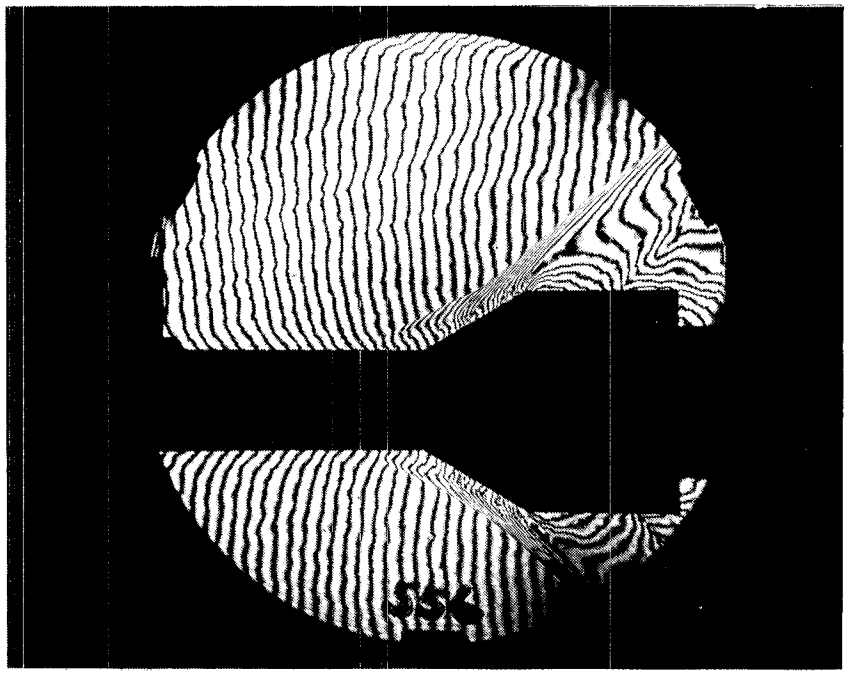

Figure 11(b). Vertical finite-fringe reconstruction for the 30° model at $M_\infty = 2.85$, $P_t = 1.7$ atm, and $Re_L = 18 \times 10^6$.

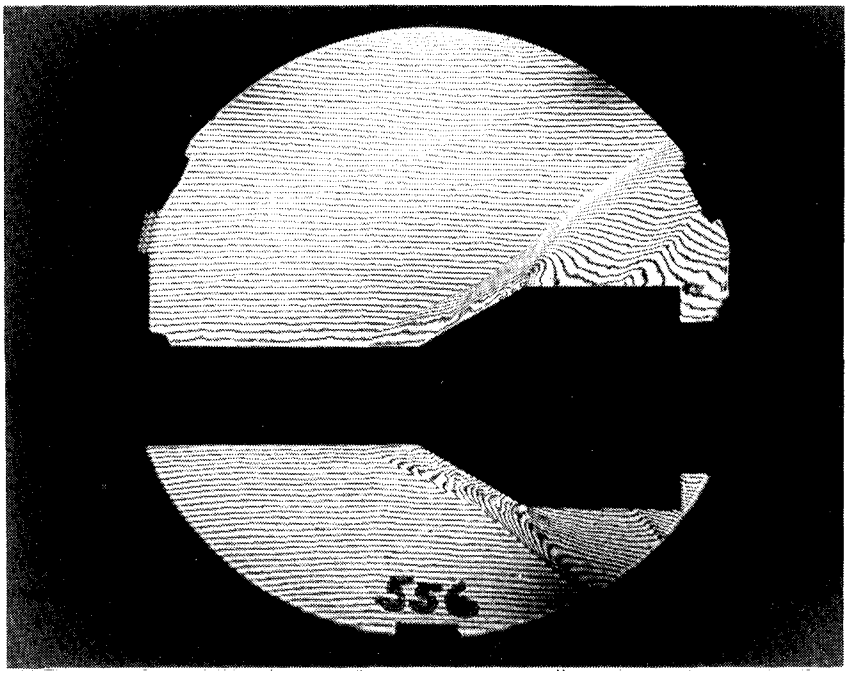

Figure 11(c). Horizontal finite-fringe reconstruction for the 30° model at $M_\infty = 2.85$, $P_t = 1.7$ atm, and $Re_L = 18 \times 10^6$.

hance boundary-layer visualization. The bending of fringes upstream at the shock and downstream at the boundary-layer edge indicates that radial density gradients have opposite signs in these regions. Mach waves may be observed in the free stream. The thickness of the boundary layer and the position of the shock and expansion fan are observable in this figure. Thus, this finite-fringe orientation proves to have a useful qualitative flow-visualization function.

The horizontal finite-fringe reconstruction of figure 11(c) is preferred for quantitative data reduction. Inversion of the refractive index integral of Equation (1) by the techniques outlined in the experimental description section is most accurate if fringe-number data are approximated at a large number of closely spaced radial positions. Fringe-profile intersections are limited for infinite-fringe interferograms (figure 11(a)) so that fringe-number values must be approximated from only a few data points. Finite-fringe reconstruction as shown in figure 11(c) greatly increases the number of fringe-profile intersections and, therefore, reduces data-approximation error. This finite-fringe reconstruction effectively superimposes a linear $\Phi(y)$ fringe-number function over the infinite-fringe field of figure 11(a). Since $\partial r/\partial y$ is positive above the model and negative below, the superposition yields the unsymmetrical fringe pattern of figure 11(c). The $\Phi(y)$ function may be calculated from fringe spacing in the free stream where the density is known to be uniform. Equation (1) now becomes

$$N(x,y) - \Phi(y) = \frac{1}{\lambda} \int [n(x,y,z) - n_0] dz \tag{7}$$

and may be solved using the least-squares, Abel integral inversion technique. Sample interferograms from each of the six flow cases (with a limited field of view) are presented in figure 12. A full complement of interferogram prints is found in Appendix D.

Digitization and Integral Inversion

Figure 13(a) shows digitized and least-squares approximated fringe-number data along a profile located 2 cm downstream of the compression corner for the

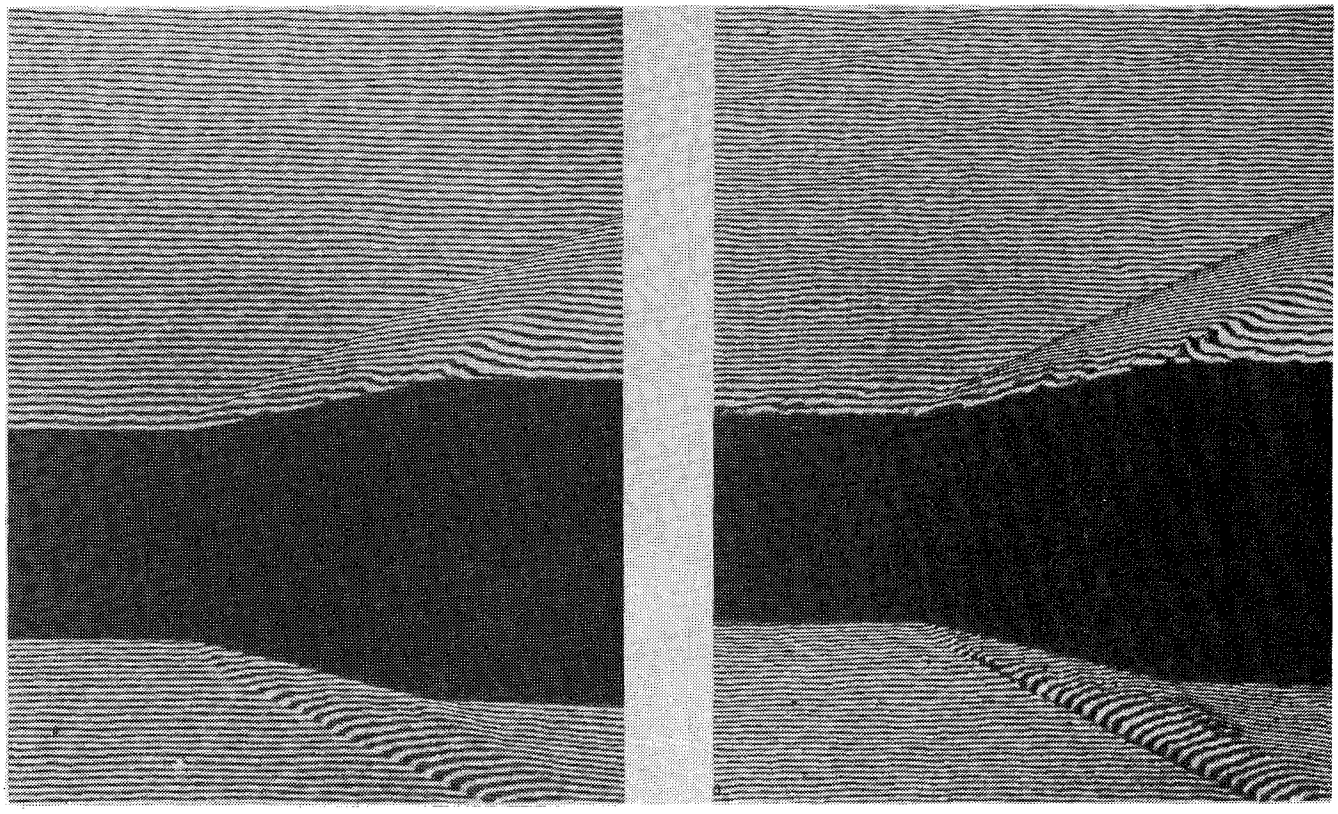

Figure 12. Horizontal finite-fringe interferogram for the 12.5° model.
(a) $P_t = 1.7$ atm, $Re_L = 18 \times 10^6$, (b) $P_t = 3.4$ atm, $Re_L = 36 \times 10^6$,

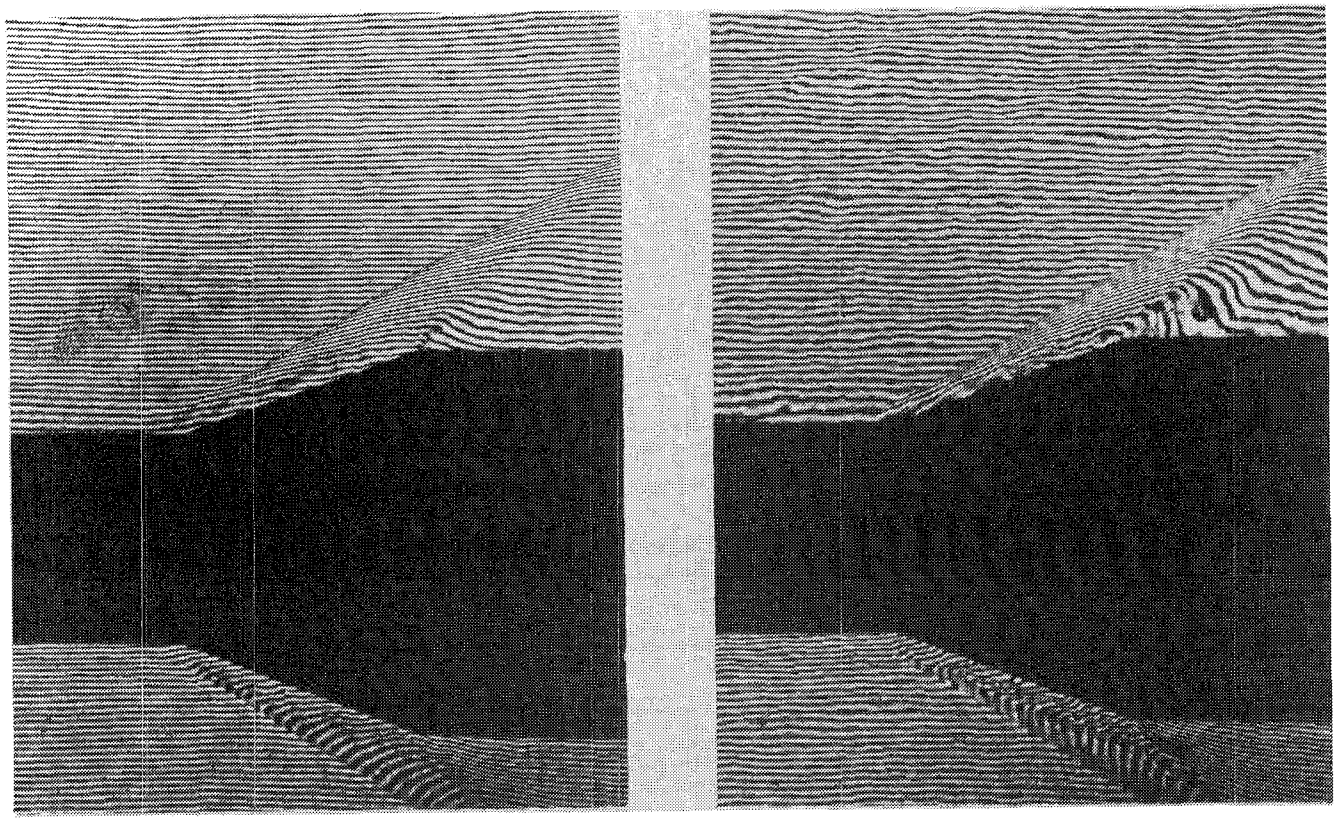

(c) (d)

Figure 12. Continued. (c) $P_t = 1.7$ atm, $Re_L = 18 \times 10^6$, (d) $P_t = 3.4$ atm, $Re_L = 36 \times 10^6$,

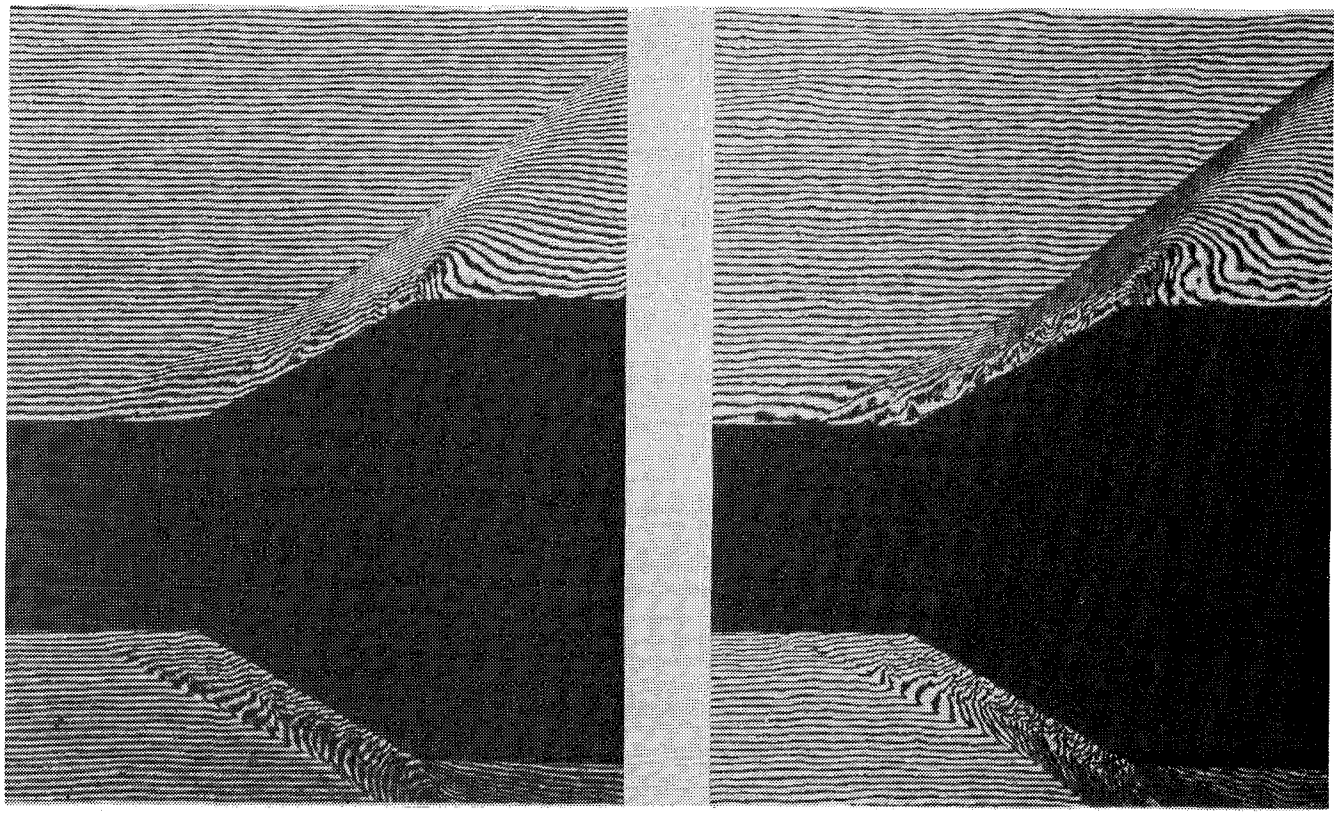

(e) (f)

Figure 12. Concluded. (e) $P_t = 1.7$ atm, $Re_L = 18 \times 10^6$, (f) $P_t = 3.4$ atm, $Re_L = 36 \times 10^6$.

30° cone model at 1.7-atm total pressure. The variation of digitized data in the free stream is an indication of turbulence related noise levels. The density profile of figure 13(b) was obtained by applying the least- squares Abel integral inversion technique to figure 13(a) fringe-number data. The presence of a weak reattachment shock system is indicated by the change in curvature observed at a y location of 1.2 cm.

Figure 14(a) shows raw and approximated fringe-number profiles at an x location of 6.20 cm, 1 cm downstream of the cone-afterbody corner. An examination of the finite-fringe interferogram of figure 11(c) for the region above the model shows a deficiency in fringe-profile intersections inside the expansion fan which is directly linked to the selection of the function, $\Phi(y)$, during reconstruction. A $\Phi(y)$ with opposite sign provided closely spaced data inside the expansion, but sparse data near the shock. To achieve more continuous raw data spacing, each interferogram was reconstructed twice with complementary $\Phi(y)$ functions, and corresponding profiles were merged. This redundant digitization was done for the 30°, 1.7-atm data only.

Figure 14(b) presents density profiles calculated from figure 14(a) fringe-number data and illustrates the need for special treatment of approximated fringe-number values in the region adjacent to the shock, as discussed in the Experimental Description section. The shape of a density profile at this location as inferred from the inviscid, conic-flow theory would consist of a step rise in density across the shock, a further isentropic compression to the expansion fan, and an isentropic expansion to the boundary-layer edge. The transformed density profile of figure 14(b) that used the previously mentioned parabolic fit approximation with outward relaxation of the shock location shows this predicted shape. In contrast, the figure 14(b) density profile calculated from the untreated fringe-number approximation of figure 14(a) displays an overprediction of density at the shock and inboard to a y location of 2 cm. For y locations less than 2 cm, the two curves differ only by a slight offset.

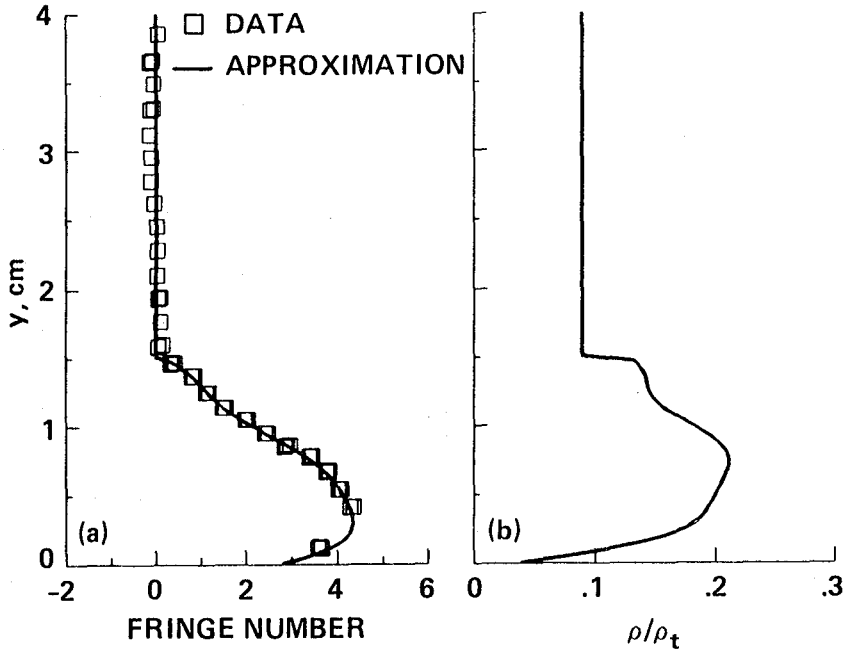

Figure 13. Profile at $x = 2$ cm for the 30° model at $P_t = 1.7$ atm and $Re_L = 18 \times 10^6$. (a) Fringe number, (b) Density.

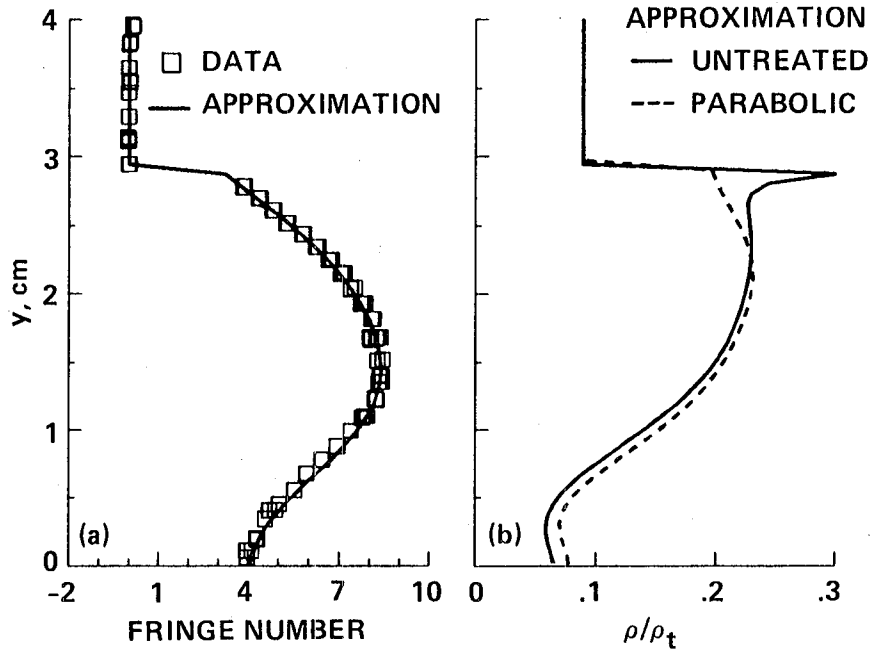

Figure 14. Profile at $x = 6.2$ cm for the 30° model at $P_t = 1.7$ atm and $Re_L = 18 \times 10^6$. (a) Fringe number, (b) Density.

Error Analysis

At this point it is appropriate to make a few observations regarding the quality of the interferometric data. A preliminary examination of the raw interferometric data (such as, the infinite-fringe interferogram of figure 11(a)) was somewhat disconcerting because the desired fringe-number data in the cylinder boundary layer and interaction regions were on the same order (1 fringe) as noise in the free stream. Finite-fringe reconstruction and filtering procedures as outlined in the Experimental Description section helped to ameliorate this problem. Furthermore, the agreement obtained in initial comparisons with computed results was quite encouraging. Nevertheless, a complete experimental investigation must determine experimental error quantitatively if the results are to be interpreted appropriately.

The standard approach to quantifying experimental error in the measurement of mean quantities involves the evaluation of a statistically significant sample of measurements for mean and standard deviation values, from which error bars associated with a given level of confidence may be computed. An equation for the computation of a $(1 - \alpha)100\%$ confidence interval for the population mean, μ, is given (Walpole & Myers, 1971) in terms of the value of the t distribution, $t_{\alpha/2}$, and the sample mean, $\bar{x}$, standard deviation, σ, and size, n.

$$\bar{x} - \frac{t_{\alpha/2}\sigma}{\sqrt{n}} < \mu < \bar{x} + \frac{t_{\alpha/2}\sigma}{\sqrt{n}} \tag{8}$$

Note that the sample size, n, appears in the denominator of the above expression, indicating the need for large samples if a high level of confidence is to be achieved. The very tedious nature of nonautomated data reduction of global interferometry data has been discussed, and the acquisition and processing of many separate interferograms for each flow condition was not feasible. A sample of four interferograms at each flow condition was selected to limit the data-reduction task but still obtain a time-averaged measurement. This sample was increased to eight for the more unsteady 30°, 1.7-atm case, which has been critically compared with the computational results. A 95% confidence interval for the mean density as computed from

such an analysis is shown in figure 15 for the sample profile of figure 13. This profile was located in the reattachment shock region of the 30° model flow field and therefore represents the upper limit of data variation resulting from flow unsteadiness. However, the smaller sample size of the other cone angle and total pressure configurations decreased confidence in their mean measurement. The number of profiles sampled and standard deviations for each profile point are tabulated along with averaged density values in Appendix D for all the interferometric data obtained.

Another aspect of the analysis of experimental error is the assessment of error arising in the reduction of any given interferogram. Such an approach is complicated by the presence of radial symmetry and the associated coupling of data across the flow field because of Abel integral inversion requirements. Nevertheless, this approach is helpful in evaluating the relative effect of the various sources of error in the interferometric data. This information may then be used to enhance the experimental technique. The sources of error in this interferometric data can be grouped as being related to the interferogram formation, data digitization, or integral inversion processes.

Sources of error related to the interferogram formation process arose from those conditions encountered by the flow on object wave during hologram construction that were inconsistent with the axisymmetric assumptions of the analysis. Of these, the principle error source was turbulence, which was inherently 3D and therefore strictly nonaxisymmetric. Turbulent effects are not normally observed in interferometric data because of the path-integration process (provided turbulent length scales are much less than the integration path length.) However, for axisymmetric flows the integration path length becomes short in regions near the axis. Figure 12 interferograms show a nonuniformity in fringes located in the boundary layer downstream of the compression corner which is more pronounced for the larger cone angle (stronger interaction) and higher total pressure flows. This distortion varied randomly from one interferogram to another and is thought to be associated

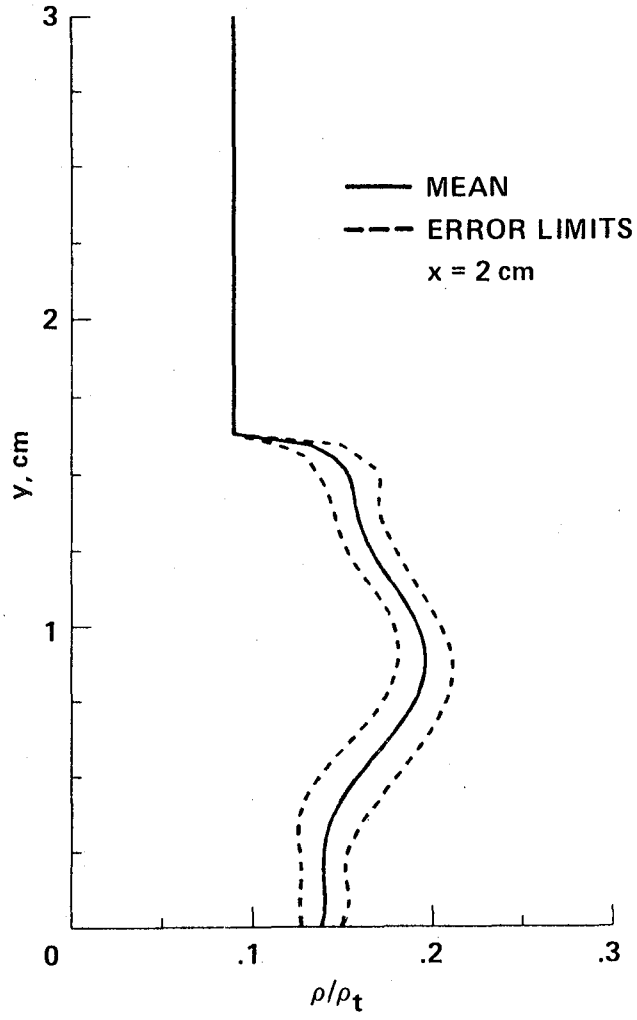

Figure 15. Mean density error limits for 95% confidence of the profile at $x = 2$ cm for the 30° model with $P_t = 1.7$ atm and $Re_L = 18 \times 10^6$.

with large-scale boundary layer turbulence downstream of the interaction region. Such turbulence not only affected the averaging requirements but also induced a degree of three dimensionality in the refractive index field and a corresponding error in transformed values. Another important turbulence-related error source was observed in the free-stream region. Fringes in this area were relatively smooth but (for finite-fringe reconstruction) exhibited some random variation in fringe spacing. Free-stream turbulence was the likely cause of this effect.

Although turbulence-related flow three dimensionality introduces error into the instantaneous flow-field measurement, accurate mean flow quantities may still be obtained. Several interferograms may be averaged to obtain a mean flow fringe field (free of 3-D effects) to which the Abel transform may be applied. Because of the linearity of the Abel transform operator, a procedure wherein interferograms are first transformed and then averaged is equally valid if one is careful not to interpret each separate density field as an instantaneous measurement.

The optical path-matching limitations of the interferometer were also a source of error which was internal to each interferogram. The fact that the two holographic plates were exposed and developed separately, then repositioned together in a different mounting apparatus must result in some slight plate warpage and relative shear. Such motions introduce error if any wavefront warpage is present in the reconstruction wave and are therefore inescapable for reconstruction systems using collimated light. The fringes observed in the free stream of figure 11(a) are thought to be caused by this type of error.

Errors introduced in the digitization process may be identified by either fringe center location or wedge-fringe removal. When using a graphics tablet to digitize fringe locations, the human judgment required to identify the darkest center of the fringe may introduce inconsistency. Such errors were alleviated for the finite-fringe interferograms (as compared with the infinite-fringe reconstruction of figure 11(a)) because the fringes were much narrower. The need to remove the wedge-fringe

function as determined by fringe spacing in the free stream was more problematic. Free-stream fringe spacing was not perfectly uniform. Thus, the wedge-fringe function slope (and therefore the derived boundary-layer or shock-internal region fringe-number field) was weakly dependent on the extent of the free-stream region evaluated.

The fringe-number approximation step that was required prior to inversion of the Abel integral was potentially the largest source of experimental error. It was recognized that the higher-order polynomial fits used would not agree with the data perfectly; however, this approximation technique provided the most credible density curves. It may be argued that this approach has a tendency to reduce free-stream turbulence related error by smoothing out large excursions in fringe number, but this is an intuitive rather than theoretically derived concept. Furthermore, the method of curve fitting employed relied on user interaction to validate the accuracy of the approximated fringe-number curvefit (with accompanying adjustments at the wall and internal to the shock) and was therefore subject to a human judgement factor.

A final source of error associated with the integral inversion process arose from the fact that the numerical finite-element technique used must precipitate some numerical error when compared to an analytical solution. This error was minimized by the use of fringe-number approximation to provide close data spacing and therefore reduce the finite-element thickness.

Of the error sources cited, only turbulence related flow three dimensionality and optical path-matching errors were dependent on averaging. The other sources of error could be evaluated for any interferogram. To illustrate the individual and combined contributions of these error sources, the sample profile of figure 13 was analyzed and is discussed in the following paragraphs.

The logical starting point was an evaluation of digitization error. The limited resolution of the graphics tablet as well as the human judgment factor associated

with fringe-center location were really spatial location errors, but the use of finite-fringe interferograms with incumbent wedge-fringe removal resulted in a coupling of this spatial error with fringe-number value. Because of this coupling, it was judged appropriate to quantify this error in terms of both position and fringe number. This was done by digitizing a single fringe-profile intersection (having a typical fringe width) many times and evaluating the scatter of position and fringe-number values. The standard deviations for these measurements were 0.0067 cm and 0.030 fringe, respectively. Since there is no method of obtaining fringe number values except through digitization, it was assumed that this digitization error is present in all the following error quantities.

The second error source addressed was that associated with wedge-fringe removal. In this case, the figure 13 profile was digitized many times with a separate wedge-fringe removal calculation each time and with a systematic variation in the free-stream location at which the profile was terminated. The scatter in fringe-number value for each fringe-profile intersection was then computed and averaged over the several intersections. Standard deviations of 0.048 and 0.099 fringe were calculated for profile and free-stream data, respectively. The deviation for free-stream data is of secondary interest since these data do not enter into the Abel inversion process. However, it is possible to say that this free-stream scatter identifies a fundamental limit to the axisymmetry of the field.

To evaluate error resulting from fringe-number approximation, each profile set with a given free-stream terminus was curvefit and the deviation of data from the curvefit value was computed, thus suppressing wedge-fringe removal error. This deviation was consistent for the various terminus sets, with an average value of 0.055 fringe. The fact that this error is on the same order as digitization and wedge-fringe removal error indicates that the least-squares curvefit approach to fringe-number approximation contributes an inherent averaging which, in some degree, counteracts error introduced by digitization and free-stream turbulence.

The most challenging error analysis task was to determine how these errors propagated through the integral inversion process. While a rigorous mathematical treatment was certainly possible, such a treatment would have been complicated. The alternative method employed herein involved the addition of some known error to a sample profile which was then processed by the integral inversion software. This error laden density profile was then compared with the unaltered case. Based on the considerations discussed above, the largest of the calculated deviations (0.055 fringe) was added or subtracted to the approximated profile. The resulting density profiles were compared with the unaltered profile and a relative error (as a percentage of the maximum density value) across the profile was calculated. This error was found to be everywhere less than 1% having a maximum adjacent to the shock and gradually decreasing inboard to the model surface. This is consistent with the discussion of figure 14 and emphasizes the pronounced effect of fringe-number data in the shock region on density values just internal to the shock. It also emphasizes the forgiving nature of the Abel integral inversion process for data nearer the surface. These results contrast with the intuitive (and inherently valid) argument that density values close to the surface are less accurate for axisymmetric phase objects because of a shorter integration path length.

Finally, it was necessary to evaluate the error associated with the numerical method of integral inversion. A straightforward approach was adopted here wherein the density profile was numerically integrated (Simpson's rule) to provide a fringe-number profile which was then evaluated against the original. Thus, two numerical procedures (integral inversion and integration) were employed and an evaluation of the numerical error associated with integral inversion alone could only be estimated as half of the total error observed. For the 50-element sample profile of figure 13 the total standard deviation was 0.072 fringe or 1.67% of the full-scale value. It follows that the error associated with numerical integral inversion is less than 1%.

This error analysis identified the sources and relative effects of the various

factors contributing to experimental error. These have been quantified for a sample profile for the 30°, 1.7-atm case which crossed the separation and reattachment shocks. A large disparity is observed in the comparison of the standard deviation of the averaged profile data from Appendix D with the 1% error predicted for the analysis of any given interferogram. There are two possible explanations for this difference. The flow may be unsteady; or the error sources which could not be analyzed for a single interferogram (turbulence related flow three dimensionality or optical path matching error) contributed significantly. Evaluation of these error sources, perhaps through the analysis of several reconstructions of a single flow-on hologram with various flow off plate combinations, might enhance the quality of interferometric data in future studies. However, I believe that larger sample sizes are essential to improve confidence in the mean values obtained.

Another type of error must be identified which relates to the spatial resolution of the imaging system. The optical imaging system used for this experiment consisted of many thick and thin element lenses, large and small flat mirrors, large schlieren-grade spherical mirrors, and holographic elements. To keep the total path length as short as possible (to reduce coherence length limitations), these elements were typically of low f-number and therefore contributed significant aberration to the image. Length scaling was obtained from the interferogram images and was therefore subject to some error from the aberrant warping of the image. This was partially treated by applying a local profile scaling correction based on model surface location. However, not all of the inconsistency could be removed. An evaluation of many interferograms indicated an average residual spatial resolution error of approximately 1 mm.

Flow-Field Data

In this experiment, as the cone angle was increased from 12.5° to 30°, the shock strength increased, the shock position moved upstream, and the boundary

layer separated. The interaction strength corresponding to the onset of separation as well as the effect of Reynolds number on this phenomena have been emphasized in previous experimental investigations of the SW/BLI. Figure 16 is a summary of an oil-flow study which illustrates these effects.

Oil applied at the surface in a compression-corner SW/BLI will tend to accumulate at one or two locations. One being an oil accumulation at location x_s upstream of the corner, and the other being an oil accumulation at location x_r downstream of the corner. These accumulations are sometimes associated with flow separation and reattachment. However, such oil accumulations are subject to pressure-gradient as well as shear-stress effects. A residual, shock-induced, adverse-pressure gradient at separation where shear stress goes to zero will cause oil to flow somewhat upstream of the separation point, depending on the thickness of the oil film. Similar conditions exist in the reattachment region when a reattachment shock is present. Thus, interpretation of the x_s and x_r oil accumulations as points of separation and reattachment can only be approximate.

These oil-flow data show the expected trends. For larger model cone angles, the associated stronger pressure rise produced an increase in the extent of the separated region at a given Reynolds number. A reduction in the extent of the separated region with increase in Reynolds number (total pressure) was observed, in agreement with results reported by Settles & Bogdonoff (1973), Law (1975), and Roshko & Thomke (1976). A linear extrapolation of oil accumulation data yielded a point of incipient separation in the neighborhood of the 16.5° value reported by Settles & Bogdonoff (1973).

Surface-pressure distributions from pressure data and computations at 1.7-atm total pressure are presented in figure 17(a), (b), and (c) for the three cone angles. Oil-flow accumulation points, x_s and x_r, are indicated. Shock and expansion fan locations are clearly identified by pressure jumps. A thickening of the shock by the boundary layer is manifest by a gradual pressure rise. In the 20° pressure data, a

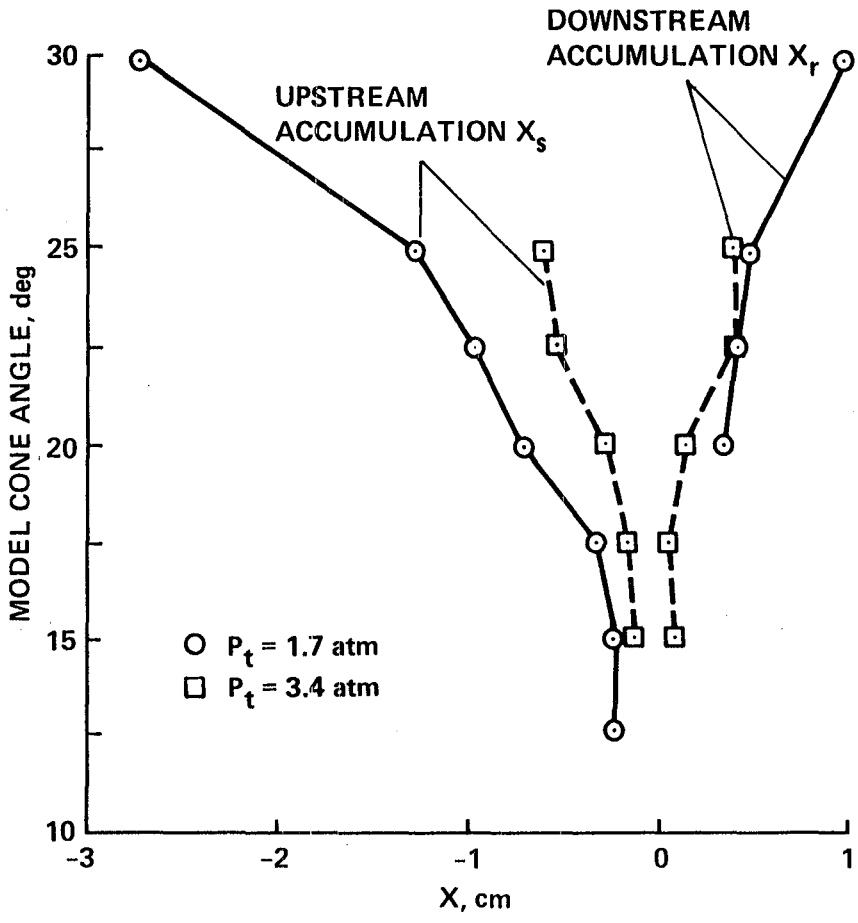

Figure 16. Oil-flow point of accumulation.

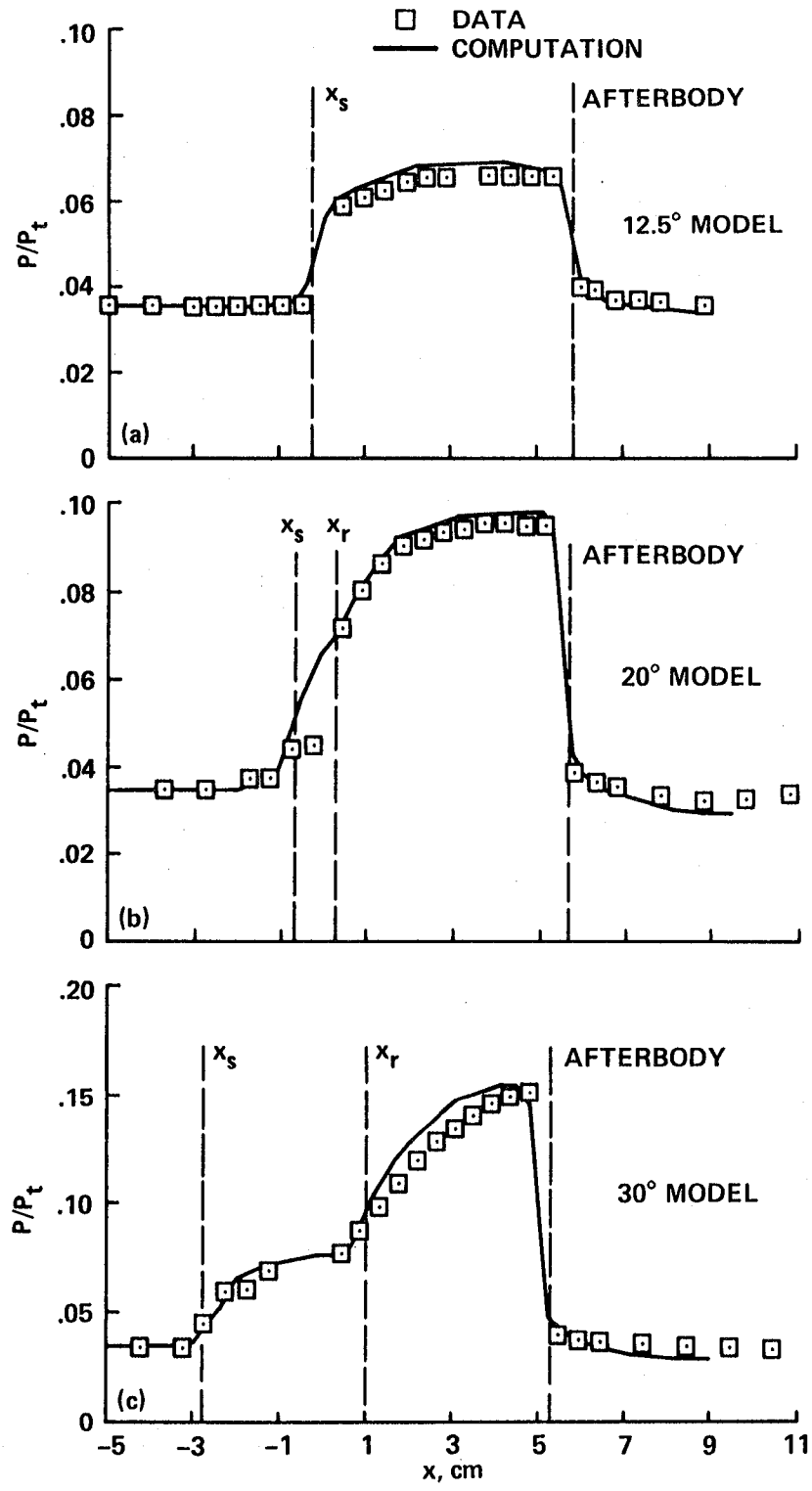

Figure 17. Surface-pressure distributions from experiment and computation at $P_t = 1.7$ atm and $Re_L = 18 \cdot 10^6$. (a) 12.5° model, (b) 20° model, (c) 30° model.

small constant surface-pressure region is observed corresponding to the separated region indicated by the oil flow. This plateau is not present in the computation. Beyond this detail, good agreement is observed between pressure data and computed pressure distributions.

Surface-pressure distributions from pressure data at both 1.7- and 3.4-atm total pressure are presented in figure 18(a), (b), and (c) for the three cone angles. These data are in agreement with oil-flow data in identifying the effect of increasing Reynolds number as reducing the extent of separation, as observed in the distributions for the 20° and 30° models. The reason for the offset observed in the 20° and 30° data is not clear, but may be caused by some discrepancy in pressure transducer calibration.

Velocity profiles from LV and computation, and density profiles from interferometry and computation at six streamwise locations for the 12.5° model at 1.7-atm total pressure are presented in figures 19 and 20. The density profile of figure 19(a) and the velocity profile of figure 20(a) show good agreement between experiment and computation at a location in the boundary layer 5 cm upstream of the cylinder-cone corner. This is to be expected since zero-pressure-gradient boundary-layer calculations are certainly within the capability of a Navier-Stokes solver. However, the agreement on density is particularly encouraging since raw interferometric data as presented in figure 11(a) suggest that data in the upstream cylinder boundary layer are near the lower resolution limit of the interferometer.

Good agreement is observed between experimental data and computed values for each of the other profiles presented in figures 19 and 20. Some general observations may be made regarding the quality of interferometric data as well as the accuracy of the computation. First, it may be noted in figure 19(b) that the interferometric data does not capture the density profile "wrinkle" which indicates the shock-wave penetration of the boundary layer in the compression corner. This is caused by the limited data resolution of interferometric data associated with

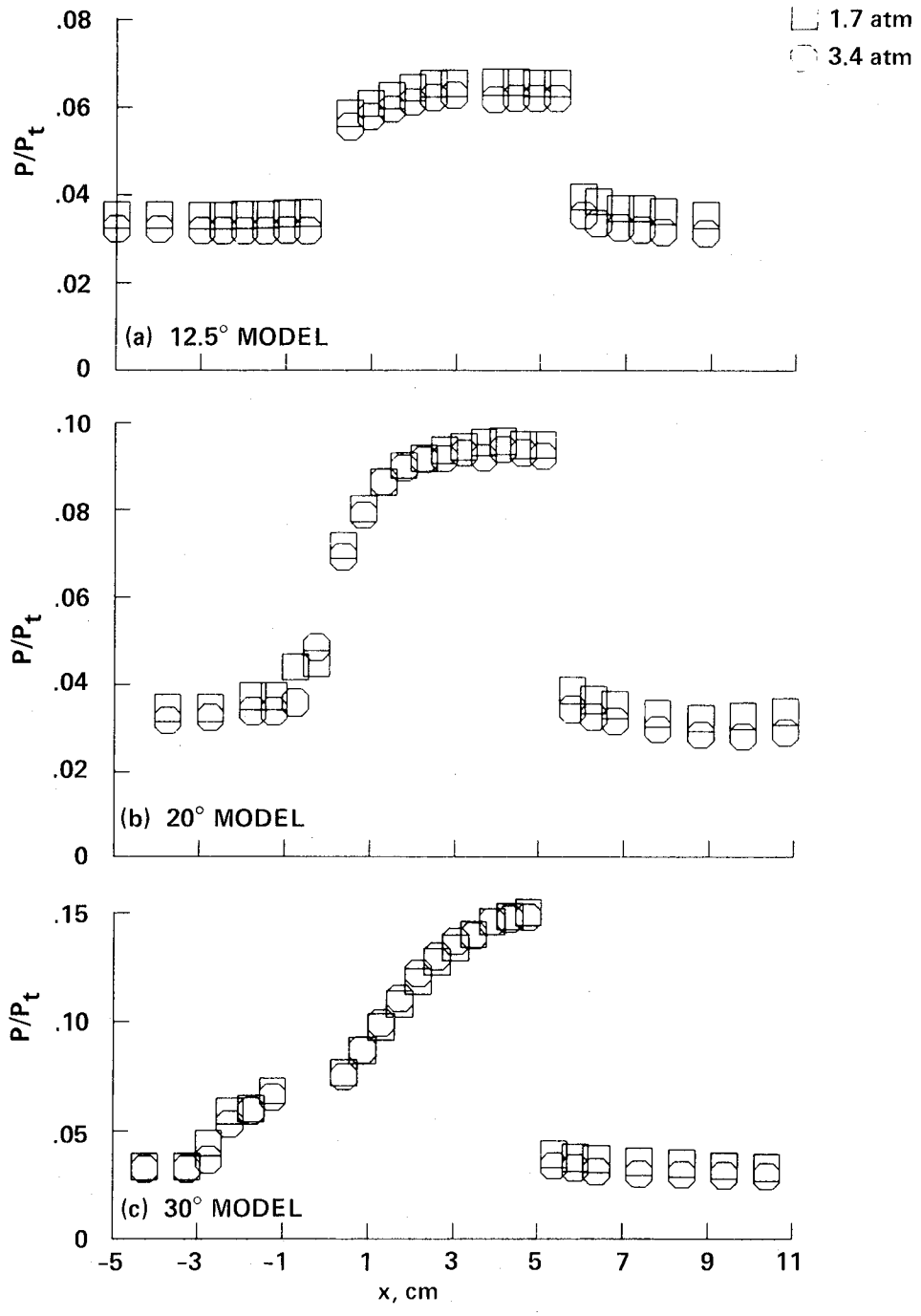

Figure 18. Surface-pressure distributions from experiment at $P_t = 1.7$ atm and $Re_L = 18 \times 10^6$. (a) 12.5° model, (b) 20° model, (c) 30° model.

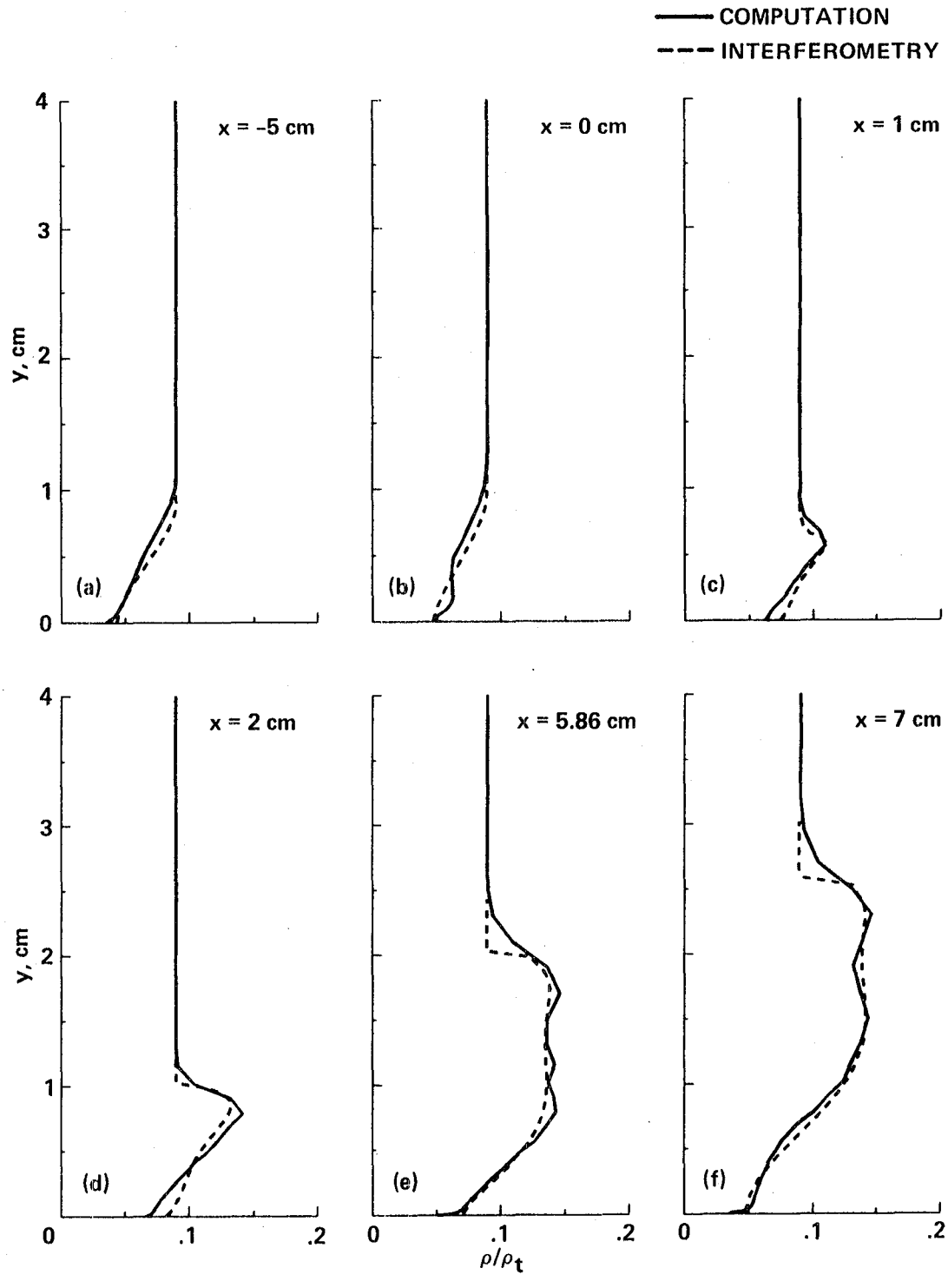

Figure 19. Density profiles for the 12.5° model at $P_t = 1.7$ atm and $Re_L = 18 \times 10^6$.

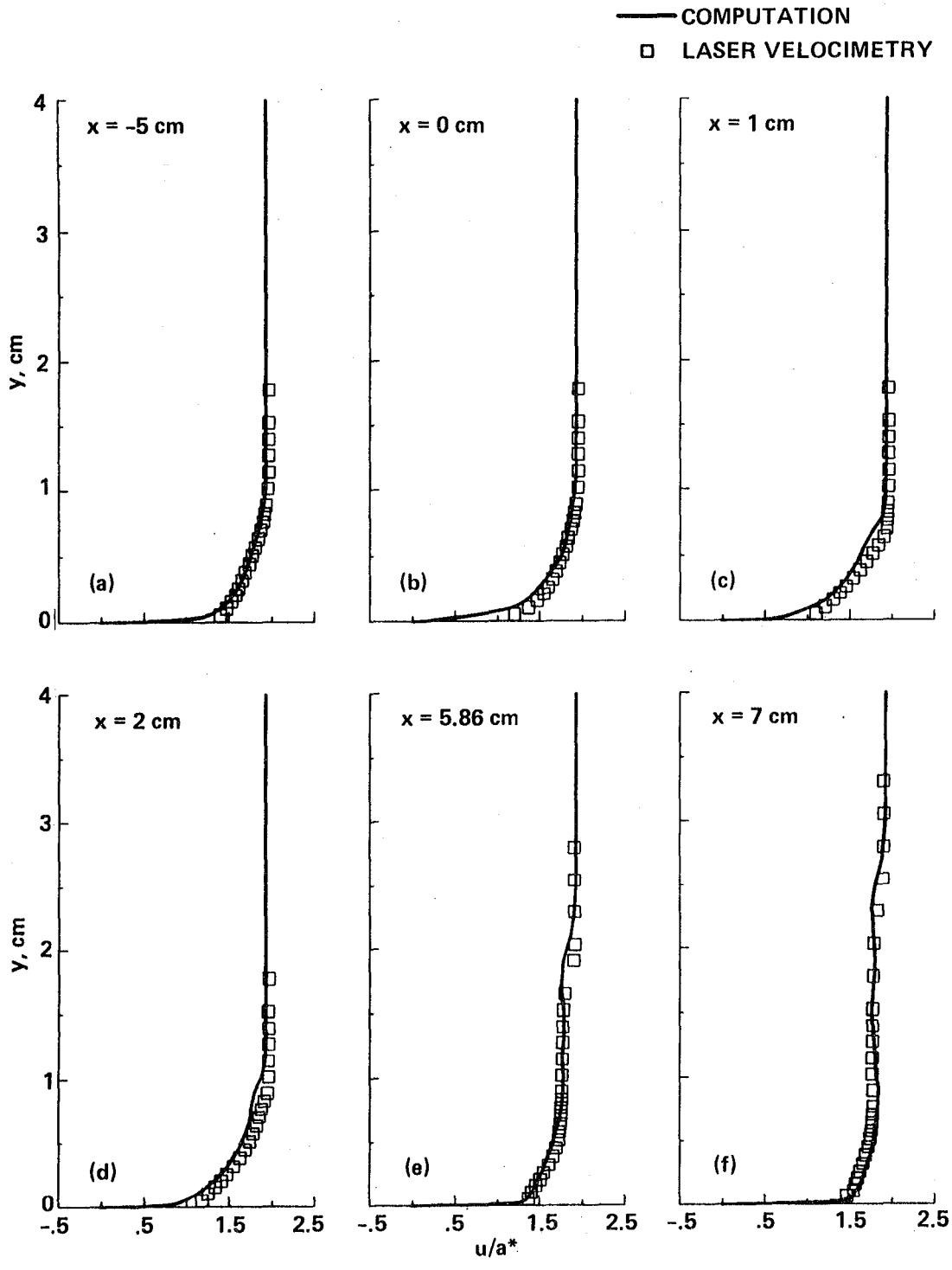

Figure 20. Velocity profiles for the 12.5° model at $P_t = 1.7$ atm and $Re_L = 18 \times 10^6$.

the analysis techniques previously described wherein a fringe-profile intersection is necessary to identify a fringe-data point. Such detail is likely contained within the interferometric data but more sophisticated analysis techniques are required to obtain it.

Secondly, for profiles crossing the shock, the interferometry data was helpful in identifying the inability of the computation to capture the sharp density gradient across the shock. In an evaluation of computed velocity profiles against the LV data of figure 20, one might be led to conclude that the computation located the shock too far outboard. This is partially true, but the density profiles of figure 19 indicate that grid resolution limitations are another contributing factor and that the computed shock location is perhaps smeared rather than too far outboard. Overall agreement between computation and experiment in both density and velocity profiles is quite good. Because of past experience, the Navier-Stokes solver can be considered capable of accurately predicting this weaker interaction flow. Furthermore, the well-established confidence in this LV system as a reliable research tool lends credibility to the quality of the acquired LV data. Therefore, the main result of this comparison for the 12.5° model is to establish the validity of the interferometric technique in the analysis of these flows. This is done directly by comparison with the computation as well as indirectly, through the consistent physical models within the Navier-Stokes solver, by comparison with LV data.

Velocity profiles from LV and computation, and density profiles from interferometry and computation at six streamwise locations for the 30° model at 1.7 atm are presented in figures 21 and 22. In this flow, the much stronger interaction and large separated zone greatly reduce confidence in the computed values. An assessment of code performance is possible with evaluation against both interferometer and LV data. An overprediction of the radial extent of separation in the calculation is apparent in the velocity profiles of figure 22(b) and 22(c). Computed density profiles show a thicker region of nearly constant density close to the wall (as compared

to interferometry profiles) at these locations, but this comparison is not nearly as informative as that of the velocity profiles.

The interferometric density profile of figure 21(d) is in the region of highest shock unsteadiness and exhibits a smoothing of shock structure detail because of averaging over several interferograms. The single interferogram density profile of figure 13(b), also at an x location of 2 cm, shows good agreement with the computed density profile of figure 22(d) on density peak and wall values, and on the relative location of the reattachment shock system; but shows the entire density field to be shifted inward. This indicates an inboard shock position for the particular interferogram of figure 13(b) compared to the average shock position.

The computed density profile located at the cone-afterbody corner shows rather strong disagreement with interferometry data. Interferometry data in this region was subject to a slight degree of fringe dropout very near the model surface but was otherwise reliable. Fluid in this region had traversed an extensive region of nonequilibrium boundary layer. The cause of the discrepancy may be related to turbulence modeling detail in this nonequilibrium region, but such a statement cannot be made conclusively within the scope of this investigation. No such disagreement is observed in the comparison of velocity profiles.

Velocity profiles do, however, give evidence of an outboard overprediction of shock location by the computation for profiles at x locations of 5.20 and 7.0 cm. This error is confirmed in the density comparison, though the more obvious grid resolution limit decreases the magnitude of the mislocation. It may be seen that both interferometric and LV data are quite useful in the assessment of code performance for this flow, and that a synergism is realized through the use of both experimental techniques together.

Experimental density contour plots for the three models at 1.7-atm total pressure are presented in figure 23. Contour plots of the computed densities are included in figure 24 for comparison. Reattachment shock detail is shown in both interfer-

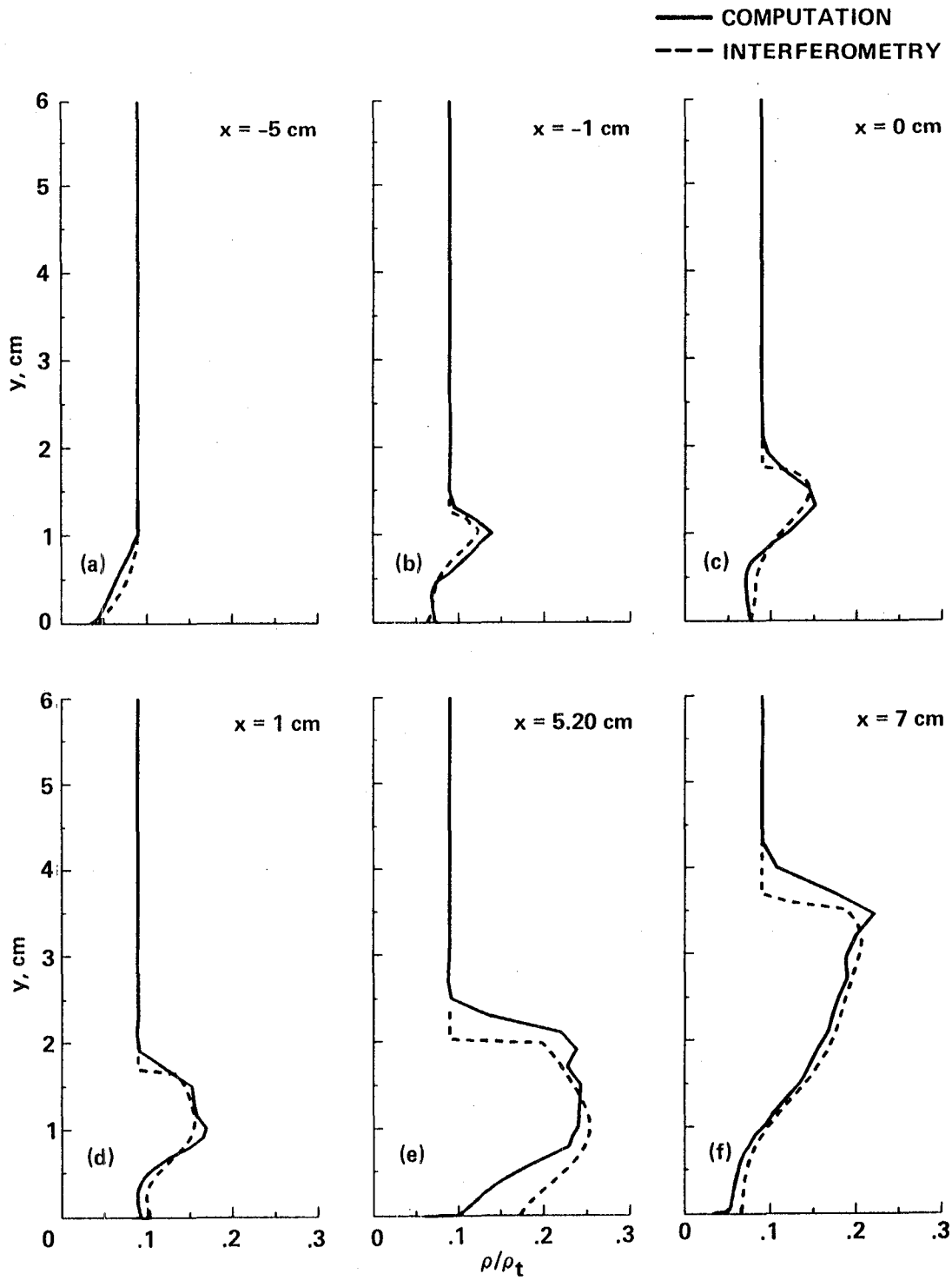

Figure 21. Density profiles for the 30° model at $P_t = 1.7$ atm and $Re_L = 18 \times 10^6$.

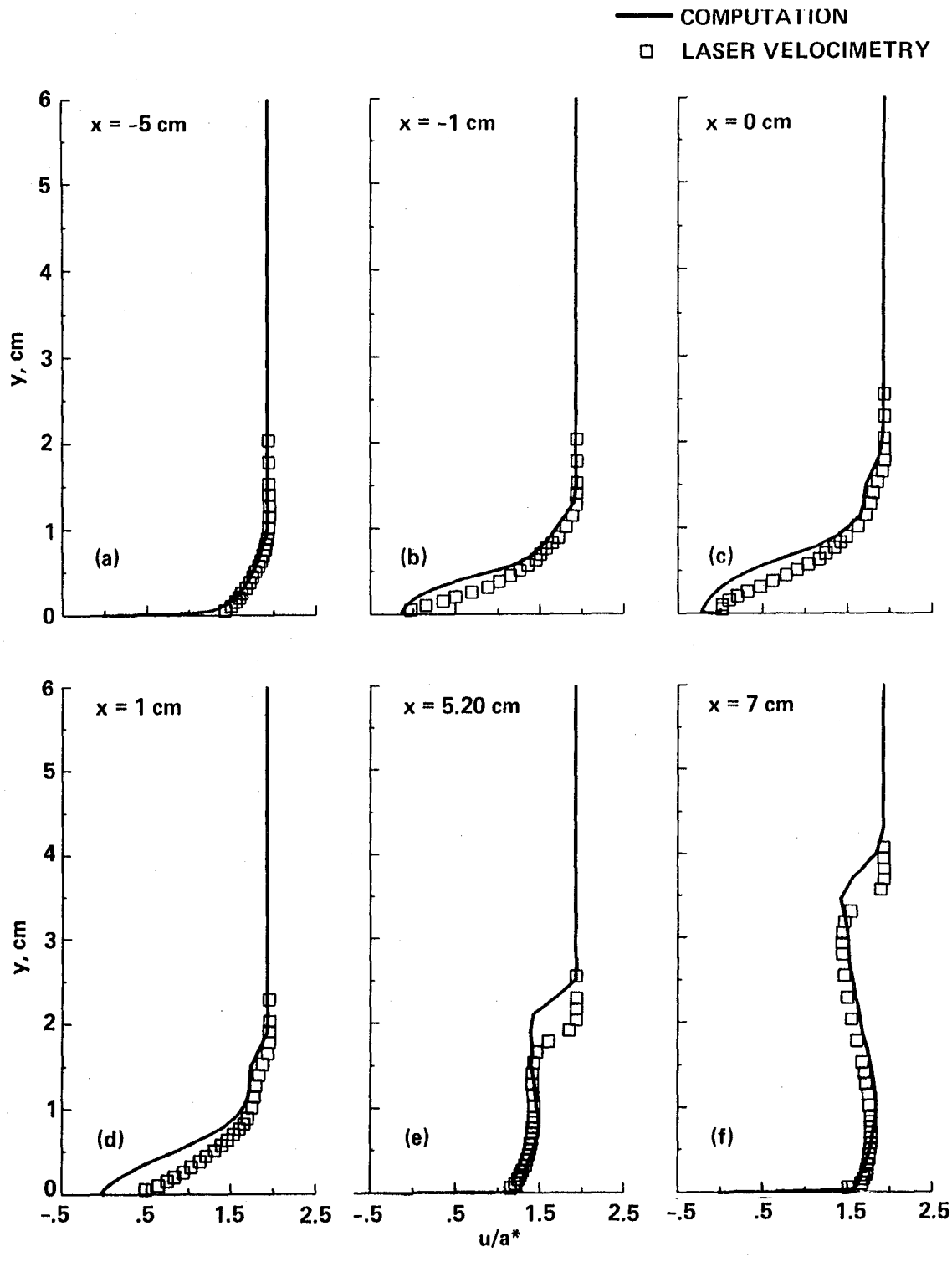

Figure 22. Velocity profiles for the 30° model at $P_t = 1.7$ atm and $Re_L = 18 \times 10^6$.

ometric and computational density contours for the 30° model. In the absence of large-scale separation, the bifurcated shock does not appear in the 12.5° and 20° cases. A comparison of density contours from interferometric data and computation emphasizes the slight outboard displacement and broadening of the shock provided by the computation. Density levels compare well over the entire field.

Figure 25 presents density contour plots from interferometry data for the 3.4-atm total pressure flows. These plots do not vary markedly from the contours of figure 23 except that the shock is represented as a sharper density jump resulting from the large fringe-number jump encountered in the reduction of these high-pressure interferograms. The contour plot of figure 25(c) for the 30° model is truncated at an x location of 2 cm. This was necessary because the refractive effects pursuant to the strong shock arising from the coalescence of separation and reattachment shocks produced a strong shadowgraph effect. This effect resulted in the washout of fringes in this region because of a reduced intensity of the object wave during interferogram reconstruction.

These contour plots illustrate the utility of the interferometric technique for the analysis of the global flow field. Although the analysis of interferograms is rather complex, the technique permits a rapid acquisition of global flow-field data with a minimum of wind tunnel run time. The interferometric data obtained in this test are tabulated in Appendix D for the benefit of those who wish to make detailed comparison with independently obtained computed, or experimental data.

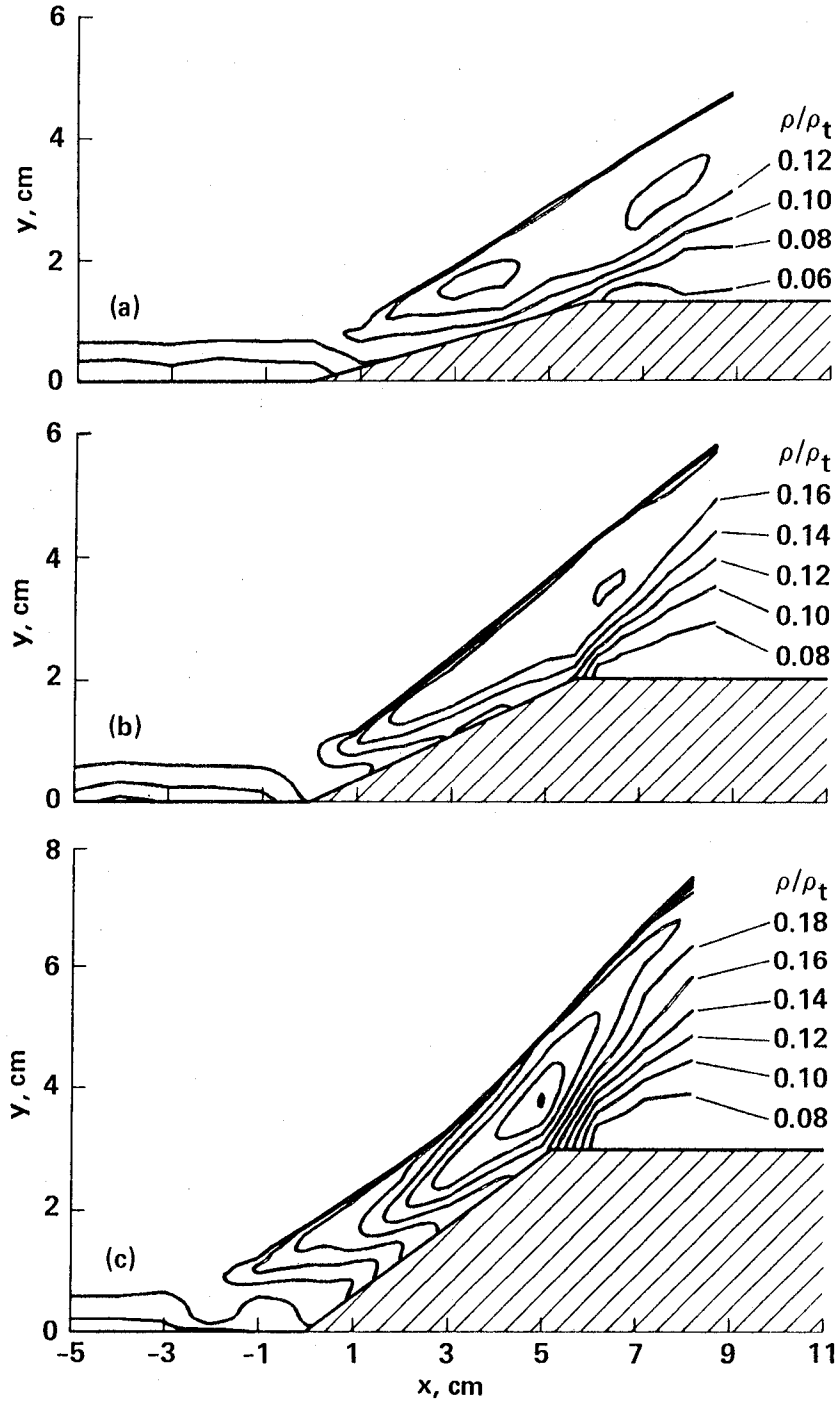

Figure 23. Density contours from interferometry at $P_t = 1.7$ atm and $Re_L = 18 \times 10^6$. (a) 12.5° model, (b) 20° model, (c) 30° model.

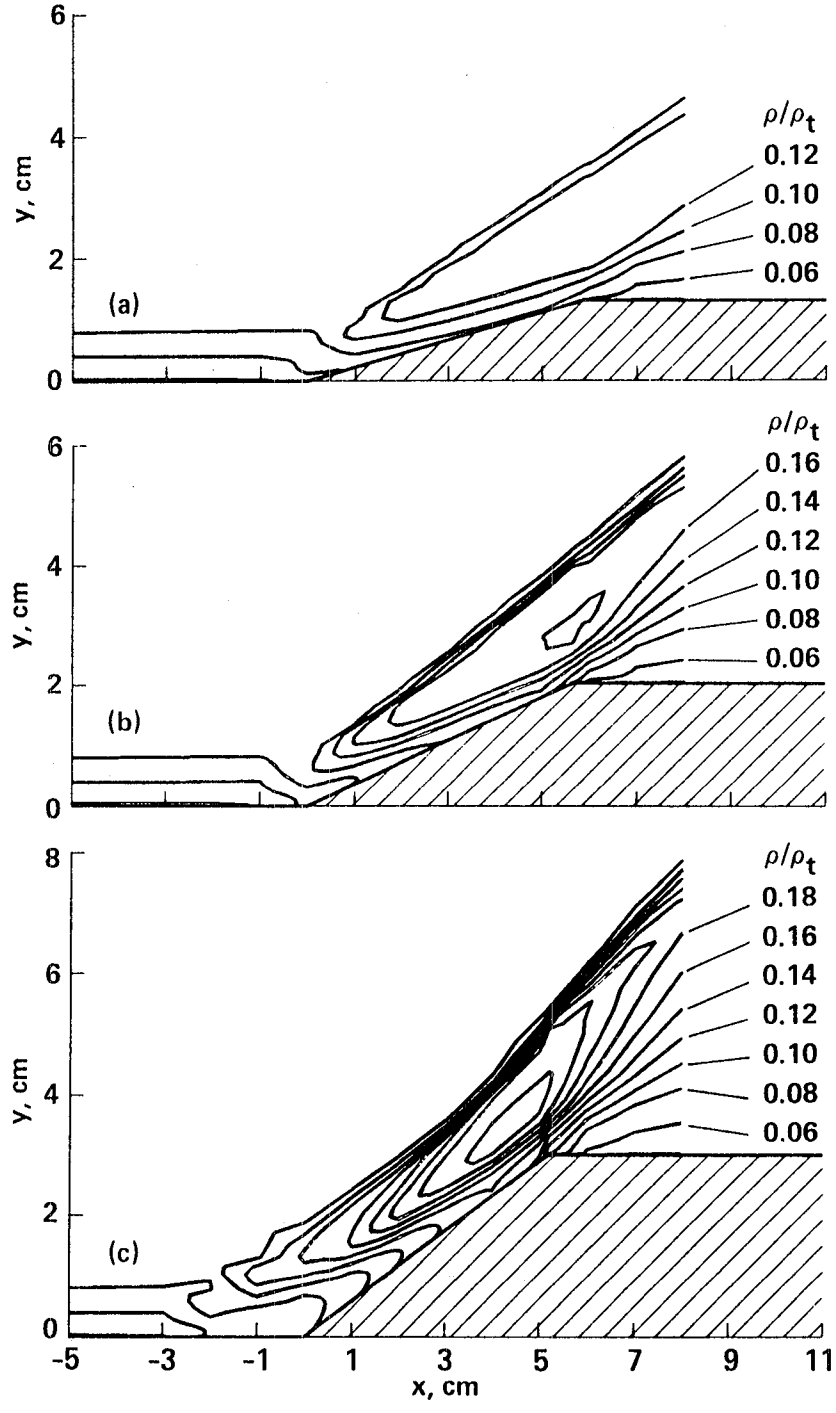

Figure 24. Density contours from computation at $P_t = 1.7$ atm and $Re_L = 18 \times 10^6$. (a) 12.5° model, (b) 20° model, (c) 30° model.

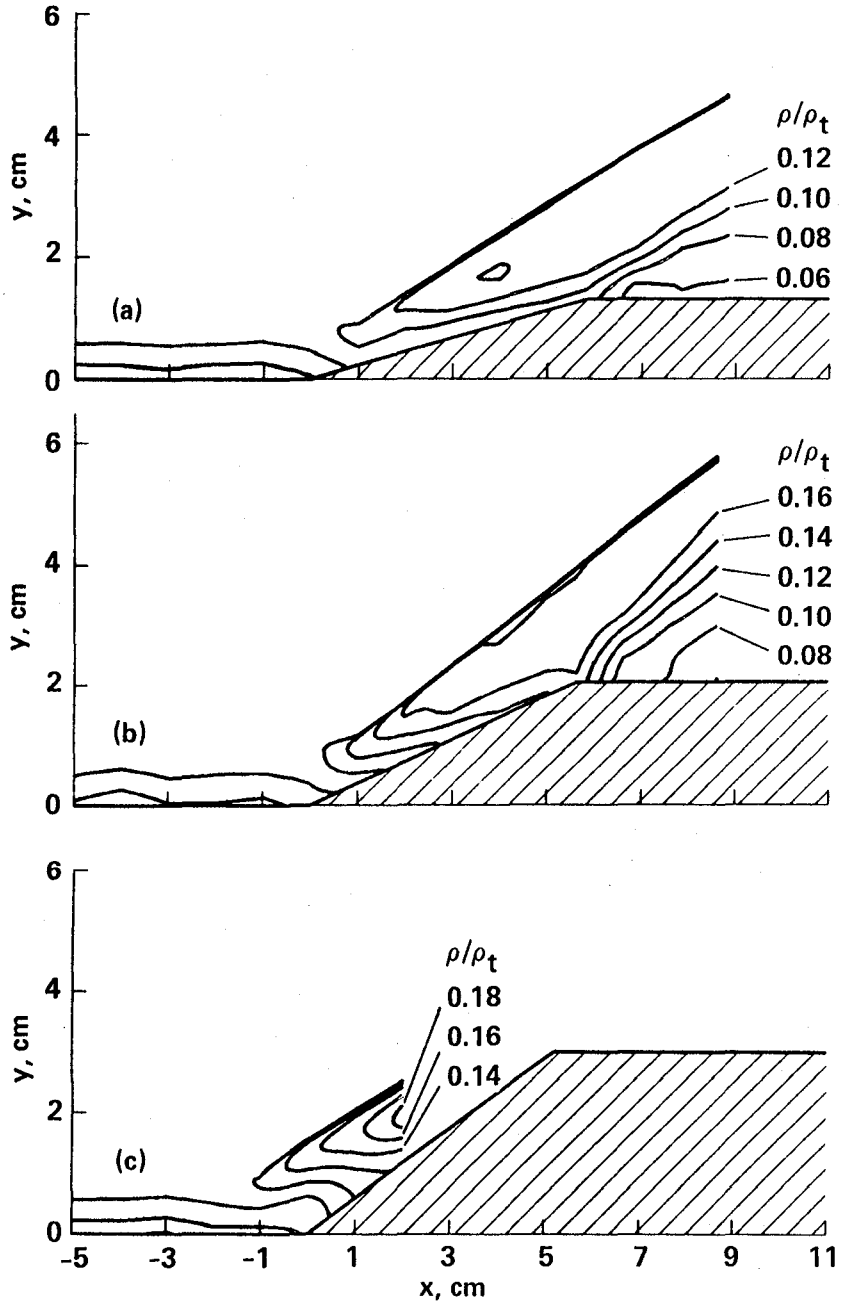

Figure 25. Density contours from interferometry data at $P_t = 3.4$ atm and $Re_L = 36 \times 10^6$. (a) 12.5° model, (b) 20° model, (c) 30° model.

CONCLUSIONS AND RECOMMENDATIONS

To provide quantitative aerodynamic data for comparison with computational and predictive schemes, an experimental study has been conducted for an axisymmetric shock-wave/turbulent-boundary-layer strong interaction in the vicinity of a cylinder-cone intersection. Primary emphasis has been on the application of holographic interferometry for density field measurement, with laser velocimeter data included to supplement interferometric techniques. Surface-pressure and oil-flow data have also been reported. The explicit second-order, predictor-corrector, finite-difference method of MacCormack (1982) with the two-equation $\kappa - \epsilon$ turbulence model has been applied and the solution has been shown to compare favorably with interferometric and laser velocimeter data.

Interferometric data is well suited for providing an instantaneous, global view of the axisymmetric density field and capturing sharp gradients (i.e., shocks). These sharp gradients may precipitate a discontinuity in the fringe number because of strong refraction effects or a degree of "ripple" (local three dimensionality) in the shock surface. Such a discontinuity requires special treatment in the analysis process to permit realization of a physically realistic density profile. Profiles are subject to error in the region adjacent to the shock but are more reliable for regions closer to the model surface. The normally encountered statistical scatter of error arising from free-stream turbulence or during the various steps of interferogram digitization and analysis was demonstrated in a similar fashion to provide larger density profile error in the region adjacent to the shock and a gradual reduction in this error for data closer to the surface.

These effects are balanced by an increase in boundary-layer turbulence in the nonequilibrium boundary layer downstream of the interaction zone for the stronger interaction flows. This inherently 3-D turbulence coupled with a shorter integration path length for this region near the model surface degrade instantaneous measure-

ment quality and increase the need for large ensemble averages for statistically significant mean measurement.

A few recommendations can be made regarding future holographic interferometry work. First, although the horizontal finite-fringe reconstruction method used in this study is helpful in increasing the spacing of fringe-profile intersections (and therefore spatial resolution of the reduced data), it must be recognized that some flow detail is lost. An approach similar to that reported by Delerey et al. (1977) employing a microdensitometer and automated scanning system or perhaps a digital image processing system similar to that reported by O'Hare & Strike (1980) and Becker & Yu (1985) would greatly enhance the resolution capability of the interferometric data as well as its accuracy. Secondly, the treatment of a statistically significant sample of interferograms in the evaluation of mean flow quantities for this study was somewhat deficient because of the tedious nature of interferogram analysis. This deficiency must be overcome (by enhanced analysis capability) to increase confidence in the mean measurements.

Laser velocimeter data are unsurpassed for nonintrusive experimental documentation of the velocity field. The LV system employed in this study has been demonstrated in previous applications to provide a highly reliable measurement capability. Nevertheless, the stronger shock waves encountered in these flows provided a reminder that seed size and particle lag considerations are critical in applying LV techniques in the study of high- speed flows with shock waves.

Oil-flow and surface-pressure data show the expected trends for the onset and extent of separation as a function of the interaction strength as well as Reynolds number. An extrapolation of the oil-flow data indicates a model cone angle in the vicinity of 16° for the onset of separation which is reasonably insensitive to Reynolds number. The extent of the interaction was seen to increase with increasing model cone angle and decrease with increasing Reynolds number. These results are in agreement with what has been reported in the literature.

The computation achieves good qualitative agreement with both interferometry and LV data. In a departure from what has usually been reported in the literature, the computation overpredicts the radial extent of the separated region for the strongest interaction. Nevertheless surface-pressure data and computed values are in agreement. Interferometry and LV data show the same shock location, while the computation places the shock slightly outboard.

The results presented herein are useful in the documentation and understanding of strong viscous-inviscid interactions and confirm the utility of holographic interferometry techniques for supersonic, axisymmetric flow-field analysis. On the foundation of this study, one may look toward the analysis of more complex weakly 3-D flows using holographic interferometry techniques with an anticipation of success.

REFERENCES

1. Ackeret, J., Feldmann, F. & Rott, N. (1947). *Investigations of Compression Shocks and Boundary Layers in Gases Moving at High Speeds.* NACA TM 1113.

2. Adamson, T. C. Jr., & Messiter, A. F. (1980). Analysis of Two-Dimensional Interactions Between Shock Waves and Boundary Layers. *Annual Review of Fluid Mechanics*, 103-138.

3. Ardonceau, P. L. (1984). The Structure of Turbulence in a Supersonic Shock Wave/Boundary-Layer Interaction. *AIAA Journal, 22*,(9), 1254-1262.

4. Bachalo, W. A., & Johnson, D. A. (1979, January). *An Experimental Investigation of Transonic Turbulent Boundary Layer Separation Generated on an Axisymmetric Flow Model*, AIAA Paper 79-1479. Presented at the AIAA 12th Fluid and Plasma Dynamics Conference, Williamsburg, VA.

5. Bachalo, W. D., & Houser, M. J. (1986). Evaluation and Application of a New Interferometry Technique for Compressible Flow Research, NASA Contractor Report 166575. also, Bachalo, W. D., & Houser, M. J. (1984, June). *A Real Time Interferometry Technique for Compressible Flow Research*, AIAA paper 84-1600. Presented at the AIAA 17th Fluid and Plasmadynamics and Lasers Conference, Snowmass, CO.

6. Becker, F., & Yu, Y. H. (1985, January). *Application of Digital Interferogram Evaluation Techniques*, AIAA-85-0037. Presented at the AIAA 23rd Aerospace Sciences Meeting, Reno, NV.

7. Belozerov, A. F., Bereskin, A. N., Razumosakaya, A. I., & Spornik, N. M. (1973). Hologram Study of Gas Flow in a Ballistic Wind Tunnel. *Soviet Physics Technical Physics, 18*, 488-490.

8. Bennett, F. D., Carter, W. C., & Bergdolt, V. E. (1952). Interferometric Analysis of Airflow about Projectiles in Free Flight. *Journal of Applied Physics, 23*(4), 453-469.

9. Bogdonoff, S. M. (1954). Remarks on Interactions Between Wholly Laminar or Wholly Turbulent Boundary Layers and Shock Waves Strong Enough to Cause Separation. *Journal of Aeronautical Sciences, 21*, 138-139.

10. Bogdonoff, S. M. (1955). *Some Experimental Studies of the Separation of Supersonic Turbulent Boundary Layers* (Report 336). Princeton: Princeton University Aeronautical Engineering Department.

11. Bogdonoff, S. M., Kepler, C. E., & SanLorenzo, E. (1953). *A Study of Shock Wave Turbulent Boundary Layer Interaction at $M = 3$* (Report 222). Princeton: Princeton University Aeronautical Engineering Department.

12. Bogdonoff, S. M., & Settles, G. S. (1980). *Separated Flow and Boundary Layer Research* (MAE Report 1494). Princeton: Princeton University, Gas Dynamics Laboratory.

13. Bradley, J. W. (1968). Density Determination from Axisymmetric Interferograms. *AIAA Journal, 6*,(6), 1190-1192.

14. Brosh, A., & Kussoy, M. I. (1983). *An Experimental Investigation of the Impingement of a Planar Shock Wave on an Axisymmetric Body at Mach 3.* NASA TM 84410.

15. Brown, J. L., & Dunagan, S. E. (1986). [A Least Squares Method for Abel Integral Inversion]. Unpublished algorithm.

16. Brown, J. L., & Viswanath, P. R. (1984, August). *An Experimental Study of a Supercritical Airfoil*, AIAA Paper 84-2187. Presented at AIAA 2nd Applied Aerodynamics Conference, Seattle, WA.

17. Bryanston-Cross, P. J., & Denton, J. D. (1984). Comparison of Measured and Predicted Transonic Flow Around an Airfoil. *AIAA Journal, 22*, 1025-1026.

18. Cebeci, T. (1971). Calculation of Compressible Turbulent Boundary Layers with Heat and Mass Transfer. *AIAA Journal, 9*,(6), 1091-1097.

19. Chapman, D. R., Kuehn, D. M., & Larson, H. K. (1957). *Investigation of Separated Flows in Supersonic and Subsonic Streams with Emphasis on the Effect of Transition.* NACA TN 3869. Also NACA Rep. 1356, 1958.

20. Collier, R. J., Burckhardt, C. B., & Lin, L. H. (1971). *Optical Holography.* New York: Academic Press.

21. Craig, J. E. (1981). *Operating Manual Holographic Interferometry System For 2x2 Foot Transonic Wind Tunnel* (NASA Contractor Report 166344). Moffett Field, CA: NASA Ames Research Center.

22. Delerey, J. M. (1983). Experimental Investigation of Turbulence Properties in Transonic Shock/Boundary-Layer Interactions. *AIAA Journal, 21*,(2), 180-185.

23. Delerey, J., Surget, J., and Lacharme, J. P. (1977) Interferometrie Holographique Quantitative en Ecoulement Transsonique Bidimensionnel [Quantitative Holographic Interferometry in Two-Dimensional Transonic Flows]. ONERA TP 1977-49. Office National D'Etudes et de Recherches Aerospatiales.

24. Dolling, D. S., & Bogdonoff, S. M. (1981, January). *Upstream Influence Scaling of Sharp Fin-Induced Shock Wave Turbulent Boundary Layer Interactions*, AIAA Paper 81-0336. Presented at the AIAA 19th Aerospace Sciences Meeting, St. Louis, MO.

25. Dunagan, S. E., Brown, J. L., & Miles, J. B. (1985, July). *A Holographic Interferometric Study of an Axisymmetric Shock-Wave/Boundary-Layer Strong*

Interaction Flow, AIAA Paper 85-1564. Presented at AIAA 18th Fluid Dynamics and Plasmadynamics and Lasers Conference, Cincinnati, OH.

26. Dussauge, J. P., & Gaviglio, J. (1981). Bulk Dilatation Effects on Reynolds Stresses in the Rapid Expansion of a Turbulent Boundary Layer at Supersonic Speeds. *Third Symposium on Turbulent Shear Flows.* University of California, Davis, CA.

27. East, L. F. (1976). *The Application of a Laser Anemometer to the Investigation of Shock-Wave Boundary-Layer Interactions.* AGARD-CP-193.

28. Fage, A., & Sargent, R. F. (1947). Shock Wave and Boundary-Layer Phenomena Near a Flat Surface. In *Proceedings of the Royal Society of London* (pp. 1-20) Series A, *190.*

29. Ferri, A. (1940). *Experimental Results With Airfoils Tested In The High-Speed Tunnel at Guidonia.* NACA TM 946. (Original work published 1939).

30. Gabor, D. (1949). Microscopy by Reconstructed Wavefronts. In *Proceedings of the Royal Society of London*, A197,(pp. 454-487), and Gabor, D. (1951). Microscopy by Reconstructed Wavefronts II. In *Proceedings of the Physics Society*, 64,(pp. 449-469).

31. Gadd, G. E. (1953). Interactions Between Wholly Laminar or Wholly Turbulent Boundary Layers and Shock Waves Strong Enough to Cause Separation. *Journal of Aeronautical Sciences, 20*, 729-739.

32. Gadd, G. E. (1957). A Theoretical Investigation of Laminar Separation in Supersonic Flow. *Journal of Aeronautical Sciences, 24*, 759-771.

33. Gadd, G. E., & Holden, D. W. (1954). Further Remarks on Interaction Between Wholly Laminar or Wholly Turbulent Boundary Layers and Shock Waves Strong Enough to Cause Separation. *Journal of Aeronautical Sciences, 21*, 571-572.

34. Gadd, G. E., Holden, D. W., & Regan, J. D. (1954). An Experimental Investigation of the Interaction Between Shock Waves and Boundary Layers. In *Proceedings of the Royal Society of London* (pp. 227-253) Series A, *226.*

35. Goldberg, T. J. (1973). Three-Dimensional Separation for Interaction of Shock Waves with Turbulent Boundary Layers. *AIAA Journal, 11*,(11), 1573-1575.

36. Green, J. E. (1971). Interactions Between Shock Waves and Turbulent Boundary Layers. *Progress in Aerospace Sciences, 11*, 235-340.

37. Green, J. E. (1970). Reflexion of an Oblique Shock Wave by a Turbulent Boundary Layer. *Journal of Fluid Mechanics, 40*, 81-95.

38. Hammitt, A. G., & Hight, S. (1959). Scale Effects in Turbulent Shock Wave Boundary Layer Interaction. Air Force Office of Scientific Research TN 60-82.

In *Proceedings of the 6th Midwestern Conference on Fluid Mechanics*, University of Texas, Austin, TX.

39. Havener, A. G. (1983, July). *Holographic Measurements of Transition and Turbulent Bursting in Supersonic Axisymmetric Boundary Layers*, AIAA paper 83-1724. Presented at the AIAA 16th Fluid and Plasma Dynamics Conference, Danvers, MA.

40. Havener, A. G. (1985, July). *Optical Measurements of Supersonic Turbulent Boundary Layer Flow Over a Roughened Surface*, AIAA paper 85-1613. Presented at the AIAA 18th Fluid Dynamics and Plasmadynamics and Lasers Conference, Cincinnati, OH.

41. Havener, A. G., & Radley, R. J., Jr. (1973, July). *Turbulent Boundary Layer Flow Separation Measurements Using Holographic Interferometry*, AIAA Paper 73-664. Presented at the AIAA 6th Fluid and Plasma Dynamics Conference, Palm Springs, CA.

42. Havener, A. G., & Radley, R. J., Jr. (1973). *Supersonic Wind Tunnel Investigations Using Pulsed Laser Holography.* ARL 73-0148, AD 771 617. Aerospace Research Laboratories, Wright Patterson AFB, OH. 642-649.

43. Heflinger, L. O., Wuerker, R. F., & Brooks, R. E. (1966). Holographic Interferometry. *Journal of Applied Physics, 37*,(2), 642-649.

44. Horman, M. H. (1965). An Application of Wavefront Reconstruction to Interferometry. *Applied Optics, 4*, 333-336.

45. Horstman, C. C., & Johnson, D. A. (1984). Prediction of Transonic Separated Flows. *AIAA Journal, 22*, 1001.

46. Horstman, C. C., Kussoy, M. I., Coakley, T. J., Rubesin, M. W., & Marvin, J. G. (1975, January). *Shock-Wave-Induced Turbulent Boundary-Layer Separation at Hypersonic Speeds*, AIAA Paper 75-4. Presented at the AIAA 13th Aerospace Sciences Meeting, Pasadena, CA.

47. Ivanov, V. F., Mustafin, L. T., Shatilov, A. P., & Yushkov, E. S. (1975). Holographic Formation of Interferograms and Shadow Patterns of Gas Flow from a Reflecting Nozzle of a Shock Tube. *Soviet Journal of Quantum Electronics, 4*, 1389-1390.

48. Jagota, R. C., & Collins, D. J. (1972). Finite Fringe Holographic Interferometry Applied to a Right Circular Cone at Angle of Attack. *Journal of Applied Mechanics*, 897-903.

49. Johnson, D. A., & Bachalo, W. A. (1978, July). *Transonic Flow About a Two-Dimensional Airfoil-Inviscid and Turbulent Flow Properties*, AIAA Paper 78-1117. Presented at the AIAA 11th Fluid and Plasma Dynamics Conference, Seattle, WA.

50. Jones, W. P., & Launder, B. E. (1972). The Prediction of Laminarization with a Two-Equation Model of Turbulence. *International Journal of Heat and Mass Transfer, 15*, 301-314.

51. Kittleson, J. K. (1983, September). *A Holographic Interferometry Technique for Measuring Transonic Flow Near A Rotor Blade.* Presented at the Ninth European Rotorcraft Forum, Stresa, Italy.

52. Kittleson, J. K., & Yu, Y. H. (1985, January). *Reconstruction of a Three-Dimensional Transonic Rotor Flow Field From Holographic Interferogram Data*, Paper No. 85-0870. Presented at the AIAA 23rd Aerospace Sciences Meeting, Reno, NV.

53. Kline, S. J., Cantwell, B. J., & Lilley, G. M. (1982). *Comparison of Computation and Experiment.* Presented at The 1980-81 AFOSR/-HTTM-Stanford Conference on Complex Turbulent Flows, III, Stanford University, Stanford, CA, 1326-1336.

54. Kosakoski, R. A., & Collins, D. J. (1974). Application of Holographic Interferometry to Density Field Determination in Transonic Corner Flow. *AIAA Journal, 12*,(6), 767-770.

55. Kuehn, D. M. (1959). *Experimental Investigation of the Pressure Rise Required for the Incipient Separation of Turbulent Boundary Layers in Two-Dimensional Supersonic Flow.* NASA Memo 1-21-59A.

56. Kuehn, D. M. (1961). *Turbulent Boundary Layer Separation Induced by Flares on Cylinders at Zero Angle of Attack.* NASA TR R-117.

57. Kussoy, M. I., & Horstman, C. C. (1981). *A Documentation of a Three-Dimensional Shock Separated Turbulent Boundary Layer.* NASA TM 81327.

58. Kussoy, M. I., Viegas, J. R., & Horstman, C. C. (1980, January). *An Experimental and Numerical Investigation of a 3-D Shock Separated Turbulent Boundary Layer*, AIAA Paper 80-0002.

59. Ladenburg, R., Winckler, J., & Van Voorhis, C. C. (1948). Interferometric Studies of Faster than Sound Phenomena. Part I. The Gas Flow around Various Objects in a Free, Homogeneous, Supersonic Air Stream. *Physical Review, 73*,(11), 1359-1377.

60. Law, C. H. (1974). Supersonic Turbulent Boundary-Layer Separation. *AIAA Journal, 12*, 794-797. Also Law, C. H. (1975, June). *Two Dimensional Compression Corner and Planar Shock Wave Interactions with a Supersonic, Turbulent Boundary Layer.* Report No. ARL-75-0157. Aerospace Research Laboratories, Wright-Patterson AFB, OH.

61. Lee, G., Trolinger, J. D., & Yu, Y. H. (1985). *Proceedings of the Workshop on Automated Reduction of Data from Images and Holograms.* To be published as NASA CP, NASA-Ames Research Center.

62. Leith, E. N., & Upatnieks, J. (1964). Wavefront Reconstruction with Diffuse Illumination and Three-Dimensional Objects. *Journal of the Optical Society of America, 54*, 1295-1301.

63. Lewis, J. E., Kubota, T., & Lees, L. (1968). Experimental Investigation of Supersonic Laminar Two-Dimensional Boundary-Layer Separation in a Compression Corner With and Without Cooling. *AIAA Journal, 6*, 7-14.

64. Liepmann, H. W. (1946). The Interaction Between Boundary Layer and Shock Waves in Transonic Flow. *Journal of Aeronautical Sciences, 13*, 623-637.

65. Lighthill, M. J. (1953). On Boundary Layers and Upstream Influence II. Supersonic Flows Without Separation. In *Proceedings of the Royal Society of London*, (pp. 478-507) Series A, No. 217.

66. MacCormack, R. W. (1971). Numerical Solution of the Interaction of a Shock Wave With a Laminar Boundary Layer. *Lecture Notes in Physics, 8*, Springer Verlag, New York, 151.

67. MacCormack, R. W. (1982). A Numerical Method for Solving the Equations of Compressible Viscous Flow. *AIAA Journal, 20*, 1275-1281.

68. Mach, E. and Weltrubski, J. (1878). Uber der Formen der Funkenwelle. *Wien. Ber., 78.*

69. Mach, L. (1892). Uber ein Interferenzrefractometer. *Wien. Ber., 101.*

70. Matulka, R. D., & Collins, D. J. (1971). Determination of Three Dimensional Density Fields from Holographic Interferograms. *Journal of Applied Physics, 42*,(3), 1109-1119.

71. Merzkirch, W. (1974). *Flow Visualization.* New New York: Academic Press.

72. Modarress, D., & Johnson, D. A. (1979). Investigation of Turbulent Boundary-Layer Separation Using Laser Velocimetry. *AIAA Journal, 17*,(7), 747-752.

73. O'Hare, J. E., & Strike, W. T. (1980). *Holographic Interferometry and Image Analysis for Aerodynamic Testing.* AEDC-TR-79-75, Arnold Engineering Development Center.

74. Pickney, S. Z. (1966). *Data on Effects of Incident-Reflection Shocks on the Turbulent Boundary Layer.* NASA TM X-1221.

75. Powell, R. L., & Stetson, K. A. (1965). Interferometric Analysis by Wavefront Reconstruction. *Journal of the Optical Society of America, 55*, 1593-1598.

76. Prandtl, L. (1928). *Motion of Fluids With Very Little Viscosity.* NACA TM 452.

77. Radley, R. J., Jr., & Havener, A. G. (1973, January). *The Application of Dual Hologram Interferometry to Wind Tunnel Testing*, AIAA Paper 73-210. Presented at the 11th Aerospace Sciences Meeting, Washington, DC.

78. Radley, R. J., Jr., & Havener, A. G. (1973). Applications of Dual Hologram Interferometry to Wind Tunnel Testing. *AIAA Journal, 11*,(9), 1332-1333.

79. Reda, D. C., & Murphy, J. D. (1972, June). *Shock Wave-Turbulent Boundary Layer Interactions in Rectangular Channels*, AIAA Paper 72-715. Presented at the AIAA 5th Fluid and Plasma Dynamics Conference, Boston, MA; and Reda, D. C., & Murphy, J. D. (1973, January). *Shock Wave-Turbulent Boundary Layer Interactions in Rectangular Channels, Part II: The Influence of Sidewall Boundary Layers on Incipient Separation and Scale of the Interaction*, AIAA Paper 73-234.

80. Robinson, S. K., Seegmiller, H. L., & Kussoy, M. I. (1983, July). *Hot Wire and Laser Anemometer Measurements in a Supersonic Boundary Layer*, AIAA Paper 83-1723. Presented at the AIAA 16th Fluid and Plasma Dynamics Conference, Danvers, MA.

81. Rose, W. C., Murphy, J. D., & Watson, E. C. (1968). Interaction of an Oblique Shock Wave With a Turbulent Boundary Layer. *AIAA Journal, 6*, 1792-1793.

82. Roshko, A., & Thomke, G. J. (1976). Flare-Induced Separation Lengths in Supersonic, Turbulent Boundary Layers. *AIAA Journal, 14*,(7), 873-879.

83. Settles, G. S. (1980). *Shock Wave/Turbulent Boundary Layer Interactions in Two and Three Dimensions* (MAE Report 1546). Princeton: Princeton University Gas Dynamics Laboratory.

84. Settles, G. S., & Bogdonoff, S. M. (1973, July). *Separation of a Supersonic Turbulent Boundary Layer at Moderate to High Reynolds Numbers*, AIAA Paper 73-666. Palm Springs, CA.

85. Settles, G. S., & Dolling, D. S. (1986). Swept Shock Wave-Boundary Layer Interactions. *AIAA Progress in Astronautics and Aeronautics Series.*

86. Settles, G. S., Perkins, J. J., & Bogdonoff, S. M. (1980). Investigation of Three-Dimensional Shock/Boundary-Layer Interactions at Swept Compression Corners. *AIAA Journal, 18*,(7), 779.

87. Settles, G. S., Perkins, J. J., & Bogdonoff, S. M. (1981, January). *Upstream Influence Scaling of 2D and 3D Shock/Turbulent Boundary Layer Interactions at Compression Corners*, AIAA Paper 81-0334. Presented at the AIAA 19th Aerospace Sciences Meeting, St. Louis, MO.

88. Shapiro, A. H. (1953). *Compressible fluid flow* (Vol. 1). New York: Ronald Press.

89. Sinclair, D. W., & Whitfield, D. L. (1978, July). *Holographic Interferometry Measurements of Subsonic Turbulent Boundary Layers*, AIAA paper 78-1193. Presented at the AIAA 11th Fluid and Plasma Dynamics Conference, Seattle, WA.

90. Surget, J. (1973). Quantitative Study of Aerodynamic Flows By Holographic Interferometry. *Recherche Aerospatiale, 154*, 161-171.

91. Tanner, L. H. (1966). Some Application of Holography in Fluid Mechanics. *Journal of Scientific Instrumentation, 43*, 81-83.

92. Trolinger, J. D. (1974). Laser Instrumentation for Flow Field Diagnostics. *AGARDograph 186.*

93. Trolinger, J. D., Belz, R. A., & O'Hare, J. E. (1974). Holography of Nozzles, Jets, and Spraying Systems. *Progress in Astronautics and Aeronautics Series, 34*, Instrumentation for Air Breathing Propulsion.

94. Vest, C. M. (1979). *Holographic Interferometry.* New York: John Wiley and Sons.

95. Walpole, R. E., & Myers, R. H. (1971). *Probability and Statistics for Engineers and Scientists.* New York: Macmillan Publishing Co.

96. Winckler, J. (1948). The Mach Interferometer Applied to Studying an Axially Symmetric Supersonic Air Jet. *Review of Scientific Instruments, 19*,(5), 307-322.

97. Zehnder, L. (1891). Ein Neuer Interferenzrefraktor. *Zeitschrift fuer Instrumentenkunde, 11.*

APPENDIX A

A Description of Holographic Processes

Holography is based on interference of light principles and, as with all interference phenomena, is only possible when the source of illumination possesses the required coherent properties. The formation of holograms is accomplished by splitting a coherent source light wave into reference and object waves. The object wave is directed at the object of interest and modified by interaction with that object, either by reflection or transmission. The object and reference waves are then recombined to create an interference pattern that makes it possible to store this modified object wave.

This interference pattern may be recorded in a photosensitive media to yield a hologram. The nature of the recording media may vary depending on the particular application. Holograms may be characterized as thick or thin, transmission or reflection, and absorption or phase. The most common type of photosensitive media used is the photographic plate which represents a thin, transmission-type absorption hologram. The recorded fringe pattern is essentially two dimensional (thin), with transmitted light that has been modified by the absorptive nature of the developed hologram responsible for the reconstruction.

Reconstruction is accomplished by illuminating the hologram with a wave similar to the original reference wave. The hologram modifies the reconstructing wave in such a way that portions of the illuminating wave exactly reconstruct the original object wave. Mathematical developments presented in Born & Wolf (1980), Goodman (1968), and Jenkins & White (1957) are helpful in modeling the phenomenological nature of interference and diffraction.

In general, waves used in holography are highly monochromatic, linearly polarized, collimated, nominally planar waves with some spatial-phase shift function, ϕ, which carries the information of interest. Figure A.1 shows object and reference

waves impinging on a holographic surface in a typical configuration. The electric field for either wave is given by

$$u(x,y,t) = U(x,y)cos[\omega t + \phi(x,y)] \qquad A.1$$

Employing complex notation, u is given by the real part of the complex cosine representation

$$u(x,y,t) = Real[U(x,y)e^{i[\omega t+\phi(x,y)]}] \qquad A.2$$

The superposition of object wave $o(x,y,t)$ and reference wave $r(x,y,t)$ yields the sum

$$s(x,y,t) = Real[O(x,y)e^{i[\omega t+\phi_o(x,y)]} + R(x,y)e^{i[\omega t+\phi_r(x,y)]}] \qquad A.3$$

The resulting intensity, $I(x,y)$, is given by the time average of the square of the electric field

$$I(x,y) = [O(s,y)]^2 + [R(x,y)]^2 + 2O(x,y)R(x,y)cos[\phi_o(x,y) - \phi_r(x,y)] \qquad A.4$$

Note that this interference pattern contains both intensity and phase information and therefore is capable of a comprehensive description of the object wave relative to the reference wave.

At this point some observations are appropriate regarding the hologram recording process. Photographic emulsions are characterized by a transmission-exposure (T-E) curve (see figure A.2) which identifies the functional dependency of the transmittance of the developed plate on the initial exposure. Generally, the T-E curve is nonlinear; however, in a selected range the curve may nearly approximate a linear relationship. This T-E linearity is a necessary condition if relative magnitude relations through an intensity field are to be preserved. Therefore, it is advantageous to match the range of exposure intensities with the linear range of the T-E curve. Assuming this is accomplished, the transmissivity of the developed hologram will be linearly proportional to the incident intensity pattern.

$$T(x,y) = t_0 + \beta I(x,y) \qquad A.5$$

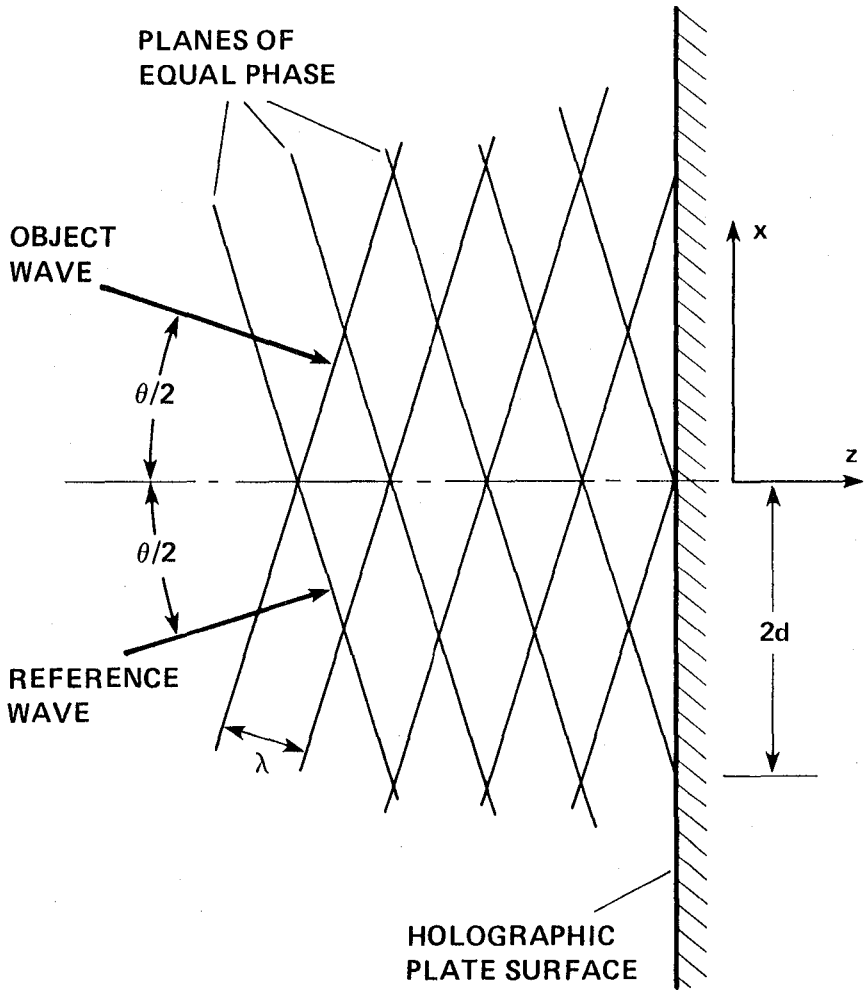

Figure A.1 Hologram formation

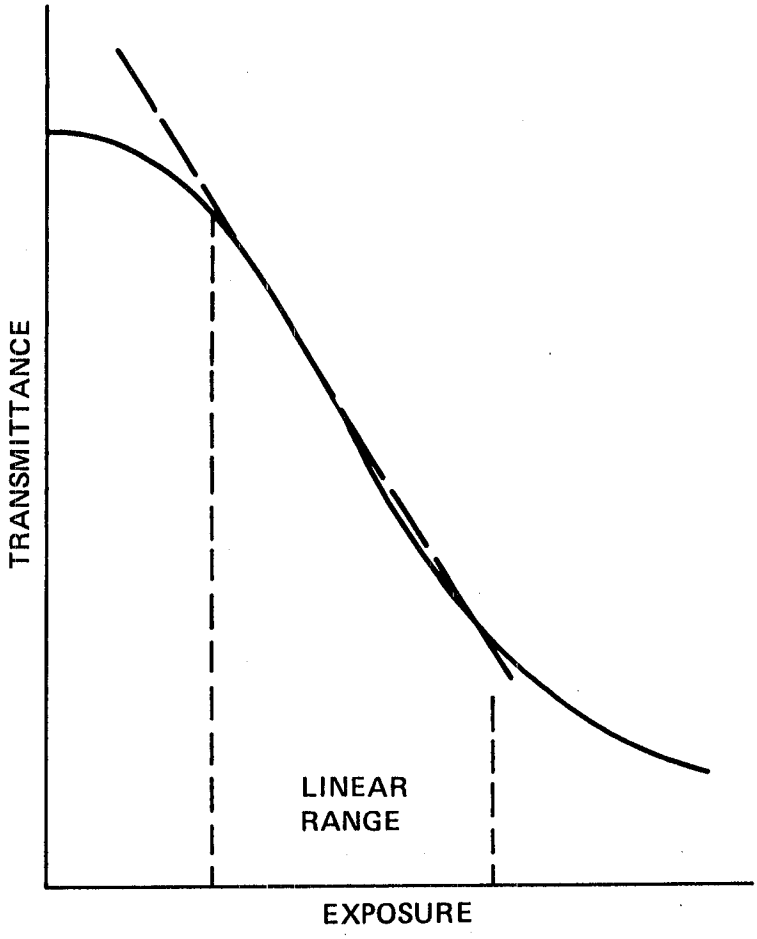

Figure A.2 Typical photographic emulsion T-E curve

where β is the slope of the T-E curve in the linear range and t_0 is the extrapolated intercept. Substituting into the expression for intensity yields

$$T(x,y) = t_0 + \beta\{[O(x,y)]^2 + [R(x,y)]^2 + 2[O(x,y)][R(x,y)]cos[\phi_o(x,y) - \phi_r(x,y)]\} \quad A.6$$

The Euler relation

$$cos\theta = \frac{e^{i\theta} + e^{-i\theta}}{2} \quad A.7$$

leads to an expression for the phase difference term

$$2O(x,y)R(x,y)cos[\phi_o(x,y) - \phi_r(x,y)] = \mathbf{O}(x,y)\mathbf{R}^*(x,y) + \mathbf{O}^*(x,y)\mathbf{R}(x,y) \quad A.8$$

where $\mathbf{O}$ and $\mathbf{R}$ are the complex amplitude vectors

$$\mathbf{O}(x,y) = O(x,y)e^{i\phi_o(x,y)} \quad A.9$$

and the star indicates complex conjugate. The transmissivity of the hologram may now be expressed as

$$T(x,y) = t_0 + \beta[O(x,y)]^2 + \beta[R(x,y)]^2 + \beta[\mathbf{O}(x,y)\mathbf{R}^*(x,y) + \mathbf{O}^*(x,y)\mathbf{R}(x,y)] \quad A.10$$

Now consider the illumination of the developed hologram with a reconstructing wave, $c(x,y,t)$. The transmitted wave is given by

$$t(x,y,t) = c(x,y,t)T(x,y) \quad A.11$$

$$\begin{aligned} t(x,y,t) = {} & t_0 c(x,y,t) + \beta[O(x,y)]^2 c(x,y,t) + \beta[R(x,y)]^2 c(x,y,t) \\ & + \beta[\mathbf{O}(x,y)\mathbf{R}^*(x,y)c(x,y,t)] + \beta[\mathbf{O}^*(x,y)\mathbf{R}(x,y)c(x,y,t)] \end{aligned} \quad A.12$$

If the reconstructing wave, $c(x,y,t)$, is identical to the original reference wave $r(x,y,t)$ the fourth term becomes

$$\begin{aligned} \beta\mathbf{O}(x,y)\mathbf{R}^*(x,y)c(x,y,t) &= \beta O(x,y)e^{i\phi_o(x,y)}R(x,y)e^{i\phi_r(x,y)}Real\{R(x,y)e^{i[\omega t + \phi_r(x,y)]}\} \\ &= \beta[R(x,y)]^2 Real\{O(x,y)e^{i[\omega t + \phi_o(x,y)]}\} \end{aligned} \quad A.13$$

Note that this represents the original object waveform with the addition of a constant coefficient, $\beta[R(x,y)]^2$. Thus we see that a fraction of the transmitted wave reconstructs the original object waveform. Similarly, if the reconstruction waveform is the conjugate of the original reference wave, the fifth term becomes

$$\beta[\mathbf{O}^*(x,y)\mathbf{R}(x,y)c(x,y,t)] = \beta[R(x,y)]^2 Real\{O(x,y)e^{i[\omega t - \phi_o(x,y)]}\} \qquad A.14$$

This yields a reconstruction of the conjugate object wave. Images reconstructed using conjugate illumination have pseudoscopic (i.e., falsely visualized) properties of parallax and image depth as a result of this form of the reconstructed wave.

It must be emphasized that only a fraction of the transmitted light is focused into the reconstructed object wave. To create useful holographically reconstructed images, it is necessary to remove transmitted light components that do not contribute to the image. Off-axis holographic techniques may be thought of in the sense that the hologram acts as a diffraction grating to spatially filter unwanted transmitted components into higher or lower diffracted orders. Reference wave reconstruction results in a virtual image, while conjugate reference wave illumination results in a real image that may be recorded directly on a photographic surface.

1 Born, M. and Wolf, E. (1980). *Principles of Optics.* Sixth Edition. New York: Pergamon Press.

2 Goodman, J. W. (1968). *Introduction to Fourier Optics.* New York: McGraw-Hill Book Co., Inc.

3 Jenkins, F. A., and White, H. (1957). *Fundamentals of Optics.* Fourth Edition. New York: McGraw-Hill Book Co., Inc.

APPENDIX B

Ames HRC-I Holographic Interferometer System Description and Operating Instructions

The Experimental Fluid Dynamics Branch holographic interferometer is a custom instrument designed for use in the High Reynolds Number Channel I at Ames Research Center. The instrument consists of two distinctly separate systems; one for hologram construction and one for hologram reconstruction. The construction system consists of three base modules which serve as mounting platforms for optical components dedicated to a particular function. These base modules are secured to the infrastructure of the wind tunnel facility to provide the greatest possible rigidity between optical components. The reconstruction system utilizes a single, highly rigid optical base as a mounting platform for optical components which provide reconstruction and imaging capability.

Construction Apparatus

The following is a listing and description of optical components as they appear in figures B.1 and B.2.

1. **Alignment Laser** Melles Griot model 05LHP151 He-Ne laser. 5-mw minimum output at 632.8 nm. 0.8-mm beam diam. 1.0-mrad full-angle beam divergence, and 500 to 1 linear polarization.

2. **Ruby Laser** Apollo Lasers Model 22. Single oscillator with water-cooled 7.62-cm-long by 0.953-cm-diam rod, and xenon flashlamp. Q-switch with KD*P active element operating in quarter wave retardation mode. Brewster stack polarizer. Intracavity mode-selection apertures. V-coat end mirror. Water-cooled output etalon. Plane-parallel cavity geometry. Single-pulse operation only (15-sec duty cycle). Remote operation.

3. **Neutral Density Filters** Combinations to permit neutral density attenuation

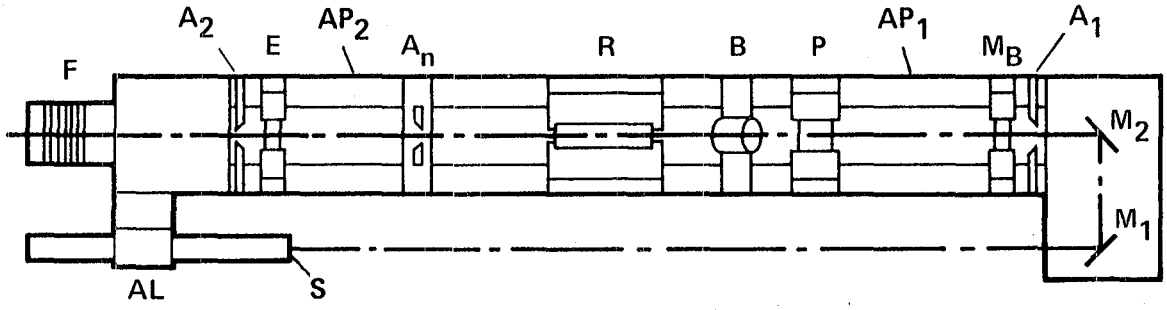

AL = ALIGNMENT LASER
M_1 = ALIGNMENT MIRROR #1
M_2 = ALIGNMENT MIRROR #2
A_1 = ALIGNMENT APERTURE #1
M_B = RUBY CAVITY BACK MIRROR
P = POCKELS CELL
B = BREWSTER STACK
R = RUBY LASER ROD
A_M = INTRACAVITY MODE SELECTING APERTURE
E = OUTPUT ETALON
A_2 = ALIGNMENT APERTURE #2
F = NEUTRAL DENSITY FILTER STACK
S = BACK REFLECTION SCREEN
AP_1 = ALIGNMENT POSITION 1
AP_2 = ALIGNMENT POSITION 2

Figure B.1 Ruby laser rail-mounted components.

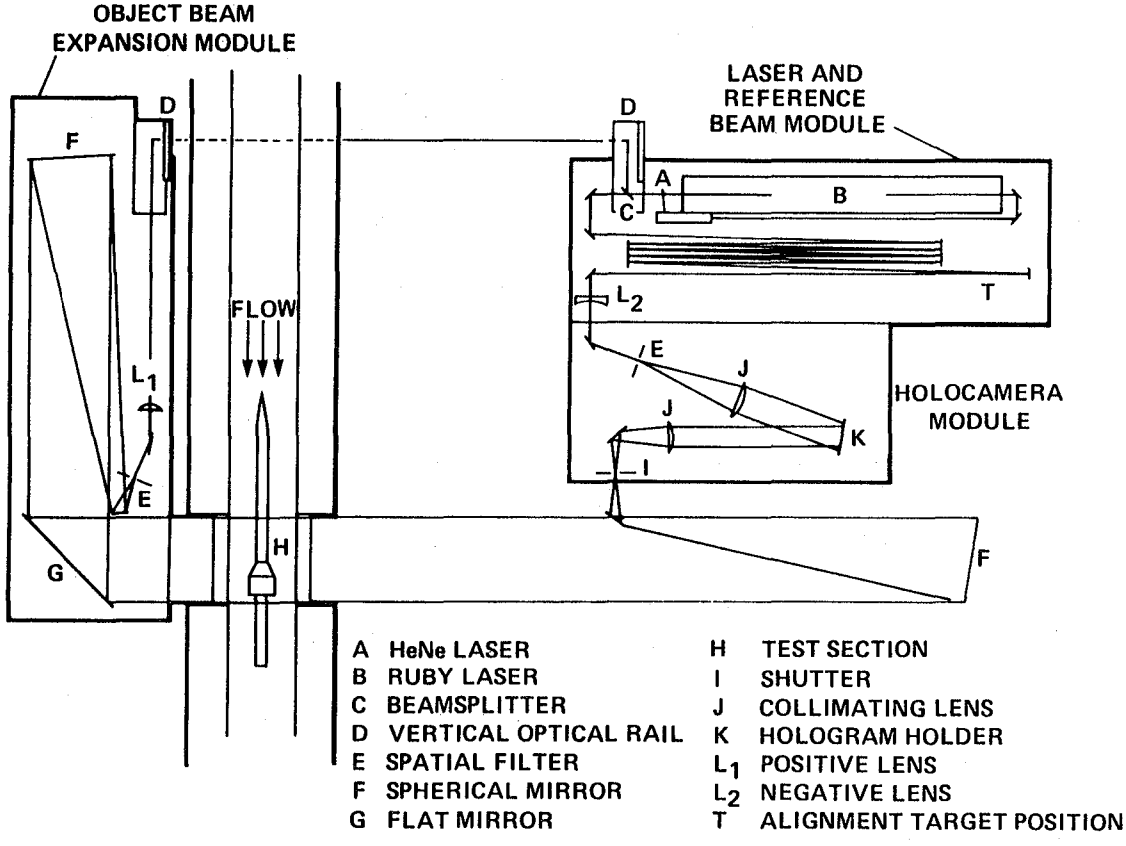

Figure B.2 Interferometer layout for hologram construction (see also figure 6 in text).

from 0.1 to 1.0 in increments of 0.1.

4. **Beamsplitter** CVI manufacturer. 0.30 or 0.20 reflectance (two beamsplitters). 50.8-mm-diam. fused silica substrate. Dielectric coatings for 694.3-nm, s-polarized 45° incidence. Rated to 5 gw/cm^2 for nanosecond pulses. $\frac{\lambda}{10}$ flatness.

5. **Vertical Optical Rails** constructed of 1.27 cm thick, 12.7-cm by 12.7-cm steel angle.

6. **Dielectric Mirror** Newport Research Corp. 50.8 mm diam. pyrex substrate and broadband dielectric coating BD.1.

7. **Positive lens** 110-mm focal length. 30-mm aperture. Lens is used to adjust object beam intensity and maintain photon adjacency condition (i.e. photons emitted from adjacent locations in the rod strike the hologram at adjacent locations, regardless of the path traveled.)

8. **Spatial Filter** Newport Research Corp. Model 900. 15-mm focal length microscope objective lens. $0.25 - \mu$m high-powered pinhole.

9. **Spherical Mirror** 30.48-cm diam. aluminized first surface mirror. 1.524 m focal length. Schlieren-grade optical quality.

10. **Flat Mirror** 33-cm by 45.72 cm aluminized first surface mirror. 6.35-mm float-glass substrate.

11. **Test Section Windows** 29.4 cm by 38.1 cm by 5.08 cm thick schlieren-grade optical crown glass.

12. **Shutter** Uniblitz electronic shutter. Aperture up to 50.8 mm. Shutter speeds as fast as 1 millisecond. Remote operation.

13. **Recollimating Lens** 395-mm focal length by 100-mm aperture. Two compound elements.

14. **Holographic Plate** Agfa-Gevaert 10E75 glass plates. Hoffman double-sided glass-plate holders. View camera back.

15. **Reference Beam Path-Length Equalization Mirrors** Two standard Newport Research Corp. mirrors mounted side by side (with independent adjustment) to provide an 8X reference beam path-length multiplier.

16. **Negative Lens** -203-mm focal length. 50.8-mm aperture. Lens is used to adjust reference beam intensity.

17. **Recollimating Lens** 585-mm focal length by 120-mm aperture. Two compound elements.

Aligning the Construction System

It may be advantageous to remove much of the sheet metal shielding from the base plate modules during major realignment operations to gain better access to the optics. Dimming the room lighting may also prove helpful for certain parts of the alignment process. It is necessary to monitor the ruby laser output indirectly by viewing the burn spot created on a target. An unexposed, developed sheet of polaroid film works well.

The first requirement for system alignment is to verify that the ruby laser is well aligned and operating consistently. Elements of the ruby laser are shown in figure B.1 along with the added alignment laser, steering mirrors, alignment apertures, mode selection apertures, and neutral density filter mounts. Generally, these components may be removed from the laser rail with no ill effects beyond the loss of alignment as long as they are returned to nearly the same location on the rail. If it is necessary to remove components (for cleaning, etc.), be certain that on reassembly all components are squared snugly against the right hand (if one were riding on the output beam) side of the rail.

Alignment is accomplished using back reflections from the front surface of the cavity back end mirror, M_b, and the etalon, E. Begin by removing the mode selection aperture, A_m, and adjusting the alignment laser in conjunction with mirrors, M_1 and M_2, to center the alignment beam in the alignment apertures, A_1 and A_2. Now

identify back reflections from M_b by blocking the beam just behind it. M_b is made with a high degree of nonparallelism to suppress resonance with the back surface. It is impossible to determine which of the two back reflections corresponds to the front surface by simple inspection. Select one of the reflections, keeping in mind that this adjustment may need to be changed. Adjust M_b until the back reflection is centered on the grid located at S. Now identify the single back reflection from E by blocking the beam just behind it. Adjust E until this back reflection is also centered at S in such a way that the two back reflections interfere to form a concentric ring pattern centered around the alignment beam. Turn off the Q-switch and fire the laser in accordance with the operating procedure specification (see below) onto a polaroid target located at the laser output. If the laser does not fire, select the other reflection from M_b and repeat this procedure. Examine the pattern of the burn spot for uniformity.

Set the Q-switch voltage to 600 and fire the laser again. Examine the new burn. It should be much hotter. (If this is not the case, the Q-switch is not operating properly and the laser operating manual must be consulted to correct the problem.) Identify a region where the output appears hottest. This region should have at least 3 mm of clean output. If this is not the case, methodically adjust E and M_b until a better output is obtained. Now adjust M_1 and M_2 to shift the output beam until it is centered on this hottest region, still providing concentric centered back reflections at S. center the 2.75 mm aperture A_m on the alignment beam and fire the laser onto a polaroid target. Examine the output for uniformity across the aperture. Systematically decrease the cavity aperture diameter and observe output. If the cavity is well aligned in a reasonably high gain portion of the rod, burn spots may be observed for cavity apertures as small as 1.50 mm.

Set the cavity aperture in the range of 2.0 to 2.5 mm. Place ND filters to the value of 0.3 on the output. Special care must be taken to never hit any optics from the beamsplitter on down beam with the full aperture or unattenuated laser

output. These values for cavity aperture and attenuation are suggested as an upper limit for energy exposure for the down beam optics. Block the object beam output and perform a cursory reference beam alignment as far as point T (see figure B.1). Place a polaroid target at T and fire the laser. Examine the output and verify that it is nearly round and has a somewhat Gaussian intensity profile. Adjust M_1 and M_2 to center the alignment beam on the burn spot at T, maintaining centered back reflections at S. Realign the reference beam to T and fire laser several times to verify reproducibility of output. This procedure permits the alignment of the ruby laser cavity and provides an alignment beam centered on the ruby output for use in aligning object and reference beams.

Now it is possible to proceed with the alignment of the down beam optics, having confidence that the ruby output will follow the He-Ne alignment beam. Begin by removing ND filters, beam intensity adjusting lenses, and spatial filter lenses and pinholes from both beam paths. First, align the object beam. Proceed down beam from the beamsplitter, keeping beam aligned with the scribe marks on the base plates, at the design elevation above the base plate (20.32 cm), and well centered on the mirrors. Particular care should be taken to hit the spherical mirrors in the exact center. Replace the spatial filter microscope objective and adjust its mounting apparatus until the expanded beam is well centered. The Airy disc interference pattern generated by the cavity aperture is helpful in this procedure. Examine the diameter of the 30.48-cm far-down beam to ensure that the spatial filter lens and first spherical mirror are located confocally. Slide the spatial filter along its rail to correct beam divergence. Remove the hologram plate holder and camera back. Slide the recollimation lens along its rail and examine its beam diameter far down beam to ensure that it is located confocally with the second spherical mirror. Mark the correct location on the rail. Remove the spatial filter microscope objective and the recollimating lens. Verify that the alignment beam is centered on the optical axis of the recollimating lens by checking the unexpanded beam location at the

hologram plate holder with the lens in and out. Iterate between mirror adjustments and lens angle adjustment (monitoring back reflections) until this condition is established. Install beam intensity adjusting lens and adjust mounting apparatus until the alignment beam is well centered far down beam. Install the remote shutter and adjust mounting apparatus to center the focus in the shutter aperture. Stop down the aperture as much as possible without disturbing the object beam image at the hologram plate holder (typically 3 mm limit because of aberration). Finally, install the spatial filter microscope objective and pinhole.

Alignment of the reference beam is more straightforward. The first mirror down beam of the beamsplitter is impacted severely by the laser output and is periodically damaged in small areas. Verify that the surface of this mirror is undamaged. If a damaged area is detected, rotate the mirror in its mount to bring a new surface into line. Proceed down beam through the reference beam path-length equalization optics, adjusting mirror mounts to keep the alignment beam at the design height and well centered on the mirrors. Align the beam with the axis of the rail on the holocamera module and adjust the recollimation lens to verify that its optical axis is coincident with the alignment beam. Install the spatial-filter microscope objective lens and adjust mounting apparatus to center the expanded beam. Again, the Airy disc interference rings are helpful in this adjustment. Remove hologram plate holder and monitor recollimated beam diameter to ensure that the microscope objective and recollimation lenses are located confocally. Make this adjustment by sliding the spatial filter assembly along the rail. When the correct location is found, mark the spatial filter and recollimating lens positions. Verify that the expanded beam is still well centered and that the recollimating lens axis is still coincident with the alignment beam. Install the reference beam intensity adjustment lens and adjust its mounting apparatus to center the expanded beam. Finally, install the spatial-filter pinhole.

It is now time to look at the ruby laser output. The alignment beam may be

blocked at the (He-Ne) laser. It is necessary to impose the light tight condition on the holocamera module. Replace all sheet metal shielding with careful attention to fit, keeping in mind that the holocamera must be well insulated from room lighting. Give special attention to the cloth shielding around the shutter. A double thickness of black felt is required to effectively block normal room lighting. Polaroid type 57 film (ISO 400) has exposure characteristics similar to the glass plates and may be used to get a quick, inexpensive indication of what the holographic plates will record. Load a sheet of polaroid into the camera back and expose for several minutes with normal room lighting to detect any light leaks. Repeat this operation and open the shutter for 1 sec to verify that room light coming through the shutter aperture is negligible.

When it has been established that the holocamera is well sealed, the ruby laser output may be checked. Block the reference beam on the laser module and fire the laser (remember to open the shutter) to expose a sheet of Polaroid film. Examine the output to verify that it is well centered and uniform across the beam aperture. Repeat with the object beam blocked. Very slight adjustments made at the beamsplitter (object beam) or the mirror M_r (reference beam) will serve to center the ruby output at the hologram without adversely affecting alignment throughout the system.

The lack of a precise quantitative method for measuring nanosecond/gigawatt beam intensities makes it difficult to arrive at a standard cookbook formula for establishing correct beam intensities. The objective is to arrive at exposure levels that fall in the linear range of the Transmission-Exposure (T-E) curve and beam ratios that provide good fringe contrast (i.e., good hologram diffraction efficiency). High diffraction efficiencies have been obtained for levels that expose the Agfa-Gevaert 10E75 plates to optical densities of 0.1 to 0.2 for developing times of 2 to 3 min. This corresponds to a uniform grey exposure on the Polaroid. Theoretically, equal beam intensities should give the best fringe contrast. However it is generally

found that a reference beam two to three times stronger works best. Adjust beam intensities by moving lenses along the optical axis, maintaining proper centering of the expanded beams. The reference beam should appear only slightly lighter on the exposed polaroid.

A glass plate may now be exposed. Load the plate in total darkness. A convention of emulsion forward for flow-on plates and emulsion backward for flow-off plates has been adopted when the dual-plate method is used. The aluminum spacer must be placed in front of the plate holder for emulsion forward shots so that the emulsions are in the same location for both plates of the dual plate set. Expose a polaroid with both beams simultaneously just prior to shooting the plate to ensure that alignment is still good. Develop the plate (in total darkness) for 2 to 3 min in Kodak D19 developer. Rinse for 30 sec in tap water. Bathe for 5 min in rapidfixer, then rinse for 5 min in water. Give the plate a final rinse in methanol to promote quick drying and reduce emulsion shrinkage. Examine the plate for diffraction efficiency. This may be done by holding the plate slightly above or below a reasonably unidirectional white light source, rotating it about the axis parallel to the (microscale) interference fringes and observing the spectrum of diffracted light. Keep in mind that the light must be diffracted at nearly the beam half-angle (10°) into the eye. High diffraction efficiency is indicated by a highly colorful spectrum.

An intermittent problem of nonuniform diffraction efficiency across the plate has been observed with this system. This nonuniformity appears as stripes of low efficiency oriented parallel to the microscale interference fringes. The effect may be a result of higher-order transverse mode output from the laser, or from secondary interference sources on the down-beam optics. The condition can usually be alleviated by a very slight realignment of the laser and optics.

The system maintains alignment reasonably well. At the start of each session, laser output quality should be checked at the laser output and far down beam in the

reference beam at location T. Coincidence of ruby laser output with the alignment beam axis should also be checked at point T. Polaroid shots of object and reference beams separately and together should be taken. Adjustment of the beamsplitter and mirror, M_r, will correct any drift of beam alignment.

GENERAL OPERATING INSTRUCTIONS FOR THE APOLLO MODEL 22 PULSED RUBY LASER AND HOLOGRAPHIC INTERFEROMETER HRC-I FACILITY

NOTE: An operating procedure in checklist form is attached and shall be followed during all laser operations.

This laser shall be operated only by authorized personnel as designated by the Branch Chief and the authorized laser user for the Experimental Fluid Dynamics Branch. All operators shall have filed form DOS 29 with the Health and Safety Officer and have had a laser eye exam.

The Apollo Model 22 pulsed ruby laser is a high-power class IV laser. Moderate levels of optical energy (50 mj per pulse) are emitted in very short pulses (20 ns duration) resulting in explosively high (megawatt range) optical power levels. **Severe eye and skin tissue damage will result from direct exposure to this optical output.**

High voltages (kilovolt range) are also present during laser operations. Careless exposure to the laser power supply cabinet internal electronics or exposure to a damaged high voltage conductor pose additional electrocution hazards.

A small, 5-mw class IIIa He-Ne alignment laser is an integral part of the Apollo laser system. The primary safety hazard associated with the operation of this laser is that of eye damage due to direct viewing of the laser beam. Precautions must be taken to keep the eyes out of the horizontal plane of the beam path. All alignment activity must be done with the use of diffusely reflecting surfaces and not by sighting along the beam. All specularly reflecting surfaces (including watches, rings, etc.) must not cross the beam path. All undesirable beam reflections must be properly terminated.

The Apollo ruby laser and holographic interferometer system have the following

safety features:

1. The ruby laser power supply is fitted with cabinet interlocks to preclude laser operation when the cabinet is open.

2. The ruby laser power supply is provided with an external interlock connection for use with door interlocks.

3. The ruby laser power supply is designed to automatically dump the stored electrical charge from the capacitor banks if the laser is not fired within one minute from the time it is charged.

4. Stored electrical charge may be dumped from the control panel or remote control panel if the charge/firing sequence needs to be interrupted.

5. The ruby laser cavity is provided with a light shield.

6. All unexpanded beams in the holographic interferometry system are provided with shielding.

7. Dumps are provided to terminate over-filled or otherwise unused radiation.

This laser is to be operated in the High Reynolds Channel bay area in building 231. This facility is currently compatible with the operation of class IV argon-ion lasers utilized in LV instrumentation. Safety features incorporated in this facility include:

1. All external doors may be locked to deny access to unauthorized personnel.

2. All doors to the bay area are interlocked.

3. All windows viewing the bay area are fitted with drapes to terminate errant beams.

4. Warning signs are provided at each of the doorways informing personnel of the laser hazard present.

5. Laser safety goggles are provided at doorways should an emergency require entrance to the restricted area.

6. A hazard light and warning sign are mounted in a highly visible area near the laser. This light is turned on whenever the laser is in operation.

Each session of laser operation will generally begin with a period of alignment when it will be necessary to remove the shielding from the laser modules to facilitate the adjustment of optical apparatus. When alignment is completed, shielding will be reinstalled prior to data acquisition. It is imperative that the bay area be clear of all unauthorized personnel when the ruby laser is energized and unshielded. The attached operating checklist will be used for laser operation.

CHECKLIST FOR RUBY LASER OPERATION

WARNING

Laser to be operated by authorized ruby laser operator only.

To proceed with laser operations, the following checklist will be used.

Prior to laser operations:

1. Clear installation (bldg. 231) of all nonessential personnel. Shift personnel are to be restricted to control room or office areas. Bay area must be clear of all personnel except authorized ruby laser operators. Should unauthorized personnel enter the bay area at any time during operation, the laser is to be turned off immediately.
2. Secure installation. Lock all doors.
3. Turn on laser power outlet switch in control room.
4. Post goggles and laser warning signs at all entrances to bay area.
5. Turn on laser warning light.
6. Verify that door interlocks are closed (eight switches).

To operate He-Ne alignment laser:

1. Verify that all personnel are clear of beam path.
2. Inform personnel that a He-Ne laser is about to be energized.
3. Turn on the He-Ne laser power supply.

To operate the ruby laser:

1. Turn on the ruby laser water cooling system. Verify that the water is circulating and the cooling system is otherwise functional.
2. Verify that ruby laser power supply is plugged in.

3. Verify that required beam dumps are in place and that all dangerous reflections are terminated.

4. Verify that all personnel are wearing correct laser safety goggles. The authorized ruby laser operator need not be wearing goggles if the laser is not charged.

5. Verify that remote firing hookup to control room is disconnected.

6. Give verbal warning that the ruby laser power supply is about to be energized.

7. Turn on the ruby laser power supply.

CAUTION: THE LASER IS NOW OPERATIONAL

To fire the ruby laser:

1. Verify that all personnel (including authorized operator) are wearing correct laser safety goggles.

2. Give verbal warning that laser is about to be charged.

3. Charge laser.

4. Fire the laser on verbal three count.

To proceed with data acquisition mode laser operation:

1. Replace all shielding on interferometer modules.

2. Turn off ruby laser power supply before shift personnel are admitted to the bay area.

3. Clear and secure installation in accordance with normal tunnel operation procedures.

4. Verify that all interlocks are closed.

5. Verify that remote firing hookup to control room is connected.

6. Energize ruby laser power supply just prior to tunnel operation.

CAUTION: THE LASER MAY NOW BE FIRED

7. Proceed with tunnel operation.

8. Laser may be charged and fired remotely from control room as the authorized ruby laser operator desires.

9. Following the completion of tunnel operation, holographic plates may be reloaded by the authorized ruby laser operator.

Upon completion of laser operation:

1. Turn off ruby laser power supply. Remove and store power cord to preclude laser operation by unauthorized personnel.

2. Turn off ruby laser cooling water supply.

3. Turn off He-Ne laser power supply.

4. Turn off laser warning light.

5. Remove drapes, laser warning signs, and safety goggles from doors.

6. Unlock doors.

7. Turn off laser power outlet switch in control room.

8. Inform all personnel that laser operations have ceased.

RUBY LASER
EMERGENCY ENTRY PROCEDURE

In the event of an emergency requiring entrance into the high bay area at a time when the ruby laser is believed to be operating, the following procedure will be observed.

1. If time permits, attempt to contact laser operator over the intercom to advise the operator of the emergency.

2. If laser operator cannot be contacted, turn off ruby laser power at switch in control room.

3. Put on ruby laser safety goggles prior to entering bay area.

4. Unplug ruby laser power supply at outlet. Verify from power supply voltage meter that capacitors are dumped.

5. Goggles may now be removed.

6. Proceed with appropriate action to deal with emergency situation.

Reconstruction Apparatus

The following is a listing and description of optical components as they appear in figure B.3

1. **Laser** Spectra Physics Model 125A He-Ne laser. 50-mw minimum output at 632.8 nm. 1.8-mm beam diam. 0.8-mrad full-angle beam divergence and 1000 to 1 linear polarization.

2. **Dielectric Mirror** Newport Research Corp. 50.8-mm-diam Pyrex substrate and broadband dielectric coating.

3. **Spatial Filter** Newport Research Corp. Model 900. 15-mm focal-length microscope objective lens. 0.15-micron high power pinhole.

4. **Recollimating Lens** 585-mm focal length by 120-mm aperture. Two compound elements.

5. **Dual-Plate Holder** Custom Construction. Gimbal Design. Adjustment in 6 degrees of freedom. Micrometer thread drives provide translational accuracy to 0.0254 mm. Differential micrometer provides translational accuracy to 0.00254 mm on critical horizontal adjustment. Micrometer thread drives provide angular adjustment to 0.25 mrad. Plate spacing to 0.25 mm.

6. **Test Section Imaging Lens** 395-mm focal length by 100-mm aperture. Two compound elements.

7. **Flat Mirror** 10-cm by 10-cm aluminized first surface mirror. 3-mm float-glass substrate.

8. **Camera** View camera body. Mechanical shutter. No lens. Frosted glass back for viewing of reconstruction. Polaroid or cut film holders.

Aligning the Reconstruction System

There are three conditions that must be met in the alignment of the reconstruction system. The reconstructing beam must duplicate the construction

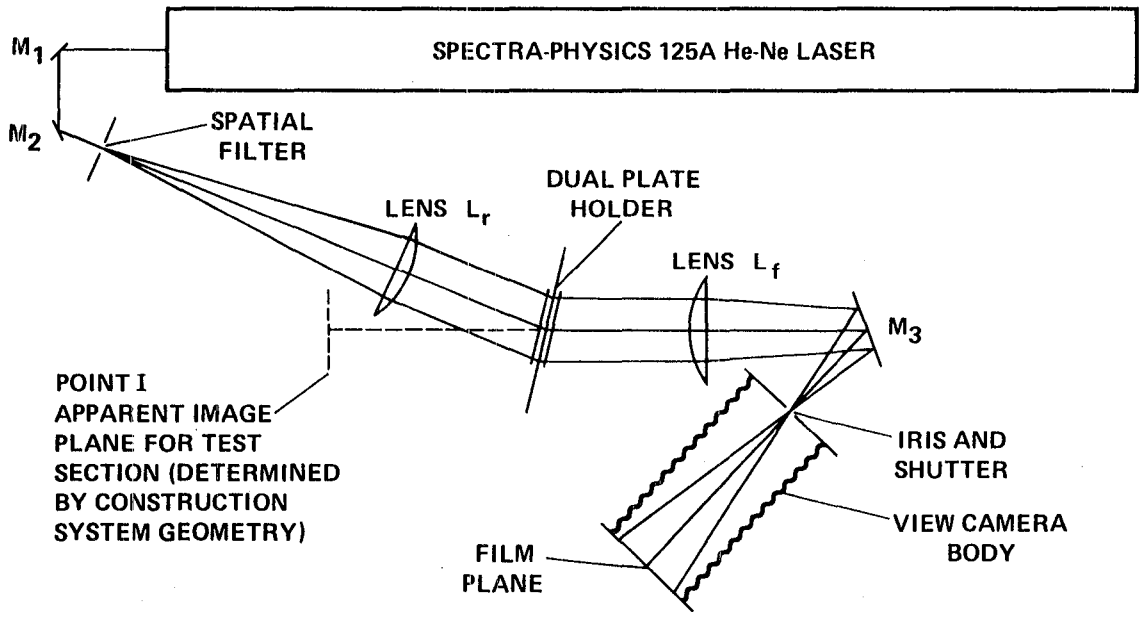

Figure B.3 Interferometer layout for hologram reconstruction (see also figure 7 in text).

reference wave as nearly as possible and impinge on the developed hologram at the same angle. The apparent image plane of the test section in the constructing object beam must be imaged at the film plane of the interferometric reconstruction. And the magnification and orientation of the camera body must be such that the interferometric reconstruction may easily be visually monitored while the dual-plate holder is being adjusted.

Begin by energizing the Spectra-Physics model 125 He-Ne laser according to approved operating procedures (listed in the operating procedure specification for this laser). Peak the laser alignment as outlined in the laser operating manual. Remove the spatial-filter microscope objective lens and pinhole and the recollimating lens L_r. Adjust mirrors, M_1 and M_2, so that the unexpanded beam travels along the path laid out on the table surface at the design height (22.86 cm). Load a plate into the dual-plate holder in the same orientation as for the construction process (emulsion forward for flow-on plates) with the dual-plate holder oriented at 10° to the reconstructing beam. Verify that the diffracted beam travels the correct path, rotate the dual-plate holder about the y axis and verify that maximum diffraction occurs at the 10° orientation. Now install the spatial-filter microscope objective and the recollimating lens and align in the same manner described for the construction reference beam.

At this time it is necessary to locate the image plane of the test section in the constructing system object beam. This may be done experimentally by placing an illuminated target in the test section plane and observing the location of best focus down beam of the object beam recollimation lens. Identify the point (I) having the same geometrical location (as referenced to the hologram plate) on the reconstruction table. To maintain a magnification of 1.0 the focusing lens, L_f, should be located at twice its focal length down beam of this virtual test section image plane and the film plane should be located at the same distance down beam of L_f. Set up the optics in this manner with attention to clearances between L_f

and the camera body. Remove the spatial-filter microscope objective and lens L_r, and align lens L_f on the unexpanded beam as was done with lens L_r. Now remove the hologram plate and place an illuminated target at I. Observe the image on the frosted screen of the camera. Bring the target into sharp focus by adjusting the film plane location and lock the camera back in this position. Replace the microscope objective, pinhole, lens L_r, and the hologram plate. Stop down the shutter aperture to a diameter of 3 to 4 mm and center the aperture over the focal point. Rotate mirror, M_3, and the camera body until the focal point passes through the shutter aperture and the image is well centered on the film plane grid. Verify that test section details (model, etc) are in sharp focus in the film plane.

Infinite-fringe dual-plate reconstruction may be performed as follows. Load flow-on and flow-off plates in the same orientation as they were when exposed (flow-off emulsion backward in front of flow on emulsion forward). Set angular adjustments to place the plates nearly parallel. Move plates close together. Observe back reflections in the vicinity of point I, adjusting angular orientation until Newton's rings are seen. The plates are now quite parallel. Further adjustments may be made with respect to an orthogonal coordinate system having x and y axes lying horizontal and vertical in the plane of the plate surface, and the z axis normal to the plate. Adjust z axis rotation until fringes in the free stream appear vertical. Adjust x and y translation until the shadows of the model exactly overlap. The interferometric reconstruction should now be very nearly infinite fringe. If a number of vertical fringes remain, adjust the y rotation to remove them. It may be necessary to increase the plate spacing. If so, the x translation will need readjustment to maintain model shadow overlap. Small iterations between x, y, and z rotation adjustments to minimize the presence of fringes in the free stream complete the infinite-fringe reconstruction process.

Finite-fringe reconstruction may now be accomplished. If vertical fringe orientation is desired, simply adjust y rotation to achieve the desired fringe field. The

effect on the reconstructed wave number for this adjustment is weak, so only a limited number (perhaps 20 fringes across the entire beam) of vertical fringes can be introduced. This number may be increased by rotating the entire dual-plate holder about the y axis and thereby changing the angle of incidence of the reconstructing beam. Such rotation introduces a degree of aberration which is primarily manifest as a longitudinal compression of the reconstructed image. Recall that any change in plate spacing will require a readjustment of x translation to maintain model shadow overlap. Plate spacing beyond 3 mm should be avoided, since aberration across the reconstruction beam aperture will be noticeable. If horizontal fringe orientation is desired, adjust z rotation to introduce the desired number of fringes. The Y axis translation is required to maintain model shadow overlap. A great number of horizontal fringes may be introduced. However if the z rotation between the plates becomes too great, it will be impossible to maintain model shadow overlap across the entire field of view.

GENERAL OPERATING INSTRUCTIONS FOR THE SPECTRA-PHYSICS 125 HELIUM-NEON LASER

NOTE: An operating procedure in checklist form is attached and shall be followed during all laser operations.

This laser shall be operated only by authorized personnel as designated by the Branch Chief and the authorized laser user for the Experimental Fluid Dynamics Branch.

NOTE: All operators shall have filed form DOS 29 with the Health and Safety Officer and have had a laser eye exam.

The Spectra-Physics model 125 He-Ne laser is a medium-power (50-mw) class IIIb continuous-wave laser. The primary safety hazard associated with the operation of this laser is that of eye damage caused by direct viewing of the laser beam. Precautions must be taken to keep the eyes out of the horizontal plane of the beam path. All alignment activity must be done using diffusely reflecting surfaces and not by sighting along the beam. Remove all specularly reflecting surfaces (including watches, rings, etc.) from the beam path. All undesirable beam reflections must be properly terminated.

An additional skin tissue hazard exists in the region of the unexpanded output beam. Care must be taken to avoid prolonged (no longer than 15 min) intrabeam skin exposure.

The Spectra-Physics model 231 power supply provides high-voltage (6-kv) DC and RF excitation to the laser. Care must be taken to minimize the electrical hazard resulting from damage to these conductors.

This laser is to be operated only in building 231, room 112. This installation has been outfitted for the operation of a class IV pulsed ruby laser (see Operating

Procedures For The Apollo Pulsed Ruby Laser in Appendix B). The existing safety features are intended to ensure safe operation of the Spectra-Physics 125 laser as well. Those features that apply to the operation of this laser are:

1. The window is boarded to prevent stray beams from leaving the area.

2. Laser safety goggles and assorted light baffles are available to personnel within the installation.

3. The entry door to the installation must be locked during laser operations to prevent entry of unauthorized personnel.

4. As additional redundant protection, a light baffle is incorporated at the entry door to shield personnel.

5. A key to the entry door and laser safety goggles are available in an enclosed unlocked box next to and outside the entry door in the event of an emergency requiring outside assistance.

6. Laser warning signs must be posted on the entry door during laser operations. A placard is also posted on the entry door advising personnel of the proper procedures for entry to the laser room during laser operations in the event of an emergency requiring outside assistance.

7. A red light outside the entry door is turned on during laser operations. A sign is posted under the red light advising personnel not to enter when the red light is on.

OPERATING PROCEDURE FOR SPECTRA-PHYSICS 125 LASER OPERATION

WARNING

LASER TO BE OPERATED BY AUTHORIZED PERSONNEL ONLY

Operators of this laser are authorized by the RFE Branch Chief after

1. A laser eye exam is done.

2. Form DDS-29 is completed.

3. The AHSM-1 (ARC Laser and Microwave Safety) and A Guide for Control of Laser Hazards, 1976, issued by The Conference of Governmental Industrial Hygienists is read.

4. A laser training course conducted by the RFE Branch is completed.

The following procedure will be used during all laser operations.

Prior to laser operation

1. Advise personnel in Bldg. 231 that laser operations are in progress.

2. Clear installation (Bldg. 231, Room 112) of nonessential personnel.

3. Post laser warning signs.

4. Ensure that appropriate safety goggles (He-Ne) and entry door key are outside the entry door.

5. Turn on red light outside entry door. Verify that red light is on.

6. Close and lock door to Room 112.

7. Close curtains on the entry door light baffle.

8. Verify that power cords are connected.

9. Verify that all required beam dumps are in place.

10. Inspect the anticipated beam path for possible reflection hazards. Remove from the beam path any items capable of introducing hazardous reflections.

To operate laser

1. Announce to personnel in room 112 that laser is to be turned on.

2. Verify that all personnel are clear of the laser beam path.

3. Verify that all personnel requiring safety goggles are wearing them.

4. Turn on the laser power supply (warmup time is less than 1 sec).

CAUTION

THE LASER IS NOW ON

NOTE: In the event of entry by unauthorized personnel, the operator shall first give verbal warning to shut eyes, then turn off the power supply.

Upon completion of laser-related activities

1. Turn off the laser power supply.

2. Announce to personnel in room 112 that the laser is turned off.

3. Disconnect power cords to laser.

4. Open door to room 112.

5. Turn off the red light.

6. Remove the laser warning signs.

7. Inform personnel in building 231 that laser operations have ceased.

APPENDIX C

Interferogram Data Reduction Software

Five programs written to perform interferometric data reduction tasks for this study are presented in flowchart form in this appendix. Programs were written in Fortran 77 and were executed on a Vax 780 computer. Interferogram digitization was accomplished using a Tektronix model 4954 graphics tablet interfaced to a Tektronix model 4014-1 graphics terminal. A brief description of the function of these programs is given in the following paragraphs.

The objective of the interferogram digitization program was to convert fringe number data from the graphic form of the raw interferogram print to a numerical form that could be used in data reduction calculations. The graphics tablet provided 0.01 in spatial resolution which permitted 0.005 in resolution for the enlarged interferograms. Tektronix Plot 10 and AG2 graphics software were used for tablet commands. This program permitted rotation of axes to accommodate skewed mounting and automatic scaling obtained from known model dimensions. Fringe number and position along radial profiles at selected streamwise locations were written to data files along with information describing flow conditions and geometry.

The data filtering program was designed to enhance interferogram data prior to the integral inversion. Two enhancements were possible. A simple radial dimension stretching to match the digitized model surface position value to the known physical dimension was used as a first order corrector for image distortion. Also, a low order filtering process (accomplished by subtracting a low order polynomial curve fit to free stream fringe number data from the entire fringe number profile) permitted first order correction for wave front distortion.

The complementary profile merging program was designed to combine profiles obtained from complementary reconstructions of the same interferogram. Comple-

mentary is used to indicate reconstructions with opposite wedge fringe functions. Profiles from complementary data files are matched. If there is sufficient profile overlap a linear regression procedure is used to split any difference in fringe number value arising from inaccurate wedge fringe function determination. Profiles are then combined to form a merged data file.

These data are then analyzed with the Abel integral inversion program. A higher-order orthogonal polynomial curve fit is used to approximate fringe-number values from the raw data. Raw data and approximated values are displayed graphically for evaluation. Polynomial order and surface and shock adjacent pseudodata adjustments may be made. Approximated values are then Inverted using either the standard or least squares Abel inversion algorithms. The resulting refractive index profiles are converted to density via the Gladstone-Dale relation.

Since several interferograms were evaluated for each flow condition, it was possible to calculate an average and standard deviation for each point in each profile. For profiles crossing the shock, position was normalized by shock location prior to averaging.

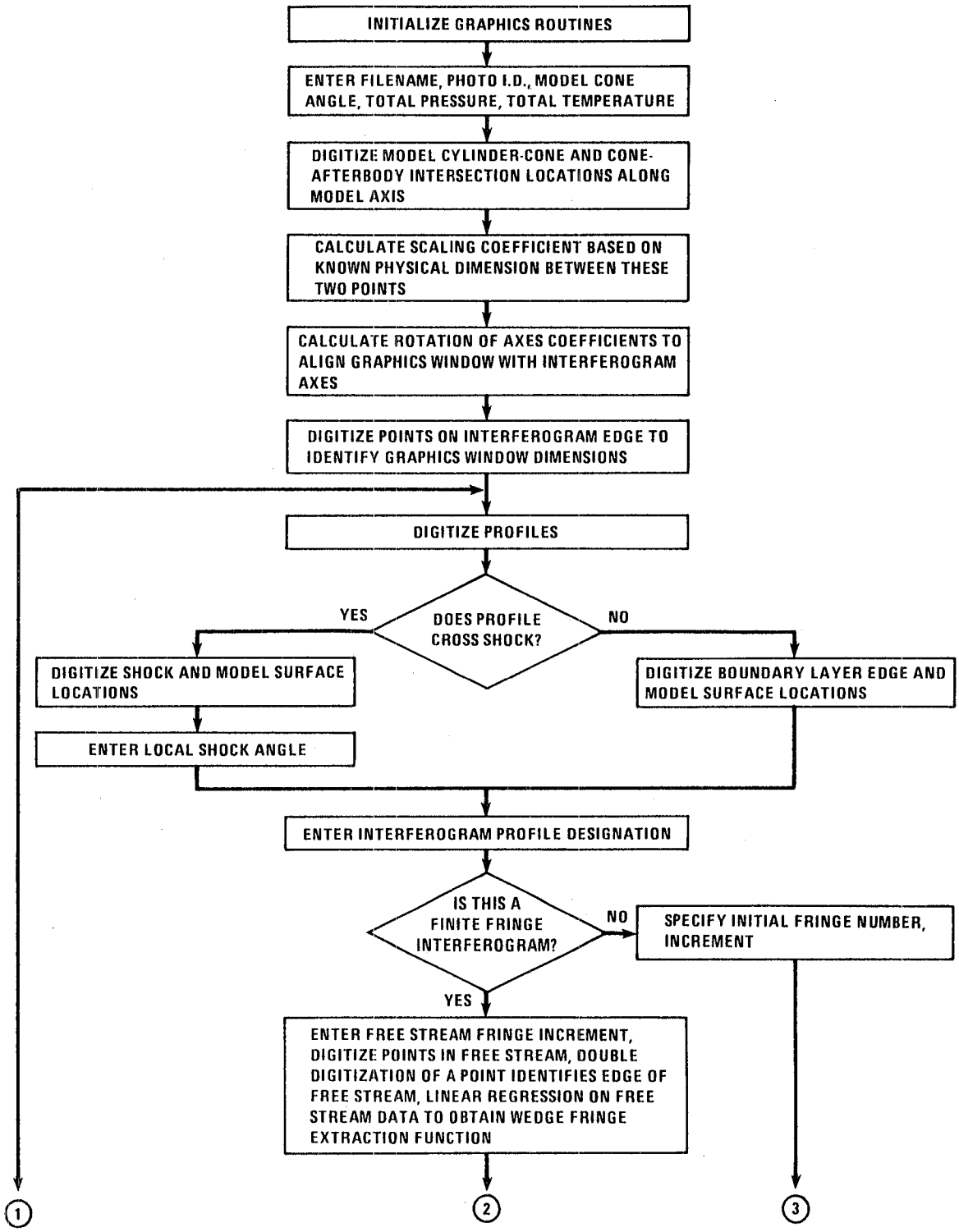

Figure C.1 Interferogram Digitization Program.

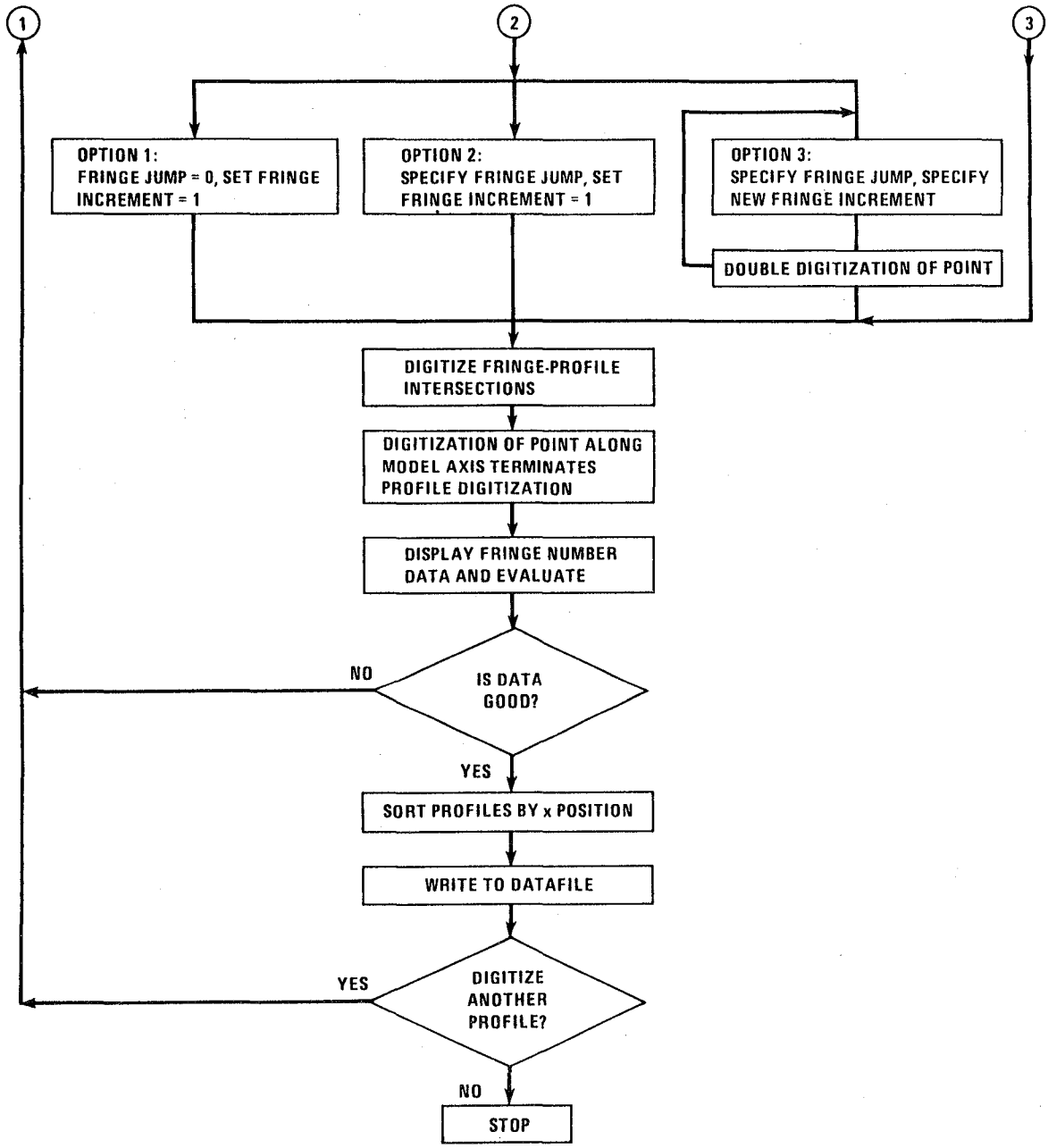

Figure C.1 Concluded.

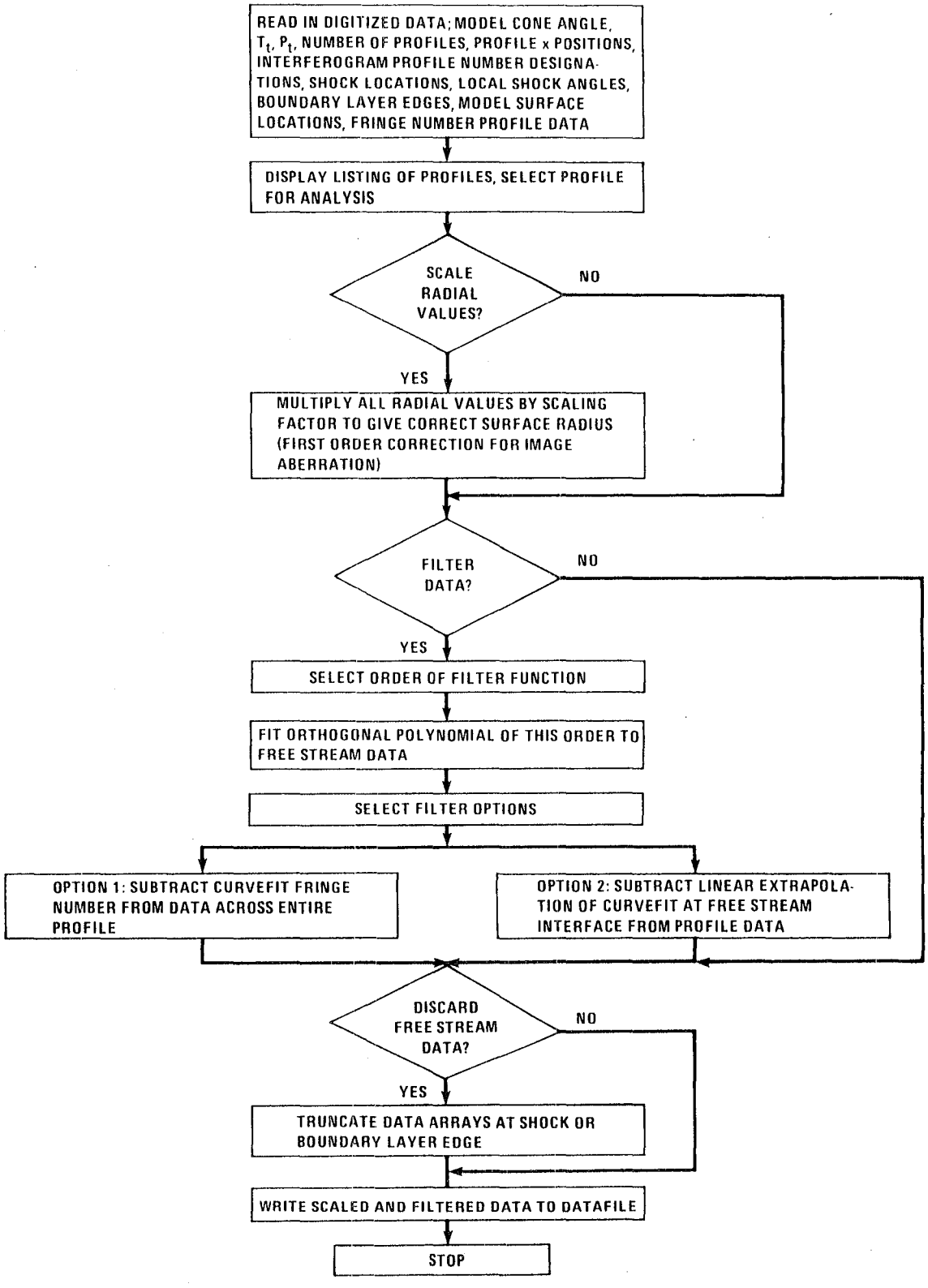

Figure C.2 Data Filtering Program.

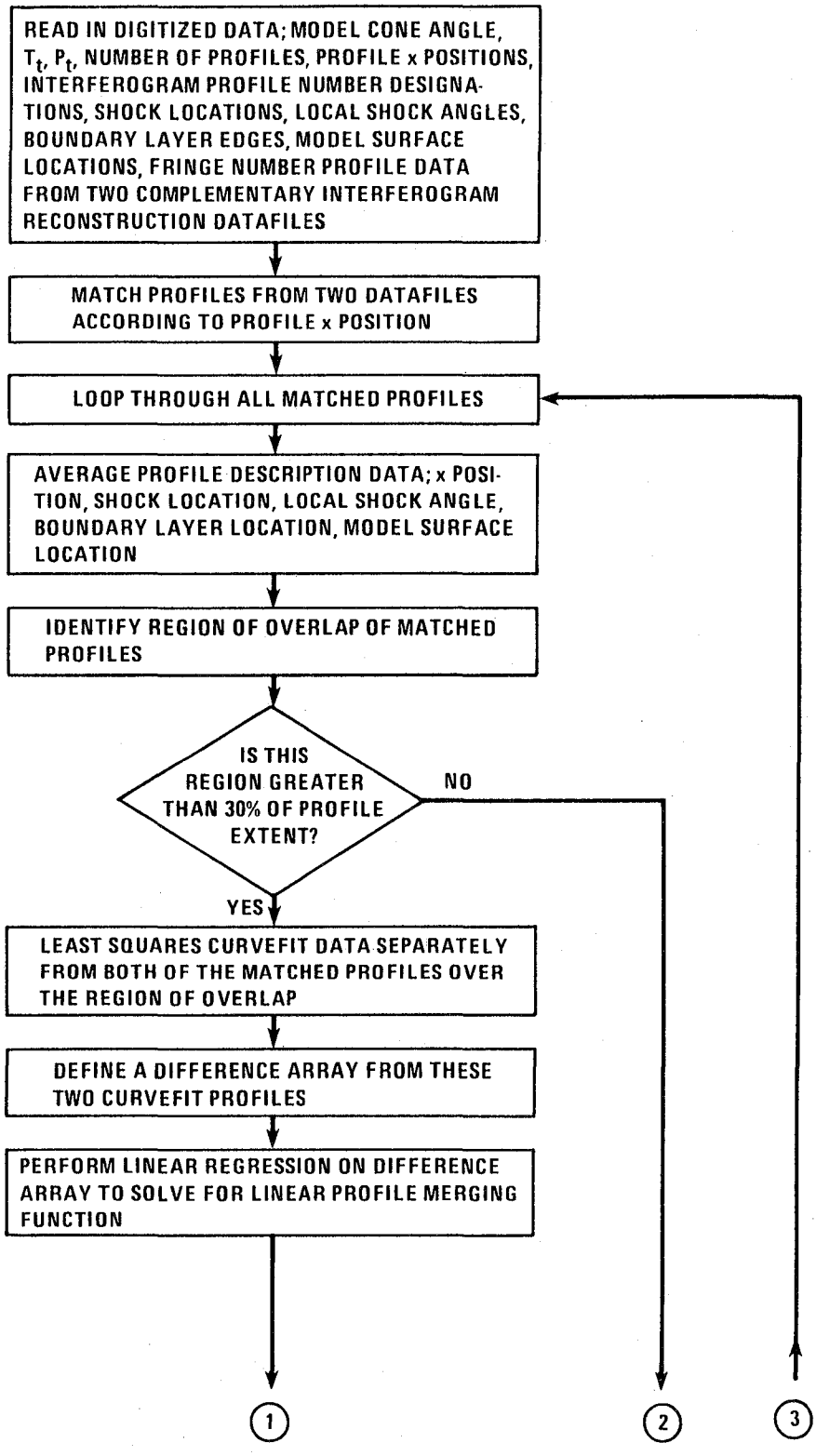

Figure C.3 Complementary Profile Merging Program.

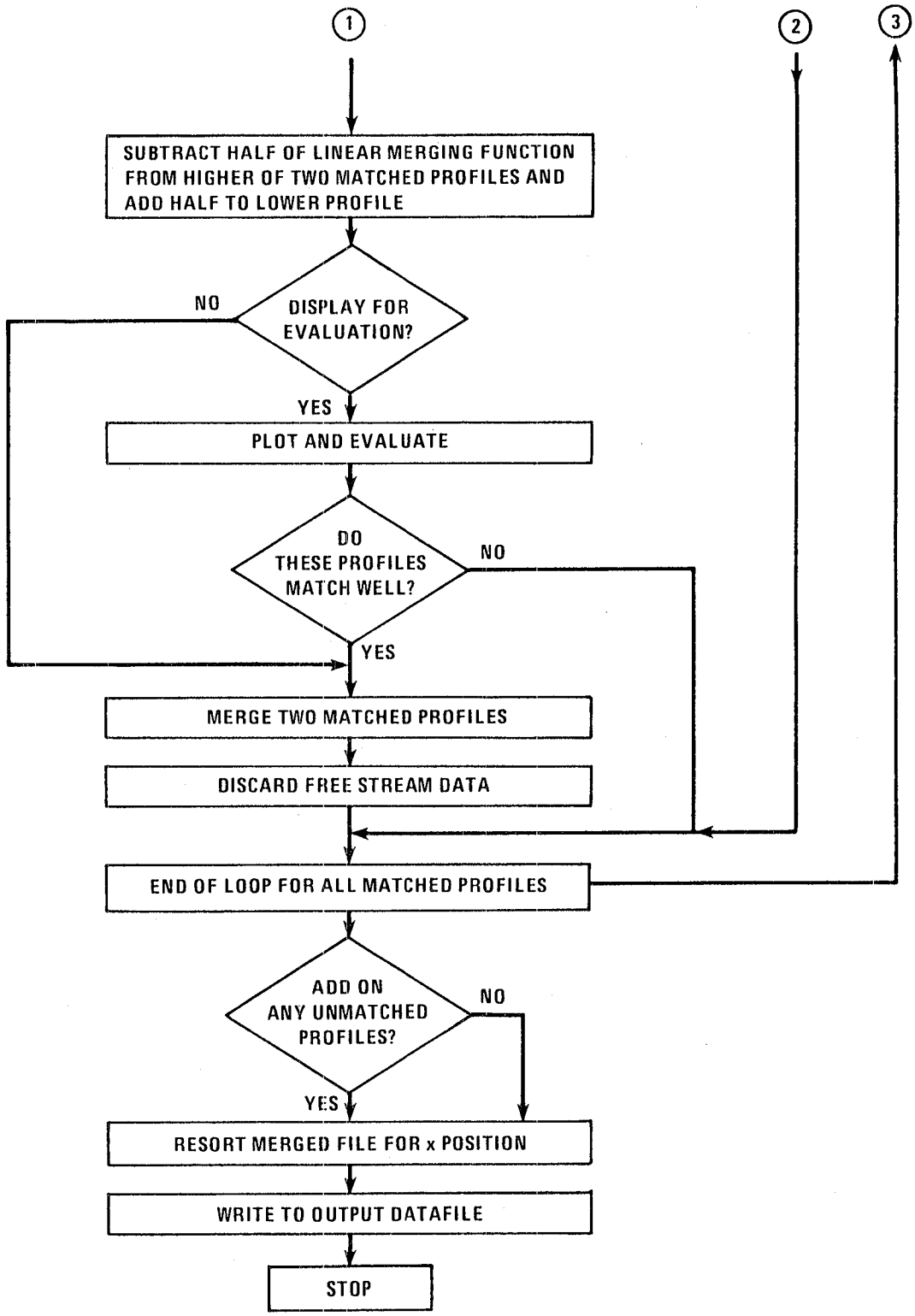

Figure C.3 Concluded.

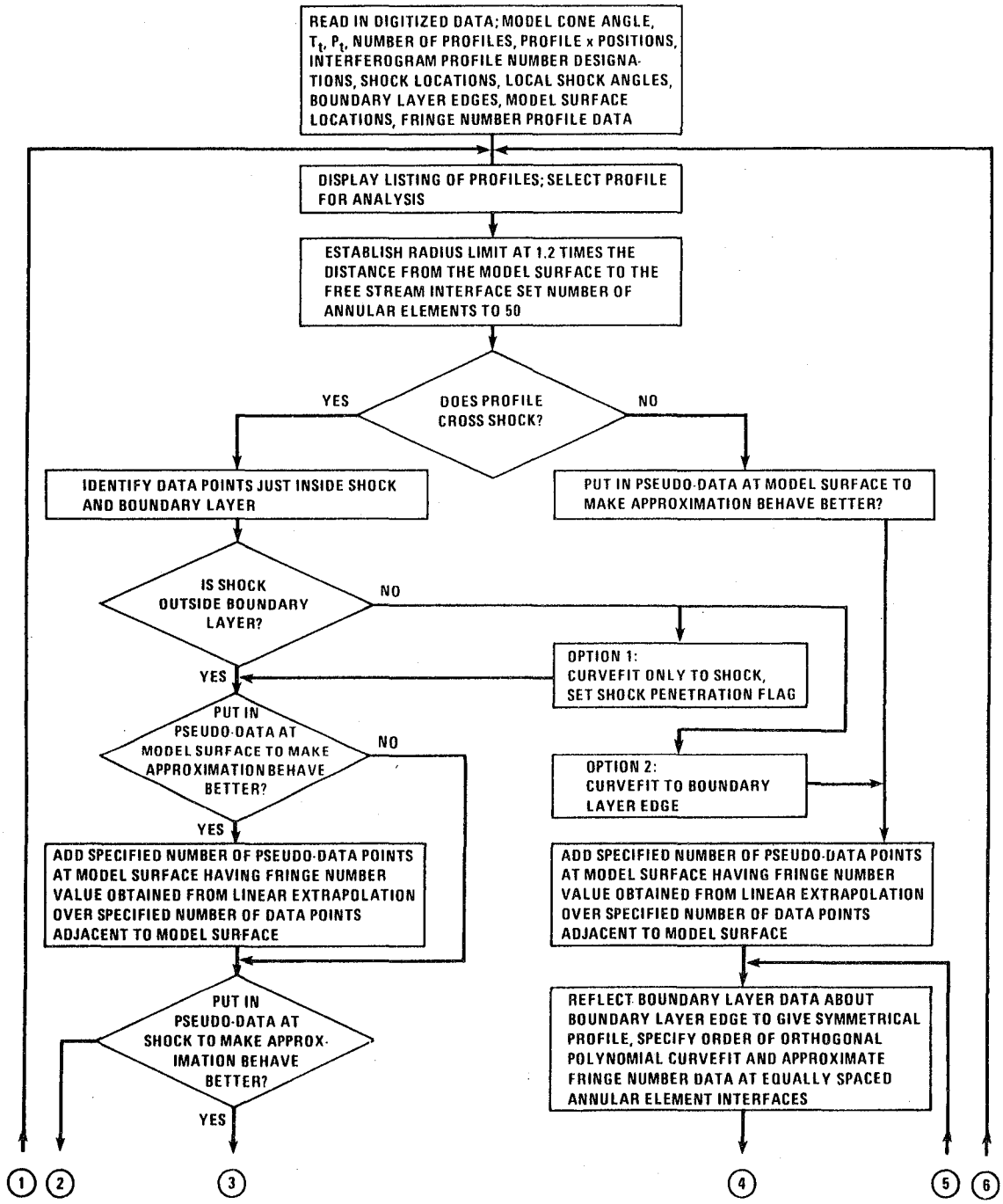

Figure C.4 Abel Integral Inversion Program.

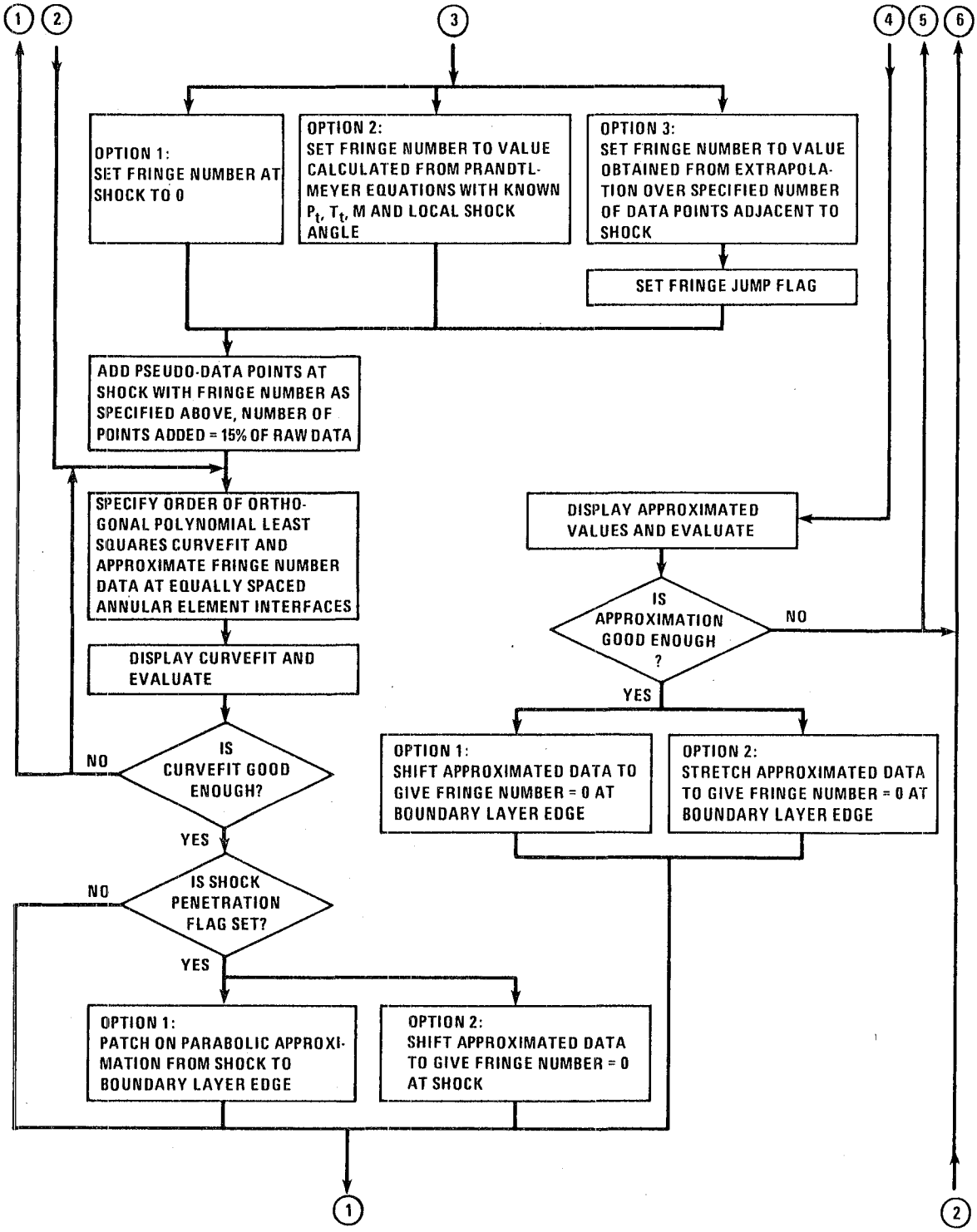

Figure C.4 Continued.

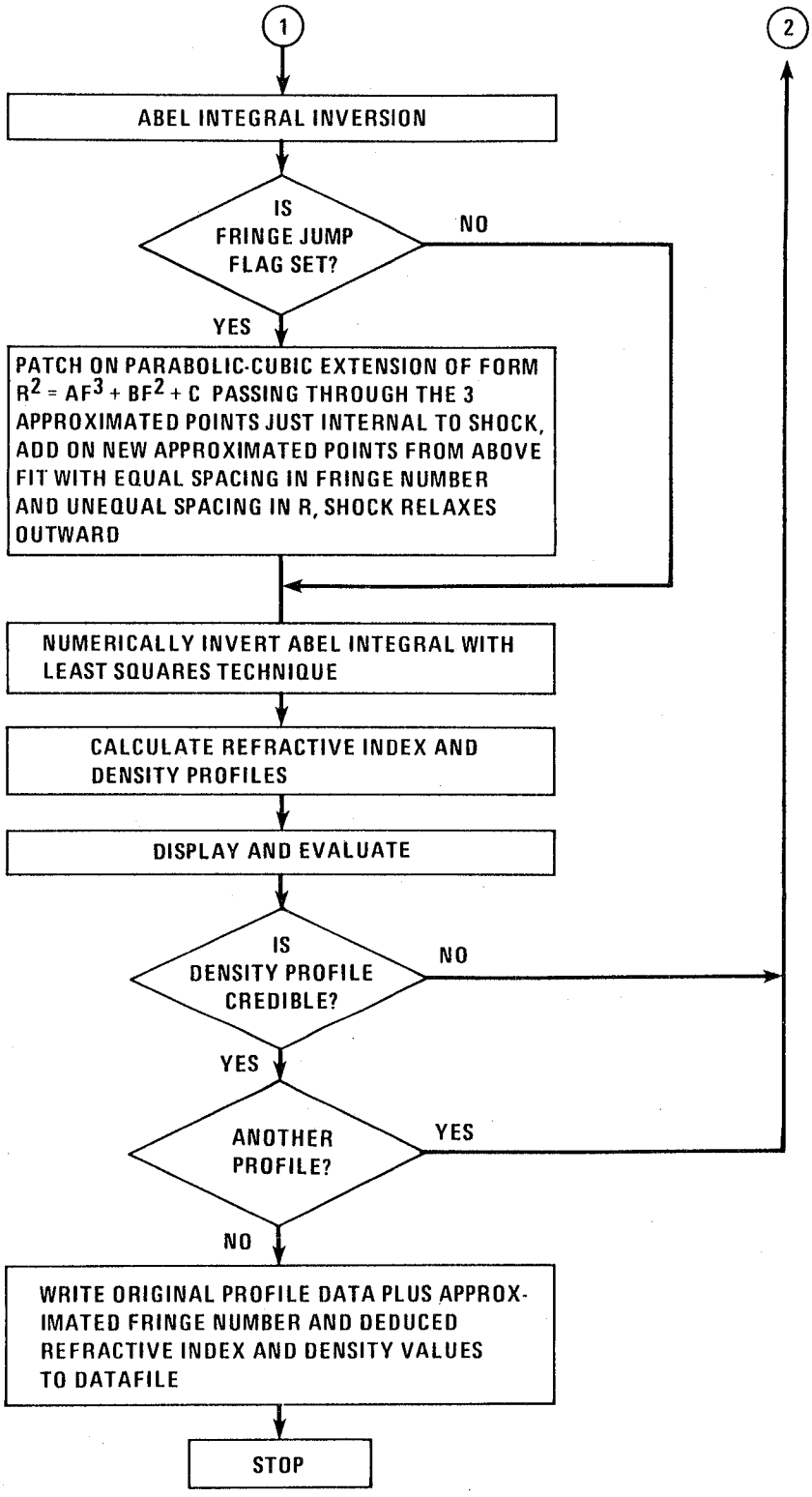

Figure C.4 Concluded.

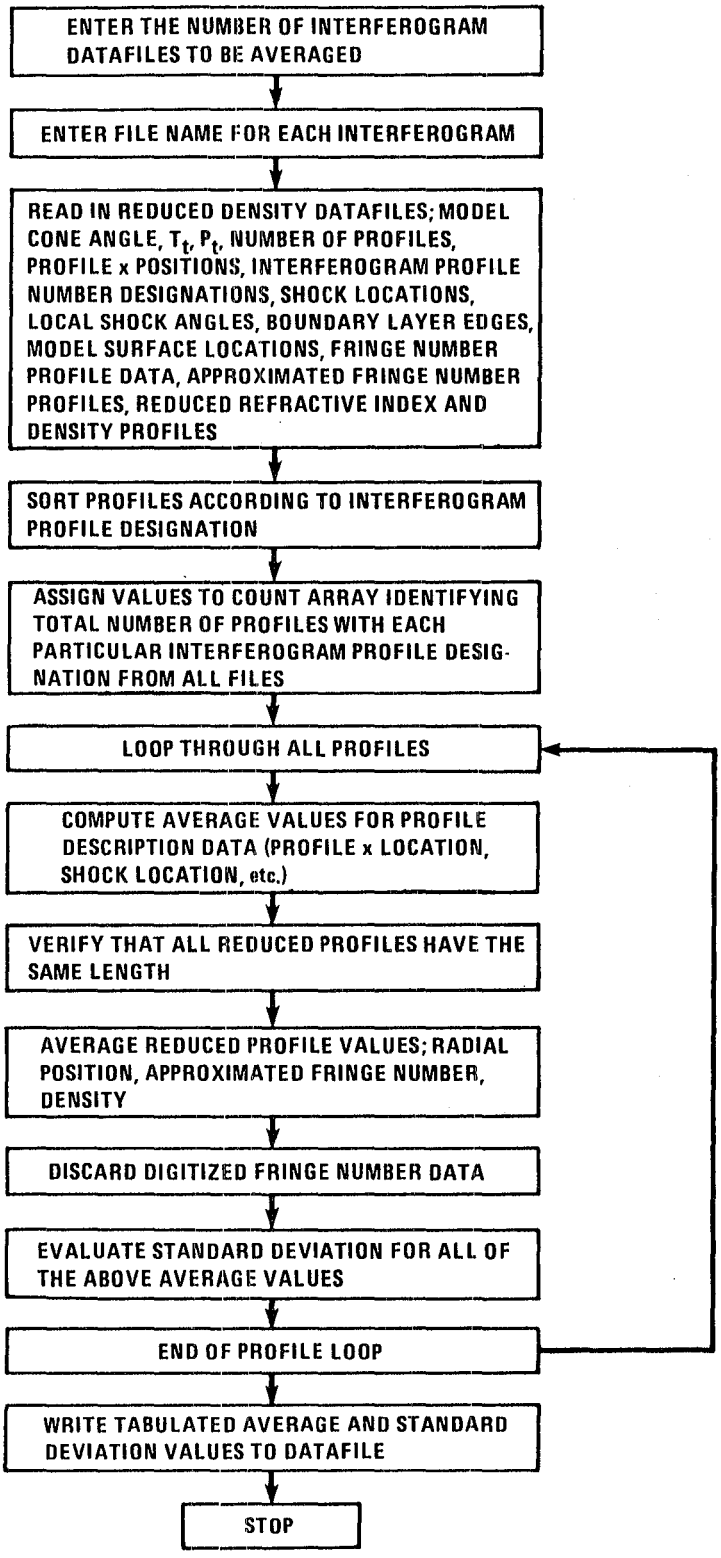

Figure C.5 Density Data Averaging Program.

APPENDIX D

Interferogram Prints and Tabulated Densities

Interferogram prints for each flow condition are included in this appendix. All interferograms have the same wedge fringe function sign. Tabulated density values are also presented for detailed comparison. A short table of profile positions summarizes the data for each flow condition. Longer tables of density as a function of position are presented for each profile. Mean and standard deviation values are listed when more than one profile was analyzed.

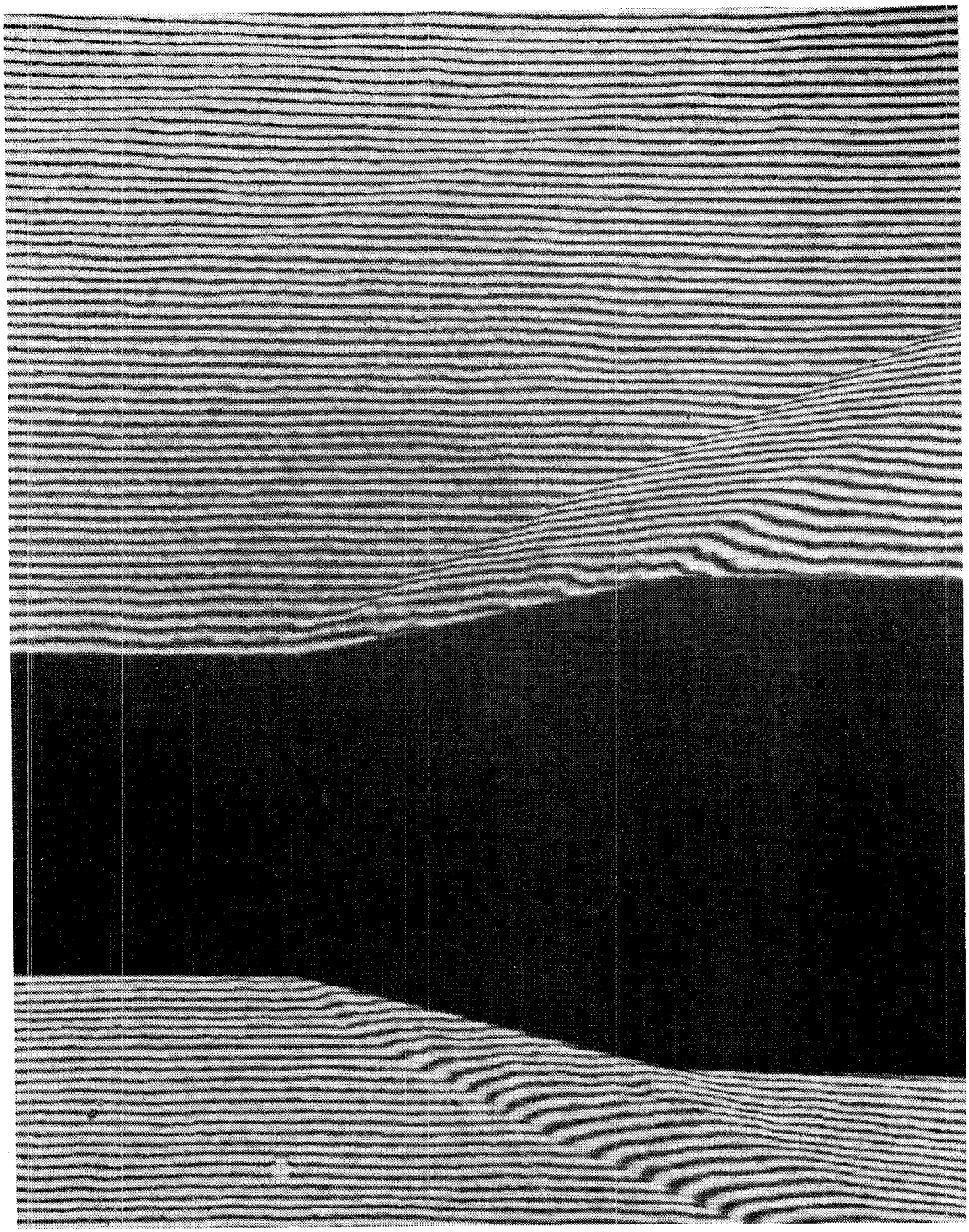

Figure D.1 Plate 583 Horizontal finite-fringe interferogram 12.5° model, $P_t = 1.7$ atm, $Re_L = 18 \cdot 10^6$.

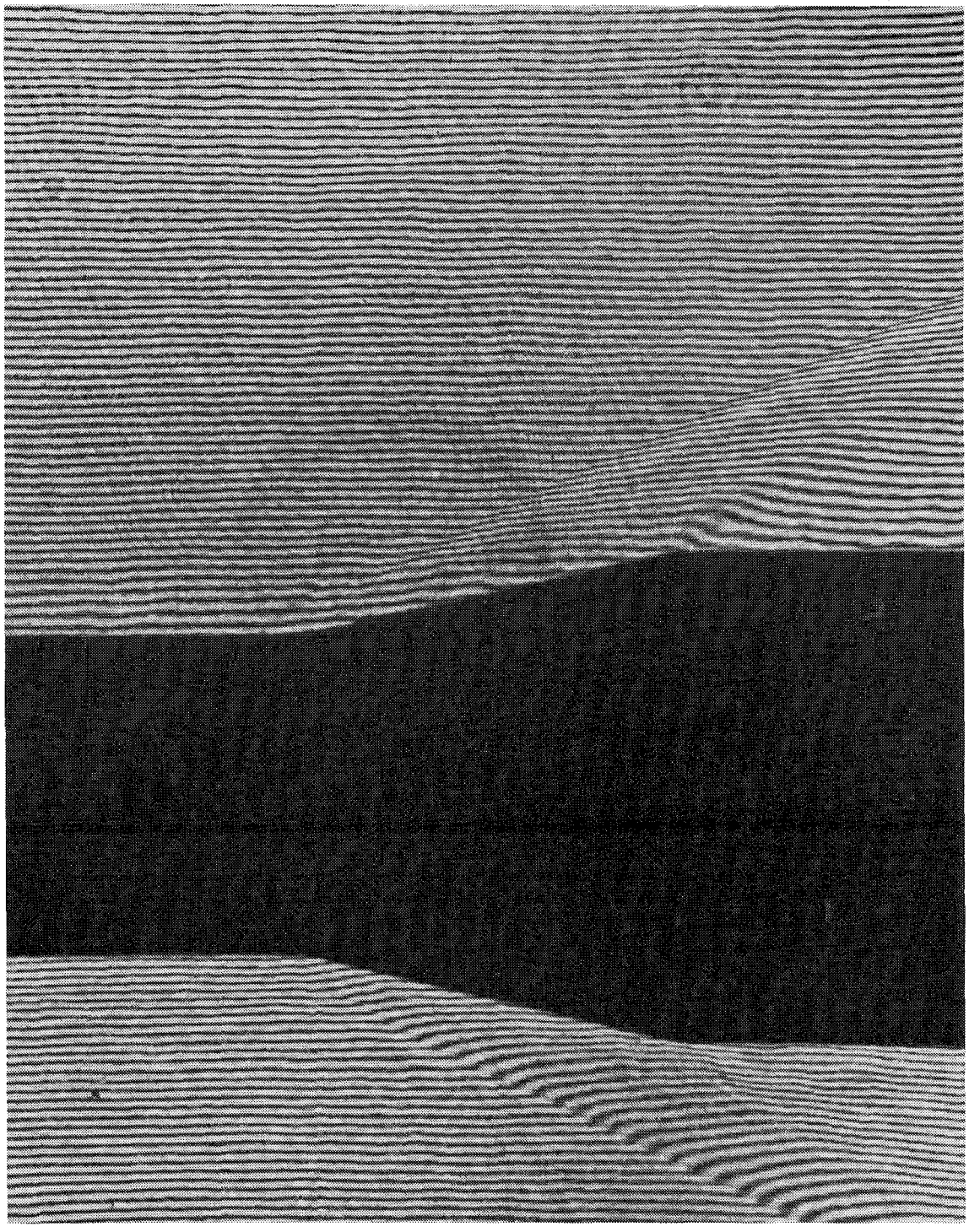

Figure D.2 Plate 584 Horizontal finite-fringe interferogram 12.5° model, $P_t = 1.7$ atm, $Re_L = 18 \cdot 10^6$.

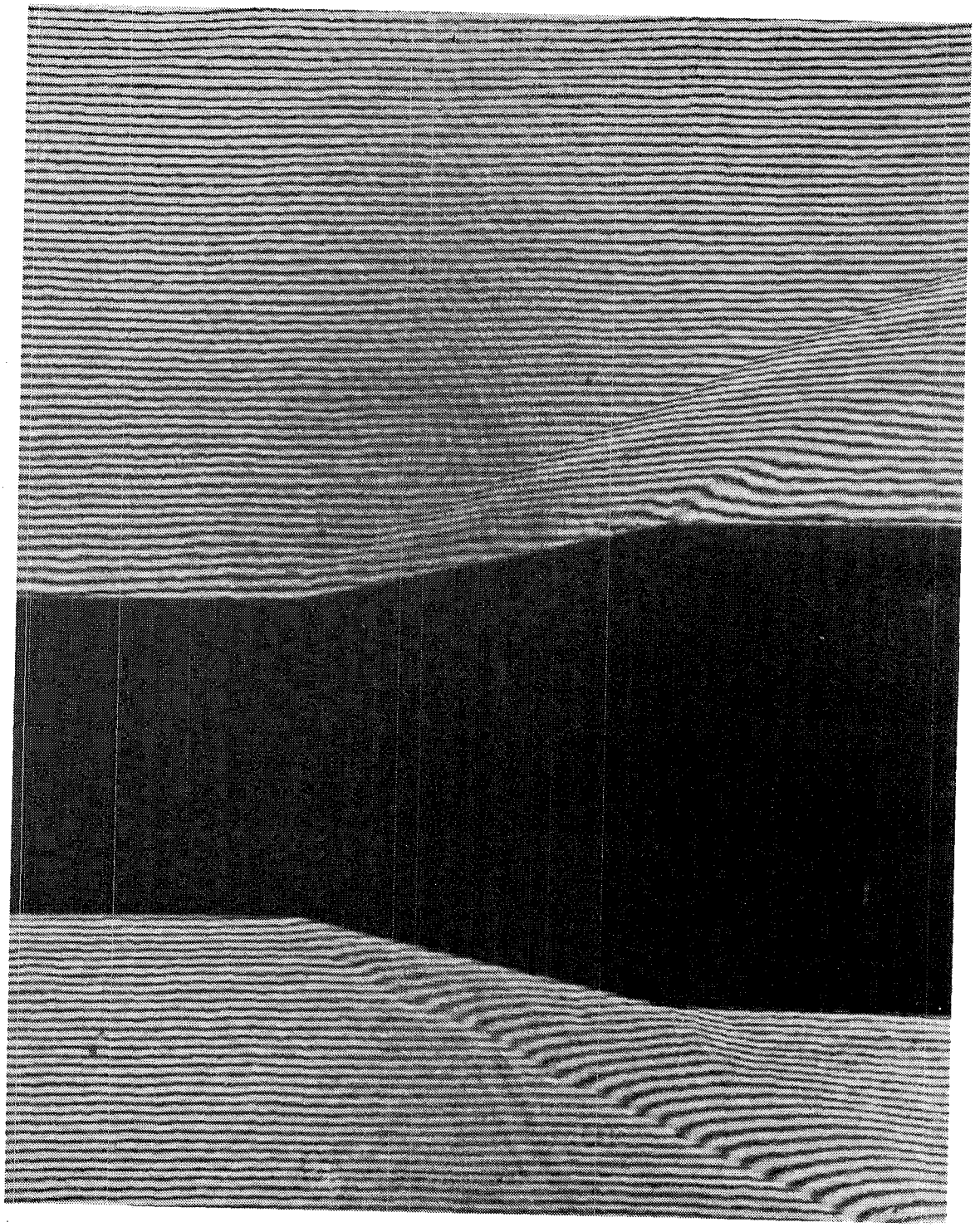

Figure D.3 Plate 585 Horizontal finite-fringe interferogram 12.5° model, $P_t = 1.7$ atm, $Re_L = 18 \cdot 10^6$.

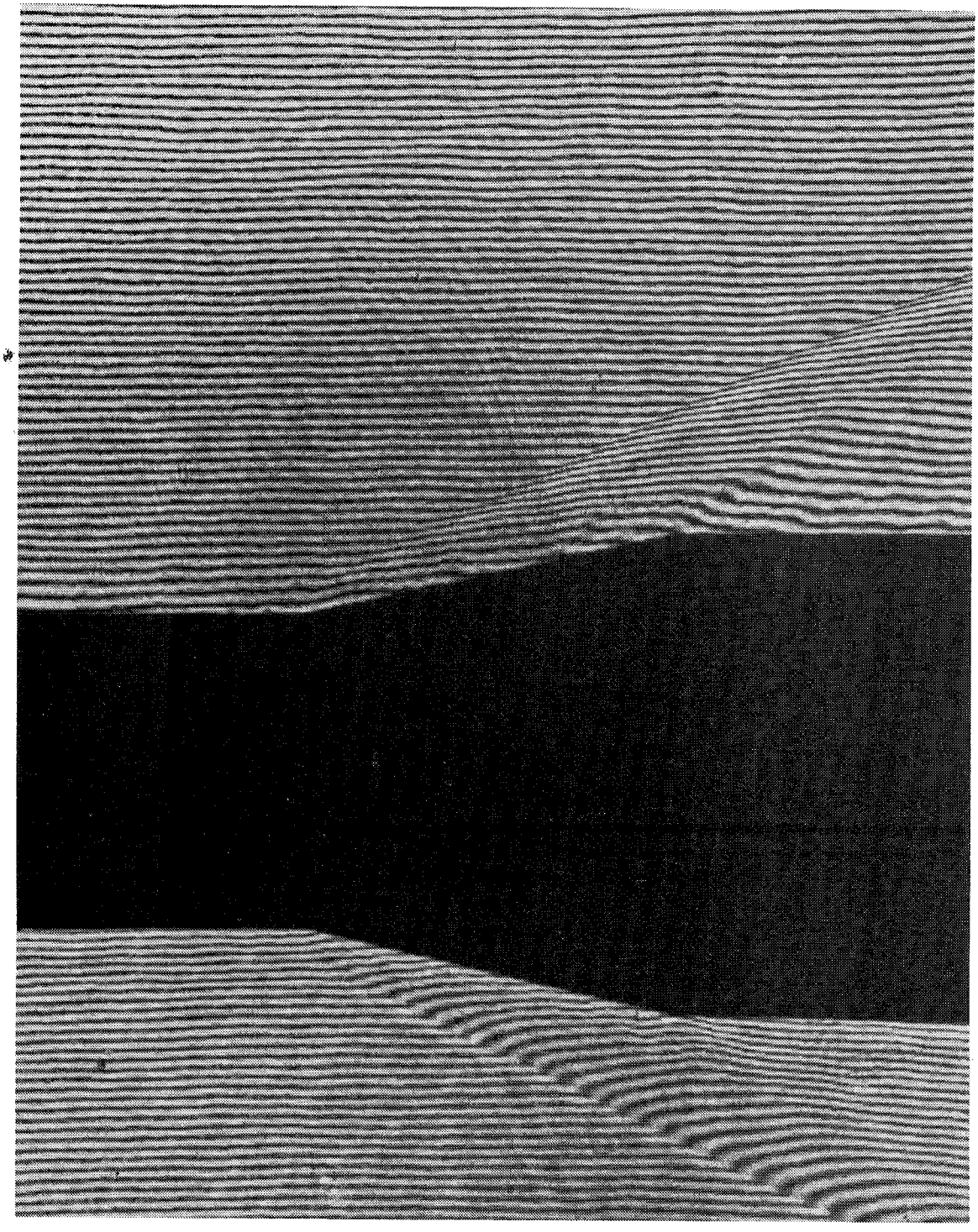

Figure D.4 Plate 586 Horizontal finite-fringe interferogram 12.5° model, $P_t = 1.7$ atm, $Re_L = 18 \cdot 10^6$.

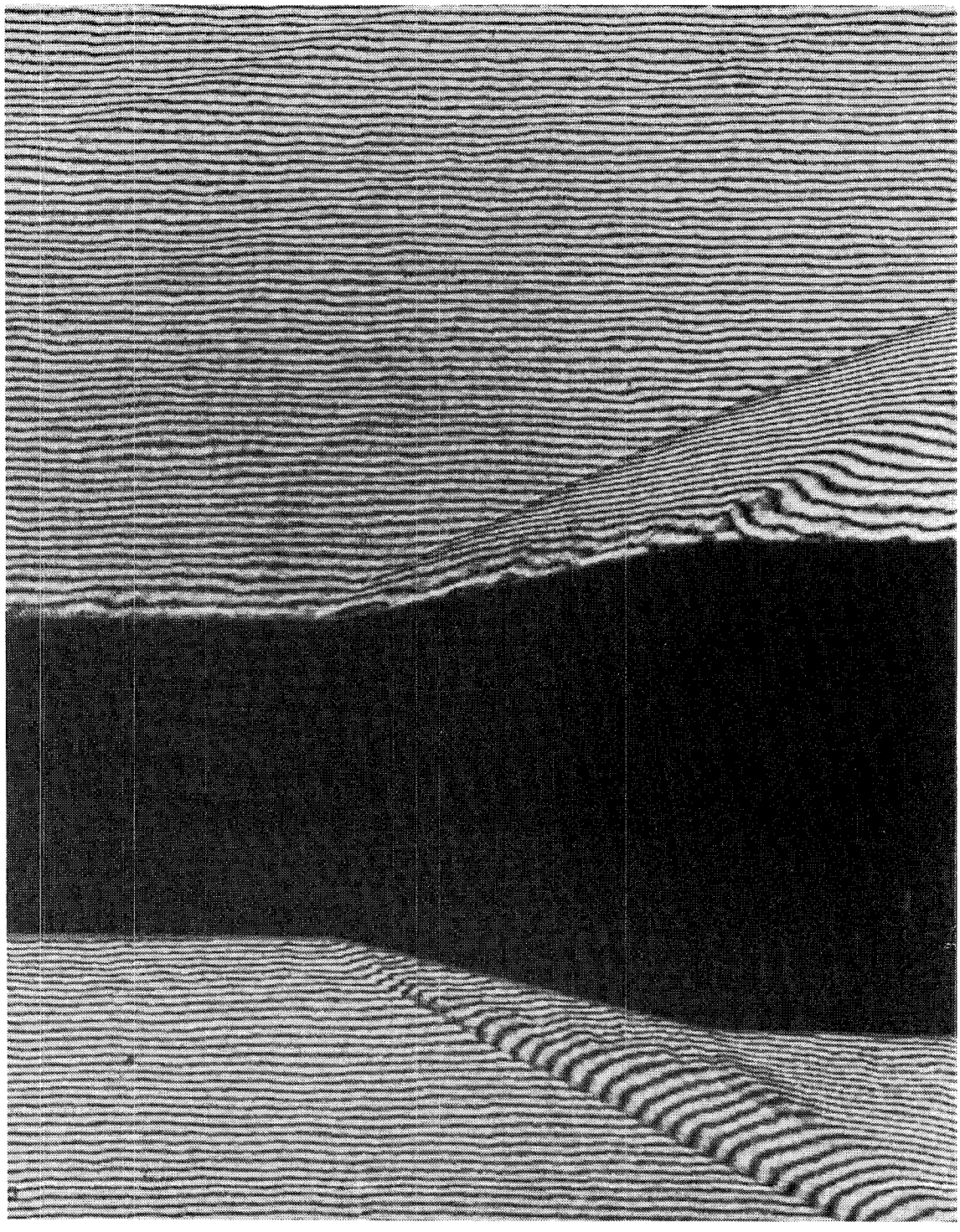

Figure D.5 Plate 579 Horizontal finite-fringe interferogram 12.5° model, $P_t = 3.4$ atm, $Re_L = 34 \cdot 10^6$.

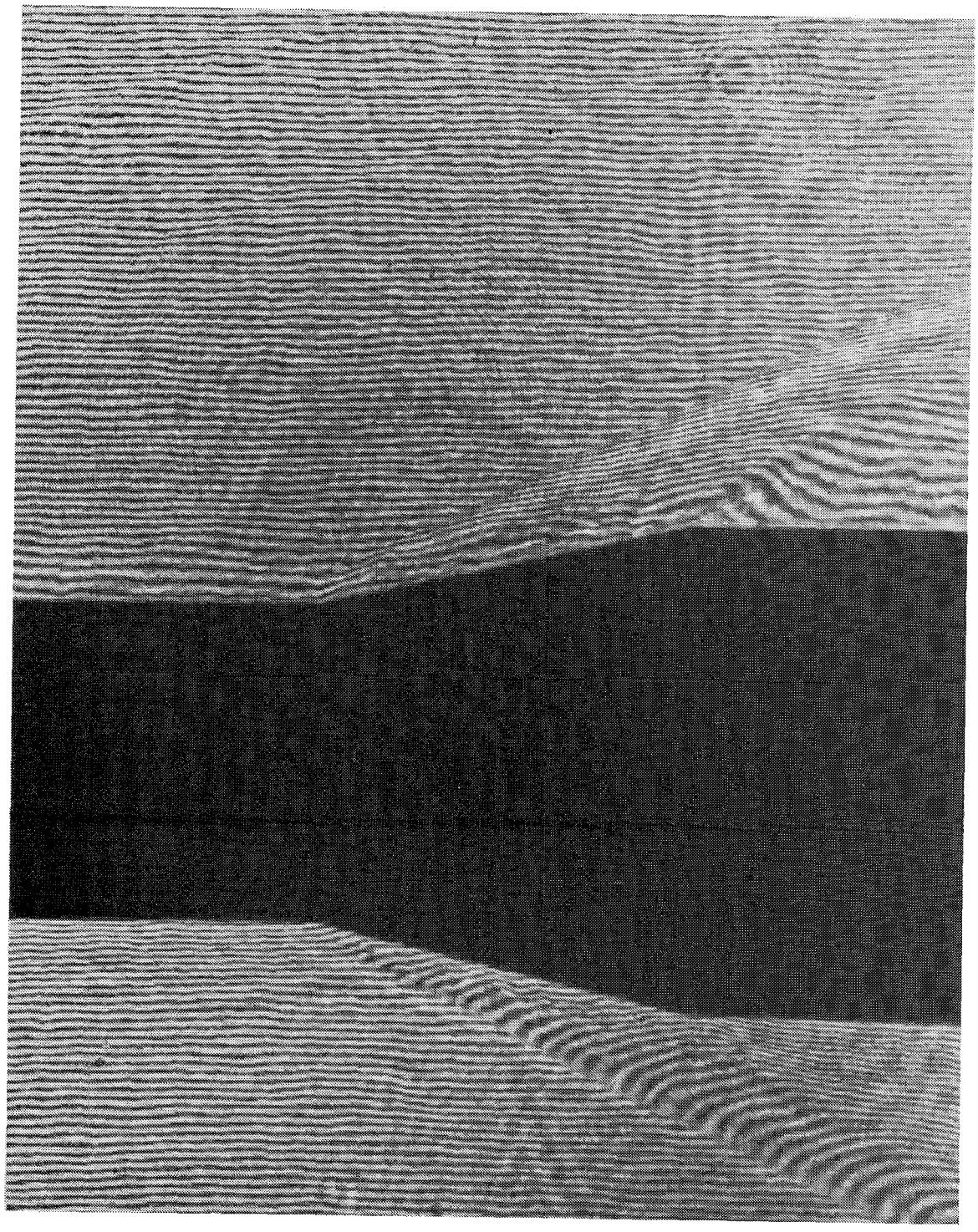

Figure D.6 Plate 580 Horizontal finite-fringe interferogram 12.5° model, $P_t = 3.4$ atm, $Re_L = 34 \cdot 10^6$.

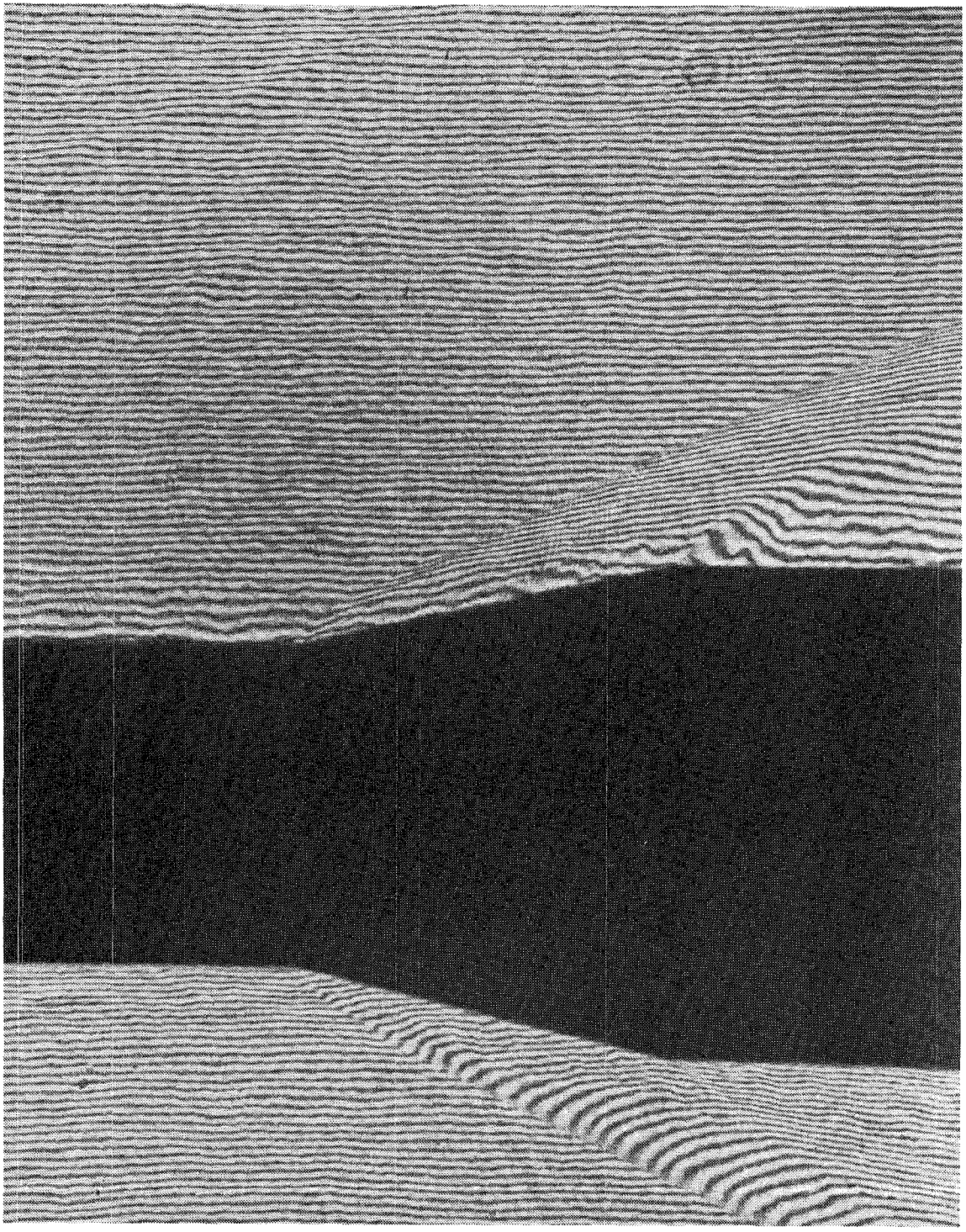

Figure D.7 Plate 589 Horizontal finite-fringe interferogram 12.5° model, $P_t = 3.4$ atm, $Re_L = 34 \cdot 10^6$.

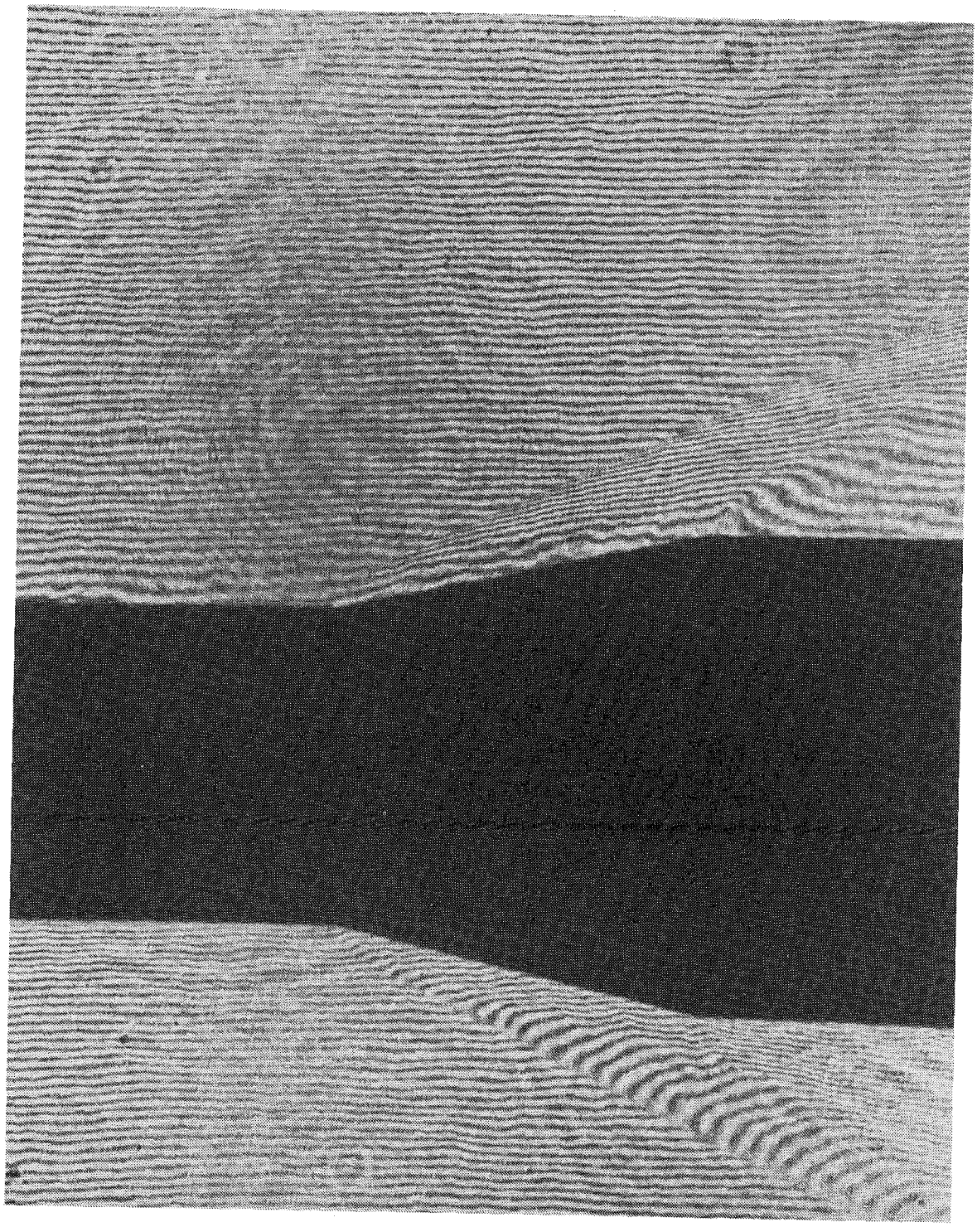

Figure D.8 Plate 590 Horizontal finite-fringe interferogram 12.5° model, $P_t = 3.4$ atm, $Re_L = 34 \cdot 10^6$.

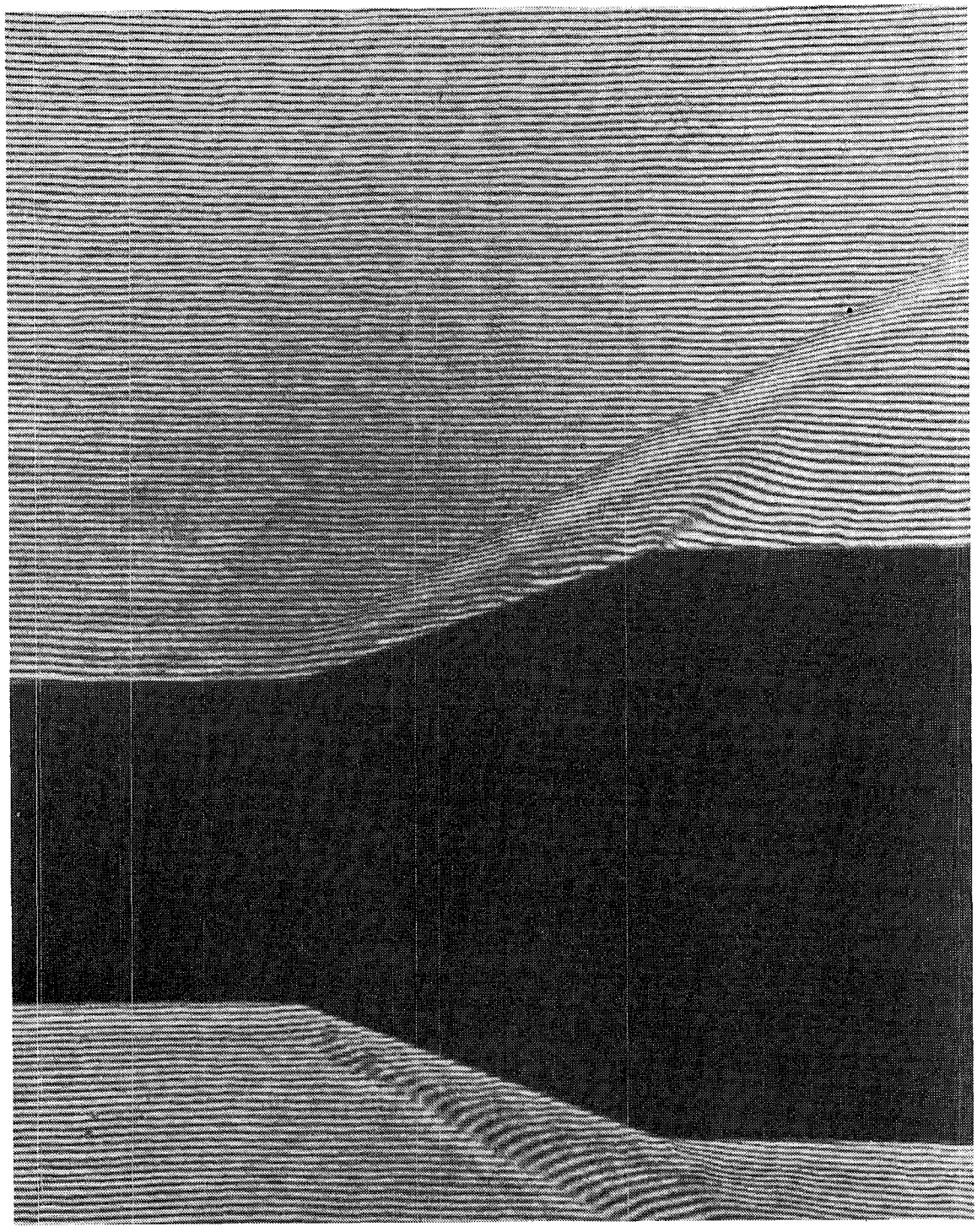

Figure D.9 Plate 569 Horizontal finite-fringe interferogram 20° model, $P_t = 1.7$ atm, $Re_L = 18 \cdot 10^6$.

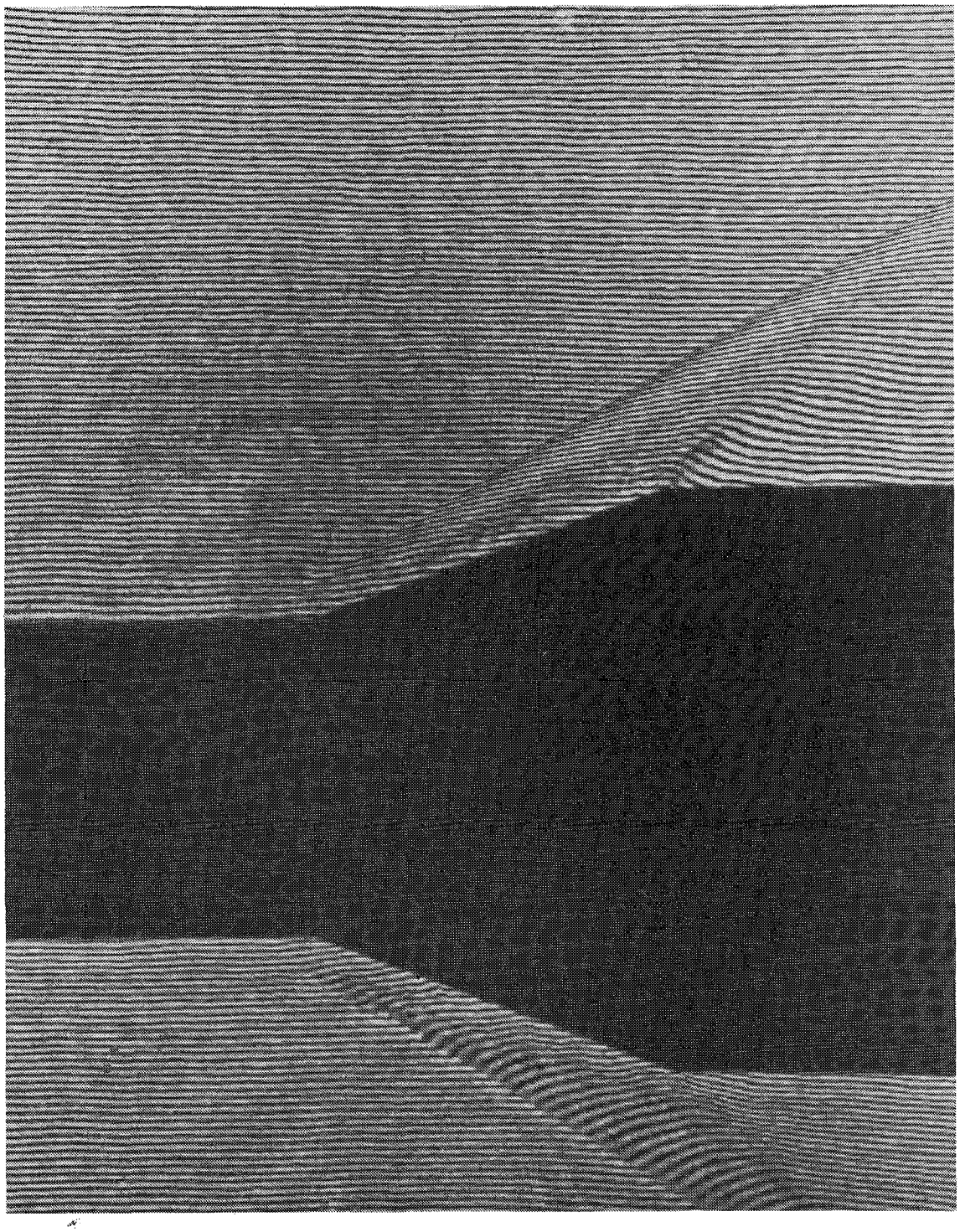

Figure D.10 Plate 570 Horizontal finite-fringe interferogram 20° model, $P_t = 1.7$ atm, $Re_L = 18 \cdot 10^6$.

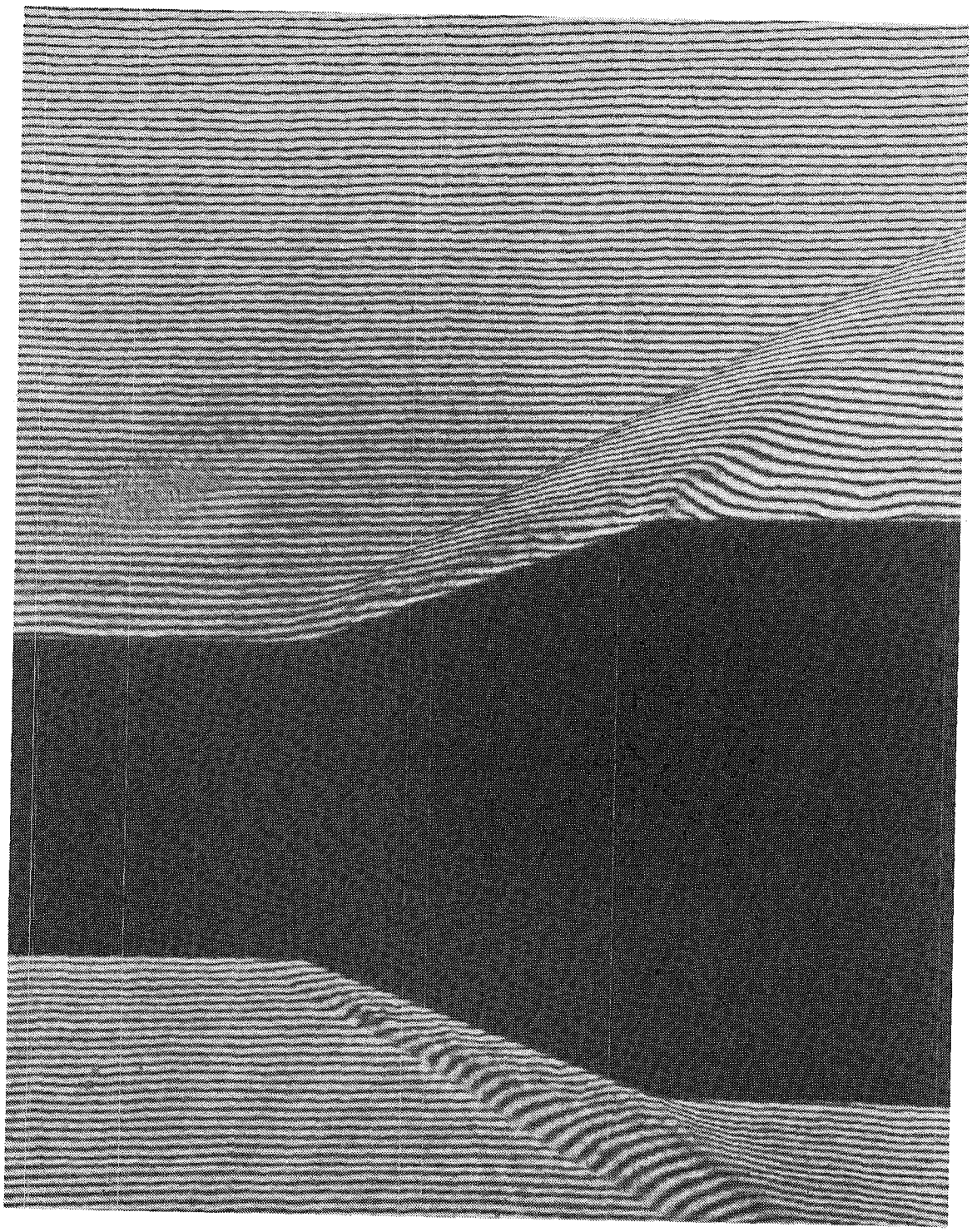

Figure D.11 Plate 571 Horizontal finite-fringe interferogram 20° model, $P_t = 1.7$ atm, $Re_L = 18 \cdot 10^6$.

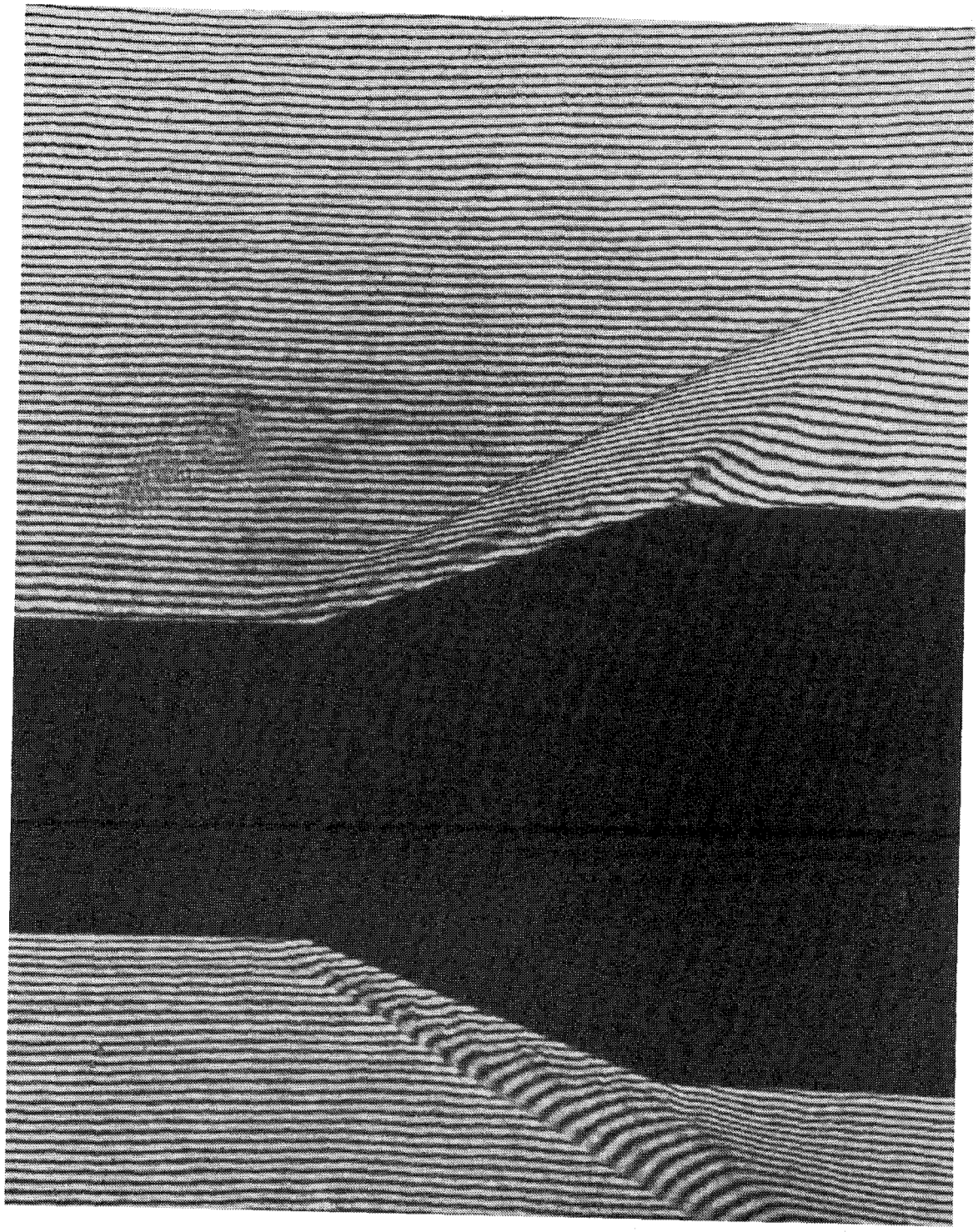

Figure D.12 Plate 572 Horizontal finite-fringe interferogram 20° model, $P_t = 1.7$ atm, $Re_L = 18 \cdot 10^6$.

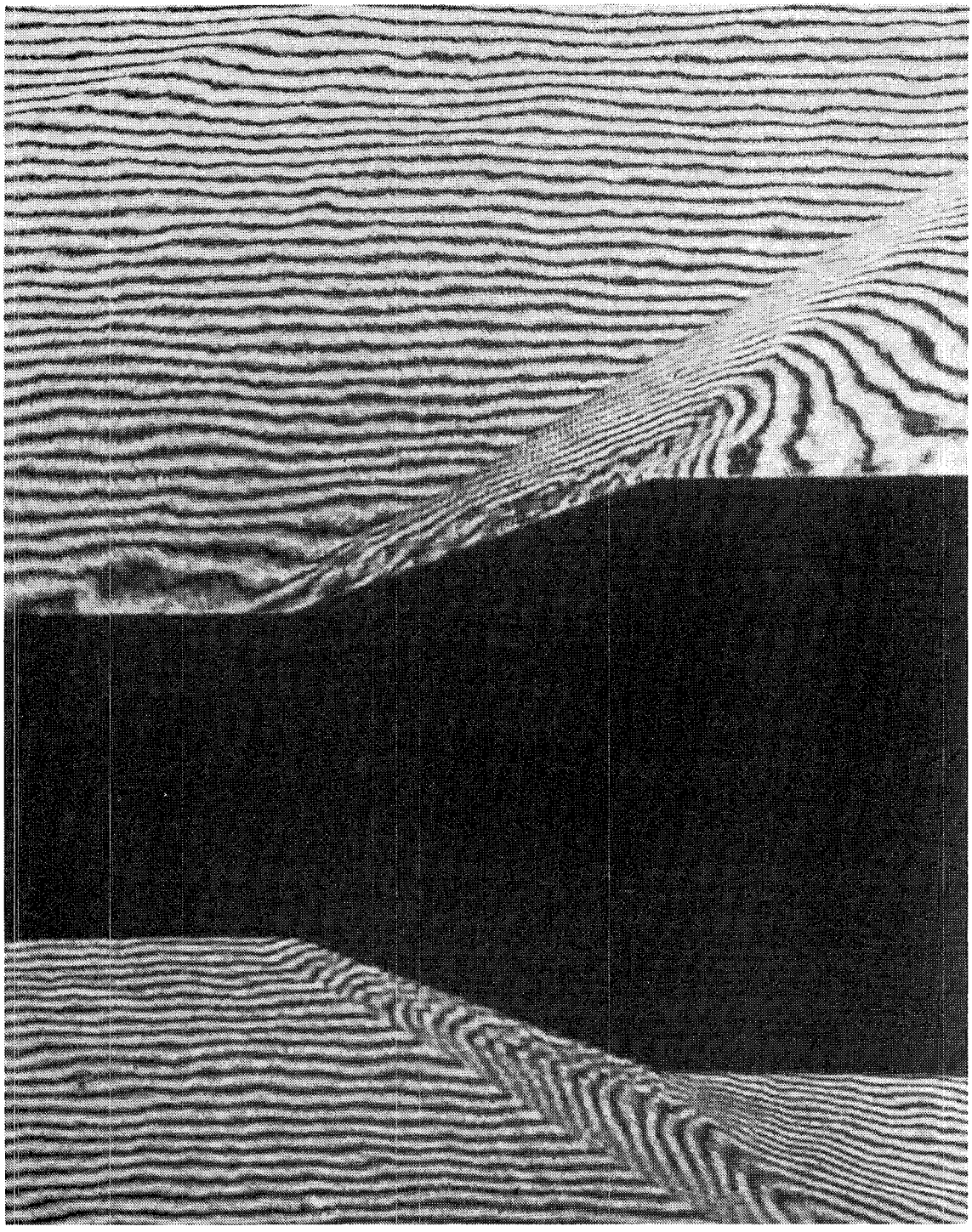

Figure D.13 Plate 565 Horizontal finite-fringe interferogram 20° model, $P_t = 3.4$ atm, $Re_L = 36 \cdot 10^6$.

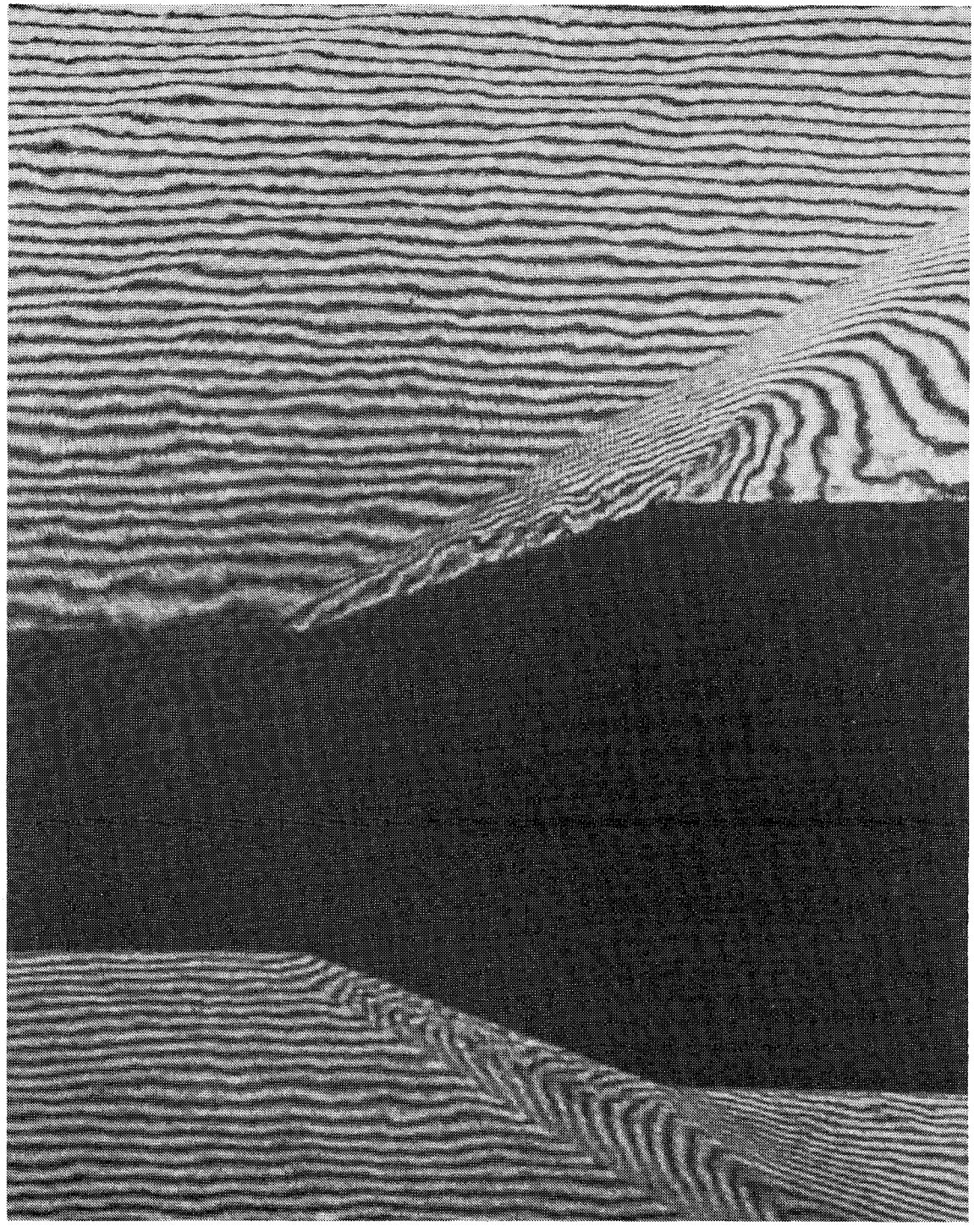

Figure D.14 Plate 566 Horizontal finite-fringe interferogram 20° model, $P_t = 3.4$ atm, $Re_L = 36 \cdot 10^6$.

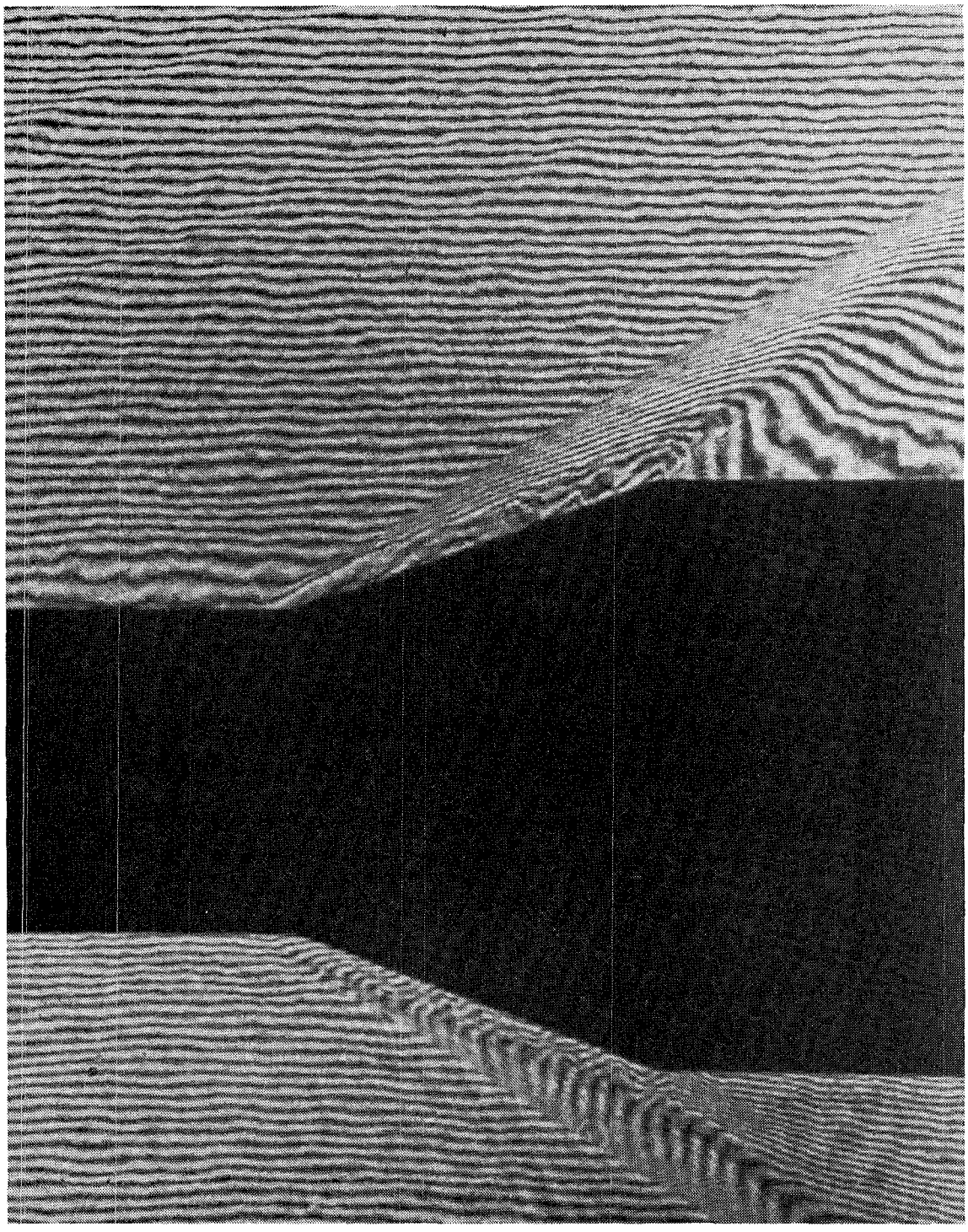

Figure D.15 Plate 575 Horizontal finite-fringe interferogram 20° model, $P_t = 3.4$ atm, $Re_L = 36 \cdot 10^6$.

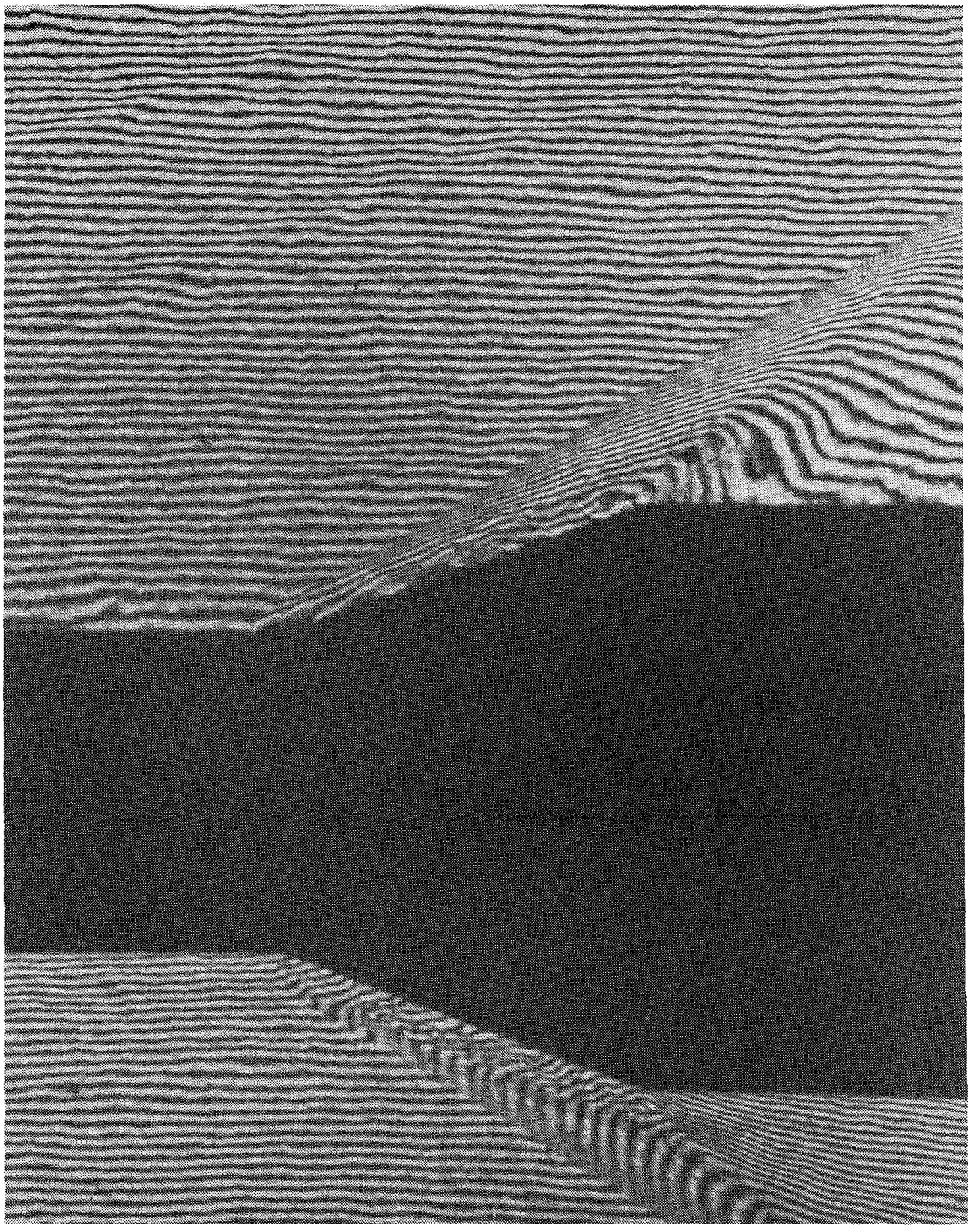

Figure D.16 Plate 576 Horizontal finite-fringe interferogram 20° model, $P_t = 3.4$ atm, $Re_L = 36 \cdot 10^6$.

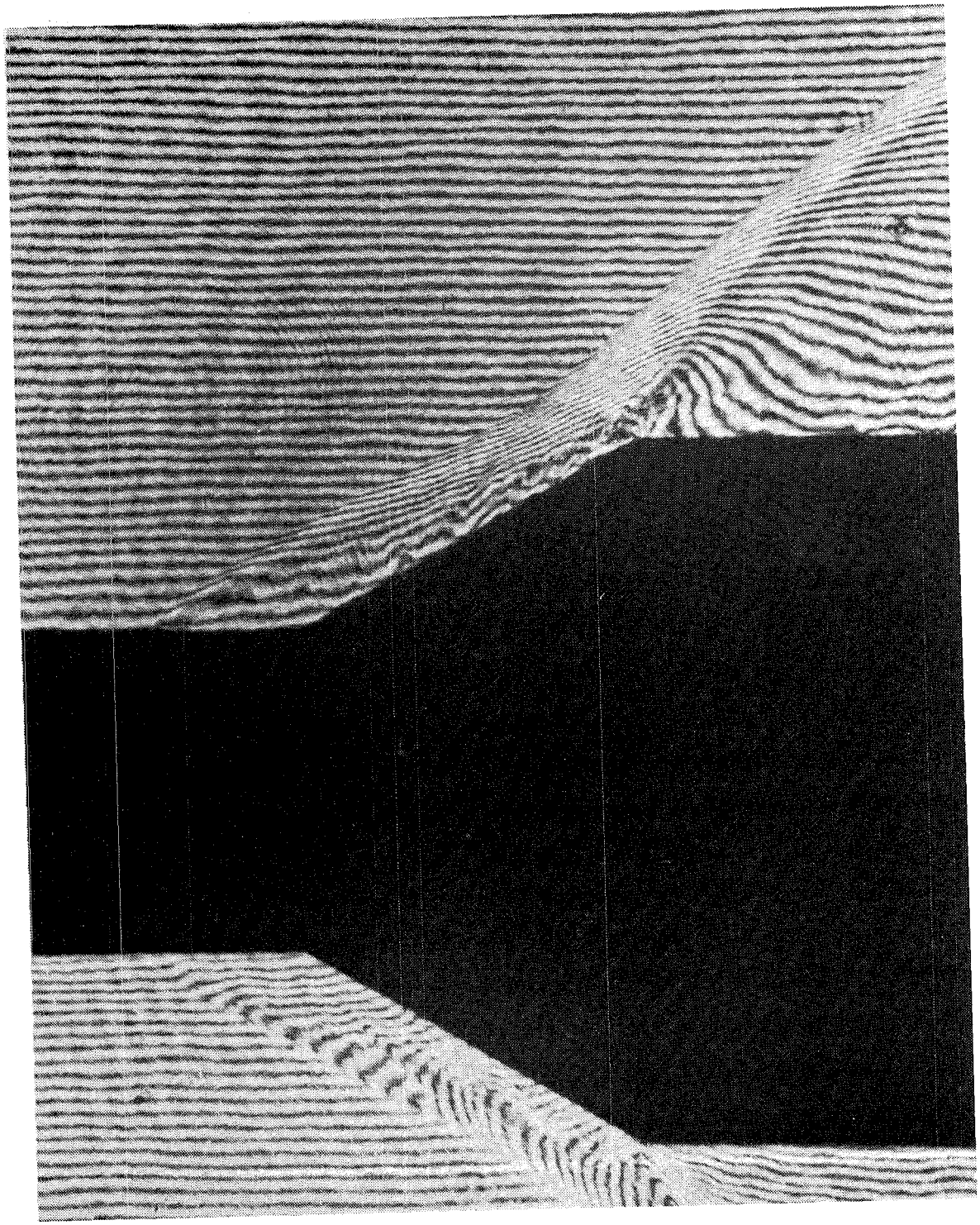

Figure D.17 Plate 342 Horizontal finite-fringe interferogram 30° model, $P_t = 1.7$ atm, $Re_L = 18 \cdot 10^6$.

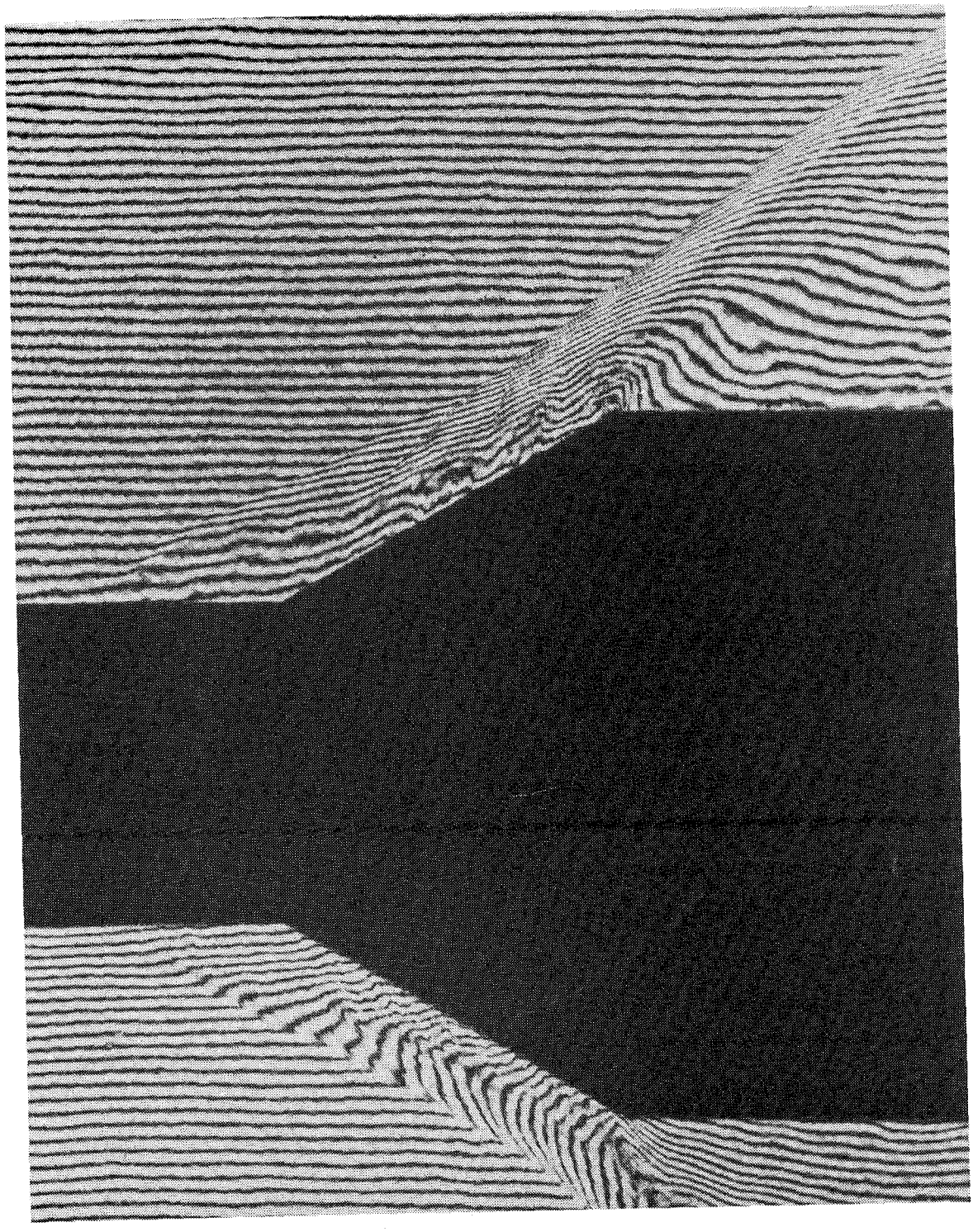

Figure D.18 Plate 366 Horizontal finite-fringe interferogram 30° model, $P_t = 1.7$ atm, $Re_L = 18 \cdot 10^6$.

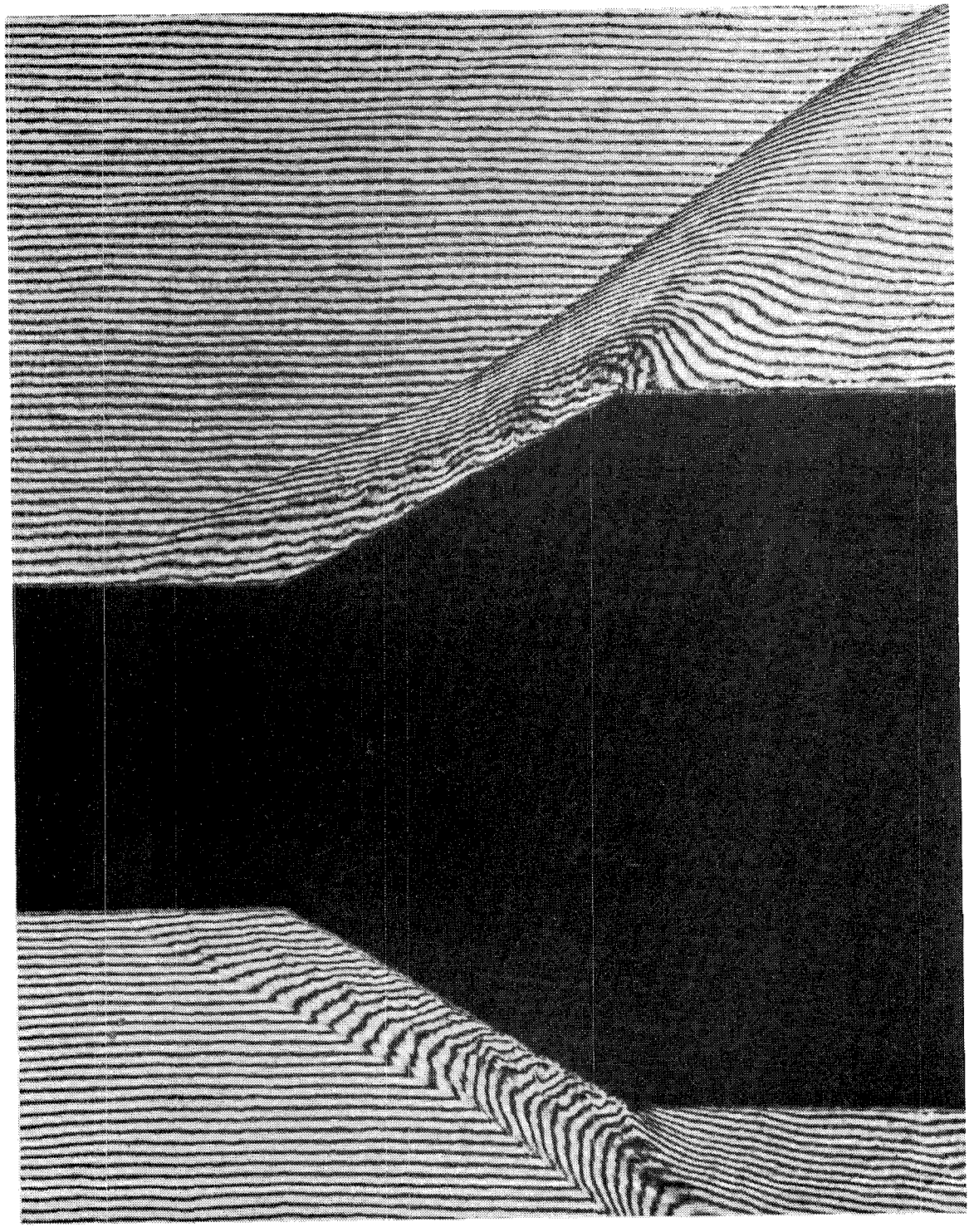

Figure D.19 Plate 368 Horizontal finite-fringe interferogram 30° model, $P_t = 1.7$ atm, $Re_L = 18 \cdot 10^6$.

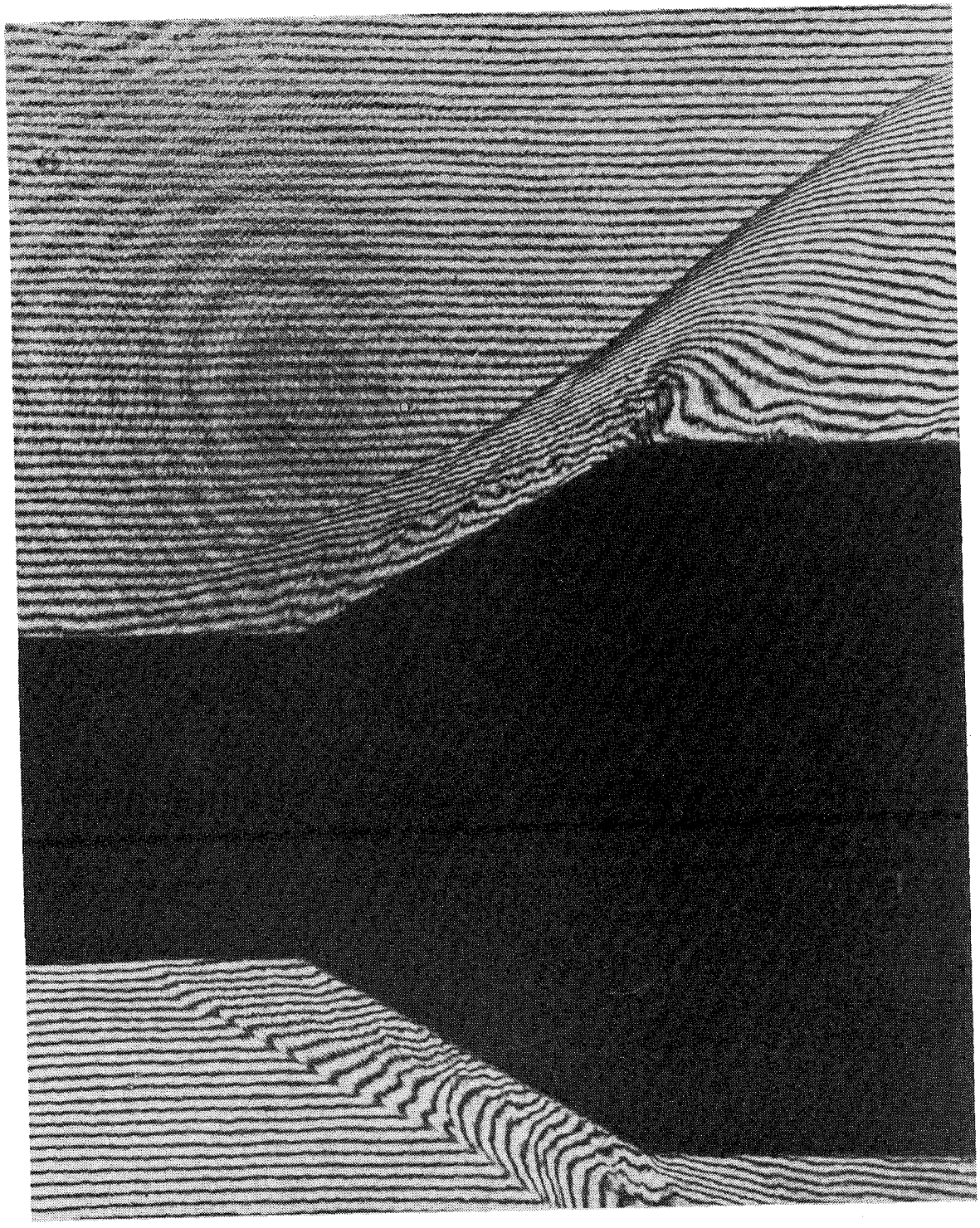

Figure D.20 Plate 377 Horizontal finite-fringe interferogram 30° model, $P_t = 1.7$ atm, $Re_L = 18 \cdot 10^6$.

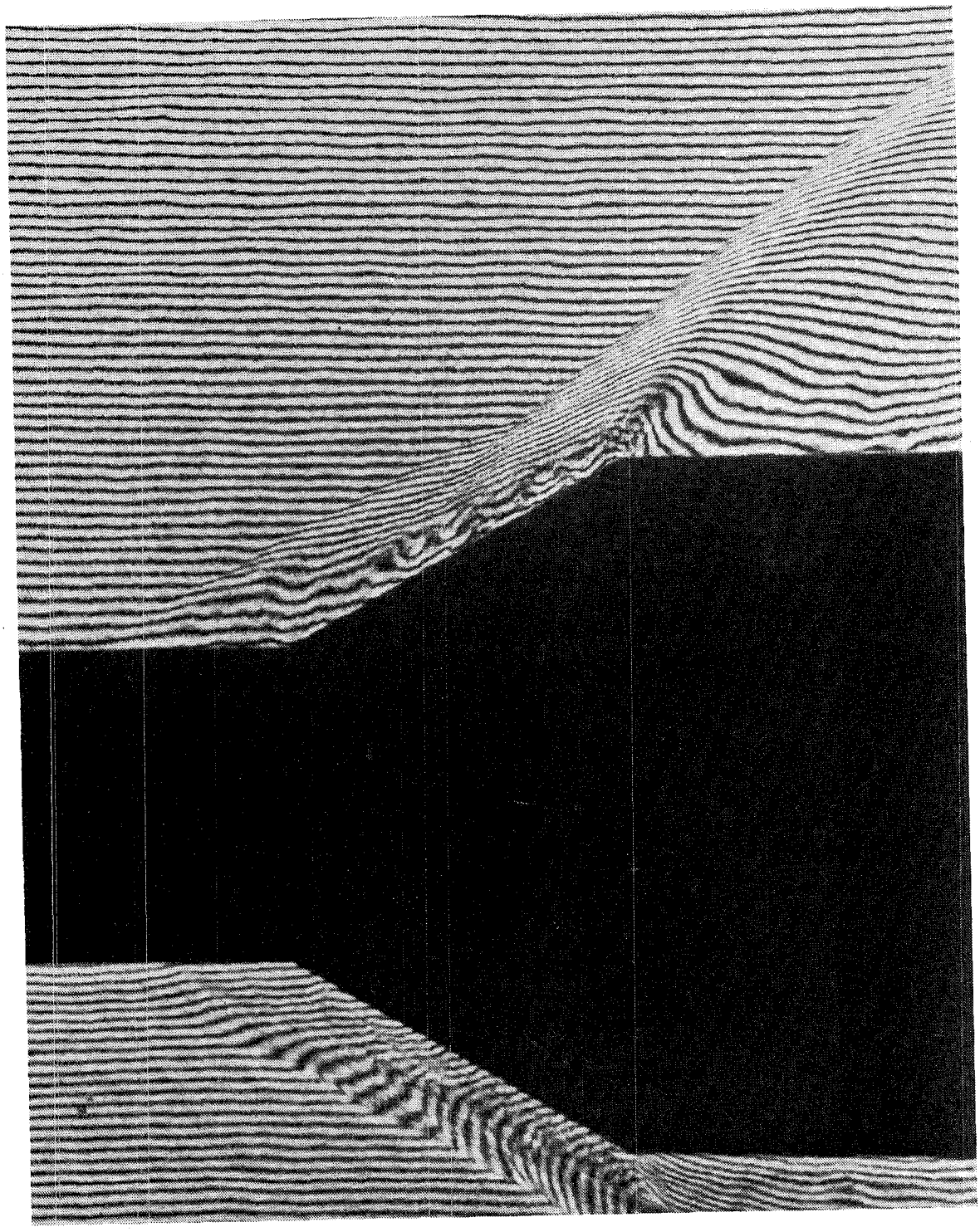

Figure D.21 Plate 555 Horizontal finite-fringe interferogram 30° model, $P_t = 1.7$ atm, $Re_L = 18 \cdot 10^6$.

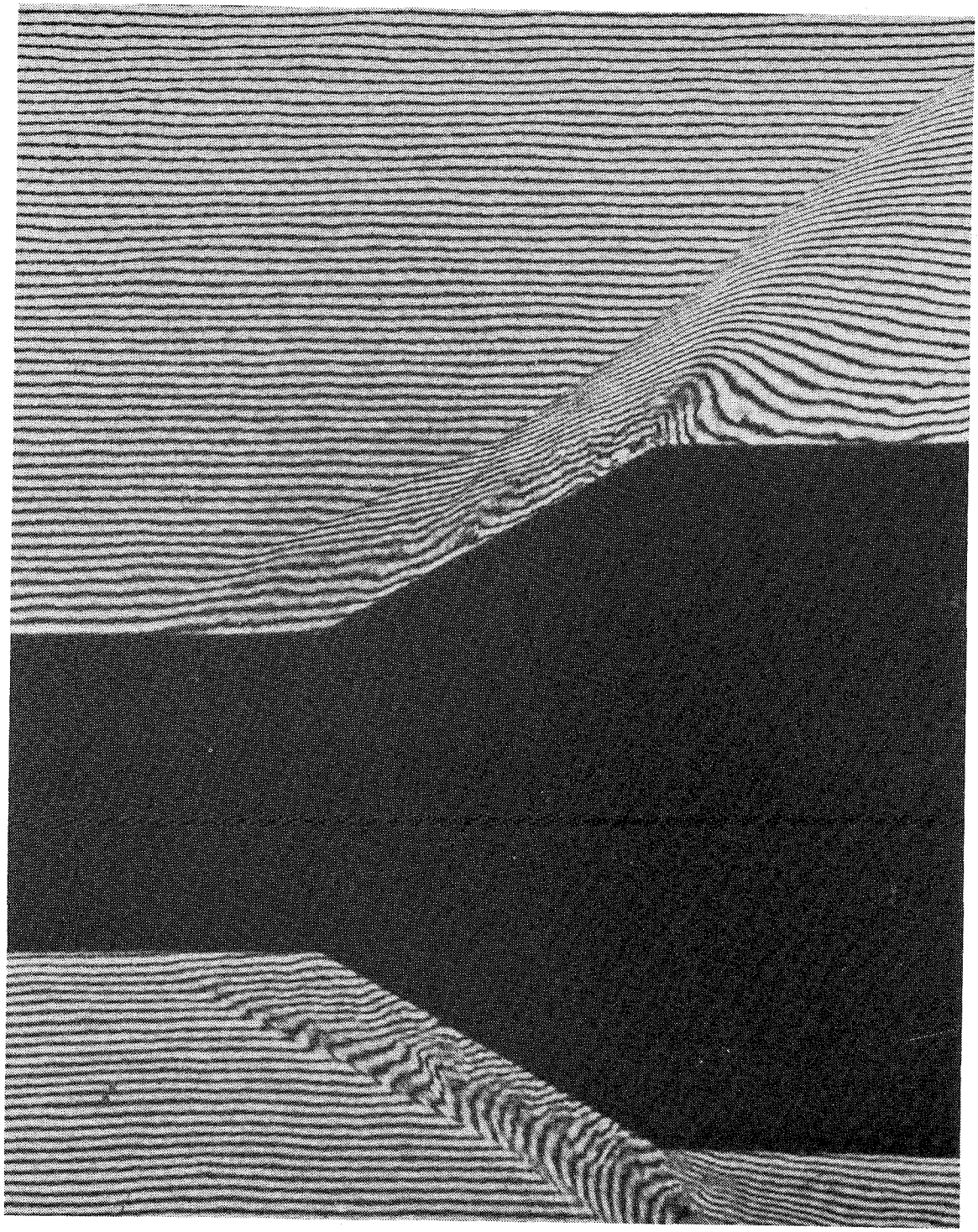

Figure D.22 Plate 556 Horizontal finite-fringe interferogram 30° model, $P_t = 1.7$ atm, $Re_L = 18 \cdot 10^6$.

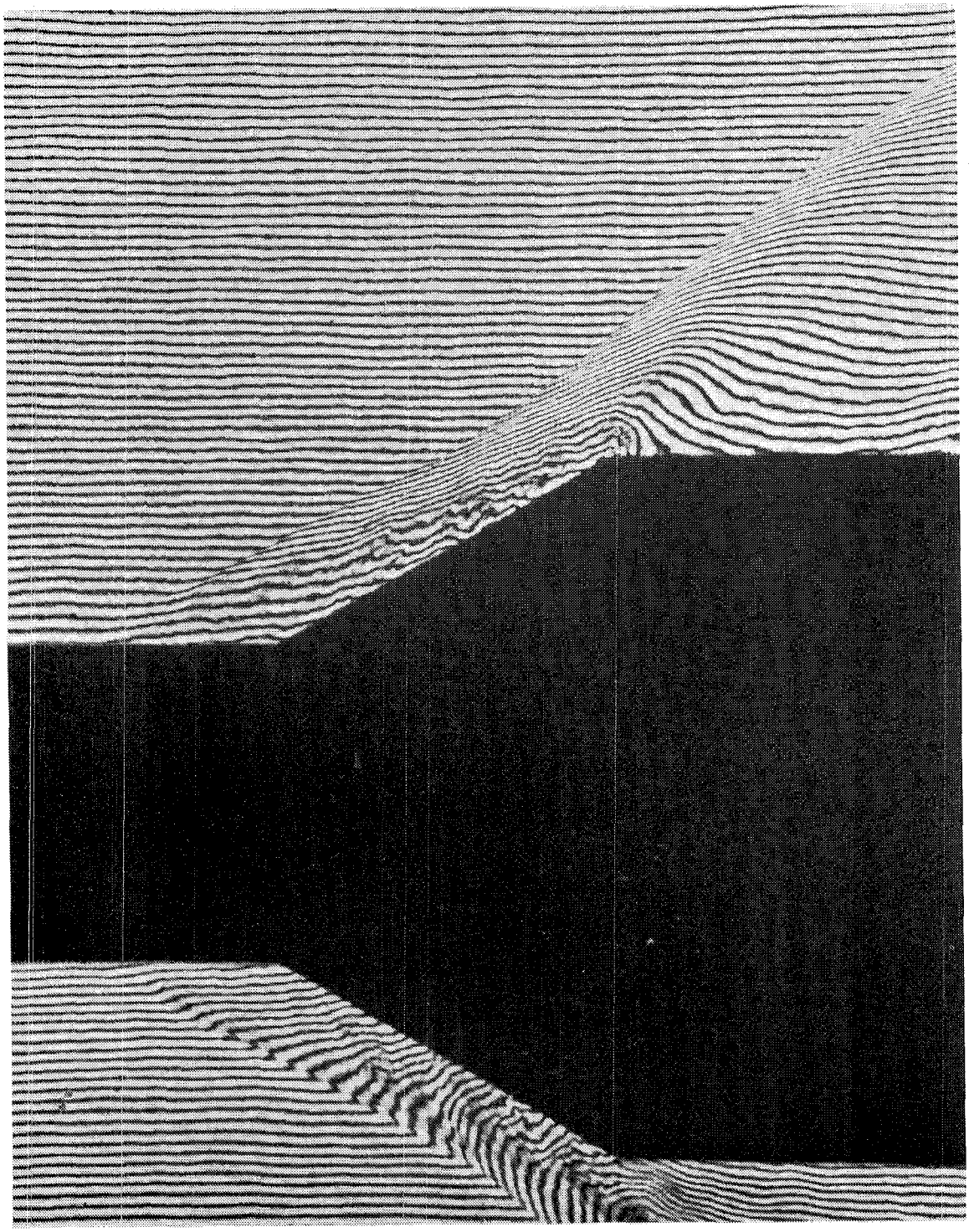

Figure D.23 Plate 557 Horizontal finite-fringe interferogram 30° model, $P_t = 1.7$ atm, $Re_L = 18 \cdot 10^6$.

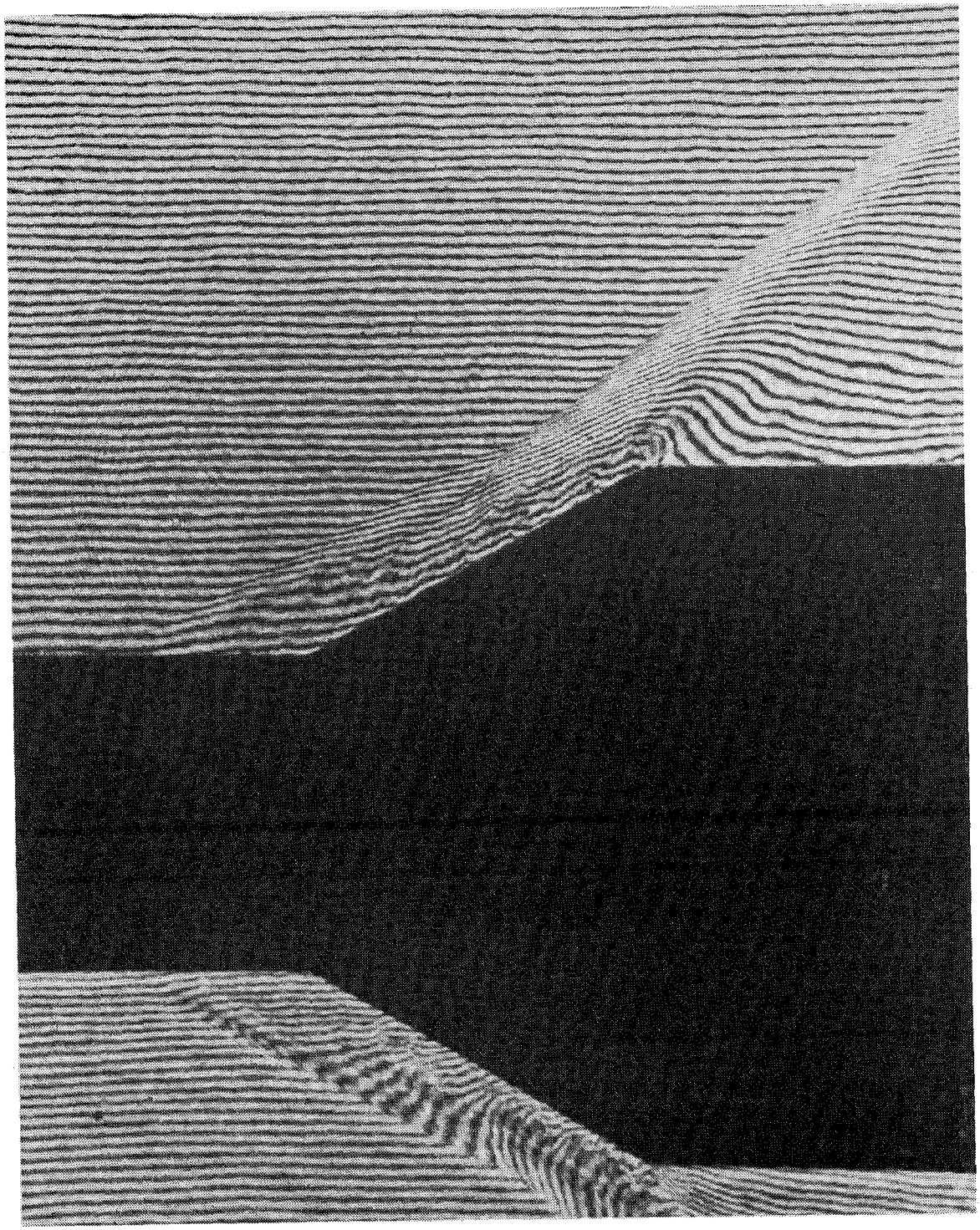

Figure D.24 Plate 558 Horizontal finite-fringe interferogram 30° model, $P_t = 1.7$ atm, $Re_L = 18 \cdot 10^6$.

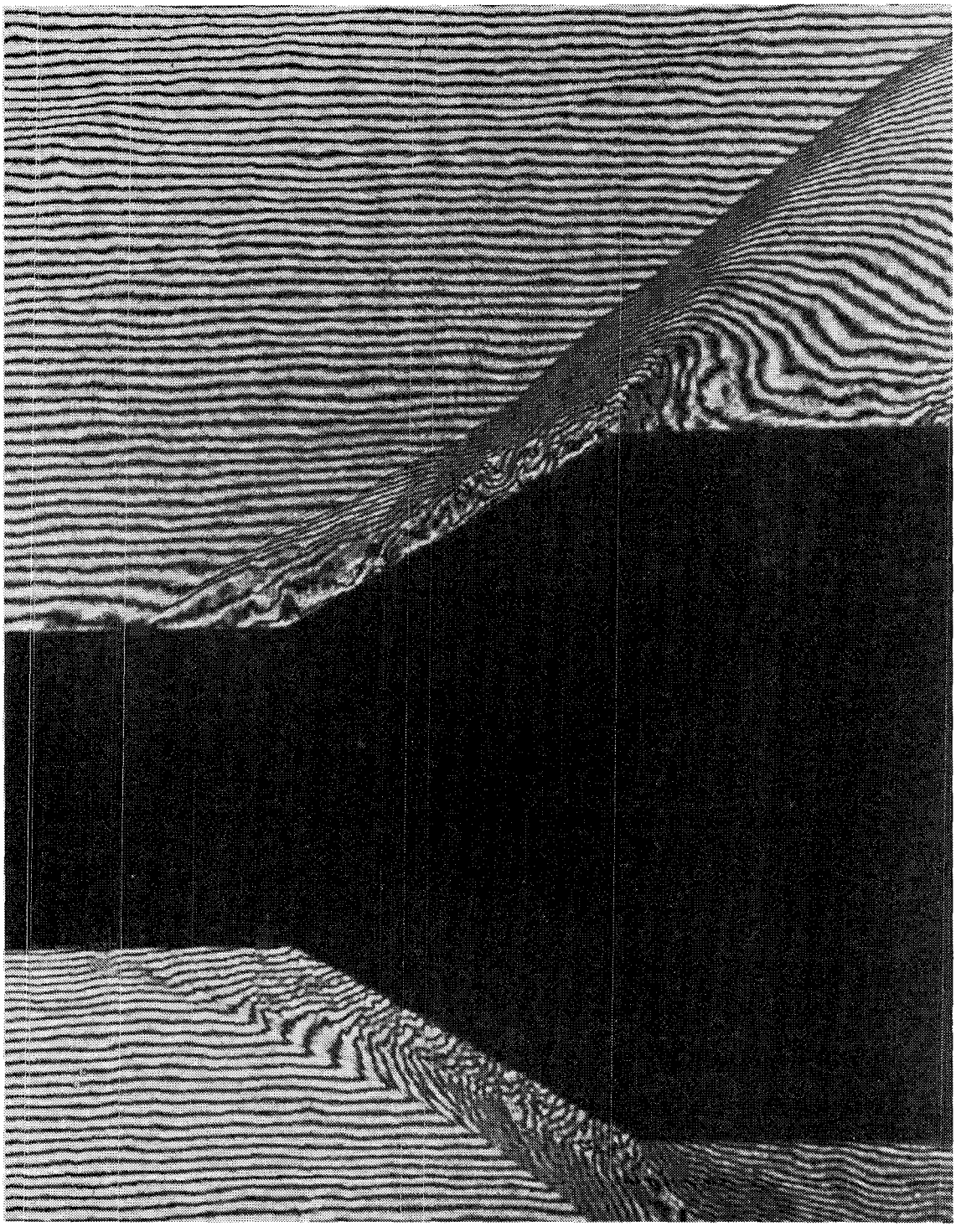

Figure D.25 Plate 551 Horizontal finite-fringe interferogram 30° model, $P_t = 3.4$ atm, $Re_L = 36 \cdot 10^6$.

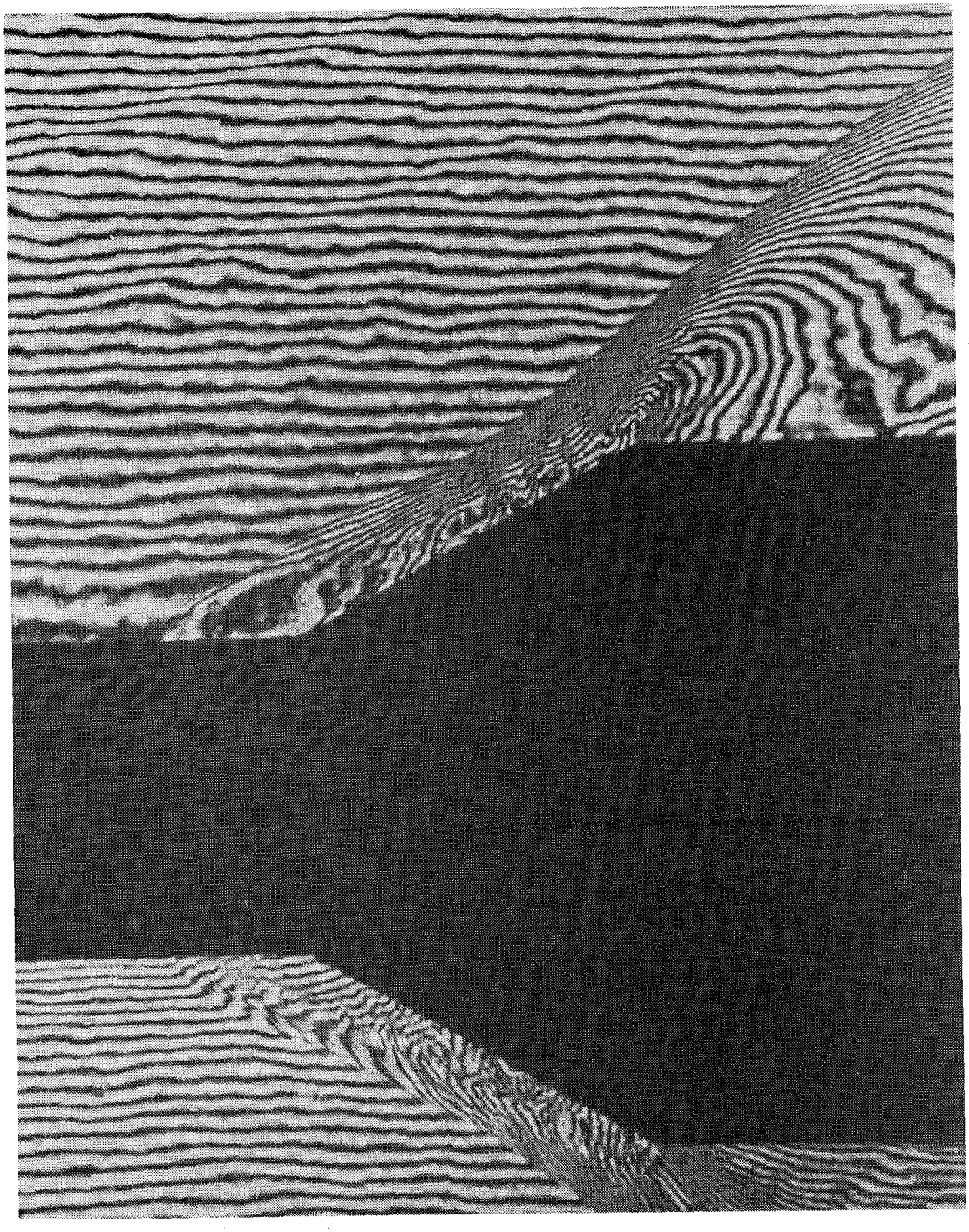

Figure D.26 Plate 552 Horizontal finite-fringe interferogram 30° model, $P_t = 3.4$ atm, $Re_L = 36 \cdot 10^6$.

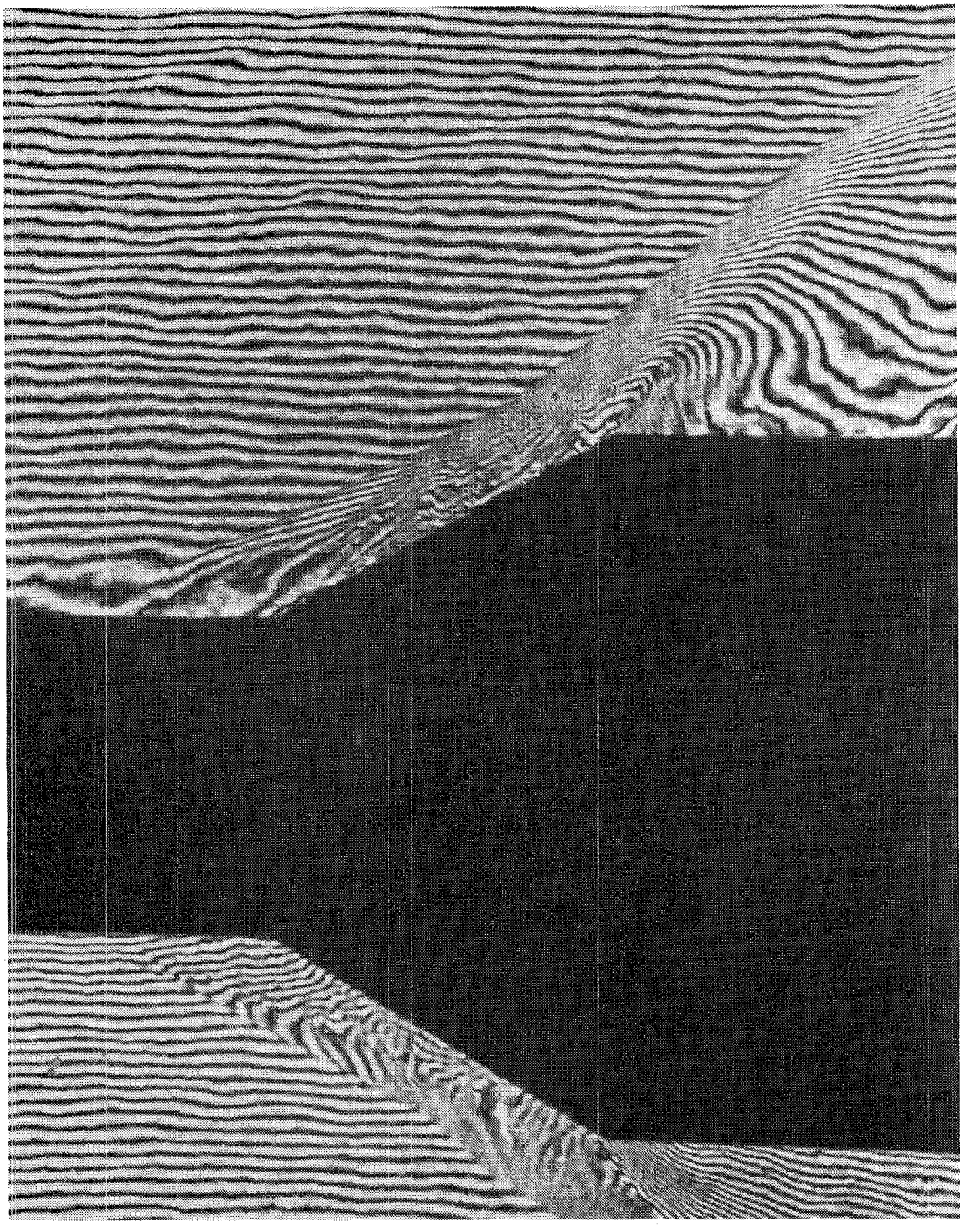

Figure D.27 Plate 561 Horizontal finite-fringe interferogram 30° model, $P_t = 3.4$ atm, $Re_L = 36 \cdot 10^6$.

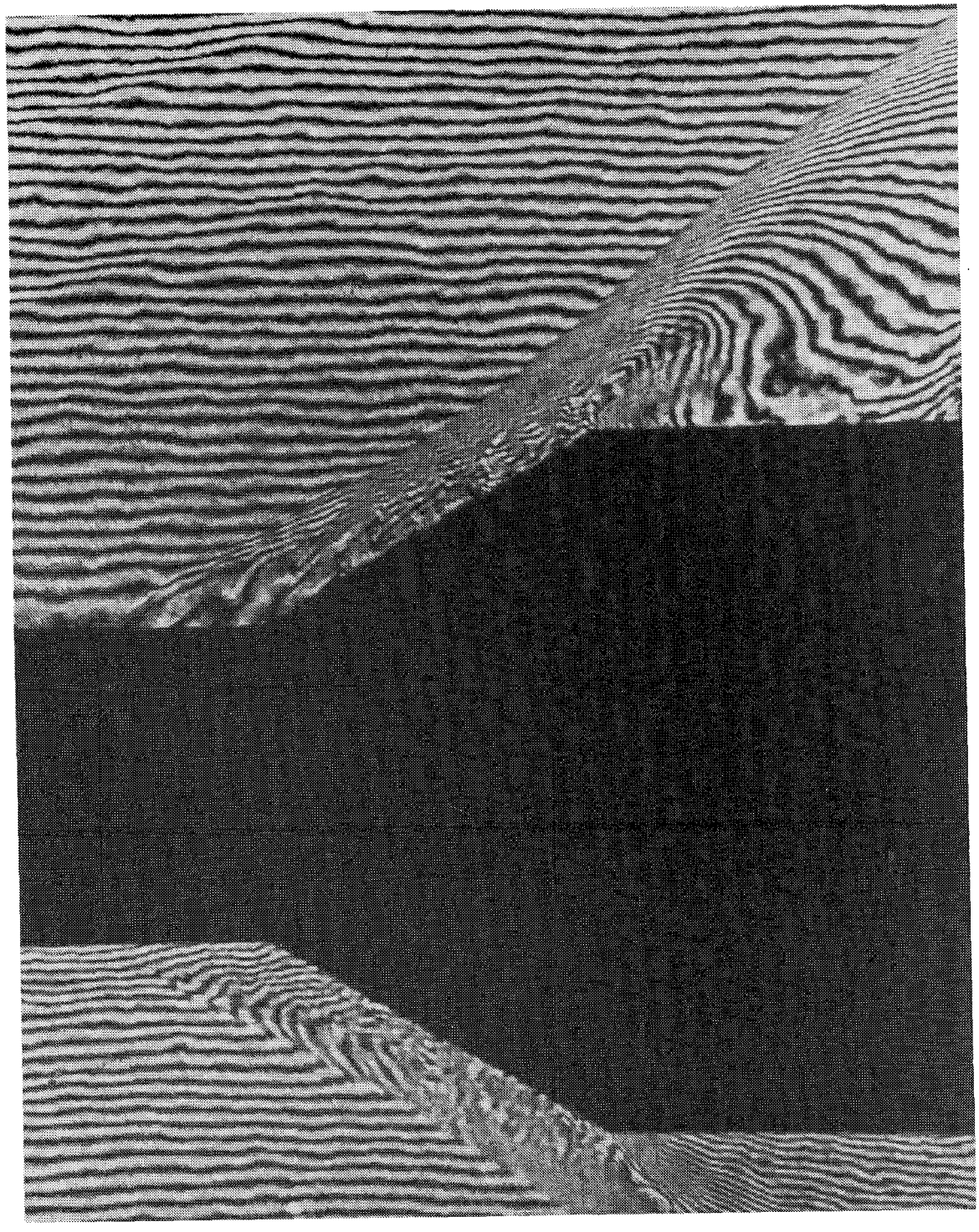

Figure D.28 Plate 562 Horizontal finite-fringe interferogram 30° model, $P_t = 3.4$ atm, $Re_L = 36 \cdot 10^6$.

TABLE D.1 Interferometry Data for 12.5° Model at 1.7 atm Total Pressure

Filename		12D25P.TEX	
Model Cone Angle		12.5 °	
Total Pressure		1.7 atm	
Total Temperature		285.0 °K	
Interferogram profile	1	X Location	-5.010 cm
Interferogram profile	2	X Location	-4.026 cm
Interferogram profile	3	X Location	-3.028 cm
Interferogram profile	4	X Location	-2.007 cm
Interferogram profile	5	X Location	-1.010 cm
Interferogram profile	6	X Location	0.005 cm
Interferogram profile	7	X Location	1.005 cm
Interferogram profile	8	X Location	1.996 cm
Interferogram profile	9	X Location	2.994 cm
Interferogram profile	10	X Location	4.004 cm
Interferogram profile	11	X Location	5.008 cm
Interferogram profile	12	X Location	5.866 cm
Interferogram profile	13	X Location	6.864 cm
Interferogram profile	14	X Location	7.872 cm
Interferogram profile	15	X Location	8.889 cm
Interferogram profile	17	X Location	6.362 cm

Interferogram Profile 1 1 Profile
X Location of Profile -5.01000 cm
Local Shock Angle 0.00000 °
R Location of Shock 0.00000 cm
R Location of Model Surface 2.54000 cm

Approximated and Abel Transformed Data

I	Radius (cm)	Fringe Number	ρ/ρ_t
1	2.542	-0.96268	0.0434626
2	2.567	-0.93164	0.0438851
3	2.591	-0.89905	0.0444680
4	2.616	-0.86515	0.0451994
5	2.640	-0.83011	0.0460679
6	2.664	-0.79414	0.0470623
7	2.689	-0.75742	0.0481716
8	2.713	-0.72014	0.0493853
9	2.738	-0.68248	0.0506931
10	2.762	-0.64460	0.0520851
11	2.787	-0.60668	0.0535514
12	2.811	-0.56886	0.0550824
13	2.836	-0.53130	0.0566691
14	2.860	-0.49415	0.0583024
15	2.884	-0.45754	0.0599736
16	2.909	-0.42162	0.0616739
17	2.933	-0.38652	0.0633951
18	2.958	-0.35234	0.0651288
19	2.982	-0.31922	0.0668673
20	3.007	-0.28726	0.0686027
21	3.031	-0.25656	0.0703271
22	3.056	-0.22724	0.0720332
23	3.080	-0.19937	0.0737131
24	3.104	-0.17304	0.0753597
25	3.129	-0.14834	0.0769653
26	3.153	-0.12534	0.0785229
27	3.178	-0.10411	0.0800245
28	3.202	-0.08471	0.0814622
29	3.227	-0.06721	0.0828285
30	3.251	-0.05164	0.0841141
31	3.276	-0.03805	0.0853097
32	3.300	-0.02650	0.0864043
33	3.324	-0.01699	0.0873851
34	3.349	-0.00957	0.0882348
35	3.373	-0.00426	0.0889288
36	3.398	-0.00107	0.0894246
37	3.422	0.00000	0.0896156
38	3.447	0.00000	0.0896156
39	3.471	0.00000	0.0896156
40	3.496	0.00000	0.0896156
41	3.520	0.00000	0.0896156
42	3.544	0.00000	0.0896156
43	3.569	0.00000	0.0896156
44	3.593	0.00000	0.0896156
45	3.618	0.00000	0.0896156
46	3.642	0.00000	0.0896156
47	3.667	0.00000	0.0896156
48	3.691	0.00000	0.0896156
49	3.716	0.00000	0.0896156
50	3.740	0.00000	0.0896156

Interferogram Profile 2 1 Profile
X Location of Profile -4.02600 cm
Local Shock Angle 0.00000 °
R Location of Shock 0.00000 cm
R Location of Model Surface 2.54000 cm

Approximated and Abel Transformed Data

I	Radius (cm)	Fringe Number	ρ/ρ_t
1	2.542	-1.00903	0.0407375
2	2.567	-0.97517	0.0413065
3	2.591	-0.93989	0.0420305
4	2.616	-0.90338	0.0428979
5	2.640	-0.86585	0.0438975
6	2.664	-0.82749	0.0450178
7	2.689	-0.78849	0.0462487
8	2.713	-0.74902	0.0475794
9	2.738	-0.70926	0.0489997
10	2.762	-0.66938	0.0505001
11	2.787	-0.62953	0.0520704
12	2.811	-0.58989	0.0537018
13	2.836	-0.55059	0.0553847
14	2.860	-0.51179	0.0571105
15	2.884	-0.47362	0.0588705
16	2.909	-0.43621	0.0606558
17	2.933	-0.39969	0.0624588
18	2.958	-0.36419	0.0642709
19	2.982	-0.32982	0.0660844
20	3.007	-0.29668	0.0678913
21	3.031	-0.26488	0.0696842
22	3.056	-0.23452	0.0714556
23	3.080	-0.20570	0.0731976
24	3.104	-0.17848	0.0749033
25	3.129	-0.15297	0.0765650
26	3.153	-0.12922	0.0781754
27	3.178	-0.10731	0.0797269
28	3.202	-0.08730	0.0812114
29	3.227	-0.06925	0.0826211
30	3.251	-0.05320	0.0839472
31	3.276	-0.03920	0.0851797
32	3.300	-0.02729	0.0863080
33	3.324	-0.01750	0.0873182
34	3.349	-0.00986	0.0881936
35	3.373	-0.00439	0.0889085
36	3.398	-0.00110	0.0894189
37	3.422	0.00000	0.0896156
38	3.447	0.00000	0.0896156
39	3.471	0.00000	0.0896156
40	3.496	0.00000	0.0896156
41	3.520	0.00000	0.0896156
42	3.544	0.00000	0.0896156
43	3.569	0.00000	0.0896156
44	3.593	0.00000	0.0896156
45	3.618	0.00000	0.0896156
46	3.642	0.00000	0.0896156
47	3.667	0.00000	0.0896156
48	3.691	0.00000	0.0896156
49	3.716	0.00000	0.0896156
50	3.740	0.00000	0.0896156

Interferogram Profile 3	1 Profile
X Location of Profile	-3.02800 cm
Local Shock Angle	0.00000 °
R Location of Shock	0.00000 cm
R Location of Model Surface	2.54000 cm

Approximated and Abel Transformed Data

I	Radius (cm)	Fringe Number	ρ/ρ_t
1	2.542	-0.80616	0.0515752
2	2.567	-0.78176	0.0517765
3	2.591	-0.75584	0.0521278
4	2.616	-0.72861	0.0526183
5	2.640	-0.70025	0.0532378
6	2.664	-0.67092	0.0539757
7	2.689	-0.64081	0.0548222
8	2.713	-0.61007	0.0557678
9	2.738	-0.57888	0.0568030
10	2.762	-0.54738	0.0579187
11	2.787	-0.51572	0.0591059
12	2.811	-0.48405	0.0603560
13	2.836	-0.45252	0.0616607
14	2.860	-0.42124	0.0630117
15	2.884	-0.39036	0.0644010
16	2.909	-0.35999	0.0658208
17	2.933	-0.33024	0.0672635
18	2.958	-0.30124	0.0687218
19	2.982	-0.27309	0.0701882
20	3.007	-0.24589	0.0716558
21	3.031	-0.21973	0.0731174
22	3.056	-0.19471	0.0745665
23	3.080	-0.17090	0.0759960
24	3.104	-0.14840	0.0773993
25	3.129	-0.12726	0.0787696
26	3.153	-0.10757	0.0801006
27	3.178	-0.08938	0.0813852
28	3.202	-0.07274	0.0826166
29	3.227	-0.05772	0.0837874
30	3.251	-0.04436	0.0848900
31	3.276	-0.03270	0.0859162
32	3.300	-0.02277	0.0868560
33	3.324	-0.01461	0.0876986
34	3.349	-0.00823	0.0884286
35	3.373	-0.00366	0.0890253
36	3.398	-0.00092	0.0894514
37	3.422	0.00000	0.0896156
38	3.447	0.00000	0.0896156
39	3.471	0.00000	0.0896156
40	3.496	0.00000	0.0896156
41	3.520	0.00000	0.0896156
42	3.544	0.00000	0.0896156
43	3.569	0.00000	0.0896156
44	3.593	0.00000	0.0896156
45	3.618	0.00000	0.0896156
46	3.642	0.00000	0.0896156
47	3.667	0.00000	0.0896156
48	3.691	0.00000	0.0896156
49	3.716	0.00000	0.0896156
50	3.740	0.00000	0.0896156

Interferogram Profile 4 1 Profile
X Location of Profile -2.00700 cm
Local Shock Angle 0.00000 °
R Location of Shock 0.00000 cm
R Location of Model Surface 2.54000 cm

Approximated and Abel Transformed Data

I	Radius (cm)	Fringe Number	ρ/ρ_t
1	2.542	-0.97866	0.0461130
2	2.567	-0.95509	0.0458529
3	2.591	-0.92908	0.0458131
4	2.616	-0.90087	0.0459787
5	2.640	-0.87073	0.0463354
6	2.664	-0.83889	0.0468695
7	2.689	-0.80559	0.0475672
8	2.713	-0.77106	0.0484154
9	2.738	-0.73553	0.0494016
10	2.762	-0.69919	0.0505128
11	2.787	-0.66227	0.0517373
12	2.811	-0.62496	0.0530633
13	2.836	-0.58745	0.0544791
14	2.860	-0.54993	0.0559738
15	2.884	-0.51258	0.0575365
16	2.909	-0.47556	0.0591563
17	2.933	-0.43905	0.0608235
18	2.958	-0.40319	0.0625274
19	2.982	-0.36814	0.0642588
20	3.007	-0.33403	0.0660075
21	3.031	-0.30101	0.0677646
22	3.056	-0.26919	0.0695209
23	3.080	-0.23871	0.0712674
24	3.104	-0.20966	0.0729947
25	3.129	-0.18216	0.0746948
26	3.153	-0.15630	0.0763582
27	3.178	-0.13218	0.0779772
28	3.202	-0.10987	0.0795421
29	3.227	-0.08946	0.0810444
30	3.251	-0.07102	0.0824746
31	3.276	-0.05459	0.0838232
32	3.300	-0.04025	0.0850793
33	3.324	-0.02804	0.0862307
34	3.349	-0.01799	0.0872635
35	3.373	-0.01014	0.0881591
36	3.398	-0.00451	0.0888910
37	3.422	-0.00113	0.0894140
38	3.447	0.00000	0.0896156
39	3.471	0.00000	0.0896156
40	3.496	0.00000	0.0896156
41	3.520	0.00000	0.0896156
42	3.544	0.00000	0.0896156
43	3.569	0.00000	0.0896156
44	3.593	0.00000	0.0896156
45	3.618	0.00000	0.0896156
46	3.642	0.00000	0.0896156
47	3.667	0.00000	0.0896156
48	3.691	0.00000	0.0896156
49	3.716	0.00000	0.0896156
50	3.740	0.00000	0.0896156

Interferogram Profile 5 1 Profile
X Location of Profile -1.01000 cm
Local Shock Angle 0.00000 °
R Location of Shock 0.00000 cm
R Location of Model Surface 2.54000 cm

Approximated and Abel Transformed Data

I	Radius (cm)	Fringe Number	ρ/ρ_t
1	2.542	-0.92514	0.0461582
2	2.567	-0.89608	0.0466106
3	2.591	-0.86580	0.0471904
4	2.616	-0.83445	0.0478886
5	2.640	-0.80220	0.0486963
6	2.664	-0.76920	0.0496048
7	2.689	-0.73560	0.0506058
8	2.713	-0.70155	0.0516910
9	2.738	-0.66717	0.0528528
10	2.762	-0.63261	0.0540833
11	2.787	-0.59800	0.0553748
12	2.811	-0.56347	0.0567201
13	2.836	-0.52913	0.0581121
14	2.860	-0.49510	0.0595437
15	2.884	-0.46151	0.0610082
16	2.909	-0.42845	0.0624990
17	2.933	-0.39603	0.0640095
18	2.958	-0.36435	0.0655332
19	2.982	-0.33351	0.0670644
20	3.007	-0.30360	0.0685964
21	3.031	-0.27470	0.0701238
22	3.056	-0.24690	0.0716403
23	3.080	-0.22027	0.0731406
24	3.104	-0.19488	0.0746186
25	3.129	-0.17082	0.0760687
26	3.153	-0.14813	0.0774854
27	3.178	-0.12688	0.0788631
28	3.202	-0.10713	0.0801957
29	3.227	-0.08893	0.0814777
30	3.251	-0.07232	0.0827029
31	3.276	-0.05734	0.0838648
32	3.300	-0.04404	0.0849568
33	3.324	-0.03244	0.0859709
34	3.349	-0.02258	0.0868986
35	3.373	-0.01448	0.0877289
36	3.398	-0.00815	0.0884479
37	3.422	-0.00363	0.0890349
38	3.447	-0.00091	0.0894542
39	3.471	0.00000	0.0896156
40	3.496	0.00000	0.0896156
41	3.520	0.00000	0.0896156
42	3.544	0.00000	0.0896156
43	3.569	0.00000	0.0896156
44	3.593	0.00000	0.0896156
45	3.618	0.00000	0.0896156
46	3.642	0.00000	0.0896156
47	3.667	0.00000	0.0896156
48	3.691	0.00000	0.0896156
49	3.716	0.00000	0.0896156
50	3.740	0.00000	0.0896156

Interferogram Profile 6 1 Profile
X Location of Profile 0.00500 cm
Local Shock Angle 0.00000 °
R Location of Shock 0.00000 cm
R Location of Model Surface 2.54100 cm

Approximated and Abel Transformed Data

I	Radius (cm)	Fringe Number	ρ/ρ_t
1	2.542	-0.90121	0.0472848
2	2.567	-0.87224	0.0478388
3	2.591	-0.84232	0.0484967
4	2.615	-0.81157	0.0492513
5	2.640	-0.78014	0.0500952
6	2.664	-0.74814	0.0510214
7	2.689	-0.71571	0.0520229
8	2.713	-0.68296	0.0530930
9	2.738	-0.65001	0.0542252
10	2.762	-0.61697	0.0554132
11	2.787	-0.58396	0.0566505
12	2.811	-0.55107	0.0579314
13	2.835	-0.51842	0.0592497
14	2.860	-0.48609	0.0606000
15	2.884	-0.45419	0.0619762
16	2.909	-0.42281	0.0633733
17	2.933	-0.39203	0.0647855
18	2.958	-0.36195	0.0662079
19	2.982	-0.33263	0.0676350
20	3.007	-0.30416	0.0690621
21	3.031	-0.27662	0.0704843
22	3.055	-0.25006	0.0718963
23	3.080	-0.22456	0.0732937
24	3.104	-0.20019	0.0746716
25	3.129	-0.17699	0.0760255
26	3.153	-0.15503	0.0773504
27	3.178	-0.13436	0.0786421
28	3.202	-0.11502	0.0798955
29	3.226	-0.09707	0.0811058
30	3.251	-0.08053	0.0822683
31	3.275	-0.06546	0.0833778
32	3.300	-0.05189	0.0844287
33	3.324	-0.03984	0.0854153
34	3.349	-0.02934	0.0863307
35	3.373	-0.02041	0.0871674
36	3.398	-0.01309	0.0879161
37	3.422	-0.00737	0.0885638
38	3.446	-0.00328	0.0890927
39	3.471	-0.00082	0.0894701
40	3.495	0.00000	0.0896156
41	3.520	0.00000	0.0896156
42	3.544	0.00000	0.0896156
43	3.569	0.00000	0.0896156
44	3.593	0.00000	0.0896156
45	3.618	0.00000	0.0896156
46	3.642	0.00000	0.0896156
47	3.666	0.00000	0.0896156
48	3.691	0.00000	0.0896156
49	3.715	0.00000	0.0896156
50	3.740	0.00000	0.0896156

Interferogram Profile 7	3 Profiles averaged	
X Location of Profile	1.00500 cm	St. Dev.= 0.00600 cm
Local Shock Angle	26.16700 °	St. Dev.= 0.28820 °
R Location of Shock	3.47500 cm	St. Dev.= 0.00048 cm
R Location of Model Surface	2.76300 cm	St. Dev.= 0.00002 cm

Approximated and Abel Transformed Data

I	Radius (cm)	Fringe Number	ρ/ρ_t	St. Dev. ρ/ρ_t
1	2.765	0.06978	0.0791830	0.0097372
2	2.785	0.09037	0.0808585	0.0090188
3	2.804	0.10850	0.0822735	0.0084304
4	2.823	0.12466	0.0834716	0.0078660
5	2.843	0.13925	0.0844941	0.0072905
6	2.862	0.15268	0.0853796	0.0067216
7	2.882	0.16527	0.0861644	0.0062130
8	2.901	0.17730	0.0868822	0.0058371
9	2.921	0.18902	0.0875641	0.0056603
10	2.940	0.20061	0.0882386	0.0057113
11	2.960	0.21223	0.0889315	0.0059630
12	2.979	0.22397	0.0896658	0.0063460
13	2.999	0.23589	0.0904618	0.0067772
14	3.018	0.24799	0.0913363	0.0071811
15	3.038	0.26023	0.0923038	0.0074995
16	3.057	0.27253	0.0933749	0.0076906
17	3.076	0.28474	0.0945568	0.0077307
18	3.096	0.29670	0.0958532	0.0076142
19	3.115	0.30816	0.0972636	0.0073568
20	3.135	0.31886	0.0987832	0.0070027
21	3.154	0.32848	0.1004021	0.0066344
22	3.174	0.33664	0.1021051	0.0063807
23	3.193	0.34293	0.1038705	0.0064003
24	3.213	0.34690	0.1056693	0.0068210
25	3.232	0.34802	0.1074633	0.0076632
26	3.252	0.34575	0.1092031	0.0088323
27	3.271	0.33949	0.1108251	0.0101702
28	3.291	0.32858	0.1122453	0.0114914
29	3.310	0.31234	0.1133510	0.0125840
30	3.329	0.29001	0.1139837	0.0131852
31	3.349	0.26081	0.1139024	0.0129383
32	3.369	0.22391	0.1126942	0.0113352
33	3.388	0.17842	0.1094738	0.0080689
34	3.408	0.12341	0.1013025	0.0124308
35	3.427	0.10802	0.1009361	0.0120950
36	3.446	0.09126	0.1005384	0.0118156
37	3.466	0.07967	0.1001517	0.0116953
38	3.486	0.06769	0.0996701	0.0116300
39	3.505	0.05532	0.0990425	0.0116685
40	3.524	0.04255	0.0981424	0.0119425
41	3.544	0.02940	0.0964844	0.0130231
42	3.563	0.00000	0.0896156	0.0000000
43	3.583	0.00000	0.0896156	0.0000000
44	3.602	0.00000	0.0896156	0.0000000
45	3.622	0.00000	0.0896156	0.0000000
46	3.641	0.00000	0.0896156	0.0000000
47	3.661	0.00000	0.0896156	0.0000000
48	3.680	0.00000	0.0896156	0.0000000
49	3.700	0.00000	0.0896156	0.0000000
50	3.719	0.00000	0.0896156	0.0000000

Interferogram Profile 8	4 Profiles averaged	
X Location of Profile	1.99600 cm	St. Dev.= 0.01000 cm
Local Shock Angle	26.25008 °	St. Dev.= 0.28820 °
R Location of Shock	4.00000 cm	St. Dev.= 0.00041 cm
R Location of Model Surface	2.98300 cm	St. Dev.= 0.00002 cm

Approximated and Abel Transformed Data

I	Radius (cm)	Fringe Number	ρ/ρ_t	St. Dev. ρ/ρ_t
1	2.986	0.43653	0.0829595	0.0211002
2	3.011	0.46659	0.0851271	0.0185750
3	3.036	0.49343	0.0870270	0.0164534
4	3.060	0.51753	0.0886972	0.0146794
5	3.085	0.53935	0.0901740	0.0131974
6	3.110	0.55928	0.0914916	0.0119540
7	3.135	0.57768	0.0926822	0.0108999
8	3.160	0.59487	0.0937761	0.0099916
9	3.184	0.61112	0.0948017	0.0091928
10	3.209	0.62666	0.0957849	0.0084742
11	3.234	0.64167	0.0967502	0.0078137
12	3.259	0.65632	0.0977196	0.0071949
13	3.284	0.67070	0.0987130	0.0066058
14	3.309	0.68487	0.0997483	0.0060380
15	3.334	0.69885	0.1008411	0.0054850
16	3.359	0.71262	0.1020047	0.0049418
17	3.384	0.72610	0.1032499	0.0044047
18	3.408	0.73919	0.1045853	0.0038718
19	3.433	0.75174	0.1060167	0.0033449
20	3.458	0.76355	0.1075473	0.0028349
21	3.483	0.77439	0.1091770	0.0023711
22	3.508	0.78397	0.1109034	0.0020218
23	3.533	0.79197	0.1127198	0.0019064
24	3.557	0.79803	0.1146166	0.0021255
25	3.582	0.80174	0.1165797	0.0026541
26	3.607	0.80264	0.1185909	0.0033984
27	3.632	0.80026	0.1206264	0.0042863
28	3.657	0.79404	0.1226569	0.0052747
29	3.681	0.78342	0.1246466	0.0063346
30	3.707	0.76776	0.1265508	0.0074402
31	3.731	0.74642	0.1283150	0.0085658
32	3.756	0.71868	0.1298724	0.0096805
33	3.781	0.68380	0.1311400	0.0107478
34	3.806	0.64097	0.1320118	0.0117219
35	3.831	0.58937	0.1323514	0.0125460
36	3.855	0.52814	0.1319745	0.0131505
37	3.880	0.45632	0.1306227	0.0134542
38	3.905	0.37299	0.1279066	0.0133792
39	3.930	0.27713	0.1232237	0.0129458
40	3.955	0.16768	0.1166872	0.0128087
41	3.980	0.07969	0.1063643	0.0192180
42	4.005	0.00000	0.0896156	0.0000000
43	4.030	0.00000	0.0896156	0.0000000
44	4.054	0.00000	0.0896156	0.0000000
45	4.079	0.00000	0.0896156	0.0000000
46	4.105	0.00000	0.0896156	0.0000000
47	4.129	0.00000	0.0896156	0.0000000
48	4.154	0.00000	0.0896156	0.0000000
49	4.179	0.00000	0.0896156	0.0000000
50	4.204	0.00000	0.0896156	0.0000000

Interferogram Profile 9	4 Profiles averaged	
X Location of Profile	2.99400 cm	St. Dev.= 0.01200 cm
Local Shock Angle	26.25008 °	St. Dev.= 0.28820 °
R Location of Shock	4.45000 cm	St. Dev.= 0.00040 cm
R Location of Model Surface	3.20400 cm	St. Dev.= 0.00003 cm

Approximated and Abel Transformed Data

I	Radius (cm)	Fringe Number	ρ/ρ_t	St. Dev. ρ/ρ_t
1	3.208	0.99115	0.0879369	0.0135812
2	3.239	1.02626	0.0894012	0.0133555
3	3.269	1.06095	0.0908261	0.0126374
4	3.299	1.09575	0.0922841	0.0115813
5	3.330	1.13095	0.0938308	0.0103225
6	3.360	1.16664	0.0955073	0.0089737
7	3.390	1.20279	0.0973412	0.0076272
8	3.421	1.23920	0.0993480	0.0063598
9	3.452	1.27557	0.1015334	0.0052396
10	3.482	1.31151	0.1038933	0.0043356
11	3.512	1.34656	0.1064169	0.0037220
12	3.542	1.38019	0.1090858	0.0034553
13	3.573	1.41188	0.1118767	0.0035254
14	3.604	1.44104	0.1147618	0.0038444
15	3.634	1.46711	0.1177102	0.0043034
16	3.665	1.48953	0.1206882	0.0048167
17	3.695	1.50776	0.1236606	0.0053274
18	3.726	1.52129	0.1265914	0.0057940
19	3.756	1.52967	0.1294446	0.0061848
20	3.786	1.53246	0.1321844	0.0064727
21	3.816	1.52930	0.1347764	0.0066340
22	3.847	1.51989	0.1371872	0.0066495
23	3.878	1.50398	0.1393861	0.0065050
24	3.908	1.48138	0.1413439	0.0061937
25	3.939	1.45196	0.1430339	0.0057192
26	3.969	1.41567	0.1444320	0.0051010
27	3.999	1.37250	0.1455161	0.0043880
28	4.030	1.32250	0.1462670	0.0036845
29	4.060	1.26576	0.1466662	0.0032013
30	4.091	1.20242	0.1466966	0.0032366
31	4.121	1.13264	0.1463404	0.0039005
32	4.151	1.05662	0.1455791	0.0049982
33	4.182	0.97455	0.1443894	0.0063013
34	4.212	0.88663	0.1427395	0.0076540
35	4.243	0.79303	0.1405860	0.0089495
36	4.273	0.69389	0.1378614	0.0101048
37	4.304	0.58931	0.1344607	0.0110597
38	4.334	0.47930	0.1302099	0.0118022
39	4.365	0.36381	0.1247978	0.0124761
40	4.395	0.24263	0.1176127	0.0138973
41	4.425	0.11609	0.1077047	0.0207491
42	4.456	0.00000	0.0896156	0.0000000
43	4.486	0.00000	0.0896156	0.0000000
44	4.516	0.00000	0.0896156	0.0000000
45	4.547	0.00000	0.0896156	0.0000000
46	4.578	0.00000	0.0896156	0.0000000
47	4.608	0.00000	0.0896156	0.0000000
48	4.639	0.00000	0.0896156	0.0000000
49	4.669	0.00000	0.0896156	0.0000000
50	4.699	0.00000	0.0896156	0.0000000

Interferogram Profile 10 1 Profile
X Location of Profile 4.00400 cm
Local Shock Angle 26.00027 °
R Location of Shock 4.93000 cm
R Location of Model Surface 3.42800 cm

Approximated and Abel Transformed Data

I	Radius (cm)	Fringe Number	ρ/ρ_t
1	3.438	1.40004	0.0818490
2	3.475	1.49805	0.0881906
3	3.511	1.58502	0.0940578
4	3.548	1.66149	0.0994751
5	3.584	1.72799	0.1044654
6	3.621	1.78500	0.1090514
7	3.658	1.83302	0.1132541
8	3.694	1.87251	0.1170944
9	3.731	1.90391	0.1205916
10	3.767	1.92764	0.1237647
11	3.804	1.94412	0.1266316
12	3.841	1.95372	0.1292095
13	3.877	1.95683	0.1315143
14	3.914	1.95378	0.1335617
15	3.950	1.94490	0.1353666
16	3.987	1.93052	0.1369423
17	4.023	1.91091	0.1383012
18	4.060	1.88636	0.1394559
19	4.097	1.85712	0.1404176
20	4.133	1.82342	0.1411965
21	4.170	1.78548	0.1418008
22	4.206	1.74350	0.1422396
23	4.243	1.69766	0.1425195
24	4.279	1.64811	0.1426470
25	4.316	1.59499	0.1426261
26	4.353	1.53843	0.1424614
27	4.389	1.47854	0.1421542
28	4.426	1.41538	0.1417046
29	4.462	1.34903	0.1411122
30	4.499	1.27954	0.1403729
31	4.535	1.20693	0.1394809
32	4.572	1.13120	0.1384286
33	4.609	1.05236	0.1372033
34	4.645	0.97036	0.1357884
35	4.682	0.88515	0.1341652
36	4.718	0.79668	0.1323059
37	4.755	0.70485	0.1301797
38	4.791	0.60955	0.1277533
39	4.828	0.51066	0.1250150
40	4.865	0.40804	0.1220845
41	4.901	0.30153	0.1201155
42	4.938	0.00000	0.0896156
43	4.974	0.00000	0.0896156
44	5.011	0.00000	0.0896156
45	5.048	0.00000	0.0896156
46	5.084	0.00000	0.0896156
47	5.121	0.00000	0.0896156
48	5.157	0.00000	0.0896156
49	5.194	0.00000	0.0896156
50	5.230	0.00000	0.0896156

Interferogram Profile 11	4 Profiles averaged	
X Location of Profile	5.00800 cm	St. Dev.= 0.01300 cm
Local Shock Angle	26.25008 °	St. Dev.= 0.28820 °
R Location of Shock	5.48000 cm	St. Dev.= 0.00039 cm
R Location of Model Surface	3.65000 cm	St. Dev.= 0.00003 cm

Approximated and Abel Transformed Data

I	Radius (cm)	Fringe Number	ρ/ρ_t	St. Dev. ρ/ρ_t
1	3.655	1.12577	0.0794137	0.0119544
2	3.699	1.20426	0.0828033	0.0106083
3	3.744	1.27931	0.0861614	0.0096718
4	3.789	1.35099	0.0895210	0.0090175
5	3.833	1.41918	0.0928983	0.0085908
6	3.878	1.48358	0.0962960	0.0083579
7	3.923	1.54378	0.0997053	0.0082781
8	3.968	1.59930	0.1031086	0.0082999
9	4.012	1.64963	0.1064814	0.0083708
10	4.057	1.69423	0.1097945	0.0084474
11	4.102	1.73259	0.1130156	0.0085016
12	4.146	1.76426	0.1161113	0.0085210
13	4.191	1.78886	0.1190483	0.0085054
14	4.236	1.80606	0.1217945	0.0084621
15	4.281	1.81568	0.1243213	0.0084018
16	4.325	1.81761	0.1266031	0.0083319
17	4.370	1.81186	0.1286196	0.0082560
18	4.415	1.79856	0.1303558	0.0081687
19	4.459	1.77796	0.1318027	0.0080608
20	4.504	1.75038	0.1329575	0.0079174
21	4.549	1.71628	0.1338243	0.0077243
22	4.594	1.67617	0.1344139	0.0074708
23	4.639	1.63061	0.1347434	0.0071525
24	4.683	1.58024	0.1348365	0.0067762
25	4.728	1.52566	0.1347211	0.0063604
26	4.773	1.46750	0.1344310	0.0059377
27	4.817	1.40630	0.1340025	0.0055556
28	4.862	1.34253	0.1334733	0.0052679
29	4.907	1.27652	0.1328807	0.0051223
30	4.952	1.20842	0.1322575	0.0051377
31	4.996	1.13816	0.1316302	0.0052945
32	5.041	1.06537	0.1310116	0.0055406
33	5.086	0.98936	0.1303951	0.0058135
34	5.130	0.90901	0.1297451	0.0060607
35	5.175	0.82276	0.1289818	0.0062535
36	5.220	0.72849	0.1279567	0.0063903
37	5.264	0.62348	0.1264159	0.0064897
38	5.309	0.50432	0.1239240	0.0065666
39	5.354	0.36681	0.1197383	0.0066132
40	5.398	0.20593	0.1131249	0.0074539
41	5.443	0.06298	0.1032662	0.0157811
42	5.488	0.00000	0.0896156	0.0000000
43	5.533	0.00000	0.0896156	0.0000000
44	5.577	0.00000	0.0896156	0.0000000
45	5.622	0.00000	0.0896156	0.0000000
46	5.667	0.00000	0.0896156	0.0000000
47	5.712	0.00000	0.0896156	0.0000000
48	5.756	0.00000	0.0896156	0.0000000
49	5.801	0.00000	0.0896156	0.0000000
50	5.846	0.00000	0.0896156	0.0000000

Interferogram Profile 12 4 Profiles averaged

X Location of Profile	5.86600 cm	St. Dev.= 0.01200 cm
Local Shock Angle	26.25008 °	St. Dev.= 0.28820 °
R Location of Shock	5.85800 cm	St. Dev.= 0.00041 cm
R Location of Model Surface	3.83900 cm	St. Dev.= 0.00001 cm

Approximated and Abel Transformed Data

I	Radius (cm)	Fringe Number	ρ/ρ_t	St. Dev. ρ/ρ_t
1	3.850	1.27629	0.0706034	0.0078667
2	3.899	1.38775	0.0743257	0.0090528
3	3.949	1.50199	0.0787851	0.0097995
4	3.998	1.61511	0.0837400	0.0101760
5	4.047	1.72388	0.0889814	0.0102599
6	4.096	1.82570	0.0943311	0.0101219
7	4.145	1.91852	0.0996391	0.0098214
8	4.195	2.00083	0.1047817	0.0094062
9	4.244	2.07157	0.1096589	0.0089138
10	4.293	2.13009	0.1141934	0.0083741
11	4.342	2.17612	0.1183278	0.0078093
12	4.391	2.20971	0.1220229	0.0072380
13	4.441	2.23119	0.1252566	0.0066751
14	4.490	2.24112	0.1280212	0.0061346
15	4.539	2.24026	0.1303228	0.0056293
16	4.589	2.22950	0.1321786	0.0051722
17	4.638	2.20987	0.1336161	0.0047751
18	4.687	2.18245	0.1346712	0.0044479
19	4.736	2.14836	0.1353870	0.0041950
20	4.785	2.10870	0.1358117	0.0040142
21	4.834	2.06456	0.1359978	0.0038952
22	4.884	2.01693	0.1360002	0.0038197
23	4.933	1.96670	0.1358745	0.0037658
24	4.982	1.91462	0.1356763	0.0037100
25	5.031	1.86129	0.1354581	0.0036305
26	5.080	1.80707	0.1352688	0.0035102
27	5.130	1.75214	0.1351517	0.0033363
28	5.179	1.69638	0.1351419	0.0031039
29	5.228	1.63941	0.1352647	0.0028183
30	5.277	1.58056	0.1355322	0.0025019
31	5.327	1.51880	0.1359400	0.0022098
32	5.376	1.45276	0.1364638	0.0020471
33	5.425	1.38071	0.1370542	0.0021465
34	5.474	1.30050	0.1376275	0.0025617
35	5.524	1.20959	0.1380572	0.0032279
36	5.573	1.10500	0.1381552	0.0040512
37	5.622	0.98331	0.1376471	0.0049638
38	5.671	0.84062	0.1361216	0.0059503
39	5.720	0.67259	0.1329528	0.0071389
40	5.770	0.47435	0.1272620	0.0091045
41	5.819	0.24056	0.1239537	0.0097592
42	5.868	0.00000	0.0896156	0.0000000
43	5.917	0.00000	0.0896156	0.0000000
44	5.966	0.00000	0.0896156	0.0000000
45	6.016	0.00000	0.0896156	0.0000000
46	6.065	0.00000	0.0896156	0.0000000
47	6.114	0.00000	0.0896156	0.0000000
48	6.164	0.00000	0.0896156	0.0000000
49	6.213	0.00000	0.0896156	0.0000000
50	6.262	0.00000	0.0896156	0.0000000

Interferogram Profile 13 4 Profiles averaged

X Location of Profile	6.86400 cm	St. Dev.= 0.01800 cm
Local Shock Angle	26.25008 °	St. Dev.= 0.28820 °
R Location of Shock	6.34800 cm	St. Dev.= 0.00042 cm
R Location of Model Surface	3.83900 cm	St. Dev.= 0.00000 cm

Approximated and Abel Transformed Data

I	Radius (cm)	Fringe Number	ρ/ρ_t	St. Dev. ρ/ρ_t
1	3.853	0.64329	0.0479486	0.0119884
2	3.914	0.75851	0.0477746	0.0099999
3	3.975	0.89885	0.0494167	0.0082217
4	4.036	1.05754	0.0525850	0.0067107
5	4.098	1.22837	0.0570031	0.0055522
6	4.159	1.40559	0.0624097	0.0048334
7	4.220	1.58405	0.0685598	0.0045720
8	4.281	1.75911	0.0752257	0.0046609
9	4.342	1.92675	0.0821983	0.0049234
10	4.403	2.08350	0.0892871	0.0052082
11	4.465	2.22650	0.0963222	0.0054221
12	4.526	2.35343	0.1031536	0.0055189
13	4.587	2.46256	0.1096517	0.0054836
14	4.648	2.55270	0.1157089	0.0053216
15	4.709	2.62319	0.1212375	0.0050540
16	4.770	2.67385	0.1261717	0.0047141
17	4.832	2.70498	0.1304652	0.0043479
18	4.893	2.71729	0.1340934	0.0040117
19	4.954	2.71187	0.1370499	0.0037674
20	5.015	2.69014	0.1393481	0.0036665
21	5.076	2.65376	0.1410188	0.0037270
22	5.137	2.60463	0.1421096	0.0039235
23	5.199	2.54477	0.1426824	0.0042004
24	5.260	2.47625	0.1428138	0.0044957
25	5.321	2.40113	0.1425899	0.0047541
26	5.382	2.32136	0.1421068	0.0049334
27	5.443	2.23869	0.1414653	0.0050031
28	5.504	2.15458	0.1407692	0.0049448
29	5.566	2.07009	0.1401193	0.0047494
30	5.627	1.98576	0.1396103	0.0044222
31	5.688	1.90152	0.1393223	0.0039829
32	5.749	1.81656	0.1393147	0.0034763
33	5.810	1.72917	0.1396151	0.0029821
34	5.871	1.63666	0.1402055	0.0026295
35	5.933	1.53521	0.1410032	0.0025557
36	5.994	1.41968	0.1418343	0.0027734
37	6.055	1.28352	0.1423887	0.0031199
38	6.116	1.11860	0.1421521	0.0033852
39	6.177	0.91500	0.1402994	0.0034883
40	6.238	0.66093	0.1356803	0.0041502
41	6.300	0.34246	0.1324546	0.0047167
42	6.361	0.00000	0.0896156	0.0000000
43	6.422	0.00000	0.0896156	0.0000000
44	6.483	0.00000	0.0896156	0.0000000
45	6.544	0.00000	0.0896156	0.0000000
46	6.605	0.00000	0.0896156	0.0000000
47	6.667	0.00000	0.0896156	0.0000000
48	6.728	0.00000	0.0896156	0.0000000
49	6.789	0.00000	0.0896156	0.0000000
50	6.850	0.00000	0.0896156	0.0000000

Interferogram Profile 14	3 Profiles averaged	
X Location of Profile	7.87200 cm	St. Dev.= 0.01600 cm
Local Shock Angle	26.33316 °	St. Dev.= 0.28820 °
R Location of Shock	6.83500 cm	St. Dev.= 0.00030 cm
R Location of Model Surface	3.83900 cm	St. Dev.= 0.00000 cm

Approximated and Abel Transformed Data

I	Radius (cm)	Fringe Number	ρ/ρ_t	St. Dev. ρ/ρ_t
1	3.851	0.40974	0.0548617	0.0056031
2	3.924	0.53374	0.0589907	0.0052898
3	3.997	0.63867	0.0616723	0.0050266
4	4.071	0.73282	0.0633545	0.0047050
5	4.144	0.82313	0.0644428	0.0046270
6	4.217	0.91510	0.0652915	0.0048586
7	4.290	1.01280	0.0661990	0.0052086
8	4.363	1.11884	0.0674048	0.0054666
9	4.436	1.23451	0.0690888	0.0055207
10	4.509	1.35988	0.0713726	0.0053478
11	4.582	1.49389	0.0743222	0.0049808
12	4.656	1.63460	0.0779527	0.0044815
13	4.729	1.77928	0.0822329	0.0039236
14	4.802	1.92471	0.0870920	0.0033845
15	4.875	2.06725	0.0924259	0.0029431
16	4.948	2.20316	0.0981054	0.0026754
17	5.021	2.32870	0.1039825	0.0026362
18	5.094	2.44034	0.1098994	0.0028288
19	5.167	2.53493	0.1156951	0.0032039
20	5.240	2.60983	0.1212138	0.0036940
21	5.314	2.66303	0.1263111	0.0042360
22	5.387	2.69323	0.1308613	0.0047737
23	5.460	2.69993	0.1347630	0.0052562
24	5.533	2.68339	0.1379433	0.0056375
25	5.606	2.64468	0.1403636	0.0058793
26	5.679	2.58558	0.1420208	0.0059523
27	5.753	2.50850	0.1429501	0.0058423
28	5.825	2.41633	0.1432229	0.0055510
29	5.899	2.31223	0.1429465	0.0050965
30	5.972	2.19943	0.1422587	0.0045155
31	6.045	2.08088	0.1413205	0.0038552
32	6.118	1.95898	0.1403036	0.0031682
33	6.191	1.83512	0.1393770	0.0025001
34	6.264	1.70928	0.1386815	0.0018949
35	6.337	1.57952	0.1382972	0.0014779
36	6.410	1.44143	0.1381962	0.0016236
37	6.484	1.28752	0.1381624	0.0025143
38	6.557	1.10661	0.1376647	0.0038618
39	6.630	0.88309	0.1356272	0.0053157
40	6.703	0.59619	0.1301488	0.0063390
41	6.776	0.21920	0.1264659	0.0065191
42	6.849	0.00000	0.0896156	0.0000000
43	6.922	0.00000	0.0896156	0.0000000
44	6.996	0.00000	0.0896156	0.0000000
45	7.068	0.00000	0.0896156	0.0000000
46	7.142	0.00000	0.0896156	0.0000000
47	7.215	0.00000	0.0896156	0.0000000
48	7.288	0.00000	0.0896156	0.0000000
49	7.361	0.00000	0.0896156	0.0000000
50	7.434	0.00000	0.0896156	0.0000000

Interferogram Profile 15	2 Profiles averaged	
X Location of Profile	8.88900 cm	St. Dev.= 0.00600 cm
Local Shock Angle	26.25008 °	St. Dev.= 0.35352 °
R Location of Shock	7.30100 cm	St. Dev.= 0.00010 cm
R Location of Model Surface	3.83900 cm	St. Dev.= 0.00000 cm

Approximated and Abel Transformed Data

I	Radius (cm)	Fringe Number	ρ/ρ_t	St. Dev. ρ/ρ_t
1	3.871	0.29974	0.0520481	0.0017256
2	3.955	0.44552	0.0564722	0.0006717
3	4.039	0.57485	0.0598744	0.0002131
4	4.123	0.69389	0.0625943	0.0001646
5	4.207	0.80733	0.0649055	0.0003772
6	4.292	0.91860	0.0670233	0.0007340
7	4.376	1.03001	0.0691122	0.0011451
8	4.460	1.14297	0.0712925	0.0015446
9	4.544	1.25807	0.0736473	0.0018864
10	4.628	1.37525	0.0762269	0.0021416
11	4.712	1.49396	0.0790551	0.0022950
12	4.796	1.61320	0.0821338	0.0023429
13	4.880	1.73170	0.0854469	0.0022901
14	4.964	1.84798	0.0889642	0.0021485
15	5.049	1.96044	0.0926462	0.0019342
16	5.133	2.06745	0.0964452	0.0016663
17	5.217	2.16741	0.1003103	0.0013652
18	5.300	2.25879	0.1041884	0.0010510
19	5.385	2.34020	0.1080275	0.0007422
20	5.469	2.41041	0.1117776	0.0004557
21	5.553	2.46835	0.1153935	0.0002039
22	5.638	2.51322	0.1188350	0.0000039
23	5.722	2.54433	0.1220681	0.0001633
24	5.806	2.56126	0.1250668	0.0002740
25	5.890	2.56373	0.1278114	0.0003418
26	5.974	2.55164	0.1302896	0.0003762
27	6.058	2.52498	0.1324965	0.0003919
28	6.143	2.48382	0.1344322	0.0004062
29	6.227	2.42823	0.1361007	0.0004407
30	6.311	2.35821	0.1375085	0.0005174
31	6.395	2.27364	0.1386593	0.0006580
32	6.479	2.17414	0.1395526	0.0008822
33	6.563	2.05903	0.1401740	0.0012019
34	6.647	1.92716	0.1404898	0.0016188
35	6.731	1.77681	0.1404314	0.0021149
36	6.816	1.60559	0.1398786	0.0026431
37	6.899	1.41028	0.1386280	0.0031045
38	6.983	1.18663	0.1363430	0.0033138
39	7.068	0.92924	0.1324755	0.0029098
40	7.152	0.63144	0.1262977	0.0011845
41	7.237	0.28500	0.1226773	0.0003514
42	7.321	0.00000	0.0896156	0.0000000
43	7.405	0.00000	0.0896156	0.0000000
44	7.489	0.00000	0.0896156	0.0000000
45	7.573	0.00000	0.0896156	0.0000000
46	7.657	0.00000	0.0896156	0.0000000
47	7.741	0.00000	0.0896156	0.0000000
48	7.825	0.00000	0.0896156	0.0000000
49	7.910	0.00000	0.0896156	0.0000000
50	7.994	0.00000	0.0896156	0.0000000

Interferogram Profile 17	3 Profiles averaged	
X Location of Profile	6.36200 cm	St. Dev.= 0.02100 cm
Local Shock Angle	26.16700 °	St. Dev.= 0.28820 °
R Location of Shock	6.09900 cm	St. Dev.= 0.00036 cm
R Location of Model Surface	3.83900 cm	St. Dev.= 0.00000 cm

Approximated and Abel Transformed Data

I	Radius (cm)	Fringe Number	ρ/ρ_t	St. Dev. ρ/ρ_t
1	3.846	0.76747	0.0506946	0.0213724
2	3.901	0.88228	0.0503450	0.0217688
3	3.956	1.02896	0.0527013	0.0204886
4	4.011	1.19648	0.0572140	0.0180267
5	4.067	1.37481	0.0633490	0.0149408
6	4.122	1.55515	0.0706049	0.0116795
7	4.177	1.73001	0.0785243	0.0085620
8	4.232	1.89331	0.0867036	0.0057964
9	4.287	2.04035	0.0947981	0.0035150
10	4.343	2.16776	0.1025250	0.0018529
11	4.398	2.27345	0.1096637	0.0012058
12	4.453	2.35649	0.1160538	0.0016136
13	4.508	2.41692	0.1215931	0.0021618
14	4.563	2.45568	0.1262311	0.0025908
15	4.618	2.47436	0.1299649	0.0029259
16	4.674	2.47510	0.1328317	0.0032298
17	4.729	2.46040	0.1349027	0.0035498
18	4.784	2.43294	0.1362748	0.0039023
19	4.839	2.39542	0.1370643	0.0042788
20	4.895	2.35047	0.1373978	0.0046551
21	4.950	2.30048	0.1374075	0.0050059
22	5.005	2.24748	0.1372223	0.0053117
23	5.060	2.19310	0.1369630	0.0055604
24	5.116	2.13848	0.1367359	0.0057487
25	5.171	2.08422	0.1366288	0.0058799
26	5.226	2.03037	0.1367065	0.0059606
27	5.281	1.97644	0.1370067	0.0059946
28	5.336	1.92142	0.1375403	0.0059827
29	5.392	1.86383	0.1382876	0.0059138
30	5.447	1.80177	0.1391974	0.0057712
31	5.502	1.73306	0.1401900	0.0055261
32	5.557	1.65525	0.1411545	0.0051504
33	5.613	1.56585	0.1419516	0.0046144
34	5.668	1.46232	0.1424130	0.0038951
35	5.723	1.34233	0.1423412	0.0029784
36	5.778	1.20374	0.1415050	0.0018618
37	5.833	1.04486	0.1396303	0.0005572
38	5.889	0.86444	0.1363779	0.0010024
39	5.944	0.66183	0.1313117	0.0027922
40	5.999	0.43698	0.1240041	0.0050738
41	6.054	0.19054	0.1203211	0.0056427
42	6.109	0.00000	0.0896156	0.0000000
43	6.165	0.00000	0.0896156	0.0000000
44	6.220	0.00000	0.0896156	0.0000000
45	6.275	0.00000	0.0896156	0.0000000
46	6.330	0.00000	0.0896156	0.0000000
47	6.385	0.00000	0.0896156	0.0000000
48	6.440	0.00000	0.0896156	0.0000000
49	6.496	0.00000	0.0896156	0.0000000
50	6.551	0.00000	0.0896156	0.0000000

TABLE D.2 Interferometry Data for 12.5° Model at 3.4 atm Total Pressure

Filename		12D50P.TEX	
Model Cone Angle		12.5 °	
Total Pressure		3.4 atm	
Total Temperature		285.0 °K	
Interferogram profile	1	X Location	-5.051 cm
Interferogram profile	2	X Location	-4.047 cm
Interferogram profile	3	X Location	-3.060 cm
Interferogram profile	4	X Location	-2.041 cm
Interferogram profile	5	X Location	-1.018 cm
Interferogram profile	6	X Location	-0.015 cm
Interferogram profile	7	X Location	0.996 cm
Interferogram profile	8	X Location	1.984 cm
Interferogram profile	9	X Location	2.992 cm
Interferogram profile	10	X Location	3.991 cm
Interferogram profile	11	X Location	4.996 cm
Interferogram profile	12	X Location	5.848 cm
Interferogram profile	14	X Location	6.852 cm
Interferogram profile	15	X Location	7.854 cm
Interferogram profile	16	X Location	8.850 cm

Interferogram Profile 1 1 Profile
X Location of Profile -5.05100 cm
Local Shock Angle 0.00000 °
R Location of Shock 0.00000 cm
R Location of Model Surface 2.54000 cm

Approximated and Abel Transformed Data

I	Radius (cm)	Fringe Number	ρ/ρ_t
1	2.542	-1.69601	0.0423183
2	2.567	-1.60557	0.0444350
3	2.591	-1.51761	0.0465066
4	2.616	-1.43213	0.0485336
5	2.640	-1.34912	0.0505158
6	2.664	-1.26860	0.0524539
7	2.689	-1.19055	0.0543478
8	2.713	-1.11498	0.0561978
9	2.738	-1.04189	0.0580041
10	2.762	-0.97127	0.0597667
11	2.787	-0.90313	0.0614857
12	2.811	-0.83747	0.0631612
13	2.836	-0.77429	0.0647933
14	2.860	-0.71359	0.0663818
15	2.884	-0.65536	0.0679266
16	2.909	-0.59961	0.0694277
17	2.933	-0.54634	0.0708847
18	2.958	-0.49555	0.0722977
19	2.982	-0.44723	0.0736663
20	3.007	-0.40139	0.0749901
21	3.031	-0.35803	0.0762684
22	3.056	-0.31715	0.0775010
23	3.080	-0.27874	0.0786874
24	3.104	-0.24282	0.0798266
25	3.129	-0.20937	0.0809179
26	3.153	-0.17840	0.0819601
27	3.178	-0.14990	0.0829521
28	3.202	-0.12389	0.0838924
29	3.227	-0.10035	0.0847795
30	3.251	-0.07929	0.0856111
31	3.276	-0.06070	0.0863845
32	3.300	-0.04460	0.0870967
33	3.324	-0.03097	0.0877433
34	3.349	-0.01982	0.0883184
35	3.373	-0.01115	0.0888143
36	3.398	-0.00496	0.0892176
37	3.422	-0.00124	0.0895049
38	3.447	0.00000	0.0896156
39	3.471	0.00000	0.0896156
40	3.496	0.00000	0.0896156
41	3.520	0.00000	0.0896156
42	3.544	0.00000	0.0896156
43	3.569	0.00000	0.0896156
44	3.593	0.00000	0.0896156
45	3.618	0.00000	0.0896156
46	3.642	0.00000	0.0896156
47	3.667	0.00000	0.0896156
48	3.691	0.00000	0.0896156
49	3.716	0.00000	0.0896156
50	3.740	0.00000	0.0896156

Interferogram Profile 2 1 Profile
X Location of Profile -4.04700 cm
Local Shock Angle 0.00000 °
R Location of Shock 0.00000 cm
R Location of Model Surface 2.54000 cm

Approximated and Abel Transformed Data

I	Radius (cm)	Fringe Number	ρ/ρ_t
1	2.542	-1.66935	0.0436761
2	2.567	-1.58265	0.0456827
3	2.591	-1.49826	0.0476472
4	2.616	-1.41617	0.0495701
5	2.640	-1.33641	0.0514515
6	2.664	-1.25895	0.0532916
7	2.689	-1.18381	0.0550908
8	2.713	-1.11097	0.0568492
9	2.738	-1.04046	0.0585670
10	2.762	-0.97225	0.0602442
11	2.787	-0.90635	0.0618810
12	2.811	-0.84277	0.0634774
13	2.836	-0.78150	0.0650334
14	2.860	-0.72254	0.0665493
15	2.884	-0.66589	0.0680246
16	2.909	-0.61156	0.0694596
17	2.933	-0.55953	0.0708540
18	2.958	-0.50982	0.0722077
19	2.982	-0.46242	0.0735204
20	3.007	-0.41734	0.0747919
21	3.031	-0.37456	0.0760217
22	3.056	-0.33410	0.0772096
23	3.080	-0.29595	0.0783551
24	3.104	-0.26011	0.0794575
25	3.129	-0.22659	0.0805161
26	3.153	-0.19537	0.0815303
27	3.178	-0.16647	0.0824990
28	3.202	-0.13988	0.0834209
29	3.227	-0.11561	0.0842951
30	3.251	-0.09364	0.0851196
31	3.276	-0.07399	0.0858925
32	3.300	-0.05665	0.0866116
33	3.324	-0.04162	0.0872736
34	3.349	-0.02890	0.0878748
35	3.373	-0.01850	0.0884096
36	3.398	-0.01040	0.0888705
37	3.422	-0.00462	0.0892456
38	3.447	-0.00116	0.0895127
39	3.471	0.00000	0.0896156
40	3.496	0.00000	0.0896156
41	3.520	0.00000	0.0896156
42	3.544	0.00000	0.0896156
43	3.569	0.00000	0.0896156
44	3.593	0.00000	0.0896156
45	3.618	0.00000	0.0896156
46	3.642	0.00000	0.0896156
47	3.667	0.00000	0.0896156
48	3.691	0.00000	0.0896156
49	3.716	0.00000	0.0896156
50	3.740	0.00000	0.0896156

Interferogram Profile 3 1 Profile
X Location of Profile -3.06000 cm
Local Shock Angle 0.00000 °
R Location of Shock 0.00000 cm
R Location of Model Surface 2.54000 cm

Approximated and Abel Transformed Data

I	Radius (cm)	Fringe Number	ρ/ρ_t
1	2.542	-1.45227	0.0491154
2	2.567	-1.37483	0.0509279
3	2.591	-1.29951	0.0527018
4	2.616	-1.22632	0.0544374
5	2.640	-1.15524	0.0561349
6	2.664	-1.08629	0.0577944
7	2.689	-1.01946	0.0594161
8	2.713	-0.95475	0.0610003
9	2.738	-0.89216	0.0625470
10	2.762	-0.83169	0.0640563
11	2.787	-0.77334	0.0655283
12	2.811	-0.71712	0.0669631
13	2.836	-0.66302	0.0683605
14	2.860	-0.61104	0.0697207
15	2.884	-0.56118	0.0710436
16	2.909	-0.51344	0.0723289
17	2.933	-0.46783	0.0735766
18	2.958	-0.42433	0.0747865
19	2.982	-0.38296	0.0759584
20	3.007	-0.34371	0.0770918
21	3.031	-0.30658	0.0781865
22	3.056	-0.27157	0.0792421
23	3.080	-0.23869	0.0802580
24	3.104	-0.20792	0.0812334
25	3.129	-0.17928	0.0821678
26	3.153	-0.15276	0.0830602
27	3.178	-0.12836	0.0839097
28	3.202	-0.10608	0.0847149
29	3.227	-0.08593	0.0854745
30	3.251	-0.06789	0.0861865
31	3.276	-0.05198	0.0868490
32	3.300	-0.03819	0.0874587
33	3.324	-0.02652	0.0880124
34	3.349	-0.01697	0.0885049
35	3.373	-0.00955	0.0889294
36	3.398	-0.00424	0.0892748
37	3.422	-0.00106	0.0895209
38	3.447	0.00000	0.0896156
39	3.471	0.00000	0.0896156
40	3.496	0.00000	0.0896156
41	3.520	0.00000	0.0896156
42	3.544	0.00000	0.0896156
43	3.569	0.00000	0.0896156
44	3.593	0.00000	0.0896156
45	3.618	0.00000	0.0896156
46	3.642	0.00000	0.0896156
47	3.667	0.00000	0.0896156
48	3.691	0.00000	0.0896156
49	3.716	0.00000	0.0896156
50	3.740	0.00000	0.0896156

Interferogram Profile 4 1 Profile
X Location of Profile -2.04100 cm
Local Shock Angle 0.00000 °
R Location of Shock 0.00000 cm
R Location of Model Surface 2.54000 cm

Approximated and Abel Transformed Data

I	Radius (cm)	Fringe Number	ρ/ρ_t
1	2.542	-1.72671	0.0408013
2	2.567	-1.63212	0.0430414
3	2.591	-1.54018	0.0452328
4	2.616	-1.45092	0.0473759
5	2.640	-1.36432	0.0494711
6	2.664	-1.28038	0.0515184
7	2.689	-1.19911	0.0535181
8	2.713	-1.12050	0.0554705
9	2.738	-1.04455	0.0573754
10	2.762	-0.97128	0.0592332
11	2.787	-0.90066	0.0610439
12	2.811	-0.83271	0.0628074
13	2.836	-0.76743	0.0645237
14	2.860	-0.70481	0.0661929
15	2.884	-0.64485	0.0678146
16	2.909	-0.58756	0.0693888
17	2.933	-0.53294	0.0709151
18	2.958	-0.48097	0.0723935
19	2.982	-0.43168	0.0738233
20	3.007	-0.38505	0.0752040
21	3.031	-0.34108	0.0765355
22	3.056	-0.29978	0.0778167
23	3.080	-0.26114	0.0790469
24	3.104	-0.22517	0.0802253
25	3.129	-0.19186	0.0813507
26	3.153	-0.16121	0.0824220
27	3.178	-0.13323	0.0834373
28	3.202	-0.10792	0.0843950
29	3.227	-0.08527	0.0852928
30	3.251	-0.06528	0.0861278
31	3.276	-0.04796	0.0868967
32	3.300	-0.03331	0.0875945
33	3.324	-0.02132	0.0882156
34	3.349	-0.01199	0.0887506
35	3.373	-0.00533	0.0891860
36	3.398	-0.00133	0.0894962
37	3.422	0.00000	0.0896156
38	3.447	0.00000	0.0896156
39	3.471	0.00000	0.0896156
40	3.496	0.00000	0.0896156
41	3.520	0.00000	0.0896156
42	3.544	0.00000	0.0896156
43	3.569	0.00000	0.0896156
44	3.593	0.00000	0.0896156
45	3.618	0.00000	0.0896156
46	3.642	0.00000	0.0896156
47	3.667	0.00000	0.0896156
48	3.691	0.00000	0.0896156
49	3.716	0.00000	0.0896156
50	3.740	0.00000	0.0896156

Interferogram Profile 5	4 Profiles averaged	
X Location of Profile	-1.01800 cm	St. Dev.= 0.02200 cm
Local Shock Angle	0.00000 °	St. Dev.= 0.00000 °
R Location of Shock	0.00000 cm	St. Dev.= 0.00000 cm
R Location of Model Surface	2.54000 cm	St. Dev.= 0.00000 cm

Approximated and Abel Transformed Data

I	Radius (cm)	Fringe Number	ρ/ρ_t	St. Dev. ρ/ρ_t
1	2.542	-1.54464	0.0468849	0.0119565
2	2.567	-1.46351	0.0487740	0.0114816
3	2.591	-1.38457	0.0506230	0.0110168
4	2.616	-1.30783	0.0524323	0.0105619
5	2.640	-1.23328	0.0542022	0.0101169
6	2.664	-1.16093	0.0559328	0.0096817
7	2.689	-1.09078	0.0576244	0.0092563
8	2.713	-1.02282	0.0592770	0.0088406
9	2.738	-0.95706	0.0608909	0.0084346
10	2.762	-0.89350	0.0624661	0.0080382
11	2.787	-0.83213	0.0640027	0.0076515
12	2.811	-0.77296	0.0655008	0.0072743
13	2.836	-0.71599	0.0669604	0.0069067
14	2.860	-0.66121	0.0683814	0.0065487
15	2.884	-0.60863	0.0697638	0.0062001
16	2.909	-0.55825	0.0711074	0.0058611
17	2.933	-0.51006	0.0724122	0.0055316
18	2.958	-0.46407	0.0736779	0.0052115
19	2.982	-0.42028	0.0749044	0.0049009
20	3.007	-0.37869	0.0760911	0.0045998
21	3.031	-0.33928	0.0772378	0.0043081
22	3.056	-0.30208	0.0783441	0.0040258
23	3.080	-0.26708	0.0794094	0.0037527
24	3.104	-0.23427	0.0804330	0.0034889
25	3.129	-0.20366	0.0814142	0.0032341
26	3.153	-0.17524	0.0823520	0.0029883
27	3.178	-0.14903	0.0832454	0.0027510
28	3.202	-0.12500	0.0840931	0.0025218
29	3.227	-0.10317	0.0848935	0.0023003
30	3.251	-0.08354	0.0856445	0.0020856
31	3.276	-0.06611	0.0863437	0.0018763
32	3.300	-0.05088	0.0869877	0.0016706
33	3.324	-0.03784	0.0875720	0.0014653
34	3.349	-0.02700	0.0880892	0.0012548
35	3.373	-0.01836	0.0885247	0.0010255
36	3.398	-0.01172	0.0888796	0.0007913
37	3.422	-0.00691	0.0891506	0.0005531
38	3.447	-0.00357	0.0893516	0.0003276
39	3.471	-0.00135	0.0895053	0.0001581
40	3.496	-0.00026	0.0895923	0.0000466
41	3.520	0.00000	0.0896156	0.0000000
42	3.544	0.00000	0.0896156	0.0000000
43	3.569	0.00000	0.0896156	0.0000000
44	3.593	0.00000	0.0896156	0.0000000
45	3.618	0.00000	0.0896156	0.0000000
46	3.642	0.00000	0.0896156	0.0000000
47	3.667	0.00000	0.0896156	0.0000000
48	3.691	0.00000	0.0896156	0.0000000
49	3.716	0.00000	0.0896156	0.0000000
50	3.740	0.00000	0.0896156	0.0000000

Interferogram Profile 6	4 Profiles averaged	
X Location of Profile	-0.01500 cm	St. Dev.= 0.00900 cm
Local Shock Angle	0.00000 °	St. Dev.= 0.00000 °
R Location of Shock	0.00000 cm	St. Dev.= 0.00000 cm
R Location of Model Surface	2.54000 cm	St. Dev.= 0.00000 cm

Approximated and Abel Transformed Data

I	Radius (cm)	Fringe Number	ρ/ρ_t	St. Dev. ρ/ρ_t
1	2.542	-1.14574	0.0566313	0.0061265
2	2.567	-1.08064	0.0581979	0.0058242
3	2.591	-1.01745	0.0597297	0.0055294
4	2.616	-0.95616	0.0612267	0.0052422
5	2.640	-0.89678	0.0626893	0.0049626
6	2.664	-0.83931	0.0641174	0.0046906
7	2.689	-0.78375	0.0655113	0.0044262
8	2.713	-0.73009	0.0668710	0.0041694
9	2.738	-0.67833	0.0681967	0.0039203
10	2.762	-0.62849	0.0694882	0.0036790
11	2.787	-0.58054	0.0707458	0.0034454
12	2.811	-0.53451	0.0719692	0.0032197
13	2.836	-0.49038	0.0731584	0.0030020
14	2.860	-0.44815	0.0743134	0.0027923
15	2.884	-0.40784	0.0754340	0.0025909
16	2.909	-0.36942	0.0765200	0.0023977
17	2.933	-0.33292	0.0775713	0.0022132
18	2.958	-0.29832	0.0785874	0.0020373
19	2.982	-0.26562	0.0795680	0.0018703
20	3.007	-0.23484	0.0805128	0.0017125
21	3.031	-0.20596	0.0814211	0.0015639
22	3.056	-0.17898	0.0822924	0.0014250
23	3.080	-0.15391	0.0831260	0.0012958
24	3.104	-0.13075	0.0839211	0.0011765
25	3.129	-0.10949	0.0846766	0.0010672
26	3.153	-0.09014	0.0853913	0.0009674
27	3.178	-0.07269	0.0860637	0.0008768
28	3.202	-0.05715	0.0866920	0.0007945
29	3.227	-0.04352	0.0872739	0.0007188
30	3.251	-0.03179	0.0878064	0.0006473
31	3.276	-0.02197	0.0882855	0.0005763
32	3.300	-0.01405	0.0887052	0.0005003
33	3.324	-0.00804	0.0890562	0.0004096
34	3.349	-0.00394	0.0893177	0.0002824
35	3.373	-0.00144	0.0894956	0.0001492
36	3.398	-0.00026	0.0895921	0.0000470
37	3.422	0.00000	0.0896156	0.0000000
38	3.447	0.00000	0.0896156	0.0000000
39	3.471	0.00000	0.0896156	0.0000000
40	3.496	0.00000	0.0896156	0.0000000
41	3.520	0.00000	0.0896156	0.0000000
42	3.544	0.00000	0.0896156	0.0000000
43	3.569	0.00000	0.0896156	0.0000000
44	3.593	0.00000	0.0896156	0.0000000
45	3.618	0.00000	0.0896156	0.0000000
46	3.642	0.00000	0.0896156	0.0000000
47	3.667	0.00000	0.0896156	0.0000000
48	3.691	0.00000	0.0896156	0.0000000
49	3.716	0.00000	0.0896156	0.0000000
50	3.740	0.00000	0.0896156	0.0000000

Interferogram Profile 7	4 Profiles averaged	
X Location of Profile	0.99600 cm	St. Dev.= 0.02700 cm
Local Shock Angle	25.93782 °	St. Dev.= 0.12548 °
R Location of Shock	3.47800 cm	St. Dev.= 0.00032 cm
R Location of Model Surface	2.76100 cm	St. Dev.= 0.00006 cm

Approximated and Abel Transformed Data

I	Radius (cm)	Fringe Number	ρ/ρ_t	St. Dev. ρ/ρ_t
1	2.763	0.35625	0.0869514	0.0108237
2	2.780	0.37554	0.0874705	0.0111308
3	2.798	0.39510	0.0880401	0.0113575
4	2.816	0.41480	0.0886571	0.0115047
5	2.833	0.43451	0.0893179	0.0115741
6	2.850	0.45408	0.0900193	0.0115682
7	2.868	0.47339	0.0907577	0.0114898
8	2.885	0.49228	0.0915296	0.0113420
9	2.903	0.51065	0.0923316	0.0111284
10	2.920	0.52833	0.0931599	0.0108527
11	2.938	0.54520	0.0940107	0.0105191
12	2.956	0.56112	0.0948802	0.0101320
13	2.973	0.57596	0.0957644	0.0096963
14	2.990	0.58957	0.0966592	0.0092170
15	3.008	0.60184	0.0975603	0.0087003
16	3.025	0.61261	0.0984633	0.0081527
17	3.043	0.62175	0.0993637	0.0075816
18	3.060	0.62914	0.1002566	0.0069964
19	3.078	0.63462	0.1011369	0.0064078
20	3.095	0.63807	0.1019993	0.0058298
21	3.113	0.63934	0.1028380	0.0052799
22	3.131	0.63832	0.1036472	0.0047806
23	3.148	0.63485	0.1044201	0.0043598
24	3.166	0.62880	0.1051500	0.0040492
25	3.183	0.62004	0.1058291	0.0038781
26	3.201	0.60843	0.1064489	0.0038622
27	3.218	0.59383	0.1070003	0.0039954
28	3.236	0.57612	0.1074727	0.0042506
29	3.253	0.55515	0.1078542	0.0045900
30	3.271	0.53078	0.1081312	0.0049750
31	3.288	0.50289	0.1082876	0.0053710
32	3.306	0.47133	0.1083041	0.0057472
33	3.323	0.43597	0.1081569	0.0060753
34	3.341	0.39668	0.1078160	0.0063276
35	3.358	0.35331	0.1072413	0.0064733
36	3.376	0.30573	0.1063780	0.0064755
37	3.393	0.25382	0.1051436	0.0062841
38	3.411	0.19742	0.1034036	0.0058233
39	3.428	0.13641	0.1009040	0.0049576
40	3.446	0.07065	0.0970426	0.0033792
41	3.463	0.00000	0.0896156	0.0000000
42	3.481	0.00000	0.0896156	0.0000000
43	3.499	0.00000	0.0896156	0.0000000
44	3.516	0.00000	0.0896156	0.0000000
45	3.533	0.00000	0.0896156	0.0000000
46	3.551	0.00000	0.0896156	0.0000000
47	3.568	0.00000	0.0896156	0.0000000
48	3.586	0.00000	0.0896156	0.0000000
49	3.603	0.00000	0.0896156	0.0000000
50	3.621	0.00000	0.0896156	0.0000000

Interferogram Profile 8	4 Profiles averaged	
X Location of Profile	1.98400 cm	St. Dev.= 0.02600 cm
Local Shock Angle	25.93782 °	St. Dev.= 0.12548 °
R Location of Shock	3.96200 cm	St. Dev.= 0.00042 cm
R Location of Model Surface	2.98000 cm	St. Dev.= 0.00006 cm

Approximated and Abel Transformed Data

I	Radius (cm)	Fringe Number	ρ/ρ_t	St. Dev. ρ/ρ_t
1	2.983	0.72181	0.0884712	0.0119998
2	3.007	0.74041	0.0884799	0.0108735
3	3.031	0.76133	0.0885958	0.0100364
4	3.055	0.78443	0.0888196	0.0093939
5	3.079	0.80954	0.0891517	0.0088659
6	3.103	0.83647	0.0895920	0.0083930
7	3.127	0.86501	0.0901398	0.0079364
8	3.151	0.89491	0.0907940	0.0074753
9	3.175	0.92595	0.0915529	0.0070026
10	3.199	0.95784	0.0924142	0.0065217
11	3.223	0.99029	0.0933751	0.0060427
12	3.247	1.02300	0.0944322	0.0055804
13	3.271	1.05564	0.0955814	0.0051514
14	3.295	1.08786	0.0968180	0.0047715
15	3.319	1.11929	0.0981366	0.0044530
16	3.343	1.14955	0.0995310	0.0042013
17	3.367	1.17824	0.1009941	0.0040120
18	3.391	1.20491	0.1025181	0.0038720
19	3.415	1.22914	0.1040941	0.0037602
20	3.439	1.25045	0.1057124	0.0036525
21	3.463	1.26836	0.1073617	0.0035253
22	3.487	1.28236	0.1090299	0.0033585
23	3.511	1.29194	0.1107033	0.0031373
24	3.535	1.29655	0.1123662	0.0028549
25	3.559	1.29563	0.1140016	0.0025152
26	3.583	1.28858	0.1155900	0.0021420
27	3.607	1.27483	0.1171092	0.0017995
28	3.631	1.25373	0.1185341	0.0016257
29	3.655	1.22466	0.1198361	0.0017897
30	3.679	1.18695	0.1209809	0.0023040
31	3.703	1.13992	0.1219295	0.0030461
32	3.727	1.08287	0.1226338	0.0039103
33	3.751	1.01508	0.1230359	0.0048258
34	3.775	0.93583	0.1230621	0.0057334
35	3.799	0.84434	0.1226170	0.0065716
36	3.823	0.73983	0.1215688	0.0072641
37	3.847	0.62153	0.1197261	0.0077085
38	3.871	0.48860	0.1167798	0.0077506
39	3.895	0.34021	0.1121586	0.0071287
40	3.918	0.17550	0.1045283	0.0052852
41	3.943	-0.00640	0.0890694	0.0005496
42	3.966	0.00000	0.0896156	0.0000000
43	3.990	0.00000	0.0896156	0.0000000
44	4.015	0.00000	0.0896156	0.0000000
45	4.038	0.00000	0.0896156	0.0000000
46	4.062	0.00000	0.0896156	0.0000000
47	4.087	0.00000	0.0896156	0.0000000
48	4.110	0.00000	0.0896156	0.0000000
49	4.134	0.00000	0.0896156	0.0000000
50	4.158	0.00000	0.0896156	0.0000000

Interferogram Profile 9	4 Profiles averaged	
X Location of Profile	2.99200 cm	St. Dev.= 0.02200 cm
Local Shock Angle	25.93782 °	St. Dev.= 0.12548 °
R Location of Shock	4.45000 cm	St. Dev.= 0.00062 cm
R Location of Model Surface	3.20300 cm	St. Dev.= 0.00005 cm

Approximated and Abel Transformed Data

I	Radius (cm)	Fringe Number	ρ/ρ_t	St. Dev. ρ/ρ_t
1	3.207	1.61053	0.0843041	0.0037159
2	3.238	1.65648	0.0833581	0.0048767
3	3.268	1.72180	0.0834230	0.0065801
4	3.299	1.80177	0.0843387	0.0075247
5	3.329	1.89215	0.0859589	0.0076965
6	3.360	1.98915	0.0881505	0.0072582
7	3.390	2.08942	0.0907931	0.0064066
8	3.421	2.19003	0.0937778	0.0053634
9	3.451	2.28842	0.0970076	0.0044050
10	3.481	2.38240	0.1003959	0.0038848
11	3.511	2.47011	0.1038667	0.0040576
12	3.542	2.55001	0.1073533	0.0047831
13	3.573	2.62085	0.1107983	0.0057259
14	3.603	2.68164	0.1141529	0.0066463
15	3.634	2.73165	0.1173765	0.0074138
16	3.664	2.77032	0.1204353	0.0079596
17	3.694	2.79735	0.1233034	0.0082506
18	3.725	2.81255	0.1259601	0.0082751
19	3.755	2.81592	0.1283914	0.0080381
20	3.786	2.80757	0.1305879	0.0075577
21	3.816	2.78768	0.1325451	0.0068628
22	3.847	2.75654	0.1342617	0.0059923
23	3.877	2.71448	0.1357403	0.0049952
24	3.908	2.66183	0.1369856	0.0039342
25	3.938	2.59898	0.1380039	0.0028978
26	3.968	2.52624	0.1388018	0.0020390
27	3.999	2.44390	0.1393870	0.0016471
28	4.030	2.35217	0.1397638	0.0018826
29	4.060	2.25119	0.1399350	0.0024026
30	4.090	2.14097	0.1398983	0.0028891
31	4.121	2.02136	0.1396446	0.0032053
32	4.151	1.89207	0.1391552	0.0032957
33	4.182	1.75260	0.1383982	0.0031532
34	4.212	1.60227	0.1373216	0.0028261
35	4.243	1.44011	0.1358451	0.0024652
36	4.273	1.26494	0.1338461	0.0023778
37	4.303	1.07526	0.1311290	0.0028353
38	4.334	0.86929	0.1273699	0.0037314
39	4.365	0.64490	0.1219709	0.0049117
40	4.395	0.39959	0.1135893	0.0070717
41	4.425	0.13051	0.0977518	0.0152029
42	4.456	0.00000	0.0896156	0.0000000
43	4.486	0.00000	0.0896156	0.0000000
44	4.517	0.00000	0.0896156	0.0000000
45	4.547	0.00000	0.0896156	0.0000000
46	4.578	0.00000	0.0896156	0.0000000
47	4.608	0.00000	0.0896156	0.0000000
48	4.638	0.00000	0.0896156	0.0000000
49	4.669	0.00000	0.0896156	0.0000000
50	4.699	0.00000	0.0896156	0.0000000

Interferogram Profile 10	4 Profiles averaged	
X Location of Profile	3.99100 cm	St. Dev.= 0.02000 cm
Local Shock Angle	25.93782 °	St. Dev.= 0.12548 °
R Location of Shock	4.93200 cm	St. Dev.= 0.00071 cm
R Location of Model Surface	3.42400 cm	St. Dev.= 0.00005 cm

Approximated and Abel Transformed Data

I	Radius (cm)	Fringe Number	ρ/ρ_t	St. Dev. ρ/ρ_t
1	3.432	2.50427	0.0923516	0.0063255
2	3.469	2.54954	0.0913042	0.0067383
3	3.506	2.61972	0.0914945	0.0073296
4	3.542	2.70792	0.0927022	0.0075620
5	3.579	2.80797	0.0947277	0.0073477
6	3.616	2.91449	0.0973902	0.0067476
7	3.653	3.02276	0.1005277	0.0058728
8	3.689	3.12873	0.1039956	0.0048629
9	3.726	3.22896	0.1076660	0.0038993
10	3.762	3.32059	0.1114267	0.0032371
11	3.800	3.40129	0.1151805	0.0031429
12	3.837	3.46924	0.1188444	0.0036078
13	3.873	3.52308	0.1223489	0.0043517
14	3.910	3.56185	0.1256366	0.0051344
15	3.947	3.58500	0.1286623	0.0058244
16	3.984	3.59231	0.1313913	0.0063552
17	4.020	3.58384	0.1337997	0.0066927
18	4.057	3.55996	0.1358721	0.0068232
19	4.094	3.52123	0.1376023	0.0067457
20	4.131	3.46840	0.1389917	0.0064689
21	4.167	3.40238	0.1400483	0.0060103
22	4.204	3.32419	0.1407863	0.0053929
23	4.241	3.23490	0.1412249	0.0046476
24	4.278	3.13562	0.1413879	0.0038104
25	4.315	3.02744	0.1413014	0.0029271
26	4.351	2.91142	0.1409945	0.0020640
27	4.388	2.78852	0.1404965	0.0013582
28	4.425	2.65959	0.1398367	0.0011381
29	4.461	2.52527	0.1390419	0.0015308
30	4.498	2.38605	0.1381362	0.0021330
31	4.535	2.24214	0.1371365	0.0027239
32	4.571	2.09347	0.1360529	0.0032460
33	4.608	1.93967	0.1348824	0.0037028
34	4.645	1.77998	0.1336058	0.0041353
35	4.682	1.61326	0.1321820	0.0046151
36	4.719	1.43791	0.1305357	0.0052311
37	4.756	1.25188	0.1285427	0.0060652
38	4.792	1.05257	0.1260005	0.0071783
39	4.829	0.83686	0.1225673	0.0086517
40	4.866	0.60099	0.1176204	0.0108228
41	4.902	0.34059	0.1098913	0.0159074
42	4.939	0.00000	0.0896156	0.0000000
43	4.976	0.00000	0.0896156	0.0000000
44	5.013	0.00000	0.0896156	0.0000000
45	5.049	0.00000	0.0896156	0.0000000
46	5.086	0.00000	0.0896156	0.0000000
47	5.123	0.00000	0.0896156	0.0000000
48	5.160	0.00000	0.0896156	0.0000000
49	5.196	0.00000	0.0896156	0.0000000
50	5.233	0.00000	0.0896156	0.0000000

Interferogram Profile 11	4 Profiles averaged	
X Location of Profile	4.99600 cm	St. Dev.= 0.01400 cm
Local Shock Angle	25.93782 °	St. Dev.= 0.12548 °
R Location of Shock	5.42400 cm	St. Dev.= 0.00060 cm
R Location of Model Surface	3.64800 cm	St. Dev.= 0.00003 cm

Approximated and Abel Transformed Data

I	Radius (cm)	Fringe Number	ρ/ρ_t	St. Dev. ρ/ρ_t
1	3.657	2.93254	0.0919007	0.0048530
2	3.700	3.03878	0.0940495	0.0039633
3	3.743	3.14780	0.0966082	0.0034310
4	3.786	3.25591	0.0994591	0.0034182
5	3.830	3.35999	0.1024977	0.0039153
6	3.873	3.45742	0.1056328	0.0047290
7	3.916	3.54606	0.1087857	0.0056711
8	3.960	3.62422	0.1118886	0.0066227
9	4.003	3.69061	0.1148852	0.0075130
10	4.047	3.74432	0.1177291	0.0082975
11	4.089	3.78479	0.1203839	0.0089476
12	4.133	3.81175	0.1228213	0.0094450
13	4.176	3.82521	0.1250221	0.0097800
14	4.220	3.82542	0.1269743	0.0099494
15	4.263	3.81282	0.1286728	0.0099553
16	4.306	3.78804	0.1301191	0.0098054
17	4.349	3.75183	0.1313201	0.0095117
18	4.393	3.70502	0.1322879	0.0090899
19	4.436	3.64855	0.1330389	0.0085594
20	4.479	3.58336	0.1335933	0.0079422
21	4.523	3.51038	0.1339733	0.0072625
22	4.566	3.43052	0.1342048	0.0065458
23	4.609	3.34461	0.1343137	0.0058185
24	4.653	3.25338	0.1343273	0.0051061
25	4.696	3.15739	0.1342716	0.0044317
26	4.740	3.05705	0.1341721	0.0038140
27	4.783	2.95256	0.1340506	0.0032658
28	4.826	2.84386	0.1339257	0.0027930
29	4.869	2.73062	0.1338103	0.0023980
30	4.913	2.61219	0.1337097	0.0020926
31	4.956	2.48757	0.1336193	0.0019159
32	4.999	2.35538	0.1335220	0.0019434
33	5.042	2.21382	0.1333841	0.0022418
34	5.086	2.06063	0.1331482	0.0028062
35	5.129	1.89309	0.1327276	0.0035782
36	5.172	1.70793	0.1319903	0.0044864
37	5.216	1.50132	0.1307383	0.0054563
38	5.259	1.26887	0.1286645	0.0064086
39	5.302	1.00555	0.1252626	0.0073010
40	5.346	0.70566	0.1196128	0.0083705
41	5.389	0.36281	0.1118725	0.0092877
42	5.432	0.00000	0.0896156	0.0000000
43	5.476	0.00000	0.0896156	0.0000000
44	5.519	0.00000	0.0896156	0.0000000
45	5.562	0.00000	0.0896156	0.0000000
46	5.606	0.00000	0.0896156	0.0000000
47	5.649	0.00000	0.0896156	0.0000000
48	5.692	0.00000	0.0896156	0.0000000
49	5.735	0.00000	0.0896156	0.0000000
50	5.779	0.00000	0.0896156	0.0000000

Interferogram Profile 12	4 Profiles averaged	
X Location of Profile	5.84800 cm	St. Dev.= 0.01900 cm
Local Shock Angle	25.93782 °	St. Dev.= 0.12548 °
R Location of Shock	5.81200 cm	St. Dev.= 0.00051 cm
R Location of Model Surface	3.83600 cm	St. Dev.= 0.00003 cm

Approximated and Abel Transformed Data

I	Radius (cm)	Fringe Number	ρ/ρ_t	St. Dev. ρ/ρ_t
1	3.844	3.37465	0.0894341	0.0133071
2	3.892	3.51646	0.0921030	0.0114698
3	3.941	3.66095	0.0952373	0.0098801
4	3.988	3.80340	0.0986971	0.0085156
5	4.037	3.93983	0.1023589	0.0073573
6	4.085	4.06690	0.1061144	0.0063884
7	4.133	4.18189	0.1098704	0.0055937
8	4.181	4.28267	0.1135468	0.0049581
9	4.230	4.36763	0.1170770	0.0044658
10	4.278	4.43567	0.1204062	0.0040984
11	4.326	4.48609	0.1234909	0.0038353
12	4.374	4.51865	0.1262986	0.0036544
13	4.422	4.53344	0.1288058	0.0035339
14	4.471	4.53085	0.1309995	0.0034542
15	4.519	4.51157	0.1328731	0.0033989
16	4.567	4.47651	0.1344293	0.0033563
17	4.615	4.42675	0.1356765	0.0033177
18	4.663	4.36353	0.1366297	0.0032780
19	4.712	4.28818	0.1373090	0.0032338
20	4.760	4.20209	0.1377396	0.0031846
21	4.808	4.10664	0.1379495	0.0031299
22	4.857	4.00320	0.1379701	0.0030715
23	4.905	3.89306	0.1378352	0.0030110
24	4.953	3.77738	0.1375786	0.0029501
25	5.001	3.65717	0.1372355	0.0028919
26	5.049	3.53322	0.1368392	0.0028385
27	5.098	3.40606	0.1364212	0.0027921
28	5.146	3.27597	0.1360095	0.0027559
29	5.194	3.14285	0.1356264	0.0027330
30	5.242	3.00622	0.1352883	0.0027269
31	5.290	2.86521	0.1350017	0.0027422
32	5.339	2.71844	0.1347613	0.0027844
33	5.387	2.56405	0.1345467	0.0028604
34	5.435	2.39961	0.1343171	0.0029792
35	5.483	2.22210	0.1340051	0.0031509
36	5.532	2.02784	0.1335069	0.0033918
37	5.580	1.81249	0.1326690	0.0037275
38	5.628	1.57095	0.1312662	0.0042104
39	5.676	1.29739	0.1289751	0.0049728
40	5.725	0.98512	0.1253966	0.0064431
41	5.773	0.62661	0.1210481	0.0108446
42	5.821	0.00000	0.0896156	0.0000000
43	5.869	0.00000	0.0896156	0.0000000
44	5.917	0.00000	0.0896156	0.0000000
45	5.965	0.00000	0.0896156	0.0000000
46	6.014	0.00000	0.0896156	0.0000000
47	6.062	0.00000	0.0896156	0.0000000
48	6.110	0.00000	0.0896156	0.0000000
49	6.158	0.00000	0.0896156	0.0000000
50	6.207	0.00000	0.0896156	0.0000000

Interferogram Profile 14	4 Profiles averaged	
X Location of Profile	6.85200 cm	St. Dev.= 0.01800 cm
Local Shock Angle	25.93782 °	St. Dev.= 0.12548 °
R Location of Shock	6.30500 cm	St. Dev.= 0.00105 cm
R Location of Model Surface	3.83900 cm	St. Dev.= 0.00000 cm

Approximated and Abel Transformed Data

I	Radius (cm)	Fringe Number	ρ/ρ_t	St. Dev. ρ/ρ_t
1	3.848	1.09391	0.0498375	0.0077593
2	3.908	1.32309	0.0502762	0.0079763
3	3.968	1.59176	0.0520877	0.0073612
4	4.029	1.89201	0.0552020	0.0061889
5	4.089	2.21466	0.0594862	0.0048495
6	4.149	2.54991	0.0647622	0.0036459
7	4.209	2.88789	0.0708236	0.0027518
8	4.269	3.21910	0.0774487	0.0021830
9	4.329	3.53480	0.0844126	0.0018140
10	4.390	3.82724	0.0914965	0.0015033
11	4.450	4.08995	0.0984963	0.0012131
12	4.510	4.31774	0.1052283	0.0010345
13	4.570	4.50692	0.1115336	0.0010873
14	4.631	4.65521	0.1172827	0.0013095
15	4.691	4.76172	0.1223759	0.0015342
16	4.751	4.82691	0.1267455	0.0016464
17	4.811	4.85243	0.1303549	0.0015880
18	4.872	4.84096	0.1331977	0.0013399
19	4.931	4.79604	0.1352953	0.0009198
20	4.992	4.72187	0.1366951	0.0004477
21	5.052	4.62310	0.1374653	0.0006325
22	5.112	4.50458	0.1376932	0.0013363
23	5.172	4.37114	0.1374782	0.0020793
24	5.233	4.22738	0.1369290	0.0027489
25	5.293	4.07744	0.1361576	0.0032709
26	5.353	3.92479	0.1352735	0.0035868
27	5.413	3.77211	0.1343791	0.0036579
28	5.474	3.62107	0.1335633	0.0034701
29	5.534	3.47226	0.1328976	0.0030429
30	5.594	3.32511	0.1324293	0.0024444
31	5.654	3.17786	0.1321770	0.0018262
32	5.714	3.02758	0.1321275	0.0014866
33	5.775	2.87030	0.1322290	0.0016520
34	5.835	2.70109	0.1323904	0.0020209
35	5.895	2.51436	0.1324752	0.0022074
36	5.955	2.30410	0.1323006	0.0020129
37	6.015	2.06430	0.1316325	0.0014898
38	6.075	1.78940	0.1301823	0.0015188
39	6.136	1.47490	0.1276104	0.0028848
40	6.196	1.11800	0.1236285	0.0048509
41	6.256	0.71837	0.1212937	0.0057207
42	6.316	0.00000	0.0896156	0.0000000
43	6.376	0.00000	0.0896156	0.0000000
44	6.436	0.00000	0.0896156	0.0000000
45	6.497	0.00000	0.0896156	0.0000000
46	6.557	0.00000	0.0896156	0.0000000
47	6.618	0.00000	0.0896156	0.0000000
48	6.678	0.00000	0.0896156	0.0000000
49	6.738	0.00000	0.0896156	0.0000000
50	6.798	0.00000	0.0896156	0.0000000

Interferogram Profile 15	4 Profiles averaged	
X Location of Profile	7.85400 cm	St. Dev.= 0.02300 cm
Local Shock Angle	25.93782 °	St. Dev.= 0.12548 °
R Location of Shock	6.75500 cm	St. Dev.= 0.00078 cm
R Location of Model Surface	3.83900 cm	St. Dev.= 0.00000 cm

Approximated and Abel Transformed Data

I	Radius (cm)	Fringe Number	ρ/ρ_t	St. Dev. ρ/ρ_t
1	3.855	0.62340	0.0549707	0.0051681
2	3.926	0.84534	0.0582832	0.0052550
3	3.997	1.03382	0.0600574	0.0061681
4	4.068	1.21043	0.0609991	0.0063760
5	4.139	1.39038	0.0616463	0.0059496
6	4.210	1.58352	0.0623947	0.0051896
7	4.281	1.79523	0.0635194	0.0043930
8	4.352	2.02733	0.0651952	0.0038001
9	4.424	2.27881	0.0675143	0.0035300
10	4.495	2.54649	0.0705026	0.0035249
11	4.566	2.82568	0.0741336	0.0036251
12	4.637	3.11066	0.0783411	0.0036973
13	4.708	3.39515	0.0830304	0.0036793
14	4.779	3.67269	0.0880873	0.0035672
15	4.850	3.93700	0.0933874	0.0033933
16	4.921	4.18220	0.0988023	0.0032089
17	4.992	4.40306	0.1042060	0.0030665
18	5.063	4.59512	0.1094799	0.0029994
19	5.134	4.75483	0.1145165	0.0030071
20	5.206	4.87958	0.1192223	0.0030574
21	5.277	4.96777	0.1235206	0.0031039
22	5.347	5.01871	0.1273527	0.0031052
23	5.419	5.03266	0.1306779	0.0030332
24	5.490	5.01065	0.1334746	0.0028797
25	5.561	4.95446	0.1357391	0.0026562
26	5.632	4.86643	0.1374841	0.0023945
27	5.703	4.74928	0.1387374	0.0021491
28	5.774	4.60601	0.1395395	0.0019855
29	5.846	4.43966	0.1399402	0.0019520
30	5.917	4.25311	0.1399956	0.0020391
31	5.988	4.04892	0.1397641	0.0021850
32	6.059	3.82906	0.1393001	0.0023272
33	6.130	3.59479	0.1386508	0.0024449
34	6.201	3.34638	0.1378474	0.0025874
35	6.272	3.08299	0.1368972	0.0028789
36	6.343	2.80242	0.1357737	0.0034460
37	6.414	2.50102	0.1344017	0.0042911
38	6.486	2.17348	0.1326411	0.0052400
39	6.557	1.81279	0.1302789	0.0059300
40	6.628	1.41003	0.1271319	0.0058005
41	6.699	0.95445	0.1249305	0.0055561
42	6.770	0.00000	0.0896156	0.0000000
43	6.841	0.00000	0.0896156	0.0000000
44	6.912	0.00000	0.0896156	0.0000000
45	6.983	0.00000	0.0896156	0.0000000
46	7.054	0.00000	0.0896156	0.0000000
47	7.125	0.00000	0.0896156	0.0000000
48	7.196	0.00000	0.0896156	0.0000000
49	7.267	0.00000	0.0896156	0.0000000
50	7.338	0.00000	0.0896156	0.0000000

Interferogram Profile 16	4 Profiles averaged	
X Location of Profile	8.85000 cm	St. Dev.= 0.02500 cm
Local Shock Angle	25.93782 °	St. Dev.= 0.12548 °
R Location of Shock	7.19900 cm	St. Dev.= 0.00081 cm
R Location of Model Surface	3.83900 cm	St. Dev.= 0.00000 cm

Approximated and Abel Transformed Data

I	Radius (cm)	Fringe Number	ρ/ρ_t	St. Dev. ρ/ρ_t
1	3.853	0.09995	0.0493654	0.0057020
2	3.935	0.35086	0.0514634	0.0054825
3	4.017	0.62000	0.0546152	0.0050555
4	4.099	0.88746	0.0580988	0.0048518
5	4.180	1.14263	0.0614695	0.0051767
6	4.263	1.38169	0.0644943	0.0057911
7	4.344	1.60539	0.0670952	0.0063191
8	4.427	1.81736	0.0693036	0.0065449
9	4.509	2.02264	0.0712203	0.0064087
10	4.591	2.22656	0.0729855	0.0059477
11	4.673	2.43392	0.0747527	0.0052530
12	4.755	2.64835	0.0766700	0.0044454
13	4.837	2.87196	0.0788658	0.0036605
14	4.919	3.10517	0.0814387	0.0030360
15	5.001	3.34661	0.0844513	0.0026765
16	5.082	3.59329	0.0879278	0.0025883
17	5.164	3.84076	0.0918536	0.0026722
18	5.246	4.08344	0.0961775	0.0028181
19	5.329	4.31495	0.1008167	0.0029747
20	5.411	4.52849	0.1056619	0.0031460
21	5.493	4.71731	0.1105845	0.0033635
22	5.575	4.87502	0.1154448	0.0036516
23	5.657	4.99605	0.1200995	0.0040069
24	5.739	5.07593	0.1244113	0.0043967
25	5.821	5.11164	0.1282563	0.0047715
26	5.903	5.10171	0.1315321	0.0050785
27	5.985	5.04641	0.1341653	0.0052733
28	6.067	4.94773	0.1361168	0.0053229
29	6.149	4.80924	0.1373862	0.0052090
30	6.231	4.63588	0.1380143	0.0049299
31	6.313	4.43355	0.1380832	0.0044968
32	6.395	4.20856	0.1377120	0.0039368
33	6.476	3.96692	0.1370511	0.0032976
34	6.559	3.71348	0.1362668	0.0026731
35	6.641	3.45085	0.1355237	0.0022696
36	6.723	3.17816	0.1349531	0.0024003
37	6.805	2.88963	0.1346074	0.0031169
38	6.887	2.57292	0.1343930	0.0041170
39	6.968	2.20736	0.1339761	0.0050117
40	7.051	1.76182	0.1327553	0.0053194
41	7.133	1.19259	0.1316966	0.0055516
42	7.214	0.00000	0.0896156	0.0000000
43	7.296	0.00000	0.0896156	0.0000000
44	7.378	0.00000	0.0896156	0.0000000
45	7.461	0.00000	0.0896156	0.0000000
46	7.542	0.00000	0.0896156	0.0000000
47	7.625	0.00000	0.0896156	0.0000000
48	7.706	0.00000	0.0896156	0.0000000
49	7.789	0.00000	0.0896156	0.0000000
50	7.870	0.00000	0.0896156	0.0000000

TABLE D.3 Interferometry Data for 20° Model at 1.7 atm Total Pressure

Filename		20D25P.TEX	
Model Cone Angle		20.0 °	
Total Pressure		1.7 atm	
Total Temperature		285.0 °K	
Interferogram profile	1	X Location	-5.033 cm
Interferogram profile	2	X Location	-4.044 cm
Interferogram profile	3	X Location	-3.030 cm
Interferogram profile	4	X Location	-2.038 cm
Interferogram profile	5	X Location	-1.038 cm
Interferogram profile	6	X Location	-0.026 cm
Interferogram profile	7	X Location	0.986 cm
Interferogram profile	8	X Location	1.975 cm
Interferogram profile	9	X Location	2.985 cm
Interferogram profile	10	X Location	3.981 cm
Interferogram profile	11	X Location	4.991 cm
Interferogram profile	12	X Location	5.627 cm
Interferogram profile	13	X Location	6.611 cm
Interferogram profile	14	X Location	7.615 cm
Interferogram profile	15	X Location	8.616 cm
Interferogram profile	17	X Location	6.116 cm

Interferogram Profile 1 1 Profile
X Location of Profile -5.03300 cm
Local Shock Angle 0.00000 °
R Location of Shock 0.00000 cm
R Location of Model Surface 2.54000 cm

Approximated and Abel Transformed Data

I	Radius (cm)	Fringe Number	ρ/ρ_t
1	2.542	-0.74801	0.0490234
2	2.567	-0.71036	0.0507348
3	2.591	-0.67367	0.0524116
4	2.616	-0.63793	0.0540541
5	2.640	-0.60315	0.0556626
6	2.664	-0.56933	0.0572373
7	2.689	-0.53647	0.0587782
8	2.713	-0.50456	0.0602859
9	2.738	-0.47362	0.0617603
10	2.762	-0.44363	0.0632017
11	2.787	-0.41459	0.0646101
12	2.811	-0.38652	0.0659856
13	2.836	-0.35940	0.0673286
14	2.860	-0.33324	0.0686387
15	2.884	-0.30804	0.0699162
16	2.909	-0.28380	0.0711613
17	2.933	-0.26051	0.0723737
18	2.958	-0.23818	0.0735536
19	2.982	-0.21681	0.0747007
20	3.007	-0.19639	0.0758152
21	3.031	-0.17694	0.0768968
22	3.056	-0.15844	0.0779455
23	3.080	-0.14090	0.0789613
24	3.104	-0.12431	0.0799437
25	3.129	-0.10869	0.0808928
26	3.153	-0.09402	0.0818084
27	3.178	-0.08031	0.0826904
28	3.202	-0.06755	0.0835388
29	3.227	-0.05576	0.0843536
30	3.251	-0.04492	0.0851353
31	3.276	-0.03504	0.0858849
32	3.300	-0.02612	0.0866049
33	3.324	-0.01815	0.0873008
34	3.349	-0.01114	0.0879858
35	3.373	-0.00509	0.0886995
36	3.398	0.00000	0.0896156
37	3.422	0.00000	0.0896156
38	3.447	0.00000	0.0896156
39	3.471	0.00000	0.0896156
40	3.496	0.00000	0.0896156
41	3.520	0.00000	0.0896156
42	3.544	0.00000	0.0896156
43	3.569	0.00000	0.0896156
44	3.593	0.00000	0.0896156
45	3.618	0.00000	0.0896156
46	3.642	0.00000	0.0896156
47	3.667	0.00000	0.0896156
48	3.691	0.00000	0.0896156
49	3.716	0.00000	0.0896156
50	3.740	0.00000	0.0896156

Interferogram Profile 2 1 Profile
X Location of Profile -4.04400 cm
Local Shock Angle 0.00000 °
R Location of Shock 0.00000 cm
R Location of Model Surface 2.54000 cm

Approximated and Abel Transformed Data

I	Radius (cm)	Fringe Number	ρ/ρ_t
1	2.542	-1.06316	0.0322689
2	2.567	-1.01017	0.0346752
3	2.591	-0.95852	0.0370327
4	2.616	-0.90822	0.0393418
5	2.640	-0.85927	0.0416028
6	2.664	-0.81166	0.0438160
7	2.689	-0.76541	0.0459817
8	2.713	-0.72050	0.0481004
9	2.738	-0.67694	0.0501720
10	2.762	-0.63472	0.0521967
11	2.787	-0.59386	0.0541750
12	2.811	-0.55434	0.0561068
13	2.836	-0.51617	0.0579922
14	2.860	-0.47935	0.0598312
15	2.884	-0.44388	0.0616241
16	2.909	-0.40975	0.0633705
17	2.933	-0.37697	0.0650709
18	2.958	-0.34554	0.0667246
19	2.982	-0.31546	0.0683320
20	3.007	-0.28673	0.0698925
21	3.031	-0.25934	0.0714061
22	3.056	-0.23330	0.0728724
23	3.080	-0.20861	0.0742910
24	3.104	-0.18527	0.0756616
25	3.129	-0.16328	0.0769837
26	3.153	-0.14263	0.0782565
27	3.178	-0.12333	0.0794797
28	3.202	-0.10538	0.0806520
29	3.227	-0.08878	0.0817730
30	3.251	-0.07352	0.0828415
31	3.276	-0.05961	0.0838564
32	3.300	-0.04705	0.0848165
33	3.324	-0.03584	0.0857212
34	3.349	-0.02598	0.0865692
35	3.373	-0.01746	0.0873617
36	3.398	-0.01029	0.0881037
37	3.422	-0.00447	0.0888168
38	3.447	0.00000	0.0896156
39	3.471	0.00000	0.0896156
40	3.496	0.00000	0.0896156
41	3.520	0.00000	0.0896156
42	3.544	0.00000	0.0896156
43	3.569	0.00000	0.0896156
44	3.593	0.00000	0.0896156
45	3.618	0.00000	0.0896156
46	3.642	0.00000	0.0896156
47	3.667	0.00000	0.0896156
48	3.691	0.00000	0.0896156
49	3.716	0.00000	0.0896156
50	3.740	0.00000	0.0896156

Interferogram Profile 3 1 Profile
X Location of Profile -3.03000 cm
Local Shock Angle 0.00000 °
R Location of Shock 0.00000 cm
R Location of Model Surface 2.54000 cm

Approximated and Abel Transformed Data

I	Radius (cm)	Fringe Number	ρ/ρ_t
1	2.542	-0.87637	0.0420576
2	2.567	-0.83226	0.0440628
3	2.591	-0.78927	0.0460273
4	2.616	-0.74740	0.0479518
5	2.640	-0.70665	0.0498362
6	2.664	-0.66703	0.0516811
7	2.689	-0.62853	0.0534865
8	2.713	-0.59115	0.0552529
9	2.738	-0.55489	0.0569803
10	2.762	-0.51975	0.0586690
11	2.787	-0.48574	0.0603192
12	2.811	-0.45285	0.0619307
13	2.836	-0.42108	0.0635040
14	2.860	-0.39043	0.0650391
15	2.884	-0.36090	0.0665358
16	2.909	-0.33250	0.0679945
17	2.933	-0.30521	0.0694149
18	2.958	-0.27905	0.0707974
19	2.982	-0.25401	0.0721412
20	3.007	-0.23009	0.0734470
21	3.031	-0.20730	0.0747143
22	3.056	-0.18563	0.0759429
23	3.080	-0.16507	0.0771329
24	3.104	-0.14565	0.0782840
25	3.129	-0.12734	0.0793961
26	3.153	-0.11015	0.0804686
27	3.178	-0.09409	0.0815021
28	3.202	-0.07915	0.0824960
29	3.227	-0.06533	0.0834506
30	3.251	-0.05263	0.0843664
31	3.276	-0.04105	0.0852448
32	3.300	-0.03060	0.0860884
33	3.324	-0.02127	0.0869035
34	3.349	-0.01305	0.0877060
35	3.373	-0.00597	0.0885424
36	3.398	0.00000	0.0896156
37	3.422	0.00000	0.0896156
38	3.447	0.00000	0.0896156
39	3.471	0.00000	0.0896156
40	3.496	0.00000	0.0896156
41	3.520	0.00000	0.0896156
42	3.544	0.00000	0.0896156
43	3.569	0.00000	0.0896156
44	3.593	0.00000	0.0896156
45	3.618	0.00000	0.0896156
46	3.642	0.00000	0.0896156
47	3.667	0.00000	0.0896156
48	3.691	0.00000	0.0896156
49	3.716	0.00000	0.0896156
50	3.740	0.00000	0.0896156

Interferogram Profile 4 1 Profile
X Location of Profile -2.03800 cm
Local Shock Angle 0.00000 °
R Location of Shock 0.00000 cm
R Location of Model Surface 2.54000 cm

Approximated and Abel Transformed Data

I	Radius (cm)	Fringe Number	ρ/ρ_t
1	2.542	-0.85592	0.0431677
2	2.567	-0.81283	0.0451260
3	2.591	-0.77085	0.0470447
4	2.616	-0.72996	0.0489242
5	2.640	-0.69016	0.0507647
6	2.664	-0.65146	0.0525665
7	2.689	-0.61386	0.0543298
8	2.713	-0.57735	0.0560549
9	2.738	-0.54194	0.0577420
10	2.762	-0.50762	0.0593913
11	2.787	-0.47440	0.0610029
12	2.811	-0.44228	0.0625769
13	2.836	-0.41125	0.0641134
14	2.860	-0.38131	0.0656126
15	2.884	-0.35248	0.0670745
16	2.909	-0.32474	0.0684991
17	2.933	-0.29809	0.0698865
18	2.958	-0.27254	0.0712365
19	2.982	-0.24808	0.0725491
20	3.007	-0.22472	0.0738244
21	3.031	-0.20246	0.0750621
22	3.056	-0.18129	0.0762621
23	3.080	-0.16122	0.0774242
24	3.104	-0.14225	0.0785485
25	3.129	-0.12437	0.0796345
26	3.153	-0.10758	0.0806822
27	3.178	-0.09189	0.0816915
28	3.202	-0.07730	0.0826622
29	3.227	-0.06380	0.0835945
30	3.251	-0.05140	0.0844890
31	3.276	-0.04009	0.0853466
32	3.300	-0.02988	0.0861707
33	3.324	-0.02077	0.0869669
34	3.349	-0.01275	0.0877506
35	3.373	-0.00583	0.0885674
36	3.398	0.00000	0.0896156
37	3.422	0.00000	0.0896156
38	3.447	0.00000	0.0896156
39	3.471	0.00000	0.0896156
40	3.496	0.00000	0.0896156
41	3.520	0.00000	0.0896156
42	3.544	0.00000	0.0896156
43	3.569	0.00000	0.0896156
44	3.593	0.00000	0.0896156
45	3.618	0.00000	0.0896156
46	3.642	0.00000	0.0896156
47	3.667	0.00000	0.0896156
48	3.691	0.00000	0.0896156
49	3.716	0.00000	0.0896156
50	3.740	0.00000	0.0896156

Interferogram Profile 5 1 Profile
X Location of Profile -1.03800 cm
Local Shock Angle 0.00000 °
R Location of Shock 0.00000 cm
R Location of Model Surface 2.54000 cm

Approximated and Abel Transformed Data

I	Radius (cm)	Fringe Number	ρ/ρ_t
1	2.542	-0.75438	0.0490529
2	2.567	-0.71696	0.0507510
3	2.591	-0.68050	0.0524145
4	2.616	-0.64499	0.0540438
5	2.640	-0.61042	0.0556392
6	2.664	-0.57681	0.0572007
7	2.689	-0.54416	0.0587287
8	2.713	-0.51245	0.0602233
9	2.738	-0.48170	0.0616847
10	2.762	-0.45189	0.0631130
11	2.787	-0.42304	0.0645084
12	2.811	-0.39514	0.0658708
13	2.836	-0.36819	0.0672004
14	2.860	-0.34220	0.0684972
15	2.884	-0.31715	0.0697612
16	2.909	-0.29306	0.0709926
17	2.933	-0.26992	0.0721909
18	2.958	-0.24773	0.0733564
19	2.982	-0.22649	0.0744890
20	3.007	-0.20620	0.0755883
21	3.031	-0.18686	0.0766541
22	3.056	-0.16848	0.0776865
23	3.080	-0.15105	0.0786848
24	3.104	-0.13457	0.0796490
25	3.129	-0.11904	0.0805784
26	3.153	-0.10446	0.0814726
27	3.178	-0.09084	0.0823311
28	3.202	-0.07816	0.0831532
29	3.227	-0.06644	0.0839380
30	3.251	-0.05567	0.0846844
31	3.276	-0.04585	0.0853917
32	3.300	-0.03698	0.0860582
33	3.324	-0.02907	0.0866823
34	3.349	-0.02210	0.0872619
35	3.373	-0.01609	0.0877944
36	3.398	-0.01103	0.0882766
37	3.422	-0.00692	0.0887036
38	3.447	-0.00376	0.0890689
39	3.471	-0.00156	0.0893617
40	3.496	-0.00030	0.0895621
41	3.520	0.00000	0.0896156
42	3.544	0.00000	0.0896156
43	3.569	0.00000	0.0896156
44	3.593	0.00000	0.0896156
45	3.618	0.00000	0.0896156
46	3.642	0.00000	0.0896156
47	3.667	0.00000	0.0896156
48	3.691	0.00000	0.0896156
49	3.716	0.00000	0.0896156
50	3.740	0.00000	0.0896156

Interferogram Profile 6	4 Profiles averaged	
X Location of Profile	-0.02600 cm	St. Dev.= 0.01900 cm
Local Shock Angle	15.81250 °	St. Dev.= 18.25903 °
R Location of Shock	1.59900 cm	St. Dev.= 0.01846 cm
R Location of Model Surface	2.54000 cm	St. Dev.= 0.00001 cm

Approximated and Abel Transformed Data

I	Radius (cm)	Fringe Number	ρ/ρ_t	St. Dev. ρ/ρ_t
1	2.545	-0.18061	0.0779079	0.0142074
2	2.570	-0.16769	0.0785069	0.0133201
3	2.595	-0.15507	0.0790866	0.0125628
4	2.622	-0.14269	0.0796565	0.0119090
5	2.647	-0.13051	0.0802241	0.0113409
6	2.672	-0.11853	0.0807957	0.0108479
7	2.698	-0.10672	0.0813763	0.0104263
8	2.723	-0.09512	0.0819696	0.0100766
9	2.749	-0.08375	0.0825781	0.0098024
10	2.774	-0.07265	0.0832030	0.0096082
11	2.799	-0.06186	0.0838444	0.0094971
12	2.825	-0.05147	0.0845011	0.0094687
13	2.851	-0.04153	0.0851710	0.0095182
14	2.876	-0.03213	0.0858505	0.0096348
15	2.901	-0.02337	0.0865351	0.0098023
16	2.927	-0.01535	0.0872187	0.0099990
17	2.952	-0.00816	0.0878940	0.0101982
18	2.978	-0.00193	0.0885521	0.0103684
19	3.003	0.00324	0.0891824	0.0104721
20	3.029	0.00721	0.0897725	0.0104641
21	3.054	0.00987	0.0903085	0.0102872
22	3.080	0.01107	0.0907771	0.0098629
23	3.105	0.01069	0.0911792	0.0090744
24	3.131	0.00860	0.0916282	0.0077511
25	3.156	0.00023	0.0907967	0.0060944
26	3.182	-0.01000	0.0887897	0.0035738
27	3.208	-0.00859	0.0888712	0.0032819
28	3.233	-0.00725	0.0889560	0.0029712
29	3.258	-0.00596	0.0890429	0.0026471
30	3.284	-0.00476	0.0891305	0.0023153
31	3.310	-0.00365	0.0892173	0.0019816
32	3.335	-0.00267	0.0893017	0.0016518
33	3.360	-0.00181	0.0893820	0.0013320
34	3.386	-0.00109	0.0894563	0.0010285
35	3.411	-0.00051	0.0895227	0.0007479
36	3.437	-0.00010	0.0895788	0.0004977
37	3.462	0.00014	0.0896214	0.0002875
38	3.488	0.00022	0.0896455	0.0001310
39	3.513	0.00013	0.0896385	0.0000458
40	3.539	0.00000	0.0896156	0.0000000
41	3.564	0.00000	0.0896156	0.0000000
42	3.590	0.00000	0.0896156	0.0000000
43	3.616	0.00000	0.0896156	0.0000000
44	3.641	0.00000	0.0896156	0.0000000
45	3.666	0.00000	0.0896156	0.0000000
46	3.692	0.00000	0.0896156	0.0000000
47	3.717	0.00000	0.0896156	0.0000000
48	3.743	0.00000	0.0896156	0.0000000
49	3.768	0.00000	0.0896156	0.0000000
50	3.793	0.00000	0.0896156	0.0000000

Interferogram Profile 7	4 Profiles averaged	
X Location of Profile	0.98600 cm	St. Dev.= 0.04100 cm
Local Shock Angle	31.56255 °	St. Dev.= 0.12490 °
R Location of Shock	3.76400 cm	St. Dev.= 0.00059 cm
R Location of Model Surface	2.89900 cm	St. Dev.= 0.00015 cm

Approximated and Abel Transformed Data

I	Radius (cm)	Fringe Number	ρ/ρ_t	St. Dev. ρ/ρ_t
1	2.901	0.52811	0.0877877	0.0092537
2	2.923	0.54276	0.0880225	0.0092474
3	2.944	0.55850	0.0883172	0.0090050
4	2.965	0.57551	0.0887069	0.0085488
5	2.986	0.59384	0.0892216	0.0079348
6	3.007	0.61352	0.0898855	0.0072337
7	3.028	0.63451	0.0907176	0.0065239
8	3.049	0.65669	0.0917324	0.0058855
9	3.071	0.67992	0.0929389	0.0053930
10	3.092	0.70398	0.0943422	0.0050997
11	3.113	0.72863	0.0959427	0.0050184
12	3.134	0.75359	0.0977366	0.0051147
13	3.155	0.77854	0.0997164	0.0053260
14	3.176	0.80312	0.1018708	0.0055860
15	3.197	0.82696	0.1041850	0.0058420
16	3.218	0.84967	0.1066407	0.0060584
17	3.239	0.87083	0.1092168	0.0062149
18	3.261	0.89002	0.1118886	0.0063028
19	3.282	0.90682	0.1146295	0.0063219
20	3.303	0.92080	0.1174097	0.0062782
21	3.324	0.93152	0.1201972	0.0061816
22	3.345	0.93857	0.1229577	0.0060447
23	3.366	0.94153	0.1256546	0.0058809
24	3.387	0.94003	0.1282500	0.0057057
25	3.409	0.93367	0.1307032	0.0055355
26	3.430	0.92212	0.1329722	0.0053901
27	3.451	0.90506	0.1350136	0.0052943
28	3.472	0.88221	0.1367808	0.0052801
29	3.493	0.85333	0.1382265	0.0053857
30	3.514	0.81821	0.1393000	0.0056514
31	3.535	0.77671	0.1399482	0.0061095
32	3.556	0.72873	0.1401133	0.0067731
33	3.578	0.67423	0.1397311	0.0076320
34	3.599	0.61322	0.1387292	0.0086518
35	3.620	0.54581	0.1370193	0.0097728
36	3.641	0.47215	0.1344887	0.0109079
37	3.662	0.39247	0.1309787	0.0119365
38	3.683	0.30709	0.1262382	0.0126969
39	3.704	0.21642	0.1198077	0.0130195
40	3.725	0.12094	0.1106244	0.0131413
41	3.746	0.02373	0.0969552	0.0177757
42	3.768	0.00000	0.0896156	0.0000000
43	3.789	0.00000	0.0896156	0.0000000
44	3.810	0.00000	0.0896156	0.0000000
45	3.831	0.00000	0.0896156	0.0000000
46	3.852	0.00000	0.0896156	0.0000000
47	3.873	0.00000	0.0896156	0.0000000
48	3.894	0.00000	0.0896156	0.0000000
49	3.915	0.00000	0.0896156	0.0000000
50	3.937	0.00000	0.0896156	0.0000000

Interferogram Profile 8	4 Profiles averaged	
X Location of Profile	1.97500 cm	St. Dev.= 0.04200 cm
Local Shock Angle	31.56255 °	St. Dev.= 0.12490 °
R Location of Shock	4.31200 cm	St. Dev.= 0.00032 cm
R Location of Model Surface	3.25900 cm	St. Dev.= 0.00015 cm

Approximated and Abel Transformed Data

I	Radius (cm)	Fringe Number	ρ/ρ_t	St. Dev. ρ/ρ_t
1	3.263	1.77673	0.1180238	0.0208244
2	3.289	1.77359	0.1169155	0.0168125
3	3.314	1.77515	0.1161340	0.0135440
4	3.340	1.78150	0.1157496	0.0108259
5	3.366	1.79242	0.1158055	0.0085401
6	3.391	1.80751	0.1163212	0.0066393
7	3.417	1.82614	0.1172962	0.0051499
8	3.443	1.84757	0.1187133	0.0041738
9	3.469	1.87094	0.1205414	0.0038216
10	3.494	1.89538	0.1227379	0.0040337
11	3.520	1.91993	0.1252527	0.0045667
12	3.546	1.94369	0.1280294	0.0051967
13	3.571	1.96575	0.1310080	0.0057949
14	3.597	1.98527	0.1341272	0.0062971
15	3.622	2.00146	0.1373260	0.0066728
16	3.649	2.01365	0.1405460	0.0069082
17	3.674	2.02121	0.1437313	0.0069986
18	3.700	2.02366	0.1468321	0.0069454
19	3.725	2.02059	0.1498037	0.0067533
20	3.751	2.01169	0.1526089	0.0064291
21	3.777	1.99676	0.1552173	0.0059824
22	3.802	1.97568	0.1576066	0.0054213
23	3.828	1.94841	0.1597619	0.0047568
24	3.854	1.91497	0.1616759	0.0039986
25	3.880	1.87541	0.1633484	0.0031615
26	3.905	1.82980	0.1647842	0.0022844
27	3.931	1.77820	0.1659924	0.0015310
28	3.957	1.72062	0.1669848	0.0015148
29	3.982	1.65701	0.1677705	0.0025222
30	4.008	1.58719	0.1683551	0.0040424
31	4.034	1.51080	0.1687325	0.0058871
32	4.059	1.42731	0.1688792	0.0080182
33	4.085	1.33593	0.1687429	0.0104168
34	4.111	1.23552	0.1682292	0.0130421
35	4.137	1.12463	0.1671750	0.0158103
36	4.162	1.00134	0.1653160	0.0185753
37	4.188	0.86324	0.1622123	0.0210989
38	4.214	0.70738	0.1571153	0.0230526
39	4.239	0.53016	0.1486504	0.0241407
40	4.265	0.32726	0.1380137	0.0177209
41	4.291	0.13749	0.1329913	0.0136693
42	4.317	0.00000	0.0896156	0.0000000
43	4.342	0.00000	0.0896156	0.0000000
44	4.368	0.00000	0.0896156	0.0000000
45	4.394	0.00000	0.0896156	0.0000000
46	4.419	0.00000	0.0896156	0.0000000
47	4.445	0.00000	0.0896156	0.0000000
48	4.470	0.00000	0.0896156	0.0000000
49	4.497	0.00000	0.0896156	0.0000000
50	4.522	0.00000	0.0896156	0.0000000

Interferogram Profile 9	4 Profiles averaged	
X Location of Profile	2.98500 cm	St. Dev.= 0.03200 cm
Local Shock Angle	31.56255 °	St. Dev.= 0.12490 °
R Location of Shock	4.94700 cm	St. Dev.= 0.00025 cm
R Location of Model Surface	3.62600 cm	St. Dev.= 0.00011 cm

Approximated and Abel Transformed Data

I	Radius (cm)	Fringe Number	ρ/ρ_t	St. Dev. ρ/ρ_t
1	3.632	2.46810	0.1202132	0.0060433
2	3.664	2.48243	0.1204754	0.0075946
3	3.697	2.50044	0.1209997	0.0090904
4	3.729	2.52239	0.1218817	0.0102935
5	3.761	2.54808	0.1231805	0.0111444
6	3.793	2.57697	0.1249233	0.0116282
7	3.825	2.60823	0.1271103	0.0117491
8	3.858	2.64083	0.1297192	0.0115274
9	3.890	2.67357	0.1327084	0.0110018
10	3.922	2.70517	0.1360224	0.0102305
11	3.954	2.73435	0.1395938	0.0092969
12	3.986	2.75979	0.1433479	0.0083107
13	4.019	2.78026	0.1472052	0.0074125
14	4.051	2.79463	0.1510835	0.0067639
15	4.083	2.80186	0.1549028	0.0064990
16	4.115	2.80107	0.1585850	0.0066496
17	4.148	2.79158	0.1620578	0.0071153
18	4.180	2.77283	0.1652555	0.0077329
19	4.212	2.74449	0.1681214	0.0083532
20	4.244	2.70640	0.1706084	0.0088691
21	4.276	2.65857	0.1726807	0.0092184
22	4.309	2.60122	0.1743137	0.0093755
23	4.341	2.53468	0.1754943	0.0093474
24	4.373	2.45946	0.1762226	0.0091715
25	4.405	2.37614	0.1765097	0.0089094
26	4.438	2.28539	0.1763762	0.0086446
27	4.470	2.18793	0.1758531	0.0084618
28	4.502	2.08443	0.1749797	0.0084250
29	4.534	1.97553	0.1737967	0.0085497
30	4.566	1.86175	0.1723487	0.0087943
31	4.599	1.74341	0.1706737	0.0090775
32	4.631	1.62061	0.1687994	0.0093132
33	4.663	1.49311	0.1667333	0.0094462
34	4.696	1.36026	0.1644475	0.0094894
35	4.728	1.22094	0.1618629	0.0095590
36	4.760	1.07344	0.1588146	0.0098777
37	4.792	0.91538	0.1550024	0.0106908
38	4.824	0.74361	0.1498961	0.0120788
39	4.857	0.55407	0.1425440	0.0138400
40	4.889	0.34172	0.1312528	0.0157817
41	4.921	0.10108	0.1216568	0.0231430
42	4.953	0.00000	0.0896156	0.0000000
43	4.985	0.00000	0.0896156	0.0000000
44	5.018	0.00000	0.0896156	0.0000000
45	5.050	0.00000	0.0896156	0.0000000
46	5.082	0.00000	0.0896156	0.0000000
47	5.114	0.00000	0.0896156	0.0000000
48	5.146	0.00000	0.0896156	0.0000000
49	5.179	0.00000	0.0896156	0.0000000
50	5.211	0.00000	0.0896156	0.0000000

Interferogram Profile 10	4 Profiles averaged	
X Location of Profile	3.98100 cm	St. Dev.= 0.03400 cm
Local Shock Angle	31.56255 °	St. Dev.= 0.12490 °
R Location of Shock	5.55100 cm	St. Dev.= 0.00034 cm
R Location of Model Surface	3.98900 cm	St. Dev.= 0.00013 cm

Approximated and Abel Transformed Data

I	Radius (cm)	Fringe Number	ρ/ρ_t	St. Dev. ρ/ρ_t
1	3.991	2.89721	0.1142358	0.0154985
2	4.029	2.93426	0.1152601	0.0163199
3	4.068	2.97564	0.1166185	0.0166511
4	4.106	3.02178	0.1184748	0.0163514
5	4.144	3.07209	0.1209020	0.0154812
6	4.182	3.12525	0.1239025	0.0141536
7	4.220	3.17950	0.1274271	0.0124941
8	4.259	3.23279	0.1313898	0.0106308
9	4.297	3.28308	0.1356823	0.0086930
10	4.335	3.32832	0.1401831	0.0068162
11	4.373	3.36668	0.1447678	0.0051563
12	4.411	3.39655	0.1493152	0.0039132
13	4.449	3.41664	0.1537137	0.0033098
14	4.488	3.42596	0.1578644	0.0033634
15	4.526	3.42387	0.1616846	0.0037628
16	4.564	3.41005	0.1651097	0.0041990
17	4.602	3.38449	0.1680926	0.0045205
18	4.641	3.34744	0.1706057	0.0046797
19	4.679	3.29942	0.1726389	0.0046793
20	4.717	3.24113	0.1741976	0.0045477
21	4.755	3.17341	0.1753044	0.0043238
22	4.794	3.09719	0.1759928	0.0040511
23	4.832	3.01346	0.1763078	0.0037725
24	4.870	2.92318	0.1763014	0.0035266
25	4.908	2.82726	0.1760319	0.0033474
26	4.946	2.72647	0.1755591	0.0032630
27	4.985	2.62144	0.1749402	0.0032931
28	5.023	2.51256	0.1742315	0.0034418
29	5.061	2.39996	0.1734777	0.0036942
30	5.099	2.28345	0.1727116	0.0040163
31	5.137	2.16252	0.1719497	0.0043576
32	5.175	2.03622	0.1711826	0.0046633
33	5.214	1.90317	0.1703693	0.0048771
34	5.252	1.76150	0.1694241	0.0049553
35	5.290	1.60880	0.1681987	0.0048764
36	5.328	1.44203	0.1664563	0.0046691
37	5.366	1.25754	0.1638216	0.0044581
38	5.405	1.05089	0.1596953	0.0045812
39	5.443	0.81684	0.1530863	0.0057991
40	5.481	0.54926	0.1423653	0.0096542
41	5.519	0.24094	0.1367117	0.0108850
42	5.558	0.00000	0.0896156	0.0000000
43	5.596	0.00000	0.0896156	0.0000000
44	5.634	0.00000	0.0896156	0.0000000
45	5.672	0.00000	0.0896156	0.0000000
46	5.711	0.00000	0.0896156	0.0000000
47	5.748	0.00000	0.0896156	0.0000000
48	5.787	0.00000	0.0896156	0.0000000
49	5.825	0.00000	0.0896156	0.0000000
50	5.863	0.00000	0.0896156	0.0000000

Interferogram Profile 11	4 Profiles averaged	
X Location of Profile	4.99100 cm	St. Dev.= 0.04000 cm
Local Shock Angle	31.56255 °	St. Dev.= 0.12490 °
R Location of Shock	6.18100 cm	St. Dev.= 0.00034 cm
R Location of Model Surface	4.35700 cm	St. Dev.= 0.00015 cm

Approximated and Abel Transformed Data

I	Radius (cm)	Fringe Number	ρ/ρ_t	St. Dev. ρ/ρ_t
1	4.364	3.91147	0.1345487	0.0125314
2	4.408	3.91693	0.1345836	0.0088415
3	4.453	3.92929	0.1351765	0.0057284
4	4.497	3.94713	0.1362962	0.0036071
5	4.542	3.96891	0.1378986	0.0034678
6	4.586	3.99300	0.1399288	0.0048435
7	4.631	4.01777	0.1423245	0.0064278
8	4.676	4.04159	0.1450173	0.0077711
9	4.720	4.06289	0.1479354	0.0087566
10	4.765	4.08019	0.1510061	0.0093596
11	4.809	4.09213	0.1541558	0.0095945
12	4.854	4.09748	0.1573140	0.0094973
13	4.898	4.09521	0.1604133	0.0091200
14	4.942	4.08442	0.1633910	0.0085245
15	4.987	4.06444	0.1661905	0.0077820
16	5.032	4.03476	0.1687624	0.0069685
17	5.076	3.99511	0.1710649	0.0061634
18	5.121	3.94538	0.1730651	0.0054430
19	5.166	3.88565	0.1747386	0.0048700
20	5.210	3.81618	0.1760716	0.0044774
21	5.255	3.73737	0.1770585	0.0042524
22	5.299	3.64976	0.1777037	0.0041417
23	5.344	3.55400	0.1780214	0.0040761
24	5.388	3.45081	0.1780329	0.0039985
25	5.433	3.34093	0.1777689	0.0038781
26	5.478	3.22513	0.1772648	0.0037092
27	5.522	3.10409	0.1765632	0.0035120
28	5.566	2.97841	0.1757087	0.0033206
29	5.611	2.84853	0.1747456	0.0031710
30	5.655	2.71467	0.1737176	0.0030842
31	5.700	2.57678	0.1726601	0.0030549
32	5.744	2.43446	0.1715972	0.0030567
33	5.789	2.28685	0.1705349	0.0030688
34	5.834	2.13264	0.1694523	0.0031069
35	5.878	1.96990	0.1682871	0.0032475
36	5.923	1.79604	0.1669225	0.0035945
37	5.967	1.60767	0.1651597	0.0041851
38	6.012	1.40060	0.1626875	0.0049064
39	6.056	1.16960	0.1590566	0.0055322
40	6.101	0.90842	0.1538357	0.0060242
41	6.146	0.60960	0.1501171	0.0063382
42	6.190	0.00000	0.0896156	0.0000000
43	6.234	0.00000	0.0896156	0.0000000
44	6.279	0.00000	0.0896156	0.0000000
45	6.323	0.00000	0.0896156	0.0000000
46	6.368	0.00000	0.0896156	0.0000000
47	6.413	0.00000	0.0896156	0.0000000
48	6.457	0.00000	0.0896156	0.0000000
49	6.502	0.00000	0.0896156	0.0000000
50	6.546	0.00000	0.0896156	0.0000000

Interferogram Profile 12	4 Profiles averaged	
X Location of Profile	5.62700 cm	St. Dev.= 0.01800 cm
Local Shock Angle	31.56255 °	St. Dev.= 0.12490 °
R Location of Shock	6.60400 cm	St. Dev.= 0.00034 cm
R Location of Model Surface	4.58600 cm	St. Dev.= 0.00004 cm

Approximated and Abel Transformed Data

I	Radius (cm)	Fringe Number	ρ/ρ_t	St. Dev. ρ/ρ_t
1	4.593	4.24796	0.1147842	0.0164642
2	4.642	4.36269	0.1204541	0.0133060
3	4.692	4.47184	0.1265586	0.0109099
4	4.741	4.57133	0.1328215	0.0087755
5	4.790	4.65811	0.1390186	0.0067538
6	4.840	4.73004	0.1449719	0.0049222
7	4.888	4.78576	0.1505458	0.0035393
8	4.938	4.82463	0.1556412	0.0030098
9	4.987	4.84655	0.1601923	0.0033683
10	5.037	4.85191	0.1641618	0.0040694
11	5.086	4.84151	0.1675375	0.0047152
12	5.135	4.81639	0.1703273	0.0051679
13	5.185	4.77786	0.1725579	0.0054121
14	5.234	4.72735	0.1742689	0.0054908
15	5.283	4.66637	0.1755119	0.0054779
16	5.332	4.59642	0.1763465	0.0054573
17	5.382	4.51897	0.1768369	0.0055008
18	5.431	4.43539	0.1770510	0.0056440
19	5.480	4.34692	0.1770564	0.0058759
20	5.529	4.25460	0.1769202	0.0061463
21	5.579	4.15927	0.1767023	0.0063905
22	5.628	4.06154	0.1764603	0.0065474
23	5.677	3.96174	0.1762426	0.0065709
24	5.726	3.85997	0.1760879	0.0064328
25	5.776	3.75601	0.1760240	0.0061284
26	5.825	3.64939	0.1760678	0.0056732
27	5.874	3.53936	0.1762213	0.0051026
28	5.923	3.42491	0.1764729	0.0044718
29	5.973	3.30479	0.1767950	0.0038500
30	6.022	3.17751	0.1771427	0.0033115
31	6.071	3.04141	0.1774543	0.0029161
32	6.120	2.89467	0.1776492	0.0026881
33	6.169	2.73534	0.1776250	0.0026255
34	6.219	2.56144	0.1772577	0.0027599
35	6.268	2.37094	0.1764000	0.0031873
36	6.318	2.16188	0.1748733	0.0039876
37	6.367	1.93243	0.1724726	0.0050969
38	6.416	1.68091	0.1689546	0.0062633
39	6.465	1.40594	0.1640815	0.0070194
40	6.515	1.10648	0.1578686	0.0067038
41	6.564	0.78193	0.1536466	0.0063186
42	6.613	0.00000	0.0896156	0.0000000
43	6.662	0.00000	0.0896156	0.0000000
44	6.712	0.00000	0.0896156	0.0000000
45	6.761	0.00000	0.0896156	0.0000000
46	6.810	0.00000	0.0896156	0.0000000
47	6.859	0.00000	0.0896156	0.0000000
48	6.909	0.00000	0.0896156	0.0000000
49	6.958	0.00000	0.0896156	0.0000000
50	7.007	0.00000	0.0896156	0.0000000

Interferogram Profile 13 4 Profiles averaged

X Location of Profile	6.61100 cm	St. Dev.= 0.01900 cm
Local Shock Angle	31.56255 °	St. Dev.= 0.12490 °
R Location of Shock	7.19300 cm	St. Dev.= 0.00039 cm
R Location of Model Surface	4.59200 cm	St. Dev.= 0.00000 cm

Approximated and Abel Transformed Data

I	Radius (cm)	Fringe Number	ρ/ρ_t	St. Dev. ρ/ρ_t
1	4.609	2.44334	0.0735456	0.0102327
2	4.672	2.54101	0.0748941	0.0092122
3	4.735	2.63557	0.0754378	0.0084620
4	4.799	2.73554	0.0757631	0.0077794
5	4.863	2.84669	0.0763362	0.0073186
6	4.926	2.97236	0.0775076	0.0072691
7	4.989	3.11364	0.0795192	0.0076396
8	5.053	3.26978	0.0825144	0.0082475
9	5.116	3.43849	0.0865473	0.0088675
10	5.179	3.61625	0.0915959	0.0093359
11	5.243	3.79871	0.0975738	0.0095703
12	5.306	3.98093	0.1043429	0.0095559
13	5.369	4.15774	0.1117266	0.0093273
14	5.433	4.32403	0.1195223	0.0089489
15	5.496	4.47494	0.1275130	0.0084987
16	5.559	4.60612	0.1354794	0.0080484
17	5.623	4.71391	0.1432098	0.0076453
18	5.686	4.79543	0.1505097	0.0073001
19	5.750	4.84873	0.1572094	0.0069873
20	5.813	4.87277	0.1631703	0.0066613
21	5.876	4.86748	0.1682917	0.0062724
22	5.940	4.83369	0.1725111	0.0057865
23	6.003	4.77307	0.1758089	0.0051927
24	6.066	4.68794	0.1782058	0.0045087
25	6.129	4.58122	0.1797626	0.0037825
26	6.193	4.45613	0.1805759	0.0031080
27	6.256	4.31604	0.1807716	0.0026425
28	6.319	4.16419	0.1804981	0.0025839
29	6.383	4.00350	0.1799175	0.0029902
30	6.446	3.83622	0.1791938	0.0037183
31	6.510	3.66373	0.1784788	0.0046055
32	6.573	3.48631	0.1778994	0.0055321
33	6.636	3.30287	0.1775387	0.0063954
34	6.700	3.11078	0.1774164	0.0070832
35	6.763	2.90576	0.1774684	0.0074784
36	6.826	2.68174	0.1775156	0.0074990
37	6.890	2.43089	0.1772362	0.0071999
38	6.954	2.14368	0.1761248	0.0069560
39	7.017	1.80908	0.1734845	0.0074888
40	7.080	1.41484	0.1686902	0.0090756
41	7.143	0.94794	0.1652459	0.0102507
42	7.207	0.00000	0.0896156	0.0000000
43	7.270	0.00000	0.0896156	0.0000000
44	7.333	0.00000	0.0896156	0.0000000
45	7.397	0.00000	0.0896156	0.0000000
46	7.460	0.00000	0.0896156	0.0000000
47	7.524	0.00000	0.0896156	0.0000000
48	7.587	0.00000	0.0896156	0.0000000
49	7.650	0.00000	0.0896156	0.0000000
50	7.714	0.00000	0.0896156	0.0000000

Interferogram Profile 14	4 Profiles averaged	
X Location of Profile	7.61500 cm	St. Dev.= 0.01600 cm
Local Shock Angle	31.56255 °	St. Dev.= 0.12490 °
R Location of Shock	7.80400 cm	St. Dev.= 0.00039 cm
R Location of Model Surface	4.59200 cm	St. Dev.= 0.00000 cm

Approximated and Abel Transformed Data

I	Radius (cm)	Fringe Number	ρ/ρ_t	St. Dev. ρ/ρ_t
1	4.614	1.57631	0.0633850	0.0076265
2	4.692	1.69666	0.0657180	0.0093897
3	4.771	1.81207	0.0676647	0.0106012
4	4.849	1.92517	0.0693315	0.0112530
5	4.927	2.03860	0.0708462	0.0113810
6	5.005	2.15469	0.0723417	0.0110533
7	5.084	2.27527	0.0739444	0.0103604
8	5.162	2.40163	0.0757658	0.0094040
9	5.240	2.53439	0.0778967	0.0082855
10	5.318	2.67352	0.0804043	0.0070992
11	5.396	2.81840	0.0833310	0.0059264
12	5.474	2.96786	0.0866944	0.0048378
13	5.553	3.12028	0.0904899	0.0038996
14	5.631	3.27364	0.0946928	0.0031850
15	5.709	3.42570	0.0992612	0.0027763
16	5.787	3.57406	0.1041406	0.0027185
17	5.866	3.71623	0.1092663	0.0029561
18	5.944	3.84977	0.1145686	0.0033671
19	6.022	3.97232	0.1199748	0.0038449
20	6.100	4.08169	0.1254146	0.0043194
21	6.178	4.17588	0.1308187	0.0047449
22	6.256	4.25311	0.1361252	0.0050916
23	6.335	4.31181	0.1412775	0.0053374
24	6.413	4.35065	0.1462267	0.0054700
25	6.491	4.36845	0.1509299	0.0054845
26	6.570	4.36418	0.1553502	0.0053863
27	6.648	4.33690	0.1594541	0.0051901
28	6.726	4.28572	0.1632087	0.0049255
29	6.804	4.20971	0.1665789	0.0046350
30	6.882	4.10790	0.1695235	0.0043673
31	6.961	3.97921	0.1719901	0.0041610
32	7.039	3.82246	0.1739121	0.0040171
33	7.117	3.63640	0.1752030	0.0038734
34	7.196	3.41974	0.1757531	0.0036167
35	7.274	3.17130	0.1754269	0.0031129
36	7.352	2.89017	0.1740633	0.0022946
37	7.430	2.57597	0.1714787	0.0015652
38	7.508	2.22916	0.1674886	0.0025413
39	7.586	1.85154	0.1619802	0.0047665
40	7.665	1.44675	0.1552639	0.0070091
41	7.743	1.02103	0.1510558	0.0077091
42	7.821	0.00000	0.0896156	0.0000000
43	7.899	0.00000	0.0896156	0.0000000
44	7.978	0.00000	0.0896156	0.0000000
45	8.056	0.00000	0.0896156	0.0000000
46	8.134	0.00000	0.0896156	0.0000000
47	8.212	0.00000	0.0896156	0.0000000
48	8.290	0.00000	0.0896156	0.0000000
49	8.368	0.00000	0.0896156	0.0000000
50	8.447	0.00000	0.0896156	0.0000000

Interferogram Profile 15	4 Profiles averaged		
X Location of Profile	8.61600 cm	St. Dev.=	0.02600 cm
Local Shock Angle	31.56255 °	St. Dev.=	0.12490 °
R Location of Shock	8.39500 cm	St. Dev.=	0.00027 cm
R Location of Model Surface	4.59200 cm	St. Dev.=	0.00000 cm

Approximated and Abel Transformed Data

I	Radius (cm)	Fringe Number	ρ/ρ_t	St. Dev. ρ/ρ_t
1	4.613	1.15213	0.0597691	0.0176619
2	4.705	1.28549	0.0622963	0.0182121
3	4.798	1.41563	0.0647443	0.0176519
4	4.891	1.54169	0.0670062	0.0163471
5	4.983	1.66424	0.0690605	0.0146564
6	5.076	1.78459	0.0709419	0.0128894
7	5.169	1.90444	0.0727191	0.0112833
8	5.262	2.02543	0.0744767	0.0099773
9	5.354	2.14895	0.0763017	0.0089964
10	5.447	2.27598	0.0782740	0.0082716
11	5.540	2.40698	0.0804599	0.0076995
12	5.632	2.54191	0.0829083	0.0072090
13	5.725	2.68018	0.0856488	0.0067958
14	5.818	2.82076	0.0886918	0.0065151
15	5.911	2.96223	0.0920301	0.0064383
16	6.004	3.10289	0.0956410	0.0065940
17	6.096	3.24083	0.0994894	0.0069339
18	6.189	3.37406	0.1035314	0.0073578
19	6.281	3.50058	0.1077179	0.0077603
20	6.374	3.61847	0.1119976	0.0080677
21	6.467	3.72595	0.1163217	0.0082521
22	6.560	3.82141	0.1206448	0.0083324
23	6.653	3.90344	0.1249289	0.0083661
24	6.745	3.97083	0.1291437	0.0084243
25	6.838	4.02254	0.1332674	0.0085629
26	6.931	4.05762	0.1372876	0.0087893
27	7.023	4.07518	0.1411984	0.0090546
28	7.116	4.07424	0.1449986	0.0092692
29	7.209	4.05369	0.1486895	0.0093364
30	7.302	4.01209	0.1522671	0.0091810
31	7.394	3.94757	0.1557199	0.0087726
32	7.487	3.85772	0.1590182	0.0081323
33	7.580	3.73946	0.1621065	0.0073234
34	7.672	3.58891	0.1648931	0.0064221
35	7.765	3.40132	0.1672346	0.0054678
36	7.858	3.17105	0.1689223	0.0044605
37	7.951	2.89154	0.1696595	0.0035879
38	8.043	2.55540	0.1690441	0.0038461
39	8.136	2.15450	0.1665793	0.0059909
40	8.229	1.68028	0.1619724	0.0088768
41	8.321	1.12397	0.1588312	0.0107734
42	8.414	0.00000	0.0896156	0.0000000
43	8.507	0.00000	0.0896156	0.0000000
44	8.600	0.00000	0.0896156	0.0000000
45	8.692	0.00000	0.0896156	0.0000000
46	8.785	0.00000	0.0896156	0.0000000
47	8.878	0.00000	0.0896156	0.0000000
48	8.971	0.00000	0.0896156	0.0000000
49	9.063	0.00000	0.0896156	0.0000000
50	9.156	0.00000	0.0896156	0.0000000

Interferogram Profile 17	4 Profiles averaged	
X Location of Profile	6.11600 cm	St. Dev.= 0.02100 cm
Local Shock Angle	31.56255 °	St. Dev.= 0.12490 °
R Location of Shock	6.91000 cm	St. Dev.= 0.00031 cm
R Location of Model Surface	4.59200 cm	St. Dev.= 0.00000 cm

Approximated and Abel Transformed Data

I	Radius (cm)	Fringe Number	ρ/ρ_t	St. Dev. ρ/ρ_t
1	4.605	2.82017	0.0695826	0.0056750
2	4.661	2.95002	0.0701157	0.0060810
3	4.718	3.10318	0.0721224	0.0056530
4	4.775	3.27667	0.0757051	0.0053271
5	4.831	3.46540	0.0807945	0.0054178
6	4.888	3.66309	0.0872017	0.0056699
7	4.944	3.86304	0.0946655	0.0057782
8	5.001	4.05861	0.1028859	0.0056312
9	5.057	4.24372	0.1115532	0.0052751
10	5.114	4.41311	0.1203693	0.0048314
11	5.170	4.56247	0.1290629	0.0044244
12	5.227	4.68861	0.1373996	0.0041237
13	5.283	4.78937	0.1451891	0.0039185
14	5.340	4.86364	0.1522869	0.0037497
15	5.396	4.91124	0.1585938	0.0035688
16	5.453	4.93281	0.1640553	0.0033774
17	5.509	4.92962	0.1686558	0.0032376
18	5.565	4.90347	0.1724133	0.0032310
19	5.622	4.85650	0.1753739	0.0033976
20	5.679	4.79107	0.1776055	0.0036860
21	5.735	4.70958	0.1791910	0.0039876
22	5.792	4.61439	0.1802217	0.0041907
23	5.848	4.50767	0.1807932	0.0042105
24	5.905	4.39136	0.1809979	0.0039971
25	5.961	4.26712	0.1809249	0.0035404
26	6.018	4.13625	0.1806528	0.0028677
27	6.074	3.99967	0.1802499	0.0020528
28	6.131	3.85796	0.1797743	0.0012665
29	6.187	3.71131	0.1792703	0.0010097
30	6.244	3.55957	0.1787717	0.0015375
31	6.300	3.40217	0.1782998	0.0022069
32	6.357	3.23820	0.1778643	0.0027296
33	6.413	3.06629	0.1774607	0.0030300
34	6.470	2.88453	0.1770676	0.0031217
35	6.526	2.69038	0.1766354	0.0030894
36	6.583	2.48041	0.1760716	0.0030645
37	6.639	2.25003	0.1752110	0.0031724
38	6.696	1.99309	0.1737769	0.0035228
39	6.752	1.70137	0.1713287	0.0043934
40	6.809	1.36390	0.1673942	0.0063237
41	6.865	0.96616	0.1644063	0.0078986
42	6.922	0.00000	0.0896156	0.0000000
43	6.978	0.00000	0.0896156	0.0000000
44	7.035	0.00000	0.0896156	0.0000000
45	7.092	0.00000	0.0896156	0.0000000
46	7.148	0.00000	0.0896156	0.0000000
47	7.204	0.00000	0.0896156	0.0000000
48	7.261	0.00000	0.0896156	0.0000000
49	7.317	0.00000	0.0896156	0.0000000
50	7.374	0.00000	0.0896156	0.0000000

TABLE D.4 Interferometry Data for 20° Model at 3.4 atm Total Pressure

Filename		20D50P.TEX	
Model Cone Angle		20.0 °	
Total Pressure		3.4 atm	
Total Temperature		285.0 °K	
Interferogram profile	1	X Location	-4.983 cm
Interferogram profile	2	X Location	-3.984 cm
Interferogram profile	3	X Location	-2.989 cm
Interferogram profile	4	X Location	-2.000 cm
Interferogram profile	5	X Location	-0.975 cm
Interferogram profile	6	X Location	-0.019 cm
Interferogram profile	7	X Location	0.994 cm
Interferogram profile	8	X Location	1.992 cm
Interferogram profile	9	X Location	2.996 cm
Interferogram profile	10	X Location	3.991 cm
Interferogram profile	11	X Location	4.998 cm
Interferogram profile	12	X Location	5.633 cm
Interferogram profile	14	X Location	6.633 cm
Interferogram profile	15	X Location	7.635 cm
Interferogram profile	16	X Location	8.627 cm

Interferogram Profile 1 1 Profile.
X Location of Profile -4.98300 cm
Local Shock Angle 0.00000 °
R Location of Shock 0.00000 cm
R Location of Model Surface 2.54000 cm

Approximated and Abel Transformed Data

I	Radius (cm)	Fringe Number	ρ/ρ_t
1	2.542	-1.23443	0.0551906
2	2.567	-1.16860	0.0567312
3	2.591	-1.10458	0.0582390
4	2.616	-1.04236	0.0597143
5	2.640	-0.98195	0.0611571
6	2.664	-0.92334	0.0625677
7	2.689	-0.86653	0.0639462
8	2.713	-0.81153	0.0652926
9	2.738	-0.75833	0.0666074
10	2.762	-0.70693	0.0678903
11	2.787	-0.65734	0.0691415
12	2.811	-0.60955	0.0703610
13	2.836	-0.56356	0.0715489
14	2.860	-0.51938	0.0727050
15	2.884	-0.47700	0.0738294
16	2.909	-0.43642	0.0749220
17	2.933	-0.39765	0.0759825
18	2.958	-0.36068	0.0770109
19	2.982	-0.32551	0.0780070
20	3.007	-0.29215	0.0789704
21	3.031	-0.26059	0.0799009
22	3.056	-0.23084	0.0807982
23	3.080	-0.20288	0.0816616
24	3.104	-0.17673	0.0824908
25	3.129	-0.15239	0.0832850
26	3.153	-0.12984	0.0840436
27	3.178	-0.10911	0.0847656
28	3.202	-0.09017	0.0854501
29	3.227	-0.07304	0.0860957
30	3.251	-0.05771	0.0867009
31	3.276	-0.04418	0.0872639
32	3.300	-0.03246	0.0877822
33	3.324	-0.02254	0.0882528
34	3.349	-0.01443	0.0886715
35	3.373	-0.00812	0.0890323
36	3.398	-0.00361	0.0893260
37	3.422	-0.00090	0.0895351
38	3.447	0.00000	0.0896156
39	3.471	0.00000	0.0896156
40	3.496	0.00000	0.0896156
41	3.520	0.00000	0.0896156
42	3.544	0.00000	0.0896156
43	3.569	0.00000	0.0896156
44	3.593	0.00000	0.0896156
45	3.618	0.00000	0.0896156
46	3.642	0.00000	0.0896156
47	3.667	0.00000	0.0896156
48	3.691	0.00000	0.0896156
49	3.716	0.00000	0.0896156
50	3.740	0.00000	0.0896156

Interferogram Profile 2 1 Profile
X Location of Profile -3.98400 cm
Local Shock Angle 0.00000 °
R Location of Shock 0.00000 cm
R Location of Model Surface 2.54000 cm

Approximated and Abel Transformed Data

I	Radius (cm)	Fringe Number	ρ/ρ_t
1	2.542	-1.80847	0.0404886
2	2.567	-1.71692	0.0425843
3	2.591	-1.62775	0.0446367
4	2.616	-1.54095	0.0466465
5	2.640	-1.45653	0.0486137
6	2.664	-1.37449	0.0505386
7	2.689	-1.29482	0.0524214
8	2.713	-1.21754	0.0542625
9	2.738	-1.14263	0.0560619
10	2.762	-1.07010	0.0578198
11	2.787	-0.99995	0.0595364
12	2.811	-0.93218	0.0612117
13	2.836	-0.86678	0.0628457
14	2.860	-0.80377	0.0644387
15	2.884	-0.74313	0.0659904
16	2.909	-0.68487	0.0675008
17	2.933	-0.62898	0.0689700
18	2.958	-0.57548	0.0703976
19	2.982	-0.52435	0.0717837
20	3.007	-0.47560	0.0731280
21	3.031	-0.42923	0.0744299
22	3.056	-0.38524	0.0756894
23	3.080	-0.34362	0.0769061
24	3.104	-0.30438	0.0780792
25	3.129	-0.26753	0.0792083
26	3.153	-0.23304	0.0802927
27	3.178	-0.20094	0.0813316
28	3.202	-0.17122	0.0823238
29	3.227	-0.14387	0.0832683
30	3.251	-0.11890	0.0841638
31	3.276	-0.09631	0.0850086
32	3.300	-0.07610	0.0858006
33	3.324	-0.05826	0.0865372
34	3.349	-0.04280	0.0872158
35	3.373	-0.02973	0.0878316
36	3.398	-0.01902	0.0883797
37	3.422	-0.01070	0.0888519
38	3.447	-0.00476	0.0892363
39	3.471	-0.00119	0.0895102
40	3.496	0.00000	0.0896156
41	3.520	0.00000	0.0896156
42	3.544	0.00000	0.0896156
43	3.569	0.00000	0.0896156
44	3.593	0.00000	0.0896156
45	3.618	0.00000	0.0896156
46	3.642	0.00000	0.0896156
47	3.667	0.00000	0.0896156
48	3.691	0.00000	0.0896156
49	3.716	0.00000	0.0896156
50	3.740	0.00000	0.0896156

Interferogram Profile 3 1 Profile
X Location of Profile -2.98900 cm
Local Shock Angle 0.00000 °
R Location of Shock 0.00000 cm
R Location of Model Surface 2.54000 cm

Approximated and Abel Transformed Data

I	Radius (cm)	Fringe Number	ρ/ρ_t
1	2.542	-1.10310	0.0579917
2	2.567	-1.04097	0.0594809
3	2.591	-0.98063	0.0609370
4	2.616	-0.92210	0.0623606
5	2.640	-0.86537	0.0637515
6	2.664	-0.81044	0.0651100
7	2.689	-0.75731	0.0664362
8	2.713	-0.70598	0.0677301
9	2.738	-0.65646	0.0689920
10	2.762	-0.60873	0.0702217
11	2.787	-0.56281	0.0714194
12	2.811	-0.51868	0.0725848
13	2.836	-0.47636	0.0737183
14	2.860	-0.43584	0.0748194
15	2.884	-0.39712	0.0758883
16	2.909	-0.36020	0.0769245
17	2.933	-0.32508	0.0779281
18	2.958	-0.29176	0.0788988
19	2.982	-0.26024	0.0798361
20	3.007	-0.23053	0.0807399
21	3.031	-0.20261	0.0816094
22	3.056	-0.17650	0.0824444
23	3.080	-0.15218	0.0832442
24	3.104	-0.12967	0.0840079
25	3.129	-0.10896	0.0847349
26	3.153	-0.09005	0.0854238
27	3.178	-0.07294	0.0860738
28	3.202	-0.05763	0.0866829
29	3.227	-0.04412	0.0872495
30	3.251	-0.03242	0.0877711
31	3.276	-0.02251	0.0882446
32	3.300	-0.01441	0.0886658
33	3.324	-0.00810	0.0890289
34	3.349	-0.00360	0.0893242
35	3.373	-0.00090	0.0895346
36	3.398	0.00000	0.0896156
37	3.422	0.00000	0.0896156
38	3.447	0.00000	0.0896156
39	3.471	0.00000	0.0896156
40	3.496	0.00000	0.0896156
41	3.520	0.00000	0.0896156
42	3.544	0.00000	0.0896156
43	3.569	0.00000	0.0896156
44	3.593	0.00000	0.0896156
45	3.618	0.00000	0.0896156
46	3.642	0.00000	0.0896156
47	3.667	0.00000	0.0896156
48	3.691	0.00000	0.0896156
49	3.716	0.00000	0.0896156
50	3.740	0.00000	0.0896156

Interferogram Profile 4 1 Profile
X Location of Profile -2.00000 cm
Local Shock Angle 0.00000 °
R Location of Shock 0.00000 cm
R Location of Model Surface 2.54000 cm

Approximated and Abel Transformed Data

I	Radius (cm)	Fringe Number	ρ/ρ_t
1	2.542	-1.16717	0.0583083
2	2.567	-1.10954	0.0596135
3	2.591	-1.05337	0.0608922
4	2.616	-0.99866	0.0621446
5	2.640	-0.94541	0.0633711
6	2.664	-0.89362	0.0645717
7	2.689	-0.84328	0.0657466
8	2.713	-0.79441	0.0668959
9	2.738	-0.74699	0.0680197
10	2.762	-0.70103	0.0691182
11	2.787	-0.65653	0.0701915
12	2.811	-0.61349	0.0712395
13	2.836	-0.57191	0.0722624
14	2.860	-0.53179	0.0732602
15	2.884	-0.49313	0.0742329
16	2.909	-0.45593	0.0751806
17	2.933	-0.42018	0.0761030
18	2.958	-0.38590	0.0770004
19	2.982	-0.35307	0.0778723
20	3.007	-0.32170	0.0787190
21	3.031	-0.29179	0.0795401
22	3.056	-0.26334	0.0803355
23	3.080	-0.23635	0.0811050
24	3.104	-0.21082	0.0818482
25	3.129	-0.18675	0.0825651
26	3.153	-0.16413	0.0832548
27	3.178	-0.14298	0.0839175
28	3.202	-0.12328	0.0845523
29	3.227	-0.10505	0.0851587
30	3.251	-0.08827	0.0857359
31	3.276	-0.07295	0.0862832
32	3.300	-0.05909	0.0867995
33	3.324	-0.04669	0.0872835
34	3.349	-0.03574	0.0877338
35	3.373	-0.02626	0.0881485
36	3.398	-0.01824	0.0885250
37	3.422	-0.01167	0.0888600
38	3.447	-0.00657	0.0891487
39	3.471	-0.00292	0.0893837
40	3.496	-0.00073	0.0895511
41	3.520	0.00000	0.0896156
42	3.544	0.00000	0.0896156
43	3.569	0.00000	0.0896156
44	3.593	0.00000	0.0896156
45	3.618	0.00000	0.0896156
46	3.642	0.00000	0.0896156
47	3.667	0.00000	0.0896156
48	3.691	0.00000	0.0896156
49	3.716	0.00000	0.0896156
50	3.740	0.00000	0.0896156

Interferogram Profile 5 1 Profile
X Location of Profile -0.97500 cm
Local Shock Angle 0.00000 °
R Location of Shock 0.00000 cm
R Location of Model Surface 2.54000 cm

Approximated and Abel Transformed Data

I	Radius (cm)	Fringe Number	ρ/ρ_t
1	2.542	-1.36132	0.0521530
2	2.567	-1.29061	0.0537894
3	2.591	-1.22179	0.0553914
4	2.616	-1.15486	0.0569594
5	2.640	-1.08981	0.0584937
6	2.664	-1.02664	0.0599943
7	2.689	-0.96537	0.0614615
8	2.713	-0.90597	0.0628954
9	2.738	-0.84847	0.0642961
10	2.762	-0.79284	0.0656639
11	2.787	-0.73911	0.0669987
12	2.811	-0.68726	0.0683004
13	2.836	-0.63729	0.0695695
14	2.860	-0.58921	0.0708055
15	2.884	-0.54302	0.0720087
16	2.909	-0.49871	0.0731789
17	2.933	-0.45629	0.0743160
18	2.958	-0.41575	0.0754199
19	2.982	-0.37710	0.0764903
20	3.007	-0.34033	0.0775272
21	3.031	-0.30545	0.0785301
22	3.056	-0.27245	0.0794988
23	3.080	-0.24134	0.0804329
24	3.104	-0.21212	0.0813320
25	3.129	-0.18478	0.0821952
26	3.153	-0.15932	0.0830223
27	3.178	-0.13575	0.0838121
28	3.202	-0.11407	0.0845640
29	3.227	-0.09427	0.0852768
30	3.251	-0.07636	0.0859492
31	3.276	-0.06034	0.0865795
32	3.300	-0.04619	0.0871659
33	3.324	-0.03394	0.0877058
34	3.349	-0.02357	0.0881960
35	3.373	-0.01508	0.0886320
36	3.398	-0.00848	0.0890080
37	3.422	-0.00377	0.0893138
38	3.447	-0.00094	0.0895317
39	3.471	0.00000	0.0896156
40	3.496	0.00000	0.0896156
41	3.520	0.00000	0.0896156
42	3.544	0.00000	0.0896156
43	3.569	0.00000	0.0896156
44	3.593	0.00000	0.0896156
45	3.618	0.00000	0.0896156
46	3.642	0.00000	0.0896156
47	3.667	0.00000	0.0896156
48	3.691	0.00000	0.0896156
49	3.716	0.00000	0.0896156
50	3.740	0.00000	0.0896156

Interferogram Profile 6	4 Profiles averaged	
X Location of Profile	-0.01900 cm	St. Dev.= 0.01900 cm
Local Shock Angle	0.00000 °	St. Dev.= 0.00000 °
R Location of Shock	0.80300 cm	St. Dev.= 0.01606 cm
R Location of Model Surface	2.54000 cm	St. Dev.= 0.00001 cm

Approximated and Abel Transformed Data

I	Radius (cm)	Fringe Number	ρ/ρ_t	St. Dev. ρ/ρ_t
1	2.542	-0.52828	0.0742951	0.0097766
2	2.565	-0.49804	0.0750289	0.0092757
3	2.587	-0.46870	0.0757461	0.0087871
4	2.610	-0.44026	0.0764468	0.0083109
5	2.632	-0.41273	0.0771311	0.0078472
6	2.654	-0.38610	0.0777990	0.0073958
7	2.677	-0.36038	0.0784506	0.0069569
8	2.699	-0.33555	0.0790859	0.0065304
9	2.722	-0.31163	0.0797050	0.0061165
10	2.744	-0.28862	0.0803078	0.0057153
11	2.767	-0.26651	0.0808943	0.0053267
12	2.789	-0.24530	0.0814645	0.0049510
13	2.812	-0.22500	0.0820184	0.0045883
14	2.834	-0.20560	0.0825559	0.0042389
15	2.856	-0.18710	0.0830768	0.0039029
16	2.879	-0.16951	0.0835811	0.0035806
17	2.901	-0.15282	0.0840686	0.0032725
18	2.924	-0.13703	0.0845392	0.0029789
19	2.946	-0.12215	0.0849926	0.0027004
20	2.969	-0.10817	0.0854286	0.0024374
21	2.991	-0.09509	0.0858469	0.0021908
22	3.014	-0.08292	0.0862470	0.0019612
23	3.036	-0.07165	0.0866287	0.0017497
24	3.058	-0.06129	0.0869912	0.0015571
25	3.081	-0.05182	0.0873340	0.0013843
26	3.103	-0.04326	0.0876563	0.0012322
27	3.126	-0.03561	0.0879569	0.0011007
28	3.148	-0.02886	0.0882346	0.0009893
29	3.171	-0.02301	0.0884875	0.0008953
30	3.193	-0.01806	0.0887127	0.0008138
31	3.215	-0.01402	0.0889056	0.0007366
32	3.238	-0.01089	0.0890558	0.0006477
33	3.260	-0.00852	0.0891605	0.0005400
34	3.283	-0.00661	0.0892415	0.0004332
35	3.305	-0.00496	0.0893161	0.0003483
36	3.328	-0.00357	0.0893837	0.0002867
37	3.350	-0.00244	0.0894434	0.0002456
38	3.373	-0.00157	0.0894934	0.0002143
39	3.395	-0.00097	0.0895290	0.0001732
40	3.417	-0.00048	0.0895609	0.0001093
41	3.440	0.00000	0.0896156	0.0000000
42	3.462	0.00000	0.0896156	0.0000000
43	3.485	0.00000	0.0896156	0.0000000
44	3.507	0.00000	0.0896156	0.0000000
45	3.530	0.00000	0.0896156	0.0000000
46	3.552	0.00000	0.0896156	0.0000000
47	3.574	0.00000	0.0896156	0.0000000
48	3.597	0.00000	0.0896156	0.0000000
49	3.619	0.00000	0.0896156	0.0000000
50	3.641	0.00000	0.0896156	0.0000000

Interferogram Profile 7	4 Profiles averaged	
X Location of Profile	0.99400 cm	St. Dev.= 0.01600 cm
Local Shock Angle	31.56255 °	St. Dev.= 0.42685 °
R Location of Shock	3.71800 cm	St. Dev.= 0.00114 cm
R Location of Model Surface	2.90200 cm	St. Dev.= 0.00006 cm

Approximated and Abel Transformed Data

I	Radius (cm)	Fringe Number	ρ/ρ_t	St. Dev. ρ/ρ_t
1	2.905	1.02636	0.0890645	0.0124355
2	2.925	1.06403	0.0901385	0.0125417
3	2.945	1.10157	0.0912918	0.0126264
4	2.965	1.13874	0.0925182	0.0126573
5	2.985	1.17529	0.0938115	0.0126126
6	3.005	1.21098	0.0951656	0.0124780
7	3.025	1.24559	0.0965742	0.0122454
8	3.045	1.27886	0.0980310	0.0119110
9	3.065	1.31057	0.0995295	0.0114748
10	3.084	1.34048	0.1010632	0.0109395
11	3.105	1.36836	0.1026257	0.0103105
12	3.124	1.39398	0.1042098	0.0095960
13	3.144	1.41711	0.1058089	0.0088072
14	3.164	1.43752	0.1074159	0.0079603
15	3.184	1.45499	0.1090233	0.0070783
16	3.204	1.46929	0.1106239	0.0061956
17	3.224	1.48021	0.1122098	0.0053679
18	3.244	1.48751	0.1137726	0.0046841
19	3.264	1.49099	0.1153046	0.0042725
20	3.284	1.49041	0.1167964	0.0042630
21	3.304	1.48557	0.1182391	0.0046928
22	3.324	1.47626	0.1196228	0.0054790
23	3.344	1.46225	0.1209373	0.0065000
24	3.364	1.44334	0.1221716	0.0076596
25	3.383	1.41932	0.1233141	0.0088925
26	3.404	1.38997	0.1243526	0.0101532
27	3.423	1.35509	0.1252753	0.0114072
28	3.443	1.31448	0.1260737	0.0126217
29	3.463	1.26793	0.1267663	0.0137466
30	3.483	1.21318	0.1270171	0.0149755
31	3.503	1.15415	0.1272542	0.0159744
32	3.523	1.08857	0.1272612	0.0168442
33	3.543	1.01626	0.1270029	0.0175569
34	3.563	0.93700	0.1264352	0.0180812
35	3.583	0.85062	0.1254999	0.0183822
36	3.602	0.75692	0.1241187	0.0184250
37	3.623	0.65570	0.1221758	0.0181777
38	3.642	0.54678	0.1194847	0.0176379
39	3.662	0.42996	0.1156992	0.0169284
40	3.682	0.30507	0.1100054	0.0167307
41	3.702	0.17190	0.0994339	0.0207600
42	3.722	0.00000	0.0896156	0.0000000
43	3.742	0.00000	0.0896156	0.0000000
44	3.762	0.00000	0.0896156	0.0000000
45	3.782	0.00000	0.0896156	0.0000000
46	3.802	0.00000	0.0896156	0.0000000
47	3.822	0.00000	0.0896156	0.0000000
48	3.841	0.00000	0.0896156	0.0000000
49	3.861	0.00000	0.0896156	0.0000000
50	3.881	0.00000	0.0896156	0.0000000

Interferogram Profile 8	4 Profiles averaged	
X Location of Profile	1.99200 cm	St. Dev.= 0.02200 cm
Local Shock Angle	31.56255 °	St. Dev.= 0.42685 °
R Location of Shock	4.24700 cm	St. Dev.= 0.00029 cm
R Location of Model Surface	3.26500 cm	St. Dev.= 0.00008 cm

Approximated and Abel Transformed Data

I	Radius (cm)	Fringe Number	ρ/ρ_t	St. Dev. ρ/ρ_t
1	3.269	3.19991	0.1072491	0.0087774
2	3.293	3.24252	0.1085557	0.0069017
3	3.317	3.28514	0.1099469	0.0053152
4	3.341	3.32747	0.1114187	0.0040260
5	3.365	3.36922	0.1129667	0.0030746
6	3.389	3.41009	0.1145868	0.0025387
7	3.413	3.44977	0.1162741	0.0024617
8	3.437	3.48796	0.1180238	0.0027370
9	3.461	3.52434	0.1198309	0.0031907
10	3.485	3.55858	0.1216903	0.0037086
11	3.509	3.59035	0.1235960	0.0042389
12	3.532	3.61932	0.1255426	0.0047611
13	3.557	3.64515	0.1275236	0.0052684
14	3.581	3.66751	0.1295328	0.0057589
15	3.604	3.68602	0.1315635	0.0062327
16	3.628	3.70035	0.1336082	0.0066889
17	3.652	3.71011	0.1356594	0.0071270
18	3.676	3.71496	0.1377093	0.0075448
19	3.700	3.71451	0.1397492	0.0079406
20	3.724	3.70838	0.1417701	0.0083118
21	3.749	3.69620	0.1437630	0.0086559
22	3.772	3.67756	0.1457163	0.0089695
23	3.796	3.65208	0.1476203	0.0092508
24	3.820	3.61935	0.1494622	0.0094981
25	3.844	3.57895	0.1512296	0.0097095
26	3.868	3.53049	0.1529091	0.0098850
27	3.892	3.47354	0.1544854	0.0100238
28	3.916	3.40767	0.1559421	0.0101272
29	3.940	3.33247	0.1572608	0.0101957
30	3.964	3.24748	0.1584230	0.0102321
31	3.988	3.15226	0.1594050	0.0102391
32	4.012	3.04638	0.1601837	0.0102203
33	4.036	2.92937	0.1607303	0.0101819
34	4.060	2.80079	0.1610137	0.0101316
35	4.084	2.66015	0.1609986	0.0100832
36	4.108	2.50701	0.1606444	0.0100606
37	4.131	2.34087	0.1599070	0.0101037
38	4.156	2.16126	0.1587425	0.0102828
39	4.180	1.96769	0.1571259	0.0107036
40	4.203	1.75966	0.1551469	0.0114713
41	4.228	1.53669	0.1536831	0.0122692
42	4.252	0.00000	0.0896156	0.0000000
43	4.275	0.00000	0.0896156	0.0000000
44	4.299	0.00000	0.0896156	0.0000000
45	4.323	0.00000	0.0896156	0.0000000
46	4.347	0.00000	0.0896156	0.0000000
47	4.371	0.00000	0.0896156	0.0000000
48	4.395	0.00000	0.0896156	0.0000000
49	4.419	0.00000	0.0896156	0.0000000
50	4.443	0.00000	0.0896156	0.0000000

Interferogram Profile 9	4 Profiles averaged	
X Location of Profile	2.99600 cm	St. Dev.= 0.02500 cm
Local Shock Angle	31.56255 °	St. Dev.= 0.42685 °
R Location of Shock	4.87200 cm	St. Dev.= 0.00031 cm
R Location of Model Surface	3.63100 cm	St. Dev.= 0.00009 cm

Approximated and Abel Transformed Data

I	Radius (cm)	Fringe Number	ρ/ρ_t	St. Dev. ρ/ρ_t
1	3.635	5.34131	0.1243122	0.0110701
2	3.666	5.36499	0.1242852	0.0099291
3	3.696	5.40114	0.1249097	0.0100550
4	3.727	5.44713	0.1261449	0.0102037
5	3.757	5.50013	0.1279335	0.0099670
6	3.787	5.55720	0.1302052	0.0093343
7	3.818	5.61541	0.1328805	0.0084413
8	3.848	5.67191	0.1358730	0.0074882
9	3.878	5.72400	0.1390934	0.0067198
10	3.909	5.76920	0.1424507	0.0063825
11	3.939	5.80531	0.1458558	0.0066038
12	3.969	5.83041	0.1492240	0.0072995
13	3.999	5.84297	0.1524753	0.0082591
14	4.030	5.84181	0.1555382	0.0092804
15	4.060	5.82615	0.1583510	0.0102163
16	4.090	5.79559	0.1608609	0.0109665
17	4.121	5.75012	0.1630288	0.0114651
18	4.151	5.69012	0.1648276	0.0116704
19	4.181	5.61628	0.1662432	0.0115608
20	4.212	5.52964	0.1672756	0.0111316
21	4.242	5.43149	0.1679386	0.0103972
22	4.272	5.32333	0.1682606	0.0093877
23	4.303	5.20684	0.1682815	0.0081532
24	4.333	5.08374	0.1680541	0.0067619
25	4.363	4.95578	0.1676439	0.0053054
26	4.393	4.82457	0.1671229	0.0039054
27	4.424	4.69157	0.1665722	0.0027376
28	4.454	4.55788	0.1660767	0.0020481
29	4.484	4.42419	0.1657205	0.0019410
30	4.515	4.29062	0.1655858	0.0020764
31	4.545	4.15657	0.1657436	0.0021244
32	4.575	4.02058	0.1662471	0.0021793
33	4.605	3.88017	0.1671248	0.0028378
34	4.636	3.73166	0.1683638	0.0045270
35	4.666	3.57002	0.1698961	0.0070891
36	4.696	3.38862	0.1715706	0.0102206
37	4.727	3.17907	0.1731220	0.0135233
38	4.757	2.93102	0.1741140	0.0163832
39	4.787	2.63191	0.1738726	0.0178236
40	4.817	2.26675	0.1715549	0.0165052
41	4.848	1.81791	0.1694412	0.0153894
42	4.878	0.00000	0.0896156	0.0000000
43	4.909	0.00000	0.0896156	0.0000000
44	4.939	0.00000	0.0896156	0.0000000
45	4.969	0.00000	0.0896156	0.0000000
46	5.000	0.00000	0.0896156	0.0000000
47	5.030	0.00000	0.0896156	0.0000000
48	5.060	0.00000	0.0896156	0.0000000
49	5.090	0.00000	0.0896156	0.0000000
50	5.120	0.00000	0.0896156	0.0000000

Interferogram Profile 10	4 Profiles averaged	
X Location of Profile	3.99100 cm	St. Dev.= 0.02100 cm
Local Shock Angle	31.56255 °	St. Dev.= 0.42685 °
R Location of Shock	5.47900 cm	St. Dev.= 0.00031 cm
R Location of Model Surface	3.99300 cm	St. Dev.= 0.00008 cm

Approximated and Abel Transformed Data

I	Radius (cm)	Fringe Number	ρ/ρ_t	St. Dev. ρ/ρ_t
1	3.998	6.91192	0.1338992	0.0098085
2	4.035	6.96199	0.1366186	0.0093960
3	4.071	7.00024	0.1389989	0.0086956
4	4.107	7.02905	0.1411453	0.0079626
5	4.144	7.05015	0.1431397	0.0073896
6	4.180	7.06471	0.1450443	0.0070758
7	4.216	7.07339	0.1469030	0.0070082
8	4.253	7.07648	0.1487476	0.0070895
9	4.289	7.07393	0.1505963	0.0071977
10	4.325	7.06543	0.1524525	0.0072346
11	4.361	7.05051	0.1543153	0.0071377
12	4.397	7.02853	0.1561738	0.0068792
13	4.434	6.99883	0.1580116	0.0064587
14	4.470	6.96067	0.1598079	0.0058951
15	4.506	6.91336	0.1615413	0.0052184
16	4.543	6.85626	0.1631812	0.0044766
17	4.579	6.78879	0.1647093	0.0037154
18	4.615	6.71051	0.1660951	0.0030031
19	4.651	6.62110	0.1673158	0.0024218
20	4.688	6.52039	0.1683546	0.0020710
21	4.724	6.40836	0.1691892	0.0020143
22	4.760	6.28516	0.1698082	0.0022045
23	4.796	6.15108	0.1702012	0.0025246
24	4.833	6.00659	0.1703657	0.0028923
25	4.869	5.85227	0.1702999	0.0032692
26	4.905	5.68883	0.1700109	0.0036482
27	4.942	5.51708	0.1695086	0.0040293
28	4.978	5.33790	0.1688103	0.0044129
29	5.014	5.15217	0.1679341	0.0047845
30	5.051	4.96080	0.1669080	0.0051188
31	5.087	4.76463	0.1657617	0.0053782
32	5.123	4.56438	0.1645179	0.0055224
33	5.159	4.36062	0.1632182	0.0055122
34	5.196	4.15369	0.1618884	0.0053389
35	5.232	3.94362	0.1605598	0.0050578
36	5.268	3.73008	0.1592594	0.0048637
37	5.304	3.51231	0.1580118	0.0051600
38	5.340	3.28897	0.1568348	0.0063732
39	5.377	3.05813	0.1557620	0.0086184
40	5.413	2.81713	0.1548988	0.0117877
41	5.449	2.56247	0.1547447	0.0156861
42	5.486	0.00000	0.0896156	0.0000000
43	5.522	0.00000	0.0896156	0.0000000
44	5.559	0.00000	0.0896156	0.0000000
45	5.595	0.00000	0.0896156	0.0000000
46	5.631	0.00000	0.0896156	0.0000000
47	5.667	0.00000	0.0896156	0.0000000
48	5.703	0.00000	0.0896156	0.0000000
49	5.740	0.00000	0.0896156	0.0000000
50	5.776	0.00000	0.0896156	0.0000000

Interferogram Profile 11	4 Profiles averaged	
X Location of Profile	4.99800 cm	St. Dev.= 0.01500 cm
Local Shock Angle	31.56255 °	St. Dev.= 0.42685 °
R Location of Shock	6.09900 cm	St. Dev.= 0.00047 cm
R Location of Model Surface	4.35900 cm	St. Dev.= 0.00005 cm

Approximated and Abel Transformed Data

I	Radius (cm)	Fringe Number	ρ/ρ_t	St. Dev. ρ/ρ_t
1	4.368	8.34950	0.1383812	0.0110963
2	4.410	8.38374	0.1398055	0.0122093
3	4.453	8.42077	0.1415507	0.0132125
4	4.495	8.45838	0.1435776	0.0138746
5	4.538	8.49426	0.1458405	0.0141154
6	4.580	8.52616	0.1482885	0.0139272
7	4.622	8.55186	0.1508684	0.0133384
8	4.665	8.56930	0.1535243	0.0123984
9	4.707	8.57655	0.1562007	0.0111669
10	4.750	8.57191	0.1588432	0.0097119
11	4.792	8.55392	0.1613996	0.0081042
12	4.834	8.52140	0.1638206	0.0064185
13	4.877	8.47342	0.1660619	0.0047345
14	4.920	8.40940	0.1680842	0.0031526
15	4.961	8.32903	0.1698537	0.0018780
16	5.004	8.23232	0.1713437	0.0014989
17	5.047	8.11957	0.1725346	0.0021744
18	5.089	7.99139	0.1734144	0.0030679
19	5.131	7.84864	0.1739772	0.0038474
20	5.174	7.69243	0.1742279	0.0044359
21	5.217	7.52407	0.1741768	0.0048175
22	5.259	7.34505	0.1738434	0.0050049
23	5.301	7.15697	0.1732536	0.0050248
24	5.344	6.96151	0.1724412	0.0049208
25	5.386	6.76037	0.1714449	0.0047447
26	5.428	6.55518	0.1703110	0.0045539
27	5.471	6.34745	0.1690872	0.0044013
28	5.513	6.13848	0.1678270	0.0043270
29	5.556	5.92929	0.1665821	0.0043526
30	5.598	5.72051	0.1654048	0.0044960
31	5.641	5.51231	0.1643425	0.0047914
32	5.683	5.30423	0.1634350	0.0053042
33	5.725	5.09515	0.1627118	0.0061193
34	5.768	4.88313	0.1621817	0.0073063
35	5.810	4.66527	0.1618316	0.0088647
36	5.853	4.43762	0.1616088	0.0107063
37	5.895	4.19501	0.1614144	0.0126377
38	5.937	3.93091	0.1610761	0.0143355
39	5.980	3.63729	0.1603303	0.0153216
40	6.022	3.30447	0.1588703	0.0150806
41	6.064	2.92092	0.1574607	0.0150286
42	6.107	0.00000	0.0896156	0.0000000
43	6.149	0.00000	0.0896156	0.0000000
44	6.192	0.00000	0.0896156	0.0000000
45	6.234	0.00000	0.0896156	0.0000000
46	6.277	0.00000	0.0896156	0.0000000
47	6.319	0.00000	0.0896156	0.0000000
48	6.361	0.00000	0.0896156	0.0000000
49	6.404	0.00000	0.0896156	0.0000000
50	6.447	0.00000	0.0896156	0.0000000

Interferogram Profile 12	4 Profiles averaged	
X Location of Profile	5.63300 cm	St. Dev.= 0.00800 cm
Local Shock Angle	31.56255 °	St. Dev.= 0.42685 °
R Location of Shock	6.50000 cm	St. Dev.= 0.00073 cm
R Location of Model Surface	4.59000 cm	St. Dev.= 0.00003 cm

Approximated and Abel Transformed Data

I	Radius (cm)	Fringe Number	ρ/ρ_t	St. Dev. ρ/ρ_t
1	4.598	10.22501	0.1570057	0.0199388
2	4.645	10.19365	0.1576141	0.0200806
3	4.692	10.16835	0.1586944	0.0197358
4	4.738	10.14435	0.1601084	0.0190209
5	4.785	10.11773	0.1617379	0.0180437
6	4.831	10.08533	0.1634818	0.0168965
7	4.878	10.04467	0.1652566	0.0156552
8	4.925	9.99389	0.1669925	0.0143778
9	4.972	9.93167	0.1686347	0.0131087
10	5.018	9.85718	0.1701394	0.0118788
11	5.065	9.76998	0.1714752	0.0107090
12	5.111	9.67002	0.1726196	0.0096129
13	5.158	9.55750	0.1735590	0.0085992
14	5.205	9.43290	0.1742888	0.0076751
15	5.251	9.29689	0.1748094	0.0068464
16	5.297	9.15025	0.1751270	0.0061214
17	5.344	8.99390	0.1752539	0.0055083
18	5.391	8.82878	0.1752054	0.0050156
19	5.438	8.65588	0.1749989	0.0046488
20	5.484	8.47612	0.1746551	0.0044087
21	5.531	8.29042	0.1741956	0.0042885
22	5.577	8.09957	0.1736426	0.0042767
23	5.624	7.90428	0.1730178	0.0043627
24	5.671	7.70508	0.1723428	0.0045408
25	5.717	7.50239	0.1716361	0.0048114
26	5.764	7.29642	0.1709152	0.0051826
27	5.810	7.08720	0.1701940	0.0056629
28	5.857	6.87454	0.1694840	0.0062584
29	5.904	6.65805	0.1687897	0.0069650
30	5.951	6.43710	0.1681132	0.0077697
31	5.997	6.21083	0.1674501	0.0086479
32	6.044	5.97818	0.1667873	0.0095619
33	6.090	5.73784	0.1661064	0.0104638
34	6.137	5.48827	0.1653791	0.0112957
35	6.183	5.22774	0.1645670	0.0119905
36	6.230	4.95432	0.1636179	0.0124685
37	6.277	4.66586	0.1624684	0.0126496
38	6.323	4.36007	0.1610384	0.0124622
39	6.370	4.03448	0.1592464	0.0118969
40	6.416	3.68654	0.1570784	0.0111611
41	6.463	3.31353	0.1552505	0.0111463
42	6.509	0.00000	0.0896156	0.0000000
43	6.556	0.00000	0.0896156	0.0000000
44	6.603	0.00000	0.0896156	0.0000000
45	6.650	0.00000	0.0896156	0.0000000
46	6.696	0.00000	0.0896156	0.0000000
47	6.742	0.00000	0.0896156	0.0000000
48	6.789	0.00000	0.0896156	0.0000000
49	6.836	0.00000	0.0896156	0.0000000
50	6.883	0.00000	0.0896156	0.0000000

Interferogram Profile 14	3 Profiles averaged	
X Location of Profile	6.63300 cm	St. Dev.= 0.01100 cm
Local Shock Angle	31.50010 °	St. Dev.= 0.49962 °
R Location of Shock	7.12300 cm	St. Dev.= 0.00073 cm
R Location of Model Surface	4.59200 cm	St. Dev.= 0.00000 cm

Approximated and Abel Transformed Data

I	Radius (cm)	Fringe Number	ρ/ρ_t	St. Dev. ρ/ρ_t
1	4.613	6.27823	0.0845194	0.0507957
2	4.675	6.49355	0.0874221	0.0447363
3	4.736	6.69583	0.0896931	0.0400254
4	4.798	6.89663	0.0917438	0.0364123
5	4.860	7.10343	0.0938840	0.0337717
6	4.921	7.32021	0.0963333	0.0319432
7	4.983	7.54809	0.0992344	0.0306794
8	5.044	7.78588	0.1026636	0.0296859
9	5.106	8.03056	0.1066429	0.0286918
10	5.167	8.27781	0.1111479	0.0275017
11	5.229	8.52236	0.1161191	0.0260152
12	5.290	8.75846	0.1214686	0.0242222
13	5.352	8.98015	0.1270893	0.0221871
14	5.413	9.18163	0.1328615	0.0200331
15	5.475	9.35747	0.1386593	0.0179195
16	5.536	9.50286	0.1443570	0.0160158
17	5.598	9.61376	0.1498343	0.0144627
18	5.659	9.68705	0.1549803	0.0133197
19	5.721	9.72064	0.1596991	0.0125310
20	5.782	9.71347	0.1639118	0.0119349
21	5.844	9.66558	0.1675594	0.0113264
22	5.906	9.57801	0.1706063	0.0105225
23	5.967	9.45282	0.1730392	0.0093981
24	6.029	9.29284	0.1748711	0.0079039
25	6.090	9.10164	0.1761386	0.0060683
26	6.152	8.88324	0.1769018	0.0040282
27	6.213	8.64191	0.1772421	0.0022895
28	6.275	8.38188	0.1772608	0.0025450
29	6.337	8.10698	0.1770716	0.0044044
30	6.398	7.82030	0.1767984	0.0063234
31	6.459	7.52380	0.1765643	0.0078495
32	6.521	7.21779	0.1764859	0.0088011
33	6.582	6.90049	0.1766562	0.0091690
34	6.644	6.56748	0.1771255	0.0092438
35	6.706	6.21109	0.1778843	0.0098025
36	6.767	5.81982	0.1788245	0.0118489
37	6.828	5.37767	0.1796903	0.0156572
38	6.890	4.86338	0.1800149	0.0205191
39	6.952	4.24976	0.1790420	0.0251588
40	7.013	3.50284	0.1758723	0.0279096
41	7.075	2.58108	0.1737546	0.0301836
42	7.137	0.00000	0.0896156	0.0000000
43	7.198	0.00000	0.0896156	0.0000000
44	7.259	0.00000	0.0896156	0.0000000
45	7.321	0.00000	0.0896156	0.0000000
46	7.383	0.00000	0.0896156	0.0000000
47	7.444	0.00000	0.0896156	0.0000000
48	7.506	0.00000	0.0896156	0.0000000
49	7.567	0.00000	0.0896156	0.0000000
50	7.629	0.00000	0.0896156	0.0000000

Interferogram Profile 15	4 Profiles averaged	
X Location of Profile	7.63500 cm	St. Dev.= 0.02300 cm
Local Shock Angle	31.56255 °	St. Dev.= 0.42685 °
R Location of Shock	7.73300 cm	St. Dev.= 0.00071 cm
R Location of Model Surface	4.59200 cm	St. Dev.= 0.00000 cm

Approximated and Abel Transformed Data

I	Radius (cm)	Fringe Number	ρ/ρ_t	St. Dev. ρ/ρ_t
1	4.610	4.52364	0.0791576	0.0259273
2	4.687	4.66106	0.0796626	0.0222552
3	4.764	4.80214	0.0799585	0.0197086
4	4.840	4.95349	0.0802548	0.0176624
5	4.917	5.11959	0.0807154	0.0158217
6	4.993	5.30305	0.0814651	0.0140972
7	5.070	5.50489	0.0825929	0.0124960
8	5.146	5.72474	0.0841570	0.0110495
9	5.223	5.96109	0.0861896	0.0097778
10	5.299	6.21148	0.0886993	0.0086758
11	5.376	6.47272	0.0916762	0.0077185
12	5.453	6.74106	0.0950942	0.0068763
13	5.529	7.01234	0.0989143	0.0061370
14	5.606	7.28214	0.1030877	0.0055213
15	5.682	7.54594	0.1075578	0.0050868
16	5.759	7.79921	0.1122627	0.0049092
17	5.835	8.03753	0.1171381	0.0050310
18	5.912	8.25665	0.1221180	0.0054178
19	5.989	8.45262	0.1271370	0.0059725
20	6.065	8.62179	0.1321319	0.0065823
21	6.142	8.76087	0.1370427	0.0071484
22	6.218	8.86697	0.1418129	0.0075941
23	6.295	8.93762	0.1463930	0.0078657
24	6.371	8.97073	0.1507369	0.0079280
25	6.448	8.96461	0.1548060	0.0077631
26	6.524	8.91790	0.1585669	0.0073707
27	6.601	8.82957	0.1619926	0.0067668
28	6.677	8.69881	0.1650602	0.0059814
29	6.754	8.52499	0.1677524	0.0050630
30	6.831	8.30753	0.1700535	0.0040733
31	6.907	8.04582	0.1719483	0.0030977
32	6.984	7.73908	0.1734203	0.0022603
33	7.060	7.38624	0.1744463	0.0017563
34	7.137	6.98575	0.1749944	0.0017612
35	7.213	6.53545	0.1750134	0.0021539
36	7.290	6.03236	0.1744273	0.0027282
37	7.366	5.47251	0.1731274	0.0034388
38	7.443	4.85067	0.1709619	0.0043155
39	7.519	4.16018	0.1677577	0.0053471
40	7.596	3.39267	0.1635203	0.0063912
41	7.672	2.53783	0.1603181	0.0069402
42	7.749	0.00000	0.0896156	0.0000000
43	7.826	0.00000	0.0896156	0.0000000
44	7.902	0.00000	0.0896156	0.0000000
45	7.979	0.00000	0.0896156	0.0000000
46	8.056	0.00000	0.0896156	0.0000000
47	8.132	0.00000	0.0896156	0.0000000
48	8.208	0.00000	0.0896156	0.0000000
49	8.285	0.00000	0.0896156	0.0000000
50	8.362	0.00000	0.0896156	0.0000000

Interferogram Profile 16	4 Profiles averaged	
X Location of Profile	8.62700 cm	St. Dev.= 0.02000 cm
Local Shock Angle	31.56255 °	St. Dev.= 0.42685 °
R Location of Shock	8.31100 cm	St. Dev.= 0.00068 cm
R Location of Model Surface	4.59200 cm	St. Dev.= 0.00000 cm

Approximated and Abel Transformed Data

I	Radius (cm)	Fringe Number	ρ/ρ_t	St. Dev. ρ/ρ_t
1	4.617	2.30269	0.0595778	0.0134349
2	4.708	2.52125	0.0603529	0.0136172
3	4.798	2.75720	0.0615119	0.0137948
4	4.889	3.00719	0.0629934	0.0139080
5	4.980	3.26845	0.0647479	0.0139136
6	5.070	3.53859	0.0667363	0.0137846
7	5.161	3.81564	0.0689281	0.0135081
8	5.251	4.09787	0.0713005	0.0130833
9	5.342	4.38380	0.0738369	0.0125192
10	5.432	4.67211	0.0765262	0.0118327
11	5.523	4.96154	0.0793605	0.0110467
12	5.613	5.25092	0.0823362	0.0101887
13	5.704	5.53904	0.0854504	0.0092886
14	5.794	5.82466	0.0887031	0.0083794
15	5.885	6.10643	0.0920934	0.0074943
16	5.976	6.38289	0.0956212	0.0066672
17	6.066	6.65241	0.0992848	0.0059304
18	6.157	6.91319	0.1030814	0.0053127
19	6.247	7.16321	0.1070065	0.0048356
20	6.338	7.40024	0.1110521	0.0045079
21	6.428	7.62183	0.1152073	0.0043233
22	6.519	7.82528	0.1194583	0.0042610
23	6.610	8.00764	0.1237866	0.0042938
24	6.700	8.16575	0.1281698	0.0043953
25	6.791	8.29620	0.1325797	0.0045468
26	6.881	8.39539	0.1369839	0.0047346
27	6.972	8.45949	0.1413445	0.0049515
28	7.062	8.48452	0.1456157	0.0051905
29	7.153	8.46635	0.1497478	0.0054448
30	7.243	8.40071	0.1536816	0.0057036
31	7.334	8.28328	0.1573518	0.0059547
32	7.424	8.10968	0.1606839	0.0061829
33	7.515	7.87556	0.1635936	0.0063728
34	7.606	7.57661	0.1659854	0.0065068
35	7.697	7.20864	0.1677523	0.0065688
36	7.787	6.76763	0.1687700	0.0065376
37	7.878	6.24982	0.1689007	0.0063881
38	7.968	5.65174	0.1679926	0.0060941
39	8.059	4.97033	0.1659123	0.0056674
40	8.149	4.20296	0.1627266	0.0053263
41	8.240	3.34757	0.1602786	0.0055164
42	8.330	0.00000	0.0896156	0.0000000
43	8.421	0.00000	0.0896156	0.0000000
44	8.511	0.00000	0.0896156	0.0000000
45	8.602	0.00000	0.0896156	0.0000000
46	8.692	0.00000	0.0896156	0.0000000
47	8.783	0.00000	0.0896156	0.0000000
48	8.873	0.00000	0.0896156	0.0000000
49	8.964	0.00000	0.0896156	0.0000000
50	9.054	0.00000	0.0896156	0.0000000

TABLE D.5 Interferometry Data for 30° Model at 1.7 atm Total Pressure

Filename		30D25P.TEX	
Model Cone Angle		30.0 °	
Total Pressure		1.7 atm	
Total Temperature		285.0 °K	
Interferogram profile	1	X Location	-5.003 cm
Interferogram profile	2	X Location	-4.013 cm
Interferogram profile	3	X Location	-3.009 cm
Interferogram profile	4	X Location	-2.007 cm
Interferogram profile	5	X Location	-1.007 cm
Interferogram profile	6	X Location	-0.012 cm
Interferogram profile	7	X Location	0.996 cm
Interferogram profile	8	X Location	1.998 cm
Interferogram profile	9	X Location	2.996 cm
Interferogram profile	10	X Location	3.991 cm
Interferogram profile	11	X Location	4.980 cm
Interferogram profile	12	X Location	5.183 cm
Interferogram profile	13	X Location	6.173 cm
Interferogram profile	14	X Location	7.173 cm
Interferogram profile	15	X Location	8.194 cm

Interferogram Profile 1	4 Profiles averaged	
X Location of Profile	-5.00300 cm	St. Dev.= 0.00500 cm
Local Shock Angle	0.00000 °	St. Dev.= 0.00000 °
R Location of Shock	0.00000 cm	St. Dev.= 0.00000 cm
R Location of Model Surface	2.54000 cm	St. Dev.= 0.00000 cm

Approximated and Abel Transformed Data

I	Radius (cm)	Fringe Number	ρ/ρ_t	St. Dev. ρ/ρ_t
1	2.542	-0.87214	0.0415627	0.0063556
2	2.567	-0.82632	0.0437248	0.0060717
3	2.591	-0.78178	0.0458423	0.0058603
4	2.616	-0.73853	0.0479141	0.0058180
5	2.640	-0.69659	0.0499386	0.0060113
6	2.664	-0.65597	0.0519147	0.0064516
7	2.689	-0.61667	0.0538415	0.0070985
8	2.713	-0.57868	0.0557184	0.0078866
9	2.738	-0.54202	0.0575446	0.0087496
10	2.762	-0.50668	0.0593200	0.0096317
11	2.787	-0.47264	0.0610441	0.0104890
12	2.811	-0.43992	0.0627169	0.0112885
13	2.836	-0.40849	0.0643383	0.0120052
14	2.860	-0.37834	0.0659085	0.0126208
15	2.884	-0.34947	0.0674276	0.0131225
16	2.909	-0.32187	0.0688958	0.0135013
17	2.933	-0.29552	0.0703135	0.0137522
18	2.958	-0.27041	0.0716810	0.0138725
19	2.982	-0.24652	0.0729987	0.0138626
20	3.007	-0.22383	0.0742669	0.0137250
21	3.031	-0.20234	0.0754862	0.0134637
22	3.056	-0.18203	0.0766568	0.0130846
23	3.080	-0.16288	0.0777790	0.0125950
24	3.104	-0.14488	0.0788534	0.0120029
25	3.129	-0.12800	0.0798798	0.0113179
26	3.153	-0.11225	0.0808583	0.0105496
27	3.178	-0.09760	0.0817886	0.0097081
28	3.202	-0.08404	0.0826699	0.0088037
29	3.227	-0.07155	0.0835007	0.0078456
30	3.251	-0.06012	0.0842777	0.0068411
31	3.276	-0.04975	0.0849936	0.0057919
32	3.300	-0.04042	0.0856274	0.0046828
33	3.324	-0.03211	0.0860903	0.0034293
34	3.349	-0.02275	0.0869504	0.0028580
35	3.373	-0.01458	0.0878689	0.0024470
36	3.398	-0.00932	0.0884075	0.0018195
37	3.422	-0.00501	0.0889564	0.0013184
38	3.447	-0.00274	0.0892185	0.0007942
39	3.471	-0.00114	0.0894307	0.0003699
40	3.496	-0.00022	0.0895765	0.0000781
41	3.520	0.00000	0.0896156	0.0000000
42	3.544	0.00000	0.0896156	0.0000000
43	3.569	0.00000	0.0896156	0.0000000
44	3.593	0.00000	0.0896156	0.0000000
45	3.618	0.00000	0.0896156	0.0000000
46	3.642	0.00000	0.0896156	0.0000000
47	3.667	0.00000	0.0896156	0.0000000
48	3.691	0.00000	0.0896156	0.0000000
49	3.716	0.00000	0.0896156	0.0000000
50	3.740	0.00000	0.0896156	0.0000000

Interferogram Profile 2	2 Profiles averaged	
X Location of Profile	-4.01300 cm	St. Dev.= 0.01800 cm
Local Shock Angle	0.00000 °	St. Dev.= 0.00000 °
R Location of Shock	0.00000 cm	St. Dev.= 0.00000 cm
R Location of Model Surface	2.54000 cm	St. Dev.= 0.00000 cm

Approximated and Abel Transformed Data

I	Radius (cm)	Fringe Number	ρ/ρ_t	St. Dev. ρ/ρ_t
1	2.542	-1.00497	0.0413816	0.0109828
2	2.567	-0.96554	0.0431414	0.0101416
3	2.591	-0.92780	0.0447322	0.0091290
4	2.616	-0.89141	0.0461855	0.0079888
5	2.640	-0.85611	0.0475293	0.0067598
6	2.664	-0.82165	0.0487882	0.0054771
7	2.689	-0.78785	0.0499843	0.0041710
8	2.713	-0.75454	0.0511369	0.0028685
9	2.738	-0.72158	0.0522626	0.0015931
10	2.762	-0.68888	0.0533759	0.0003642
11	2.787	-0.65637	0.0544886	0.0008007
12	2.811	-0.62400	0.0556108	0.0018882
13	2.836	-0.59174	0.0567506	0.0028869
14	2.860	-0.55959	0.0579144	0.0037879
15	2.884	-0.52758	0.0591065	0.0045849
16	2.909	-0.49573	0.0603301	0.0052736
17	2.933	-0.46408	0.0615870	0.0058515
18	2.958	-0.43271	0.0628775	0.0063180
19	2.982	-0.40168	0.0642008	0.0066739
20	3.007	-0.37106	0.0655550	0.0069219
21	3.031	-0.34096	0.0669374	0.0070656
22	3.056	-0.31146	0.0683441	0.0071099
23	3.080	-0.28267	0.0697705	0.0070610
24	3.104	-0.25469	0.0712121	0.0069252
25	3.129	-0.22763	0.0726622	0.0067107
26	3.153	-0.20158	0.0741151	0.0064256
27	3.178	-0.17665	0.0755636	0.0060788
28	3.202	-0.15296	0.0770005	0.0056801
29	3.227	-0.13059	0.0784186	0.0052392
30	3.251	-0.10965	0.0798097	0.0047666
31	3.276	-0.09024	0.0811659	0.0042732
32	3.300	-0.07242	0.0824791	0.0037708
33	3.324	-0.05629	0.0837416	0.0032726
34	3.349	-0.04193	0.0849465	0.0027934
35	3.373	-0.02938	0.0860905	0.0023551
36	3.398	-0.01874	0.0871820	0.0019987
37	3.422	-0.01002	0.0882972	0.0018645
38	3.447	-0.00547	0.0888214	0.0011231
39	3.471	-0.00227	0.0892457	0.0005231
40	3.496	-0.00044	0.0895375	0.0001105
41	3.520	0.00000	0.0896156	0.0000000
42	3.544	0.00000	0.0896156	0.0000000
43	3.569	0.00000	0.0896156	0.0000000
44	3.593	0.00000	0.0896156	0.0000000
45	3.618	0.00000	0.0896156	0.0000000
46	3.642	0.00000	0.0896156	0.0000000
47	3.667	0.00000	0.0896156	0.0000000
48	3.691	0.00000	0.0896156	0.0000000
49	3.716	0.00000	0.0896156	0.0000000
50	3.740	0.00000	0.0896156	0.0000000

Interferogram Profile 3	3 Profiles averaged	
X Location of Profile	-3.00900 cm	St. Dev.= 0.01500 cm
Local Shock Angle	0.00000 °	St. Dev.= 0.00000 °
R Location of Shock	0.00000 cm	St. Dev.= 0.00000 cm
R Location of Model Surface	2.54000 cm	St. Dev.= 0.00000 cm

Approximated and Abel Transformed Data

I	Radius (cm)	Fringe Number	ρ/ρ_t	St. Dev. ρ/ρ_t
1	2.542	-0.72101	0.0568395	0.0003791
2	2.567	-0.69900	0.0573658	0.0012897
3	2.591	-0.67684	0.0578868	0.0020657
4	2.616	-0.65446	0.0584141	0.0027265
5	2.640	-0.63180	0.0589573	0.0032972
6	2.664	-0.60882	0.0595247	0.0037984
7	2.689	-0.58550	0.0601229	0.0042454
8	2.713	-0.56184	0.0607576	0.0046493
9	2.738	-0.53784	0.0614328	0.0050166
10	2.762	-0.51355	0.0621518	0.0053509
11	2.787	-0.48898	0.0629165	0.0056532
12	2.811	-0.46419	0.0637277	0.0059228
13	2.836	-0.43923	0.0645858	0.0061579
14	2.860	-0.41418	0.0654899	0.0063560
15	2.884	-0.38909	0.0664383	0.0065149
16	2.909	-0.36405	0.0674289	0.0066325
17	2.933	-0.33915	0.0684588	0.0067071
18	2.958	-0.31448	0.0695245	0.0067375
19	2.982	-0.29012	0.0706218	0.0067235
20	3.007	-0.26616	0.0717462	0.0066653
21	3.031	-0.24271	0.0728927	0.0065639
22	3.056	-0.21986	0.0740560	0.0064210
23	3.080	-0.19771	0.0752303	0.0062388
24	3.104	-0.17635	0.0764095	0.0060201
25	3.129	-0.15587	0.0775872	0.0057683
26	3.153	-0.13636	0.0787566	0.0054870
27	3.178	-0.11792	0.0799109	0.0051800
28	3.202	-0.10062	0.0810427	0.0048514
29	3.227	-0.08455	0.0821445	0.0045053
30	3.251	-0.06978	0.0832080	0.0041451
31	3.276	-0.05637	0.0842248	0.0037741
32	3.300	-0.04439	0.0851852	0.0033939
33	3.324	-0.03391	0.0860783	0.0030042
34	3.349	-0.02497	0.0868905	0.0026003
35	3.373	-0.01761	0.0876020	0.0021686
36	3.398	-0.01187	0.0881725	0.0016663
37	3.422	-0.00745	0.0886301	0.0011434
38	3.447	-0.00402	0.0890259	0.0006900
39	3.471	-0.00162	0.0893466	0.0003237
40	3.496	-0.00025	0.0895714	0.0000766
41	3.520	0.00000	0.0896156	0.0000000
42	3.544	0.00000	0.0896156	0.0000000
43	3.569	0.00000	0.0896156	0.0000000
44	3.593	0.00000	0.0896156	0.0000000
45	3.618	0.00000	0.0896156	0.0000000
46	3.642	0.00000	0.0896156	0.0000000
47	3.667	0.00000	0.0896156	0.0000000
48	3.691	0.00000	0.0896156	0.0000000
49	3.716	0.00000	0.0896156	0.0000000
50	3.740	0.00000	0.0896156	0.0000000

Interferogram Profile 4	8 Profiles averaged	
X Location of Profile	-2.00700 cm	St. Dev.= 0.01200 cm
Local Shock Angle	3.37530 °	St. Dev.= 6.25499 °
R Location of Shock	0.83300 cm	St. Dev.= 0.01548 cm
R Location of Model Surface	2.54000 cm	St. Dev.= 0.00000 cm

Approximated and Abel Transformed Data

I	Radius (cm)	Fringe Number	ρ/ρ_t	St. Dev. ρ/ρ_t
1	2.543	-0.39132	0.0454917	0.0404717
2	2.569	-0.28292	0.0578016	0.0232907
3	2.594	-0.21064	0.0653470	0.0155797
4	2.620	-0.15709	0.0706295	0.0114059
5	2.645	-0.11425	0.0748445	0.0093856
6	2.670	-0.07907	0.0784550	0.0090987
7	2.696	-0.05069	0.0815613	0.0097533
8	2.721	-0.02891	0.0841265	0.0105073
9	2.747	-0.01336	0.0861009	0.0108621
10	2.772	-0.00331	0.0874791	0.0106743
11	2.798	0.00240	0.0883144	0.0100930
12	2.823	0.00511	0.0887102	0.0094831
13	2.848	0.00621	0.0887997	0.0092564
14	2.874	0.00690	0.0887232	0.0095865
15	2.899	0.00811	0.0886085	0.0102751
16	2.925	0.01038	0.0885559	0.0109544
17	2.950	0.01391	0.0886305	0.0113286
18	2.976	0.01856	0.0888603	0.0112542
19	3.001	0.02395	0.0892393	0.0107293
20	3.027	0.02955	0.0897344	0.0098590
21	3.052	0.03478	0.0902950	0.0088173
22	3.077	0.03912	0.0908623	0.0078044
23	3.103	0.04217	0.0913791	0.0069933
24	3.128	0.04367	0.0917973	0.0064675
25	3.153	0.04357	0.0920828	0.0061918
26	3.179	0.04199	0.0922179	0.0060565
27	3.205	0.03920	0.0921968	0.0059599
28	3.230	0.03554	0.0920009	0.0058696
29	3.255	0.03243	0.0918910	0.0056774
30	3.281	0.02924	0.0917656	0.0054232
31	3.306	0.02601	0.0916254	0.0051078
32	3.332	0.02275	0.0914712	0.0047342
33	3.357	0.01951	0.0913038	0.0043070
34	3.382	0.01631	0.0911243	0.0038318
35	3.408	0.01319	0.0909353	0.0033143
36	3.434	0.01020	0.0907461	0.0027588
37	3.459	0.00718	0.0905013	0.0021990
38	3.485	0.00443	0.0902408	0.0016198
39	3.510	0.00222	0.0900271	0.0009925
40	3.536	0.00010	0.0897303	0.0003303
41	3.561	-0.00136	0.0893829	0.0006581
42	3.586	0.00000	0.0896156	0.0000000
43	3.612	0.00000	0.0896156	0.0000000
44	3.637	0.00000	0.0896156	0.0000000
45	3.662	0.00000	0.0896156	0.0000000
46	3.687	0.00000	0.0896156	0.0000000
47	3.713	0.00000	0.0896156	0.0000000
48	3.739	0.00000	0.0896156	0.0000000
49	3.764	0.00000	0.0896156	0.0000000
50	3.790	0.00000	0.0896156	0.0000000

Interferogram Profile 5	8 Profiles averaged	
X Location of Profile	-1.00700 cm	St. Dev.= 0.01500 cm
Local Shock Angle	25.70348 °	St. Dev.= 4.69826 °
R Location of Shock	3.76900 cm	St. Dev.= 0.00100 cm
R Location of Model Surface	2.54000 cm	St. Dev.= 0.00000 cm

Approximated and Abel Transformed Data

I	Radius (cm)	Fringe Number	ρ/ρ_t	St. Dev. ρ/ρ_t
1	2.547	-0.07857	0.0694039	0.0108404
2	2.579	-0.05033	0.0705528	0.0094689
3	2.611	-0.02326	0.0715809	0.0088223
4	2.642	0.00283	0.0724969	0.0087242
5	2.674	0.02820	0.0733134	0.0089956
6	2.706	0.05310	0.0740466	0.0094867
7	2.738	0.07780	0.0747158	0.0100874
8	2.770	0.10257	0.0753428	0.0107206
9	2.802	0.12766	0.0759519	0.0113321
10	2.834	0.15335	0.0765688	0.0118826
11	2.866	0.17986	0.0772208	0.0123434
12	2.897	0.20739	0.0779359	0.0126936
13	2.929	0.23610	0.0787425	0.0129186
14	2.961	0.26610	0.0796688	0.0130094
15	2.993	0.29747	0.0807423	0.0129611
16	3.025	0.33020	0.0819894	0.0127732
17	3.057	0.36422	0.0834345	0.0124492
18	3.088	0.39938	0.0850996	0.0119970
19	3.120	0.43544	0.0870033	0.0114307
20	3.152	0.47207	0.0891603	0.0107727
21	3.184	0.50884	0.0915802	0.0100594
22	3.216	0.54520	0.0942669	0.0093476
23	3.248	0.58049	0.0972166	0.0087245
24	3.280	0.61391	0.1004171	0.0083107
25	3.312	0.64453	0.1038453	0.0082431
26	3.343	0.67127	0.1074655	0.0086227
27	3.375	0.69292	0.1112258	0.0094572
28	3.407	0.70807	0.1150539	0.0106523
29	3.439	0.71519	0.1188518	0.0120478
30	3.471	0.71252	0.1224860	0.0134443
31	3.503	0.69818	0.1257733	0.0145987
32	3.534	0.67002	0.1284546	0.0151942
33	3.566	0.62575	0.1301414	0.0147902
34	3.598	0.56285	0.1301876	0.0128075
35	3.630	0.47857	0.1272796	0.0096618
36	3.662	0.36995	0.1173318	0.0196428
37	3.694	0.31667	0.1164972	0.0195247
38	3.726	0.25194	0.1142626	0.0190302
39	3.757	0.17458	0.1096010	0.0193671
40	3.789	0.10984	0.1040079	0.0208301
41	3.821	0.09543	0.1041242	0.0203714
42	3.853	0.00000	0.0896156	0.0000000
43	3.885	0.00000	0.0896156	0.0000000
44	3.917	0.00000	0.0896156	0.0000000
45	3.948	0.00000	0.0896156	0.0000000
46	3.980	0.00000	0.0896156	0.0000000
47	4.012	0.00000	0.0896156	0.0000000
48	4.044	0.00000	0.0896156	0.0000000
49	4.076	0.00000	0.0896156	0.0000000
50	4.108	0.00000	0.0896156	0.0000000

Interferogram Profile 6	8 Profiles averaged	
X Location of Profile	-0.01200 cm	St. Dev.= 0.01100 cm
Local Shock Angle	27.45329 °	St. Dev.= 0.97747 °
R Location of Shock	4.28200 cm	St. Dev.= 0.00085 cm
R Location of Model Surface	2.54100 cm	St. Dev.= 0.00002 cm

Approximated and Abel Transformed Data

I	Radius (cm)	Fringe Number	ρ/ρ_t	St. Dev. ρ/ρ_t
1	2.551	0.33895	0.0738114	0.0096288
2	2.594	0.37759	0.0759254	0.0085710
3	2.636	0.41115	0.0775276	0.0080923
4	2.679	0.44092	0.0787080	0.0078125
5	2.721	0.46811	0.0795537	0.0075806
6	2.763	0.49384	0.0801482	0.0073544
7	2.806	0.51909	0.0805711	0.0071261
8	2.848	0.54475	0.0808969	0.0068947
9	2.890	0.57157	0.0811954	0.0066648
10	2.933	0.60018	0.0815304	0.0064531
11	2.975	0.63106	0.0819598	0.0062933
12	3.018	0.66457	0.0825352	0.0062343
13	3.060	0.70092	0.0833015	0.0063257
14	3.103	0.74017	0.0842967	0.0065973
15	3.145	0.78225	0.0855515	0.0070435
16	3.187	0.82695	0.0870894	0.0076237
17	3.230	0.87390	0.0889263	0.0082763
18	3.272	0.92264	0.0910707	0.0089343
19	3.315	0.97255	0.0935230	0.0095356
20	3.357	1.02290	0.0962762	0.0100281
21	3.399	1.07284	0.0993155	0.0103724
22	3.442	1.12143	0.1026179	0.0105424
23	3.484	1.16763	0.1061531	0.0105266
24	3.527	1.21032	0.1098826	0.0103281
25	3.569	1.24830	0.1137606	0.0099660
26	3.612	1.28034	0.1177330	0.0094744
27	3.654	1.30516	0.1217385	0.0089032
28	3.697	1.32145	0.1257077	0.0083147
29	3.739	1.32791	0.1295636	0.0077785
30	3.781	1.32324	0.1332206	0.0073567
31	3.824	1.30620	0.1365848	0.0070887
32	3.866	1.27559	0.1395525	0.0069738
33	3.909	1.23029	0.1420094	0.0069723
34	3.951	1.16929	0.1438274	0.0070224
35	3.994	1.09173	0.1448614	0.0070645
36	4.036	0.99688	0.1449414	0.0070540
37	4.078	0.88421	0.1438610	0.0069569
38	4.121	0.75339	0.1413552	0.0067301
39	4.163	0.60437	0.1370683	0.0063736
40	4.206	0.43735	0.1305843	0.0067679
41	4.248	0.25285	0.1236333	0.0148264
42	4.291	0.00000	0.0896156	0.0000000
43	4.333	0.00000	0.0896156	0.0000000
44	4.375	0.00000	0.0896156	0.0000000
45	4.418	0.00000	0.0896156	0.0000000
46	4.460	0.00000	0.0896156	0.0000000
47	4.503	0.00000	0.0896156	0.0000000
48	4.545	0.00000	0.0896156	0.0000000
49	4.588	0.00000	0.0896156	0.0000000
50	4.630	0.00000	0.0896156	0.0000000

Interferogram Profile 7	8 Profiles averaged	
X Location of Profile	0.99600 cm	St. Dev.= 0.01400 cm
Local Shock Angle	27.45329 °	St. Dev.= 0.97747 °
R Location of Shock	4.79500 cm	St. Dev.= 0.00076 cm
R Location of Model Surface	3.11500 cm	St. Dev.= 0.00008 cm

Approximated and Abel Transformed Data

I	Radius (cm)	Fringe Number	ρ/ρ_t	St. Dev. ρ/ρ_t
1	3.124	1.61064	0.1030623	0.0137328
2	3.165	1.61563	0.1025450	0.0131239
3	3.206	1.62087	0.1016041	0.0122518
4	3.246	1.62969	0.1005894	0.0112914
5	3.287	1.64430	0.0997691	0.0104581
6	3.329	1.66591	0.0993398	0.0099011
7	3.369	1.69495	0.0994354	0.0096462
8	3.410	1.73115	0.1001353	0.0096033
9	3.451	1.77371	0.1014725	0.0096315
10	3.492	1.82139	0.1034411	0.0096043
11	3.533	1.87265	0.1060034	0.0094425
12	3.574	1.92576	0.1090953	0.0091191
13	3.615	1.97885	0.1126339	0.0086519
14	3.656	2.03005	0.1165217	0.0080939
15	3.697	2.07751	0.1206520	0.0075231
16	3.738	2.11950	0.1249140	0.0070283
17	3.779	2.15446	0.1291967	0.0066867
18	3.820	2.18101	0.1333922	0.0065348
19	3.861	2.19806	0.1374000	0.0065513
20	3.902	2.20473	0.1411293	0.0066658
21	3.943	2.20048	0.1445015	0.0067883
22	3.984	2.18500	0.1474528	0.0068377
23	4.025	2.15831	0.1499352	0.0067558
24	4.066	2.12068	0.1519177	0.0065137
25	4.107	2.07263	0.1533873	0.0061144
26	4.148	2.01487	0.1543491	0.0055931
27	4.189	1.94832	0.1548248	0.0050242
28	4.230	1.87398	0.1548528	0.0045266
29	4.271	1.79291	0.1544857	0.0042470
30	4.312	1.70615	0.1537867	0.0042966
31	4.353	1.61465	0.1528270	0.0046644
32	4.394	1.51916	0.1516797	0.0052318
33	4.435	1.42011	0.1504114	0.0058703
34	4.476	1.31755	0.1490750	0.0065012
35	4.517	1.21098	0.1476938	0.0071125
36	4.558	1.09925	0.1462439	0.0077482
37	4.599	0.98039	0.1446266	0.0084739
38	4.639	0.85151	0.1426283	0.0093043
39	4.680	0.70856	0.1398736	0.0101400
40	4.721	0.54624	0.1358999	0.0108555
41	4.762	0.35778	0.1334770	0.0115865
42	4.803	0.00000	0.0896156	0.0000000
43	4.844	0.00000	0.0896156	0.0000000
44	4.885	0.00000	0.0896156	0.0000000
45	4.926	0.00000	0.0896156	0.0000000
46	4.967	0.00000	0.0896156	0.0000000
47	5.008	0.00000	0.0896156	0.0000000
48	5.049	0.00000	0.0896156	0.0000000
49	5.090	0.00000	0.0896156	0.0000000
50	5.131	0.00000	0.0896156	0.0000000

Interferogram Profile 8	8 Profiles averaged	
X Location of Profile	1.99800 cm	St. Dev.= 0.01800 cm
Local Shock Angle	27.45329 °	St. Dev.= 0.97747 °
R Location of Shock	5.31700 cm	St. Dev.= 0.00097 cm
R Location of Model Surface	3.69400 cm	St. Dev.= 0.00010 cm

Approximated and Abel Transformed Data

I	Radius (cm)	Fringe Number	ρ/ρ_t	St. Dev. ρ/ρ_t
1	3.699	3.53249	0.1382510	0.0136594
2	3.739	3.53744	0.1397447	0.0160058
3	3.778	3.53361	0.1401303	0.0165070
4	3.818	3.52710	0.1398957	0.0157693
5	3.858	3.52266	0.1394724	0.0148763
6	3.897	3.52368	0.1392227	0.0147969
7	3.937	3.53214	0.1394334	0.0159254
8	3.976	3.54881	0.1403119	0.0179497
9	4.016	3.57325	0.1419873	0.0202884
10	4.056	3.60409	0.1445134	0.0224685
11	4.095	3.63914	0.1478751	0.0242033
12	4.135	3.67559	0.1519963	0.0253571
13	4.175	3.71028	0.1567495	0.0259035
14	4.214	3.73981	0.1619662	0.0258946
15	4.254	3.76083	0.1674491	0.0254368
16	4.293	3.77016	0.1729817	0.0246669
17	4.333	3.76497	0.1783420	0.0237279
18	4.373	3.74295	0.1833132	0.0227446
19	4.413	3.70240	0.1876923	0.0217983
20	4.452	3.64230	0.1913029	0.0209161
21	4.492	3.56240	0.1940008	0.0200757
22	4.532	3.46321	0.1956821	0.0192269
23	4.571	3.34598	0.1962898	0.0183236
24	4.611	3.21268	0.1958138	0.0173595
25	4.650	3.06586	0.1942970	0.0163883
26	4.690	2.90856	0.1918317	0.0155287
27	4.730	2.74414	0.1885571	0.0149404
28	4.769	2.57610	0.1846548	0.0147522
29	4.809	2.40786	0.1803411	0.0149755
30	4.848	2.24251	0.1758546	0.0154662
31	4.888	2.08258	0.1714444	0.0159739
32	4.928	1.92976	0.1673506	0.0162392
33	4.968	1.78460	0.1637830	0.0160961
34	5.007	1.64626	0.1608939	0.0155839
35	5.047	1.51222	0.1587402	0.0150798
36	5.086	1.37805	0.1572364	0.0153316
37	5.126	1.23713	0.1560796	0.0169670
38	5.166	1.08051	0.1546295	0.0195374
39	5.205	0.89669	0.1516759	0.0210282
40	5.245	0.67157	0.1449285	0.0175558
41	5.285	0.38838	0.1317147	0.0207978
42	5.324	0.00000	0.0896156	0.0000000
43	5.364	0.00000	0.0896156	0.0000000
44	5.403	0.00000	0.0896156	0.0000000
45	5.443	0.00000	0.0896156	0.0000000
46	5.483	0.00000	0.0896156	0.0000000
47	5.522	0.00000	0.0896156	0.0000000
48	5.562	0.00000	0.0896156	0.0000000
49	5.602	0.00000	0.0896156	0.0000000
50	5.641	0.00000	0.0896156	0.0000000

Interferogram Profile 9	8 Profiles averaged	
X Location of Profile	2.99600 cm	St. Dev.= 0.02800 cm
Local Shock Angle	27.53122 °	St. Dev.= 0.92991 °
R Location of Shock	5.86800 cm	St. Dev.= 0.00077 cm
R Location of Model Surface	4.27000 cm	St. Dev.= 0.00016 cm

Approximated and Abel Transformed Data

I	Radius (cm)	Fringe Number	ρ/ρ_t	St. Dev. ρ/ρ_t
1	4.276	5.44241	0.1643454	0.0261983
2	4.315	5.43780	0.1648539	0.0264750
3	4.354	5.43486	0.1652754	0.0259780
4	4.393	5.43572	0.1658510	0.0248710
5	4.432	5.44172	0.1667838	0.0234491
6	4.471	5.45335	0.1682310	0.0220057
7	4.510	5.47029	0.1703014	0.0207736
8	4.549	5.49149	0.1730509	0.0198868
9	4.588	5.51528	0.1764880	0.0193682
10	4.627	5.53945	0.1805734	0.0191510
11	4.666	5.56146	0.1852264	0.0191259
12	4.705	5.57849	0.1903327	0.0191889
13	4.744	5.58767	0.1957494	0.0192667
14	4.783	5.58619	0.2013142	0.0193255
15	4.822	5.57142	0.2068541	0.0193555
16	4.861	5.54104	0.2121914	0.0193575
17	4.900	5.49313	0.2171548	0.0193250
18	4.939	5.42628	0.2215835	0.0192371
19	4.978	5.33963	0.2253372	0.0190531
20	5.017	5.23288	0.2283002	0.0187202
21	5.056	5.10633	0.2303845	0.0181826
22	5.095	4.96086	0.2315384	0.0173962
23	5.134	4.79787	0.2317433	0.0163367
24	5.173	4.61922	0.2310178	0.0150114
25	5.212	4.42711	0.2294147	0.0134717
26	5.251	4.22403	0.2270208	0.0118237
27	5.290	4.01255	0.2239512	0.0102572
28	5.329	3.79521	0.2203418	0.0090602
29	5.368	3.57436	0.2163462	0.0085739
30	5.407	3.35197	0.2121195	0.0089757
31	5.446	3.12949	0.2078126	0.0101013
32	5.485	2.90764	0.2035539	0.0116007
33	5.525	2.68631	0.1994339	0.0131691
34	5.563	2.46436	0.1954857	0.0146205
35	5.602	2.23957	0.1916581	0.0158922
36	5.642	2.00850	0.1877857	0.0170509
37	5.681	1.76650	0.1835418	0.0182638
38	5.719	1.50772	0.1783713	0.0196866
39	5.758	1.22518	0.1714112	0.0211958
40	5.797	0.91092	0.1616215	0.0221949
41	5.836	0.55626	0.1560751	0.0221551
42	5.876	0.00000	0.0896156	0.0000000
43	5.915	0.00000	0.0896156	0.0000000
44	5.954	0.00000	0.0896156	0.0000000
45	5.993	0.00000	0.0896156	0.0000000
46	6.032	0.00000	0.0896156	0.0000000
47	6.071	0.00000	0.0896156	0.0000000
48	6.110	0.00000	0.0896156	0.0000000
49	6.148	0.00000	0.0896156	0.0000000
50	6.188	0.00000	0.0896156	0.0000000

Interferogram Profile 10	8 Profiles averaged	
X Location of Profile	3.99100 cm	St. Dev.= 0.03200 cm
Local Shock Angle	35.68728 °	St. Dev.= 6.66350 °
R Location of Shock	6.59200 cm	St. Dev.= 0.00084 cm
R Location of Model Surface	4.84500 cm	St. Dev.= 0.00018 cm

Approximated and Abel Transformed Data

I	Radius (cm)	Fringe Number	ρ/ρ_t	St. Dev. ρ/ρ_t
1	4.851	6.96336	0.1714483	0.0236534
2	4.894	6.97591	0.1721739	0.0200330
3	4.936	7.00071	0.1741818	0.0185863
4	4.979	7.03203	0.1771244	0.0176382
5	5.022	7.06545	0.1807408	0.0164708
6	5.064	7.09760	0.1848348	0.0150054
7	5.107	7.12577	0.1892573	0.0134605
8	5.150	7.14783	0.1938919	0.0121535
9	5.193	7.16196	0.1986446	0.0113490
10	5.235	7.16662	0.2034346	0.0111184
11	5.278	7.16043	0.2081893	0.0113021
12	5.320	7.14219	0.2128406	0.0116303
13	5.363	7.11080	0.2173216	0.0118687
14	5.406	7.06530	0.2215668	0.0118798
15	5.448	7.00487	0.2255117	0.0116206
16	5.491	6.92887	0.2290948	0.0111256
17	5.534	6.83683	0.2322563	0.0104842
18	5.576	6.72851	0.2349443	0.0098227
19	5.619	6.60387	0.2371130	0.0092757
20	5.662	6.46315	0.2387254	0.0089519
21	5.704	6.30678	0.2397568	0.0088946
22	5.747	6.13547	0.2401928	0.0090719
23	5.790	5.95010	0.2400326	0.0093999
24	5.832	5.75177	0.2392881	0.0097891
25	5.875	5.54170	0.2379835	0.0101704
26	5.917	5.32121	0.2361529	0.0105038
27	5.960	5.09166	0.2338414	0.0107700
28	6.003	4.85439	0.2310981	0.0109587
29	6.046	4.61066	0.2279769	0.0110554
30	6.088	4.36158	0.2245292	0.0110379
31	6.131	4.10807	0.2208021	0.0108861
32	6.174	3.85083	0.2168319	0.0106061
33	6.216	3.59026	0.2126411	0.0102849
34	6.259	3.32656	0.2082349	0.0101626
35	6.302	3.05965	0.2035942	0.0106719
36	6.344	2.78932	0.1986832	0.0122878
37	6.387	2.51531	0.1934499	0.0152033
38	6.430	2.23747	0.1878526	0.0192304
39	6.472	1.95603	0.1819269	0.0238816
40	6.515	1.67185	0.1760623	0.0282517
41	6.557	1.38688	0.1728193	0.0296142
42	6.600	0.00000	0.0896156	0.0000000
43	6.643	0.00000	0.0896156	0.0000000
44	6.686	0.00000	0.0896156	0.0000000
45	6.728	0.00000	0.0896156	0.0000000
46	6.771	0.00000	0.0896156	0.0000000
47	6.814	0.00000	0.0896156	0.0000000
48	6.856	0.00000	0.0896156	0.0000000
49	6.899	0.00000	0.0896156	0.0000000
50	6.942	0.00000	0.0896156	0.0000000

Interferogram Profile 11 1 Profile
X Location of Profile 4.98000 cm
Local Shock Angle 40.24974 °
R Location of Shock 7.40500 cm
R Location of Model Surface 5.41500 cm

Approximated and Abel Transformed Data

I	Radius (cm)	Fringe Number	ρ/ρ_t
1	5.428	9.43924	0.1934286
2	5.477	9.43615	0.1936242
3	5.525	9.45110	0.1953395
4	5.574	9.47762	0.1983081
5	5.622	9.50979	0.2022777
6	5.671	9.54229	0.2070124
7	5.719	9.57039	0.2122907
8	5.767	9.58992	0.2179103
9	5.816	9.59731	0.2236843
10	5.864	9.58954	0.2294419
11	5.913	9.56416	0.2350330
12	5.961	9.51927	0.2403251
13	6.010	9.45347	0.2451994
14	6.058	9.36589	0.2495617
15	6.107	9.25612	0.2533318
16	6.155	9.12421	0.2564471
17	6.204	8.97060	0.2588646
18	6.252	8.79614	0.2605568
19	6.301	8.60200	0.2615147
20	6.349	8.38965	0.2617438
21	6.397	8.16082	0.2612660
22	6.446	7.91743	0.2601172
23	6.494	7.66156	0.2583454
24	6.543	7.39536	0.2560149
25	6.591	7.12103	0.2531968
26	6.640	6.84072	0.2499715
27	6.688	6.55652	0.2464328
28	6.737	6.27030	0.2426712
29	6.785	5.98372	0.2387851
30	6.834	5.69809	0.2348751
31	6.882	5.41435	0.2310311
32	6.931	5.13293	0.2273420
33	6.979	4.85369	0.2238830
34	7.028	4.57584	0.2207109
35	7.076	4.29781	0.2178608
36	7.124	4.01718	0.2153322
37	7.173	3.73056	0.2130882
38	7.221	3.43352	0.2110388
39	7.270	3.12044	0.2090546
40	7.318	2.78440	0.2069927
41	7.367	2.41711	0.2050573
42	7.415	0.00000	0.0896156
43	7.464	0.00000	0.0896156
44	7.512	0.00000	0.0896156
45	7.561	0.00000	0.0896156
46	7.609	0.00000	0.0896156
47	7.658	0.00000	0.0896156
48	7.706	0.00000	0.0896156
49	7.755	0.00000	0.0896156
50	7.803	0.00000	0.0896156

Interferogram Profile 12	8 Profiles averaged	
X Location of Profile	5.18300 cm	St. Dev.= 0.02600 cm
Local Shock Angle	40.31220 °	St. Dev.= 0.49103 °
R Location of Shock	7.55700 cm	St. Dev.= 0.00048 cm
R Location of Model Surface	5.52800 cm	St. Dev.= 0.00010 cm

Approximated and Abel Transformed Data

I	Radius (cm)	Fringe Number	ρ/ρ_t	St. Dev. ρ/ρ_t
1	5.534	8.94421	0.1726536	0.0192724
2	5.584	9.01003	0.1764771	0.0206277
3	5.633	9.07483	0.1806339	0.0214012
4	5.683	9.13779	0.1851718	0.0215344
5	5.732	9.19732	0.1900872	0.0210628
6	5.782	9.25140	0.1953367	0.0200602
7	5.832	9.29770	0.2008484	0.0186279
8	5.881	9.33379	0.2065293	0.0168922
9	5.931	9.35729	0.2122752	0.0150007
10	5.980	9.36601	0.2179756	0.0131197
11	6.030	9.35799	0.2235207	0.0114219
12	6.079	9.33162	0.2288066	0.0100629
13	6.129	9.28566	0.2337365	0.0091370
14	6.178	9.21926	0.2382279	0.0086253
15	6.228	9.13200	0.2422105	0.0083960
16	6.278	9.02384	0.2456315	0.0082664
17	6.327	8.89514	0.2484527	0.0080799
18	6.377	8.74658	0.2506539	0.0077432
19	6.426	8.57915	0.2522305	0.0072288
20	6.476	8.39410	0.2531928	0.0065741
21	6.525	8.19283	0.2535644	0.0058797
22	6.575	7.97689	0.2533830	0.0053088
23	6.625	7.74788	0.2526933	0.0050590
24	6.674	7.50738	0.2515474	0.0052546
25	6.724	7.25690	0.2500038	0.0058478
26	6.773	6.99782	0.2481205	0.0066718
27	6.823	6.73131	0.2459544	0.0075590
28	6.872	6.45833	0.2435591	0.0083933
29	6.922	6.17953	0.2409765	0.0091004
30	6.971	5.89528	0.2382418	0.0096415
31	7.021	5.60565	0.2353746	0.0099929
32	7.070	5.31036	0.2323794	0.0101376
33	7.120	5.00888	0.2292410	0.0100605
34	7.169	4.70043	0.2259286	0.0097539
35	7.219	4.38402	0.2223881	0.0092533
36	7.269	4.05861	0.2185531	0.0087098
37	7.318	3.72313	0.2143469	0.0085108
38	7.368	3.37671	0.2097027	0.0092461
39	7.417	3.01879	0.2046219	0.0112081
40	7.467	2.64935	0.1993618	0.0138790
41	7.516	2.26914	0.1955506	0.0156087
42	7.566	0.00000	0.0896156	0.0000000
43	7.615	0.00000	0.0896156	0.0000000
44	7.665	0.00000	0.0896156	0.0000000
45	7.715	0.00000	0.0896156	0.0000000
46	7.764	0.00000	0.0896156	0.0000000
47	7.814	0.00000	0.0896156	0.0000000
48	7.863	0.00000	0.0896156	0.0000000
49	7.913	0.00000	0.0896156	0.0000000
50	7.962	0.00000	0.0896156	0.0000000

Interferogram Profile 13	8 Profiles averaged	
X Location of Profile	6.17300 cm	St. Dev.= 0.02500 cm
Local Shock Angle	40.37465 °	St. Dev.= 0.47670 °
R Location of Shock	8.43300 cm	St. Dev.= 0.00061 cm
R Location of Model Surface	5.54000 cm	St. Dev.= 0.00000 cm

Approximated and Abel Transformed Data

I	Radius (cm)	Fringe Number	ρ/ρ_t	St. Dev. ρ/ρ_t
1	5.554	4.39917	0.0661657	0.0101722
2	5.625	4.57785	0.0679919	0.0097510
3	5.695	4.76199	0.0694938	0.0095038
4	5.766	4.96145	0.0714283	0.0097530
5	5.836	5.18028	0.0742551	0.0104256
6	5.907	5.41827	0.0782044	0.0112156
7	5.978	5.67230	0.0833369	0.0118837
8	6.048	5.93736	0.0895922	0.0123394
9	6.119	6.20747	0.0968279	0.0125967
10	6.189	6.47626	0.1048531	0.0127096
11	6.260	6.73751	0.1134530	0.0127259
12	6.330	6.98551	0.1224085	0.0126633
13	6.401	7.21526	0.1315117	0.0125101
14	6.472	7.42259	0.1405742	0.0122410
15	6.542	7.60426	0.1494342	0.0118388
16	6.613	7.75790	0.1579607	0.0113120
17	6.683	7.88193	0.1660517	0.0107040
18	6.754	7.97552	0.1736353	0.0100933
19	6.824	8.03840	0.1806647	0.0095802
20	6.895	8.07078	0.1871168	0.0092591
21	6.965	8.07319	0.1929846	0.0091747
22	7.036	8.04634	0.1982744	0.0093003
23	7.107	7.99104	0.2030001	0.0095440
24	7.177	7.90809	0.2071788	0.0097860
25	7.248	7.79820	0.2108269	0.0099198
26	7.318	7.66198	0.2139557	0.0098741
27	7.389	7.49987	0.2165692	0.0096226
28	7.459	7.31220	0.2186639	0.0091919
29	7.530	7.09919	0.2202267	0.0086636
30	7.601	6.86102	0.2212361	0.0081696
31	7.671	6.59785	0.2216628	0.0078666
32	7.742	6.30995	0.2214733	0.0078748
33	7.812	5.99775	0.2206337	0.0082052
34	7.883	5.66188	0.2191121	0.0087502
35	7.953	5.30324	0.2168831	0.0093514
36	8.024	4.92298	0.2139349	0.0098880
37	8.094	4.52247	0.2102725	0.0103314
38	8.165	4.10319	0.2059332	0.0107683
39	8.235	3.66655	0.2010192	0.0113563
40	8.306	3.21358	0.1958379	0.0121051
41	8.376	2.74453	0.1918006	0.0125228
42	8.447	0.00000	0.0896156	0.0000000
43	8.518	0.00000	0.0896156	0.0000000
44	8.588	0.00000	0.0896156	0.0000000
45	8.659	0.00000	0.0896156	0.0000000
46	8.729	0.00000	0.0896156	0.0000000
47	8.800	0.00000	0.0896156	0.0000000
48	8.871	0.00000	0.0896156	0.0000000
49	8.941	0.00000	0.0896156	0.0000000
50	9.012	0.00000	0.0896156	0.0000000

Interferogram Profile 14	8 Profiles averaged	
X Location of Profile	7.17300 cm	St. Dev.= 0.03100 cm
Local Shock Angle	40.37465 °	St. Dev.= 0.47670 °
R Location of Shock	9.29700 cm	St. Dev.= 0.00053 cm
R Location of Model Surface	5.54000 cm	St. Dev.= 0.00000 cm

Approximated and Abel Transformed Data

I	Radius (cm)	Fringe Number	ρ/ρ_t	St. Dev. ρ/ρ_t
1	5.562	3.34935	0.0694916	0.0083299
2	5.654	3.47657	0.0705188	0.0072955
3	5.745	3.60319	0.0710757	0.0065144
4	5.837	3.73477	0.0713522	0.0066813
5	5.929	3.87732	0.0716274	0.0073438
6	6.020	4.03600	0.0722053	0.0078766
7	6.112	4.21437	0.0733667	0.0080624
8	6.203	4.41393	0.0753379	0.0079937
9	6.295	4.63402	0.0782714	0.0078970
10	6.386	4.87191	0.0822384	0.0079778
11	6.478	5.12305	0.0872275	0.0082989
12	6.569	5.38156	0.0931531	0.0087655
13	6.661	5.64063	0.0998660	0.0092140
14	6.752	5.89306	0.1071694	0.0095022
15	6.844	6.13176	0.1148352	0.0095487
16	6.936	6.35023	0.1226222	0.0093342
17	7.027	6.54294	0.1302937	0.0088904
18	7.119	6.70562	0.1376345	0.0082834
19	7.210	6.83549	0.1444632	0.0075976
20	7.302	6.93139	0.1506457	0.0069163
21	7.393	6.99369	0.1561020	0.0063072
22	7.485	7.02417	0.1608114	0.0058077
23	7.576	7.02580	0.1648112	0.0054227
24	7.668	7.00233	0.1681949	0.0051347
25	7.760	6.95792	0.1711023	0.0049224
26	7.851	6.89657	0.1737071	0.0047732
27	7.943	6.82164	0.1762011	0.0046883
28	8.035	6.73529	0.1787744	0.0046715
29	8.126	6.63800	0.1815920	0.0047219
30	8.218	6.52815	0.1847705	0.0048243
31	8.309	6.40175	0.1883500	0.0049521
32	8.401	6.25233	0.1922745	0.0050727
33	8.492	6.07111	0.1963649	0.0051578
34	8.584	5.84746	0.2003059	0.0052149
35	8.676	5.56974	0.2036397	0.0053562
36	8.767	5.22662	0.2057738	0.0058764
37	8.859	4.80897	0.2060194	0.0071501
38	8.950	4.31228	0.2036741	0.0092164
39	9.042	3.73991	0.1982252	0.0114407
40	9.133	3.10712	0.1899668	0.0123762
41	9.225	2.44602	0.1844127	0.0124376
42	9.317	0.00000	0.0896156	0.0000000
43	9.408	0.00000	0.0896156	0.0000000
44	9.500	0.00000	0.0896156	0.0000000
45	9.591	0.00000	0.0896156	0.0000000
46	9.683	0.00000	0.0896156	0.0000000
47	9.774	0.00000	0.0896156	0.0000000
48	9.866	0.00000	0.0896156	0.0000000
49	9.957	0.00000	0.0896156	0.0000000
50	10.049	0.00000	0.0896156	0.0000000

Interferogram Profile 15	7 Profiles averaged	
X Location of Profile	8.19400 cm	St. Dev.= 0.01000 cm
Local Shock Angle	40.53565 °	St. Dev.= 0.58499 °
R Location of Shock	10.09000 cm	St. Dev.= 0.00032 cm
R Location of Model Surface	5.54000 cm	St. Dev.= 0.00000 cm

Approximated and Abel Transformed Data

I	Radius (cm)	Fringe Number	ρ/ρ_t	St. Dev. ρ/ρ_t
1	5.571	2.72059	0.0607582	0.0089808
2	5.682	2.91625	0.0641479	0.0085836
3	5.792	3.10420	0.0673733	0.0098262
4	5.903	3.28158	0.0701070	0.0114308
5	6.014	3.45104	0.0723323	0.0123618
6	6.125	3.61774	0.0742079	0.0122635
7	6.235	3.78726	0.0759707	0.0112251
8	6.346	3.96424	0.0778681	0.0095589
9	6.457	4.15161	0.0801138	0.0076701
10	6.568	4.35035	0.0828636	0.0059870
11	6.679	4.55948	0.0862045	0.0048949
12	6.790	4.77635	0.0901550	0.0045488
13	6.900	4.99706	0.0946726	0.0047259
14	7.011	5.21690	0.0996669	0.0051050
15	7.122	5.43087	0.1050135	0.0055403
16	7.233	5.63408	0.1105712	0.0060261
17	7.343	5.82219	0.1161960	0.0065782
18	7.454	5.99165	0.1217550	0.0071659
19	7.565	6.13990	0.1271379	0.0077035
20	7.676	6.26539	0.1322641	0.0080830
21	7.786	6.36762	0.1370880	0.0082085
22	7.898	6.44691	0.1416000	0.0080196
23	8.008	6.50424	0.1458255	0.0075060
24	8.119	6.54092	0.1498172	0.0067183
25	8.230	6.55828	0.1536516	0.0057824
26	8.341	6.55727	0.1574157	0.0049177
27	8.451	6.53816	0.1611962	0.0044265
28	8.562	6.50019	0.1650691	0.0045178
29	8.673	6.44130	0.1690836	0.0050695
30	8.784	6.35791	0.1732515	0.0057747
31	8.894	6.24485	0.1775338	0.0064077
32	9.005	6.09533	0.1818285	0.0068993
33	9.116	5.90105	0.1859613	0.0073070
34	9.227	5.65240	0.1896720	0.0077487
35	9.338	5.33878	0.1926024	0.0082657
36	9.449	4.94899	0.1942733	0.0086830
37	9.559	4.47172	0.1940443	0.0085775
38	9.670	3.89595	0.1910192	0.0074849
39	9.781	3.21149	0.1837950	0.0067120
40	9.892	2.40925	0.1696282	0.0152477
41	10.002	1.48146	0.1401045	0.0472585
42	10.113	0.00000	0.0896156	0.0000000
43	10.224	0.00000	0.0896156	0.0000000
44	10.335	0.00000	0.0896156	0.0000000
45	10.446	0.00000	0.0896156	0.0000000
46	10.556	0.00000	0.0896156	0.0000000
47	10.667	0.00000	0.0896156	0.0000000
48	10.778	0.00000	0.0896156	0.0000000
49	10.889	0.00000	0.0896156	0.0000000
50	10.999	0.00000	0.0896156	0.0000000

TABLE D.6 Interferometry Data for 30° Model at 3.4 atm Total Pressure

Filename		30D50P.TEX	
Model Cone Angle		30.0 °	
Total Pressure		3.4 atm	
Total Temperature		285.0 °K	
Interferogram profile	1	X Location	-4.985 cm
Interferogram profile	2	X Location	-3.986 cm
Interferogram profile	3	X Location	-2.987 cm
Interferogram profile	4	X Location	-2.006 cm
Interferogram profile	5	X Location	-0.999 cm
Interferogram profile	6	X Location	-0.014 cm
Interferogram profile	7	X Location	1.000 cm
Interferogram profile	8	X Location	2.006 cm

Interferogram Profile 1	4 Profiles averaged	
X Location of Profile	-4.98500 cm	St. Dev.= 0.05800 cm
Local Shock Angle	0.00000 °	St. Dev.= 0.00000 °
R Location of Shock	0.00000 cm	St. Dev.= 0.00000 cm
R Location of Model Surface	2.54000 cm	St. Dev.= 0.00000 cm

Approximated and Abel Transformed Data

I	Radius (cm)	Fringe Number	ρ/ρ_t	St. Dev. ρ/ρ_t
1	2.542	-1.69011	0.0417626	0.0085349
2	2.567	-1.59721	0.0439669	0.0082074
3	2.591	-1.50694	0.0461231	0.0078863
4	2.616	-1.41929	0.0482317	0.0075716
5	2.640	-1.33427	0.0502928	0.0072633
6	2.664	-1.25188	0.0523067	0.0069612
7	2.689	-1.17213	0.0542735	0.0066653
8	2.713	-1.09500	0.0561935	0.0063757
9	2.738	-1.02050	0.0580667	0.0060923
10	2.762	-0.94864	0.0598933	0.0058149
11	2.787	-0.87940	0.0616733	0.0055436
12	2.811	-0.81279	0.0634067	0.0052783
13	2.836	-0.74881	0.0650934	0.0050190
14	2.860	-0.68747	0.0667334	0.0047655
15	2.884	-0.62875	0.0683265	0.0045180
16	2.909	-0.57266	0.0698725	0.0042763
17	2.933	-0.51920	0.0713713	0.0040404
18	2.958	-0.46837	0.0728223	0.0038103
19	2.982	-0.42017	0.0742254	0.0035858
20	3.007	-0.37461	0.0755799	0.0033669
21	3.031	-0.33167	0.0768853	0.0031536
22	3.056	-0.29136	0.0781409	0.0029457
23	3.080	-0.25368	0.0793459	0.0027432
24	3.104	-0.21863	0.0804995	0.0025456
25	3.129	-0.18621	0.0816002	0.0023532
26	3.153	-0.15642	0.0826469	0.0021654
27	3.178	-0.12926	0.0836380	0.0019821
28	3.202	-0.10473	0.0845712	0.0018027
29	3.227	-0.08283	0.0854444	0.0016264
30	3.251	-0.06356	0.0862543	0.0014527
31	3.276	-0.04692	0.0869971	0.0012797
32	3.300	-0.03291	0.0876672	0.0011055
33	3.324	-0.02153	0.0882571	0.0009262
34	3.349	-0.01278	0.0887543	0.0007335
35	3.373	-0.00665	0.0891324	0.0005066
36	3.398	-0.00283	0.0893881	0.0002650
37	3.422	-0.00071	0.0895523	0.0000737
38	3.447	0.00000	0.0896156	0.0000000
39	3.471	0.00000	0.0896156	0.0000000
40	3.496	0.00000	0.0896156	0.0000000
41	3.520	0.00000	0.0896156	0.0000000
42	3.544	0.00000	0.0896156	0.0000000
43	3.569	0.00000	0.0896156	0.0000000
44	3.593	0.00000	0.0896156	0.0000000
45	3.618	0.00000	0.0896156	0.0000000
46	3.642	0.00000	0.0896156	0.0000000
47	3.667	0.00000	0.0896156	0.0000000
48	3.691	0.00000	0.0896156	0.0000000
49	3.716	0.00000	0.0896156	0.0000000
50	3.740	0.00000	0.0896156	0.0000000

Interferogram Profile 2	4 Profiles averaged	
X Location of Profile	-3.98600 cm	St. Dev.= 0.05300 cm
Local Shock Angle	0.00000 °	St. Dev.= 0.00000 °
R Location of Shock	0.00000 cm	St. Dev.= 0.00000 cm
R Location of Model Surface	2.54000 cm	St. Dev.= 0.00000 cm

Approximated and Abel Transformed Data

I	Radius (cm)	Fringe Number	ρ/ρ_t	St. Dev. ρ/ρ_t
1	2.542	-1.66322	0.0429593	0.0059573
2	2.567	-1.57342	0.0450750	0.0056121
3	2.591	-1.48611	0.0471449	0.0052774
4	2.616	-1.40131	0.0491696	0.0049531
5	2.640	-1.31901	0.0511493	0.0046394
6	2.664	-1.23920	0.0530841	0.0043366
7	2.689	-1.16190	0.0549743	0.0040449
8	2.713	-1.08710	0.0568200	0.0037644
9	2.738	-1.01480	0.0586214	0.0034956
10	2.762	-0.94499	0.0603785	0.0032388
11	2.787	-0.87770	0.0620915	0.0029945
12	2.811	-0.81289	0.0637603	0.0027632
13	2.836	-0.75060	0.0653848	0.0025456
14	2.860	-0.69080	0.0669653	0.0023424
15	2.884	-0.63350	0.0685013	0.0021546
16	2.909	-0.57870	0.0699927	0.0019829
17	2.933	-0.52641	0.0714394	0.0018286
18	2.958	-0.47661	0.0728411	0.0016924
19	2.982	-0.42931	0.0741975	0.0015754
20	3.007	-0.38451	0.0755080	0.0014778
21	3.031	-0.34222	0.0767722	0.0013997
22	3.056	-0.30242	0.0779896	0.0013402
23	3.080	-0.26513	0.0791593	0.0012977
24	3.104	-0.23034	0.0802805	0.0012696
25	3.129	-0.19804	0.0813522	0.0012528
26	3.153	-0.16825	0.0823731	0.0012439
27	3.178	-0.14096	0.0833420	0.0012387
28	3.202	-0.11617	0.0842568	0.0012337
29	3.227	-0.09388	0.0851155	0.0012250
30	3.251	-0.07409	0.0859153	0.0012086
31	3.276	-0.05680	0.0866526	0.0011805
32	3.300	-0.04201	0.0873229	0.0011357
33	3.324	-0.02972	0.0879190	0.0010679
34	3.349	-0.01993	0.0884297	0.0009664
35	3.373	-0.01264	0.0888304	0.0008085
36	3.398	-0.00748	0.0891314	0.0006316
37	3.422	-0.00406	0.0893444	0.0004641
38	3.447	-0.00209	0.0894670	0.0002972
39	3.471	-0.00093	0.0895418	0.0001476
40	3.496	-0.00023	0.0895951	0.0000410
41	3.520	0.00000	0.0896156	0.0000000
42	3.544	0.00000	0.0896156	0.0000000
43	3.569	0.00000	0.0896156	0.0000000
44	3.593	0.00000	0.0896156	0.0000000
45	3.618	0.00000	0.0896156	0.0000000
46	3.642	0.00000	0.0896156	0.0000000
47	3.667	0.00000	0.0896156	0.0000000
48	3.691	0.00000	0.0896156	0.0000000
49	3.716	0.00000	0.0896156	0.0000000
50	3.740	0.00000	0.0896156	0.0000000

Interferogram Profile 3	4 Profiles averaged	
X Location of Profile	-2.98700 cm	St. Dev.= 0.05100 cm
Local Shock Angle	0.00000 °	St. Dev.= 0.00000 °
R Location of Shock	0.00000 cm	St. Dev.= 0.00000 cm
R Location of Model Surface	2.54000 cm	St. Dev.= 0.00000 cm

Approximated and Abel Transformed Data

I	Radius (cm)	Fringe Number	ρ/ρ_t	St. Dev. ρ/ρ_t
1	2.542	-1.87728	0.0379576	0.0068424
2	2.567	-1.77977	0.0402148	0.0065435
3	2.591	-1.68487	0.0424246	0.0062515
4	2.616	-1.59256	0.0445876	0.0059662
5	2.640	-1.50286	0.0467038	0.0056879
6	2.664	-1.41576	0.0487738	0.0054164
7	2.689	-1.33126	0.0507975	0.0051517
8	2.713	-1.24937	0.0527752	0.0048938
9	2.738	-1.17007	0.0547073	0.0046428
10	2.762	-1.09338	0.0565937	0.0043986
11	2.787	-1.01929	0.0584345	0.0041613
12	2.811	-0.94780	0.0602299	0.0039309
13	2.836	-0.87892	0.0619800	0.0037073
14	2.860	-0.81264	0.0636846	0.0034908
15	2.884	-0.74896	0.0653438	0.0032813
16	2.909	-0.68788	0.0669573	0.0030789
17	2.933	-0.62941	0.0685253	0.0028837
18	2.958	-0.57353	0.0700472	0.0026956
19	2.982	-0.52026	0.0715231	0.0025150
20	3.007	-0.46959	0.0729526	0.0023417
21	3.031	-0.42152	0.0743351	0.0021761
22	3.056	-0.37606	0.0756704	0.0020180
23	3.080	-0.33320	0.0769577	0.0018677
24	3.104	-0.29294	0.0781967	0.0017252
25	3.129	-0.25528	0.0793862	0.0015907
26	3.153	-0.22022	0.0805254	0.0014639
27	3.178	-0.18777	0.0816134	0.0013451
28	3.202	-0.15792	0.0826487	0.0012340
29	3.227	-0.13067	0.0836299	0.0011303
30	3.251	-0.10602	0.0845550	0.0010336
31	3.276	-0.08398	0.0854218	0.0009430
32	3.300	-0.06453	0.0862273	0.0008574
33	3.324	-0.04769	0.0869682	0.0007750
34	3.349	-0.03346	0.0876394	0.0006935
35	3.373	-0.02182	0.0882345	0.0006088
36	3.398	-0.01279	0.0887437	0.0005152
37	3.422	-0.00636	0.0891499	0.0004009
38	3.447	-0.00253	0.0894140	0.0002331
39	3.471	-0.00063	0.0895595	0.0000648
40	3.496	0.00000	0.0896156	0.0000000
41	3.520	0.00000	0.0896156	0.0000000
42	3.544	0.00000	0.0896156	0.0000000
43	3.569	0.00000	0.0896156	0.0000000
44	3.593	0.00000	0.0896156	0.0000000
45	3.618	0.00000	0.0896156	0.0000000
46	3.642	0.00000	0.0896156	0.0000000
47	3.667	0.00000	0.0896156	0.0000000
48	3.691	0.00000	0.0896156	0.0000000
49	3.716	0.00000	0.0896156	0.0000000
50	3.740	0.00000	0.0896156	0.0000000

Interferogram Profile 4	4 Profiles averaged	
X Location of Profile	-2.00600 cm	St. Dev.= 0.03300 cm
Local Shock Angle	0.00000 °	St. Dev.= 0.00000 °
R Location of Shock	0.00000 cm	St. Dev.= 0.00000 cm
R Location of Model Surface	2.54000 cm	St. Dev.= 0.00000 cm

Approximated and Abel Transformed Data

I	Radius (cm)	Fringe Number	ρ/ρ_t	St. Dev. ρ/ρ_t
1	2.542	-1.33126	0.0514484	0.0047504
2	2.567	-1.25624	0.0532477	0.0045295
3	2.591	-1.18340	0.0550070	0.0043147
4	2.616	-1.11274	0.0567267	0.0041060
5	2.640	-1.04425	0.0584071	0.0039034
6	2.664	-0.97794	0.0600481	0.0037068
7	2.689	-0.91382	0.0616500	0.0035164
8	2.713	-0.85186	0.0632130	0.0033322
9	2.738	-0.79210	0.0647370	0.0031541
10	2.762	-0.73450	0.0662221	0.0029823
11	2.787	-0.67909	0.0676685	0.0028168
12	2.811	-0.62586	0.0690759	0.0026576
13	2.836	-0.57480	0.0704443	0.0025048
14	2.860	-0.52592	0.0717738	0.0023584
15	2.884	-0.47922	0.0730641	0.0022184
16	2.909	-0.43470	0.0743148	0.0020849
17	2.933	-0.39236	0.0755261	0.0019580
18	2.958	-0.35220	0.0766973	0.0018376
19	2.982	-0.31421	0.0778281	0.0017236
20	3.007	-0.27841	0.0789182	0.0016160
21	3.031	-0.24478	0.0799668	0.0015147
22	3.056	-0.21333	0.0809734	0.0014192
23	3.080	-0.18406	0.0819372	0.0013296
24	3.104	-0.15697	0.0828573	0.0012450
25	3.129	-0.13206	0.0837324	0.0011651
26	3.153	-0.10932	0.0845613	0.0010890
27	3.178	-0.08877	0.0853426	0.0010157
28	3.202	-0.07039	0.0860739	0.0009437
29	3.227	-0.05419	0.0867530	0.0008714
30	3.251	-0.04017	0.0873767	0.0007964
31	3.276	-0.02833	0.0879404	0.0007154
32	3.300	-0.01867	0.0884382	0.0006234
33	3.324	-0.01119	0.0888598	0.0005106
34	3.349	-0.00588	0.0891837	0.0003533
35	3.373	-0.00244	0.0894168	0.0001864
36	3.398	-0.00055	0.0895659	0.0000574
37	3.422	0.00000	0.0896156	0.0000000
38	3.447	0.00000	0.0896156	0.0000000
39	3.471	0.00000	0.0896156	0.0000000
40	3.496	0.00000	0.0896156	0.0000000
41	3.520	0.00000	0.0896156	0.0000000
42	3.544	0.00000	0.0896156	0.0000000
43	3.569	0.00000	0.0896156	0.0000000
44	3.593	0.00000	0.0896156	0.0000000
45	3.618	0.00000	0.0896156	0.0000000
46	3.642	0.00000	0.0896156	0.0000000
47	3.667	0.00000	0.0896156	0.0000000
48	3.691	0.00000	0.0896156	0.0000000
49	3.716	0.00000	0.0896156	0.0000000
50	3.740	0.00000	0.0896156	0.0000000

Interferogram Profile 5	3 Profiles averaged	
X Location of Profile	-0.99900 cm	St. Dev.= 0.02100 cm
Local Shock Angle	26.08335 °	St. Dev.= 0.38159 °
R Location of Shock	3.57400 cm	St. Dev.= 0.00045 cm
R Location of Model Surface	2.54000 cm	St. Dev.= 0.00000 cm

Approximated and Abel Transformed Data

I	Radius (cm)	Fringe Number	ρ/ρ_t	St. Dev. ρ/ρ_t
1	2.543	-1.04890	0.0544450	0.0051556
2	2.569	-0.98135	0.0554356	0.0061304
3	2.594	-0.91219	0.0565476	0.0068917
4	2.621	-0.84178	0.0577715	0.0073659
5	2.646	-0.77049	0.0590977	0.0075652
6	2.672	-0.69866	0.0605173	0.0075323
7	2.698	-0.62664	0.0620209	0.0073251
8	2.724	-0.55478	0.0635997	0.0070108
9	2.749	-0.48339	0.0652449	0.0066653
10	2.775	-0.41283	0.0669476	0.0063691
11	2.801	-0.34339	0.0686994	0.0061993
12	2.826	-0.27539	0.0704916	0.0062128
13	2.853	-0.20915	0.0723159	0.0064293
14	2.878	-0.14494	0.0741637	0.0068270
15	2.904	-0.08308	0.0760266	0.0073567
16	2.930	-0.02383	0.0778964	0.0079602
17	2.956	0.03252	0.0797644	0.0085842
18	2.981	0.08570	0.0816223	0.0091852
19	3.007	0.13544	0.0834613	0.0097307
20	3.033	0.18150	0.0852729	0.0101984
21	3.059	0.22362	0.0870481	0.0105755
22	3.084	0.26156	0.0887777	0.0108582
23	3.110	0.29508	0.0904522	0.0110522
24	3.136	0.32395	0.0920618	0.0111722
25	3.162	0.34797	0.0935959	0.0112431
26	3.188	0.36689	0.0950435	0.0112988
27	3.213	0.38053	0.0963926	0.0113811
28	3.239	0.38867	0.0976299	0.0115351
29	3.265	0.39113	0.0987406	0.0118027
30	3.291	0.38772	0.0997081	0.0122130
31	3.316	0.37825	0.1005126	0.0127737
32	3.342	0.36256	0.1011306	0.0134652
33	3.368	0.34047	0.1015325	0.0142383
34	3.394	0.31184	0.1016796	0.0150139
35	3.419	0.27649	0.1015178	0.0156818
36	3.446	0.23430	0.1009656	0.0160936
37	3.471	0.18512	0.0998823	0.0160489
38	3.497	0.12882	0.0979713	0.0152833
39	3.523	0.06527	0.0942942	0.0137487
40	3.549	0.02633	0.0922120	0.0090644
41	3.574	-0.01229	0.0885870	0.0017730
42	3.600	0.00000	0.0896156	0.0000000
43	3.626	0.00000	0.0896156	0.0000000
44	3.652	0.00000	0.0896156	0.0000000
45	3.678	0.00000	0.0896156	0.0000000
46	3.703	0.00000	0.0896156	0.0000000
47	3.729	0.00000	0.0896156	0.0000000
48	3.755	0.00000	0.0896156	0.0000000
49	3.781	0.00000	0.0896156	0.0000000
50	3.806	0.00000	0.0896156	0.0000000

Interferogram Profile 6	4 Profiles averaged	
X Location of Profile	-0.01400 cm	St. Dev.= 0.00900 cm
Local Shock Angle	26.18763 °	St. Dev.= 0.37471 °
R Location of Shock	4.12800 cm	St. Dev.= 0.00035 cm
R Location of Model Surface	2.54000 cm	St. Dev.= 0.00000 cm

Approximated and Abel Transformed Data

I	Radius (cm)	Fringe Number	ρ/ρ_t	St. Dev. ρ/ρ_t
1	2.551	-0.41308	0.0610874	0.0034877
2	2.590	-0.34621	0.0615825	0.0013437
3	2.629	-0.27851	0.0619669	0.0013172
4	2.667	-0.20855	0.0623105	0.0026717
5	2.706	-0.13520	0.0626751	0.0037734
6	2.744	-0.05758	0.0631142	0.0045131
7	2.783	0.02491	0.0636738	0.0048943
8	2.822	0.11267	0.0643930	0.0049433
9	2.861	0.20584	0.0653037	0.0047029
10	2.899	0.30437	0.0664314	0.0042399
11	2.938	0.40800	0.0677955	0.0036672
12	2.977	0.51629	0.0694094	0.0031914
13	3.015	0.62860	0.0712810	0.0031351
14	3.054	0.74417	0.0734129	0.0037135
15	3.093	0.86206	0.0758026	0.0048029
16	3.131	0.98121	0.0784425	0.0061728
17	3.170	1.10042	0.0813207	0.0076611
18	3.209	1.21840	0.0844208	0.0091626
19	3.247	1.33376	0.0877220	0.0105998
20	3.286	1.44500	0.0911995	0.0119088
21	3.325	1.55058	0.0948248	0.0130333
22	3.363	1.64888	0.0985647	0.0139226
23	3.402	1.73827	0.1023832	0.0145311
24	3.441	1.81702	0.1062398	0.0148177
25	3.479	1.88345	0.1100904	0.0147479
26	3.518	1.93584	0.1138870	0.0142937
27	3.557	1.97247	0.1175769	0.0134362
28	3.595	1.99165	0.1211033	0.0121676
29	3.634	1.99173	0.1244041	0.0104958
30	3.672	1.97108	0.1274107	0.0084558
31	3.711	1.92814	0.1300471	0.0061430
32	3.750	1.86143	0.1322274	0.0038816
33	3.789	1.76954	0.1338527	0.0030613
34	3.827	1.65116	0.1348050	0.0050030
35	3.866	1.50508	0.1349384	0.0079579
36	3.904	1.33024	0.1340613	0.0109721
37	3.943	1.12567	0.1319026	0.0135881
38	3.982	0.89059	0.1280358	0.0152972
39	4.021	0.62434	0.1216784	0.0152861
40	4.059	0.32648	0.1110048	0.0118817
41	4.098	-0.00329	0.0893999	0.0004861
42	4.137	0.00000	0.0896156	0.0000000
43	4.175	0.00000	0.0896156	0.0000000
44	4.214	0.00000	0.0896156	0.0000000
45	4.253	0.00000	0.0896156	0.0000000
46	4.292	0.00000	0.0896156	0.0000000
47	4.330	0.00000	0.0896156	0.0000000
48	4.369	0.00000	0.0896156	0.0000000
49	4.408	0.00000	0.0896156	0.0000000
50	4.446	0.00000	0.0896156	0.0000000

Interferogram Profile 7	4 Profiles averaged	
X Location of Profile	1.00000 cm	St. Dev.= 0.02100 cm
Local Shock Angle	26.18763 °	St. Dev.= 0.37471 °
R Location of Shock	4.63200 cm	St. Dev.= 0.00045 cm
R Location of Model Surface	3.11700 cm	St. Dev.= 0.00012 cm

Approximated and Abel Transformed Data

I	Radius (cm)	Fringe Number	ρ/ρ_t	St. Dev. ρ/ρ_t
1	3.123	2.96777	0.0997119	0.0098454
2	3.160	3.01881	0.1008037	0.0077411
3	3.197	3.06952	0.1018799	0.0060048
4	3.234	3.12059	0.1029829	0.0046987
5	3.271	3.17246	0.1041482	0.0039518
6	3.308	3.22536	0.1054052	0.0038413
7	3.345	3.27935	0.1067769	0.0042203
8	3.382	3.33426	0.1082815	0.0048212
9	3.419	3.38979	0.1099311	0.0054470
10	3.456	3.44545	0.1117330	0.0059917
11	3.493	3.50063	0.1136895	0.0064039
12	3.530	3.55459	0.1157988	0.0066625
13	3.567	3.60648	0.1180544	0.0067653
14	3.604	3.65533	0.1204461	0.0067256
15	3.641	3.70011	0.1229589	0.0065713
16	3.678	3.73969	0.1255757	0.0063460
17	3.714	3.77291	0.1282750	0.0061109
18	3.752	3.79855	0.1310321	0.0059422
19	3.788	3.81536	0.1338201	0.0059203
20	3.826	3.82210	0.1366082	0.0061082
21	3.862	3.81749	0.1393640	0.0065279
22	3.899	3.80030	0.1420518	0.0071523
23	3.936	3.76930	0.1446341	0.0079244
24	3.973	3.72331	0.1470705	0.0087754
25	4.010	3.66122	0.1493192	0.0096392
26	4.047	3.58197	0.1513347	0.0104573
27	4.084	3.48459	0.1530706	0.0111794
28	4.121	3.36822	0.1544769	0.0117624
29	4.158	3.23209	0.1555009	0.0121712
30	4.195	3.07558	0.1560861	0.0123791
31	4.232	2.89819	0.1561708	0.0123681
32	4.269	2.69958	0.1556872	0.0121316
33	4.306	2.47959	0.1545575	0.0116744
34	4.343	2.23824	0.1526896	0.0110168
35	4.380	1.97573	0.1499683	0.0101960
36	4.417	1.69249	0.1462402	0.0092622
37	4.454	1.38916	0.1412793	0.0082671
38	4.491	1.06664	0.1347173	0.0072252
39	4.528	0.72605	0.1258436	0.0060136
40	4.565	0.36883	0.1129229	0.0041383
41	4.602	-0.00330	0.0894088	0.0004196
42	4.639	0.00000	0.0896156	0.0000000
43	4.676	0.00000	0.0896156	0.0000000
44	4.713	0.00000	0.0896156	0.0000000
45	4.750	0.00000	0.0896156	0.0000000
46	4.787	0.00000	0.0896156	0.0000000
47	4.824	0.00000	0.0896156	0.0000000
48	4.861	0.00000	0.0896156	0.0000000
49	4.898	0.00000	0.0896156	0.0000000
50	4.935	0.00000	0.0896156	0.0000000

Interferogram Profile 8	3 Profiles averaged	
X Location of Profile	2.00600 cm	St. Dev.= 0.01200 cm
Local Shock Angle	26.08335 °	St. Dev.= 0.38159 °
R Location of Shock	5.11900 cm	St. Dev.= 0.00026 cm
R Location of Model Surface	3.69800 cm	St. Dev.= 0.00007 cm

Approximated and Abel Transformed Data

I	Radius (cm)	Fringe Number	ρ/ρ_t	St. Dev. ρ/ρ_t
1	3.702	5.91225	0.1261874	0.0228790
2	3.737	5.98010	0.1290340	0.0194437
3	3.771	6.03612	0.1313372	0.0160506
4	3.806	6.08594	0.1333830	0.0126852
5	3.841	6.13334	0.1353910	0.0094771
6	3.875	6.18044	0.1375218	0.0065987
7	3.910	6.22805	0.1398847	0.0042270
8	3.945	6.27583	0.1425434	0.0025571
9	3.979	6.32257	0.1455236	0.0018188
10	4.014	6.36640	0.1488178	0.0018841
11	4.049	6.40491	0.1523919	0.0022638
12	4.084	6.43542	0.1561901	0.0029041
13	4.118	6.45508	0.1601394	0.0039811
14	4.153	6.46104	0.1641560	0.0055413
15	4.188	6.45056	0.1681465	0.0074994
16	4.223	6.42110	0.1720153	0.0097250
17	4.257	6.37047	0.1756656	0.0120875
18	4.292	6.29687	0.1790044	0.0144631
19	4.326	6.19894	0.1819439	0.0167396
20	4.361	6.07583	0.1844059	0.0188220
21	4.396	5.92722	0.1863220	0.0206310
22	4.431	5.75330	0.1876380	0.0221098
23	4.466	5.55483	0.1883125	0.0232245
24	4.500	5.33305	0.1883203	0.0239617
25	4.535	5.08968	0.1876519	0.0243345
26	4.570	4.82686	0.1863147	0.0243750
27	4.605	4.54707	0.1843301	0.0241315
28	4.639	4.25305	0.1817366	0.0236637
29	4.674	3.94769	0.1785836	0.0230283
30	4.708	3.63391	0.1749329	0.0222743
31	4.743	3.31452	0.1708509	0.0214276
32	4.778	2.99208	0.1664066	0.0204901
33	4.813	2.66873	0.1616635	0.0194444
34	4.847	2.34597	0.1566650	0.0182670
35	4.882	2.02450	0.1514240	0.0169630
36	4.917	1.70396	0.1458899	0.0155921
37	4.952	1.38276	0.1399050	0.0142789
38	4.986	1.05772	0.1331071	0.0131226
39	5.021	0.72392	0.1246884	0.0118700
40	5.056	0.37434	0.1126245	0.0091776
41	5.090	-0.00044	0.0895877	0.0001232
42	5.125	0.00000	0.0896156	0.0000000
43	5.160	0.00000	0.0896156	0.0000000
44	5.194	0.00000	0.0896156	0.0000000
45	5.229	0.00000	0.0896156	0.0000000
46	5.264	0.00000	0.0896156	0.0000000
47	5.299	0.00000	0.0896156	0.0000000
48	5.334	0.00000	0.0896156	0.0000000
49	5.368	0.00000	0.0896156	0.0000000
50	5.403	0.00000	0.0896156	0.0000000

1. Report No.	2. Government Accession No.	3. Recipient's Catalog No.
NASA TM 88227		

4. Title and Subtitle	5. Report Date
INTERFEROMETRIC DATA FOR A SHOCK-WAVE/BOUNDARY-LAYER INTERACTION	September 1986
	6. Performing Organization Code

7. Author(s)	8. Performing Organization Report No.
Stephen E. Dunagan, James L. Brown, and John B. Miles	A-86158
	10. Work Unit No.

9. Performing Organization Name and Address	11. Contract or Grant No.
Ames Research Center Moffett Field, CA 94035	

12. Sponsoring Agency Name and Address	13. Type of Report and Period Covered
National Aeronautics and Space Administration Washington, DC 20546	Technical Memorandum
	14. Sponsoring Agency Code 505-61-51

15. Supplementary Notes

Point of Contact: Stephen E. Dunagan, Ames Research Center, MS 247-1, Moffett Field, CA 94035
(415) 694-6653 or FTS 464-6653

16. Abstract

An experimental study of the axisymmetric shock-wave/turbulent boundary-layer strong-interaction flow generated in the vicinity of a cylinder-cone intersection has been conducted. The present data are useful in the documentation and understanding of compressible turbulent strong-interaction flows, and are part of a more general effort to improve turbulence modeling for compressible two- and three-dimensional strong viscous/inviscid interactions. The nominal free-stream Mach number was 2.85. Tunnel total pressures of 1.7 and 3.4 atm provided Reynolds number values of $18 \cdot 10^6$ and $36 \cdot 10^6$ based on model length. Three cone angles (12.5°, 20°, and 30°) were studied giving negligible, incipient, and large scale flow separation respectively. The initial cylinder boundary layer upstream of the interaction had a boundary-layer thickness of 1.0 cm. The subsonic layer of the cylinder boundary layer was quite thin, and in all cases, the shock wave penetrated a significant portion of the boundary layer. Owing to the thickness of the cylinder boundary layer, considerable structural detail was resolved for the three shock-wave/boundary-layer interaction cases considered.

The primary emphasis in this study was on the application of the holographic interferometry technique to these flow cases. The density field was deduced from an interferometric analysis based on the Abel transform. Supporting data were obtained using a 2-D laser velocimeter, as well as mean wall pressure and oil flow measurements. The attached flow case was observed to be steady, while the separated cases exhibited shock unsteadiness. Comparisons with Navier-Stokes computations using a two-equation turbulence model are presented. The study illustrates the utility of holographic interferometry for detailed instantaneous flow-field characterization and provides documented data useful in the evaluation of computational schemes.

17. Key Words (Suggested by Author(s))	18. Distribution Statement
Holographic interferometry Viscous/inviscid interaction Turbulent boundary layer Shock wave Supersonic flow symmetric flow	Unlimited Subject category - 02

19. Security Classif. (of this report)	20. Security Classif. (of this page)	21. No. of Pages	22. Price*
Unclassified	Unclassified	267	A12

*For sale by the National Technical Information Service, Springfield, Virginia 22161

End of Document